

UC Santa Cruz

UC Santa Cruz Electronic Theses and Dissertations

Title

Drug Discovery Efforts for Antibiotic Resistant Bacteria and Anti-Inflammatories

Permalink

<https://escholarship.org/uc/item/3wf039cz>

Author

Lau, Tannia

Publication Date

2021

Copyright Information

This work is made available under the terms of a Creative Commons Attribution License, available at <https://creativecommons.org/licenses/by/4.0/>

Peer reviewed|Thesis/dissertation

UNIVERSITY OF CALIFORNIA
SANTA CRUZ

**DRUG DISCOVERY EFFORTS FOR ANTIBIOTIC RESISTANT BACTERIA
AND ANTI-INFLAMMATORIES**

A dissertation submitted in partial satisfaction
of the requirements for the degree of

DOCTOR OF PHILOSOPHY

in

MOLECULAR, CELL AND DEVELOPMENTAL BIOLOGY

by

Tannia A. Lau

March 2021

The Dissertation of Tannia A. Lau is
approved:

Professor Scott Lokey, Chair

Professor Victoria Auerbuch-Stone

Professor John MacMillan

Assistant Professor Susan Carpenter

Quentin Williams
Interim Vice Provost and Dean of Graduate Studies

Copyright © by

Tannia A. Lau

2021

Table of Contents

List of Figures	vii
Abstract	xi
Acknowledgements	xiv
CHAPTER 1	1
1.1 Synthetic Cyclic Peptomers as Type III Secretion System	
Inhibitors	2
Summary	3
Reprint.....	6
1.2 Broad-spectrum inhibitors of the Type III secretion system	39
Summary	40
Abstract.....	42
Introduction	44
Results.....	46
Structure-activity relationship study of cyclic peptomers.	46
Cyclic peptomers affect the T3SS basal body.	49
Cyclic peptomers do not inhibit T3SS gene expression.	50
Cyclic peptomers block <i>Chlamydia</i> infection.	52
Structure activity relationship analysis resulted in a T3SS inhibitor with an IC ₅₀ in the low μM range.	53

Cyclic peptomers act as broad-spectrum, but specific, inhibitors of the injectisome T3SS.	54
Cyclic peptomers decrease cell envelope localization of the T3SS basal body protein YscD and inhibit secretion of T3SS effector proteins, but do not inhibit T3SS gene expression.	55
Cyclic peptomers strongly inhibit <i>Chlamydia</i> primary and secondary infection.	57
Discussion	58
Structure activity relationship analysis resulted in a T3SS inhibitor with an IC ₅₀ in the low μM range.	58
Cyclic peptomers act as broad-spectrum, but specific, inhibitors of the injectisome T3SS.	59
Cyclic peptomers decrease cell envelope localization of the T3SS basal body protein YscD and inhibit secretion of T3SS effector proteins, but do not inhibit T3SS gene expression.	60
Cyclic peptomers strongly inhibit <i>Chlamydia</i> primary and secondary infection.	61
Materials and Methods	63
Acknowledgements	74
References	138
CHAPTER 2	148
Summary	149

2.1 Macrophage cytological profiling and anti-inflammatory drug discovery	153
Reprint.....	154
Abstract.....	158
Introduction.....	158
Results and Discussion	161
Optimization of BMDM conditions: BMDMs not suitable for large HCS	161
Cytological profiling comparison for HeLa and Raw264.7 +/- LPS	163
HeLa CP outperforms Raw264.7 CP to associate target classes	163
Bioactive natural product fraction comparisons based on CP-Score.....	166
Conclusion.....	168
2.2 High-content image-based screening and deep learning for the detection of anti-inflammatory drug leads	169
Abstract.....	170
Introduction	171
Workflow to identify anti-inflammatory hits using deep learning	173
Results and Discussion	175

Measured morphological feature changes between unstimulated and LPS-stimulated Raw264.7 cells	175
Supervised deep learning parameters: input format and DNN model	177
Training a deep neural network classifier on images of unstimulated and LPS-stimulated macrophage controls	180
Deep learning primary hits	181
Selected deep learning hits that reverse the LPS-stimulated Raw264.7 phenotype	182
Quantitative analysis of inflammatory cytokines released from drug treated LPS-stimulated Raw264.7 cells.....	183
Conclusion.....	188
Materials and Methods	191
2.3 Online image viewer database:	
https://immunocp.pbsci.ucsc.edu/	233
HCS image accessibility challenges	234
The HCS project and data generated	234
Overcoming image accessibility barriers with costume-built online image database.....	236

List of Figures

1.2	FIGURES FOR: Broad spectrum inhibitors of the T3SS	75
Figure 1:	Stereochemistry scan of cyclic peptomers results in a more potent derivative, 4EpDN.	76
Figure 2:	Sarcosine replacement of 4EpDN at position 1 or 2 eliminates activity.....	77
Figure 3:	Effect of cyclic peptomers on secretion of <i>Yersinia Ysa</i> T3SS substrates.....	78
Figure 4:	Cyclic peptomers inhibit the Salmonella SPI-1 T3SS.	79
Figure 5:	The cyclic peptomer 4EpDN disrupts localization of the Yersinia T3SS basal body component YscD.....	80
Figure 6:	Cyclic peptomers do not affect transcription of T3SS genes in <i>P. aeruginosa</i>	81
Figure 7:	The cyclic peptomer 4EpDN inhibits secretion of the effector protein ExoS, but not the regulator ExsE.	82
Figure 8:	Cyclic peptomers do not affect the twin arginine translocation (Tat) system.....	83
Figure 9:	The cyclic peptomer 4EpDN inhibits <i>Chlamydia</i> infection.....	84
1.2	SUPPORTING INFORMATION FOR: Broad-spectrum inhibitors of the Type III secretion system	91

Figure S1: 1EpDN alanine/Sarcosine scan suggests peptoid sidechains are important for biological activity.....	95
Figure S2: Secretion of <i>Salmonella</i> T3SS substrate in the presence of non-ionic detergents.	96
Figure S3: Cyclic peptomers do not affect secretion of flagellar proteins.	97
Figure S4: Relationship between solubility and activity of cyclic peptomers..	98
Figure S5: Cyclic peptomers do not affect transcription of T3SS genes in <i>Salmonella</i>	99
Figure S6: Effect of cyclic peptomers on HeLa cells.	100
Figure S7: Characterization of cyclic peptomers.	101
Figure 1. HeLa cells exhibit limited biological features compared to macrophages, Raw264.7 , and primary bone marrow derived macrophages (BMDM), under LPS inflammatory stimuli.	159
Figure 2. Primary BMDMs stimulated with LPS (TLR4/TLR2) and LPS-EB Ultrapure (TLR4) exhibit dramatic morphological changes in comparison to unstimulated BMDMs.	162
Figure 3. Comparison of in-class target annotation vs out-of-class annotation KS-test p-values <0.01 in Raw264.7 and HeLa cells for SelleckChem.....	165
Table 1. List of unique and shared target drug classes for Raw264.7_all and HeLa.	165
Figure 4. Comparison of Active Natural Product Fractions based on CP Score.	167

2.2	FIGURES FOR: High-content image-based screening and deep learning for the detection of anti-inflammatory drug leads	198
	Figure 1. Workflow to identify anti-inflammatory hits using deep learning. ..	199
	Figure 2. Measured differences in Raw264.7 cellular features with LPS stimulation.	200
	Figure 3. Deep learning parameters: image resolution and DNN models....	202
	Figure 4. Best classification performance. Image resolution r1080 and cr540 and DNN architecture: CTM, EM(ss1), and EM(ss2)	203
	Figure 5. The largest target classes from deep learning hits are PI3K, MEK, mTOR, and natural products.	204
	Figure 6. Deep learning selected hits exhibit the reversal of the LPS-phenotype.....	208
	Figure 7. Deep learning selected hits exhibit anti-inflammatory effects based on pro-inflammatory mediators' expression profiles.	209
2.2	SUPPORTING INFORMATION FOR:	210
	High content image-based screening and deep learning for the detection of anti-inflammatory drug leads	210
	SI Table 1. Deep learning hits for CTM, EM(ss1), and EM(ss2)	211
	SI Table 2. Comparison of target classes for EM(ss1) and EM(ss2)	218
	SI Table 3. Deep learning primary hits for dose response assay.....	219
	SI Figure 1. iNOS dose-response curves.....	221
	SI Figure 2. 32-plex cytokine/chemokine data	223

2.3 FIGURES FOR Online Image Viewer Database	237
Figure 1. Experiment tab: displays a list of experiments and shows the entire drug plate layout.	237
Figure 2. Molecule tab: displays a list of molecules and provides search options to narrow your search.	239

Abstract

**Drug Discovery Efforts for Antibiotic Resistant Bacteria
and Anti-Inflammatories**

by

Tannia A. Lau

Millions of people world-wide are affected by diseases and conditions related to microbial pathogens and the immune system. The demand for new therapies against antibiotic resistant bacteria and anti-inflammatories is urgent. My dissertation encompasses two distinct avenues of modern drug discovery: 1) A chemical biology approach to improve the physical properties and potency of novel cyclic peptide inhibitors to combat the virulence of aggressive gram negative bacteria by inhibiting the Type 3 Secretion System (T3SS) and 2) The development of a high-content image-based screening assay for the detection of anti-inflammatories. Chapter 1 describes the structural activity relationship studies of a novel cyclic peptide T3SS inhibitor and its potency against various gram negative bacteria T3SS. Chapter 2 describes the development of a high content image-based screen using macrophages and pro-inflammatory endotoxin lipopolysaccharide (LPS). We compare this screening platform to classic HeLa cytological profiling (CP) and observe the limitations of image based feature extraction techniques to cluster by MOA based on similarity

profiles. Furthermore, we use supervised deep learning approaches to identify compounds that reverse the LPS-stimulated phenotype and confirm the selected deep learning hits exhibit an immunomodulatory response to LPS. Lastly we briefly describe our efforts in developing a custom-built online database for viewing the images generated from the HCS screen. This database brings side-by-side comparisons of macrophages treated with compounds \pm LPS stimuli and both stain sets. In addition, it's searchable and includes compound metadata associated with every image, allowing for quick inspection of the images.

This work is dedicated to

my brother and hero,

Joe Lau

the love of my life,

Elmar Mair

my uncle and aunty,

Roger and Christine Begay

and to my ancestors,

whose resilience brought me to this achievement

Ahéhee'

(Thank you in Navajo)

Acknowledgements

This dissertation would not have been possible without my friends, family, and mentors' love and support. I would first like to thank my graduate advisor, Professor Scott Lokey, for providing me the freedom and resources to explore various areas of the drug discovery realm and my passion for promoting diversity in STEM. I admire his honesty, humor, and wit, but most of all, his optimism for science. Thanks to his training and support, I have succeeded in numerous goals and awards. That has propelled me to be a competitive scientist as I take my next career steps. Scott was incredibly kind, understanding, and patient as the world spun into chaos from 2020-2021 due to the COVID-19 pandemic that highlighted and magnified racial inequalities and many other injustices. During these sad and challenging times I feel incredibly fortunate and honored to have Scott as my Ph.D. advisor. I admire his compassion and felt that he genuinely cared for my success and well-being. His support, guidance, and advice have profoundly impacted my development as a scientist, and I am forever grateful for his time and mentorship.

I would like to acknowledge my thesis committee members Victoria Auerbuch Stone, John MacMillan, and Susan Carpenter, for their feedback and mentorship throughout my graduate career. Their dedication and passion for research and teaching are admirable. They will serve as a compass as I navigate my science career. Thanks for

the collaboration and letters of support for the NIH pre-doctoral F31 fellowship. This fellowship allowed me to focus and gain valuable graduate research training experiences.

I would like to thank the following for their contributions to this work. Lokey researchers for everything related to cyclic peptides. Joshua Schwochert and Shero Lao for cyclic peptide design and synthesis training. Victoria Klein, Colin Kelly, Andrew Ly, Cameron Pye, Matthew Naylor, Chad Townsend, and Grant Koch for assisting and advising with cyclic peptide library design and characterization studies (PAMPA, solubility, and NMR). Special thanks, Colin, for always taking the time to answer all of my chemistry questions. Akshar Lohith, for fantastic bioinformatics skills and willingness to assist with large dataset analyses and data visualizations. Thanks for taking the time to answer my data management and statistics questions. Alejandro Cabrera-Cortez, my talented mentee, for his work and dedication towards the cyclic peptomer T3SS inhibitor project. Thanks for bringing positive energy and enthusiasm to the lab and the research. Andrew Ly, for your generous time and help with synthesis questions. Grant, it was a pleasure being office buddies and making the holiday short films. We need to finish writing and filming our 2020 movie! The Auerbuch Stone Lab collaborators, Hahn Lam, and Adam Lentz, for their hard work and dedication regarding the microbiology and the T3SS studies. Li Zhang for keeping the LTQ and OrbiTrap mass spectrometry operating and in good shape. Jack Lee assisted with proton NMRs and a brief attempt at DOSY experiments. Walter Bray for assisting and

advising for all things related to chemical screening assays. The Carpenter Lab for sharing their resources, advice, and guidance for the innate immunity studies (BMDMs and cytokine assays). The MacMillan Lab for sharing your resources and expertise about natural product chemistry/biochemistry, especially Aswad Khadilkar and Anam Shaikh. Britney Hernandez for managing the chemical screening center, being dependable, fixing screening center equipment, and enthusiasm to learn high content screening assays. Elmar Mair for taking the time to design and implement the convolutional deep learning neural network studies. Thanks for all of your patience and assistance with python scripts and deep learning discussions. Finally, thanks to Joe Lau for taking evenings and weekends to develop the website that displays all of the cell images generated from the HCS assay.

I owe all of my success to my eldest brother Joe for being a huge role model in my life. We faced several hardships involving a mostly absent father and an alcoholic mother and her struggles. That involved her three-year imprisonment and shortly after her release, grappling with her stage four lymphoma that quickly ended in defeat. It was up to Joe to raise and care for us during all of this. He used a lot of humor and kept us interested in our education. I recognize his strength and perseverance, and it motivates me to keep reaching for the stars, so his sacrifices are not in vain. This Ph.D. is for you, Joe Joe!

Fortunately, with the support of STEM diversity programs and great mentorship throughout my academic career, I overcame those disadvantaged barriers and built a research career focusing on drug discovery with an emphasis on immunology. I am eternally grateful to all of the mentors who provided me with a welcoming and engaging scientific environment to thrive and succeed my dreams. Thank you to all of the following: Angus Dawe, Paul Laybourn, Mark Swanson, John Kurhanewicz, Sulyman Barkho, Patricia Jennings, Yvonne Vercoulen, Jeroen Roose, Daniel Lafkas, Ruchi Shah, Marjoke Debets, Michelle Hall, and Scott Lokey.

I am also grateful for the UCSC STEM diversity program directed by Yuliana Ortega, Xingci Situ, and Melissa Jurica, who made this graduate journey possible. Thank you for being fantastic role models and ensuring we have all of the tools and support that we need to succeed. It was an honor to work with Yuli and Xingci as vice-president of the UCSC SACNAS Chapter with the best team of proactive and passionate students, Amanda Brambila, Jesse Cisneros, Joanna Tran, and Francisco Mendez. The STEM diversity team's mentorship, support, and friendship allowed us to fulfill our goals of promoting diversity in STEM and give back to the community. Importance of these programs, interactions, and community-building events are critical for student success. I am eternally grateful for everyone who puts their heart and soul into them. It certainly changed my life, and I will continue to pass it forward.

To my graduate cohort, thank you for all of the fun times. I will miss celebrating our successes with karaoke and sushi. Special thanks to all of the following for your friendship. Amanda Brambila, for your love and support and for being the best conference buddy. Oscar Cazares, for your love and support, including the tough love where you made me get up at 6 am to exercise with you. Sydney Weiser, for letting me be on your championship-winning inner tube water polo team and for your generous time helping me with python scripts. Braden Larson, for your fruitful discussions and singing Sweet Cat of Mine at karaoke.

With lots of love and admiration, I would like to thank my husband Elmar for all of his love and support during my graduate career. He fills my life with adventure and much laughter. Thank you for all of your encouragement and unconditional love.

Finally, thanks to all of my friends and family who supported and encouraged my dreams to get a Ph.D.

The research presented in this dissertation is the result of many collaborative efforts. I specifically acknowledge the fantastic collaborative efforts with Victoria Auerbuch Stone's lab, especially with Hahn Lam and Adam Lentz, who performed all of the microbiology work.

The text of this dissertation includes reprints of the following published material:

Hanh Lam, Joshua Schwochert , Yongtong Lao , Cameron Lloyd , **Tannia Lau**, Cameron Lloyd, Justin Luu , Olivia Kooner, Jessica Morgan, Scott Lokey and Victoria Auerbuch. "Synthetic Cyclic Peptomers as Type III Secretion System Inhibitors," Antimicrobial Agents and Chemotherapy, April 2017; 61(9):e00060-17. doi: 10.1128/AAC.00060-17

Tannia A. Lau, Walter M. Bray, R. Scott Lokey. "Macrophage Cytological Profiling and Anti-Inflammatory Drug Discovery," ASSAY and Drug Development Technologies, January 2019; 17, 14-16. doi.org/10.1089/adt.2018-894

The text of this dissertation includes data from the following manuscript under review and available on bioRxiv:

Hanh N. Lam*, **Tannia Lau***, Adam Lentz, Jessica Sherry, Alejandro Cabrera-Cortez, Karen Hug, Joanne Engel, R. Scott Lokey, Victoria Auerbuch. "Developing cyclic peptomers as broad-spectrum gram negative bacterial Type III secretion system inhibitors," *Co-first authors.

bioRxiv2020.08.03.235622;doi.org/10.1101/2020.08.03.235622.

The text of this dissertation includes data from the following manuscript in preparation:

Tannia A. Lau, Elmar Mair, R. Scott Lokey (2021). "High Content Screening and Deep Learning for the Detection of Anti-Inflammatory Drug Leads". In preparation.

The journals that published the papers, *Antimicrobial Agents and Chemotherapy* and *ASSAY and Drug Development Technologies*, both allow reproduction of published articles in the author's dissertation.

R. Scott Lokey, Victoria Auerbuch, and Hanh Lam listed in these publications directed and supervised the research which forms the basis of this dissertation. I acknowledge the permission from the co-authors and copyright holders giving their approval for the material to be used in this dissertation, and I also acknowledge the contribution of all co-authors to the publications.

Chapter 1 and 2 of this dissertation are multi-author publications.

Chapter 1.1 and 1.2: In collaboration with the Auerbuch Stone Lab. I am responsible for the cyclic peptide solubility assay figure (Ch. 1.1, SFig. 4.) and I am responsible for the design, synthesis, characterization, for all of the cyclic peptides used in the study for Chapter 1.2.

Chapter 2.1 and 2.2: Working with the UCSC Chemical Screening Center I developed the high content image-based screen with macrophages and lipopolysaccharide to compare MOA clustering performance and natural product bioactivity to HeLa CP (Ch. 2.1) and identify anti-inflammatories (Ch. 2.2). With the exception of the bioinformatics analysis using the KS-test (Ch. 2.1, Fig. 3A) and the design and implementation of the Deep Neural Network models (Ch. 2.2, Fig. 3) the contributions were entirely mine.

Chapter 2.3: I am responsible for the cell image data and the design of the website user interface. Joe developed the entire website with JavaScript using the nodeJS framework.

CHAPTER 1

Type Three Secretion System

Cyclic Peptomer Inhibitors

1.1 Synthetic Cyclic Peptomers as Type III Secretion System

Inhibitors

The following work was completed as a collaboration between all of the following authors:

Hanh Lam,^a Joshua Schwochert,^b Yongtong Lao,^b **Tannia Lau**,^b Cameron Lloyd,^a Justin Luu,^a Olivia Kooner,^a Jessica Morgan,^b Scott Lokey,^b Victoria Auerbuch^a

^aDepartment of Microbiology and Environmental Toxicology University of California Santa Cruz, Santa Cruz, California, USA

^bDepartment of Chemistry and Biochemistry University of California Santa Cruz, Santa Cruz, California, USA

Summary

Chapter 1 describes chemical biology approaches to improve the physical properties and potency of novel cyclic peptide inhibitors to combat the virulence of aggressive gram negative bacteria by inhibiting the Type 3 Secretion System (T3SS). Microbial pathogens continue to be a major global health threat. There is an urgent demand for new antibiotics and anti-infective drugs to address multidrug resistant bacteria and new pathogens. Since microbes have the ability to evade and evolve sophisticated strategies to subvert host defenses. Treatment with antibiotics not only leads to resistance, but it also destroys our healthy microbiota. In contrast to traditional antibiotics, which kill bacteria, virulence blockers suppress the pathogenicity of bacteria without killing or inhibiting growth. Our chemical biology approach to blocking virulence will provide new opportunities to understand microbe interactions and may pave the way for new therapeutic strategies. We aim to improve the physical properties and potency of novel cyclic peptide inhibitors to combat the virulence of aggressive gram negative bacteria by inhibiting the T3SS. The T3SS is a conserved needle-like appendage that bacteria use to secrete toxins (Yops) into the host cell to suppress its defenses against the bacteria (Cornelis & Van Gijsegem, 2000). Studies have shown that marine-derived natural products piericidin A1 and Mer-A 2026B are effective inhibitors of T3SS protein secretion in *Yersinia pseudotuberculosis* (Duncan et al., 2016) (Morgan et al., 2017), although the toxicity of these compounds to mammalian cells raises questions about their therapeutic potential. A T3SS inhibitor screen in collaboration between the Lokey and Auerbuch Stone labs yielded a peptoid containing analog of cyclic peptide

epiphepropeptin D (EpD). Peptoids, or N-alkylglycines, are amino acids that are modified such that the side chain is connected to the amide nitrogen instead of the alpha carbon. Peptide-to-peptoid substitutions in EpD led to increased activity relative to the parent compound and yielded compounds that were more potent than the published inhibitors in an NF-kappaB luciferase assay designed to report on T3SS-mediated insertion of inflammatory proteins into mammalian cells. In addition, the position and length of the peptoid side chains influenced the activity of the YopE secretion assay. These initial results confirm that the position and nature of the peptoid group influenced activity. Taken together these novel synthetic cyclic peptomers, inspired by the natural product phepropeptin D, are a new class of T3SS inhibitors that significantly decrease type III secretion in *Y. pseudotuberculosis* and *Psuedomonas aeruginosa* without affecting bacterial survival, motility, or other secretion systems, and without host cell toxicity (Lam et al., 2017)

References

- Cornelis, G. R., & Van Gijsegem, F. (2000). Assembly and function of type III secretory systems. *Annu Rev Microbiol*, *54*, 735-774. doi:10.1146/annurev.micro.54.1.735
- Duncan, M. C., Wong, W. R., Dupzyk, A. J., Bray, W. M., Linington, R. G., & Auerbuch, V. (2016). Erratum for Duncan et al., An NF-kappaB-Based High-Throughput Screen Identifies Piericidins as Inhibitors of the Yersinia pseudotuberculosis Type III Secretion System. *Antimicrob Agents Chemother*, *60*(7), 4427. doi:10.1128/AAC.00973-16
- Lam, H., Schwochert, J., Lao, Y., Lau, T., Lloyd, C., Luu, J., . . . Auerbuch, V. (2017). Synthetic Cyclic Peptomers as Type III Secretion System Inhibitors. *Antimicrob Agents Chemother*, *61*(9). doi:10.1128/AAC.00060-17
- Morgan, J. M., Duncan, M. C., Johnson, K. S., Diepold, A., Lam, H., Dupzyk, A. J., . . . Auerbuch, V. (2017). Piericidin A1 Blocks Yersinia Ysc Type III Secretion System Needle Assembly. *mSphere*, *2*(1). doi:10.1128/mSphere.00030-17

Reprint:

Hanh Lam, Joshua Schwochert , Yongtong Lao , Cameron Lloyd , **Tannia Lau**,
Cameron Lloyd, Justin Luu , Olivia Kooner, Jessica Morgan, Scott Lokey and Victoria
Auerbuch. “Synthetic Cyclic Peptomers as Type III Secretion System Inhibitors,”
Antimicrobial Agents and Chemotherapy, April 2017; 61(9):e00060-17. doi:
10.1128/AAC.00060-17



Synthetic Cyclic Peptomers as Type III Secretion System Inhibitors

Hanh Lam,^a Joshua Schwochert,^b Yongtong Lao,^b Tannia Lau,^b Cameron Lloyd,^a Justin Luu,^a Olivia Kooner,^a Jessica Morgan,^b Scott Lokey,^b Victoria Auerbuch^a

Department of Microbiology and Environmental Toxicology^a and Department of Chemistry and Biochemistry,^b University of California Santa Cruz, Santa Cruz, California, USA

ABSTRACT Antibiotic-resistant bacteria are an emerging threat to global public health. New classes of antibiotics and tools for antimicrobial discovery are urgently needed. Type III secretion systems (T3SS), which are required by dozens of Gram-negative bacteria for virulence but largely absent from nonpathogenic bacteria, are promising virulence blocker targets. The ability of mammalian cells to recognize the presence of a functional T3SS and trigger NF- κ B activation provides a rapid and sensitive method for identifying chemical inhibitors of T3SS activity. In this study, we generated a HEK293 stable cell line expressing green fluorescent protein (GFP) driven by a promoter containing NF- κ B enhancer elements to serve as a readout of T3SS function. We identified a family of synthetic cyclic peptide-peptoid hybrid molecules (peptomers) that exhibited dose-dependent inhibition of T3SS effector secretion in *Yersinia pseudotuberculosis* and *Pseudomonas aeruginosa* without affecting bacterial growth or motility. Among these inhibitors, EpD-3'N, EpD-1,2N, EpD-1,3'N, EpD-1,2,3'N, and EpD-1,2,4'N exhibited strong inhibitory effects on translocation of the *Yersinia* YopM effector protein into mammalian cells (>40% translocation inhibition at 7.5 μ M) and showed no toxicity to mammalian cells at 240 μ M. In addition, EpD-3'N and EpD-1,2,4'N reduced the rounding of HeLa cells caused by the activity of *Yersinia* effector proteins that target the actin cytoskeleton. In summary, we have discovered a family of novel cyclic peptomers that inhibit the injectisome T3SS but not the flagellar T3SS.

KEYWORDS *Yersinia*, type III secretion system, T3SS, cyclic peptides, peptoids, peptomers, virulence blocker, *Pseudomonas aeruginosa*

As currently available antibiotics become ineffective due to the rise in antibiotic resistance among pathogenic bacteria, development of completely new classes of antibiotics is critical (1). Classic antibiotics target pathogens and commensal bacteria indiscriminately; therefore, their use puts selective pressure on both populations. Because of the abundance of commensals within a mammalian host (10^{13} to 10^{14}), antibiotic resistance is thought to arise more frequently in commensal bacteria and is horizontally transferred to pathogens (2–4). In contrast to classic antibiotics, virulence blockers are compounds that selectively inhibit the expression or function of a virulence factor in a pathogen or group of pathogens (5). Advantages of virulence blockers are twofold. For one, selective pressure on a limited number of microbes, i.e., only pathogens expressing the molecular target of the virulence blocker, should limit the evolution of resistance (6). Second, the decreased commensal killing by virulence blockers has the potential to preserve a healthy microbiota, which is critical for maintaining gut homeostasis and defending against opportunistic pathogens (7, 8).

Type III secretion systems (T3SS) are bacterial appendages required by dozens of pathogens to cause disease, including *Salmonella*, enteropathogenic *Escherichia coli* (EPEC), *Shigella*, *Pseudomonas*, and *Yersinia*, but they are largely absent in nonpatho-

Received 13 January 2017 Returned for modification 19 February 2017 Accepted 10 June 2017

Accepted manuscript posted online 26 June 2017

Citation Lam H, Schwochert J, Lao Y, Lau T, Lloyd C, Luu J, Kooner O, Morgan J, Lokey S, Auerbuch V. 2017. Synthetic cyclic peptomers as type III secretion system inhibitors. *Antimicrob Agents Chemother* 61:e00060-17. <https://doi.org/10.1128/AAC.00060-17>.

Copyright © 2017 American Society for Microbiology. All Rights Reserved.

Address correspondence to Scott Lokey, slokey@ucsc.edu, or Victoria Auerbuch, vastone@ucsc.edu.

Downloaded from <http://aac.asm.org/> on April 4, 2018 by guest

genic bacteria (9). Bacteria use T3SS to inject bacterial effector proteins into target host cells to manipulate host processes for the benefit of the pathogen. Seven T3SS injectisome families have been identified (9) and share a number of homologous membrane-associated components with the flagellar basal body (10). While many aspects of T3SS structure are similar among different T3SS families, the repertoire of encoded T3SS effector proteins is unique for each genus or even species (11, 12). For example, pathogenic *Yersinia* species, which include the plague agent *Yersinia pestis* and the enteropathogens *Yersinia enterocolitica* and *Yersinia pseudotuberculosis*, and the opportunistic pathogen *Pseudomonas aeruginosa* encode a Ysc family T3SS that contributes to virulence. However, the *Yersinia* T3SS translocates the *Yersinia* gutter proteins (Yops) YopH, YopE, YopM, YopO, YopJ, and YopT, whereas *Pseudomonas* secretes the proteins ExoS, ExoU, and ExoT (13, 14). *Yersinia* avoids phagocytosis by using effectors targeting the actin polymerization process and signaling pathways. YopE has RhoGAP activity and leads to depolymerization of actin stress fibers in eukaryotic cells (15, 16). YopH, a protein tyrosine phosphatase, antagonizes several signaling pathways associated with focal adhesions (17, 18). YopO, also known as YpkA, binds to actin monomers, blocking actin filament polymerization, and sequesters actin polymerization regulators, which disrupts phagocytosis (19).

P. aeruginosa is a major cause of hospital-acquired infections (20, 21), and its T3SS is important in infection establishment, dissemination, and survival in animals (14, 22). *P. aeruginosa* is resistant to a number of antibiotics because its outer membrane is highly restrictive (20, 21, 23); therefore, new drugs to treat *P. aeruginosa* are of high interest. The widespread importance and structural conservation of T3SS among bacterial pathogens make T3SS optimal targets for antimicrobial agents.

NF- κ B (nuclear factor kappa light chain-enhancer of activated B cells) is a family of mammalian transcription factors involved in inflammation and development (24). *Yersinia* lacking the YopHEMOJT T3SS effector proteins but expressing an otherwise functional Ysc T3SS triggers NF- κ B activation in HEK293T cells, while *Yersinia* lacking the YopB translocator protein essential for translocation of T3SS cargo inside host cells does not activate NF- κ B (25). Previously, we used host NF- κ B-driven luciferase in HEK293T cells as a readout for *Yersinia* T3SS activity in a pilot T3SS inhibitor screen and identified a family of T3SS inhibitors called piericidins (26). In order to improve our screening strategy, we generated a HEK293 stable cell line expressing an NF- κ B-driven green fluorescent protein (GFP) reporter gene. Using this cell line, we identified a group of eight cyclic peptomers that inhibit type III secretion in *Yersinia* and *Pseudomonas aeruginosa*.

RESULTS

Development and use of an NF- κ B-GFP stable cell line for identification of T3SS inhibitors. To reduce the variability and batch effects from transient transfection of an NF- κ B reporter, we improved upon our previous NF- κ B-based screen for T3SS inhibitors by generating an NF- κ B-driven GFP-expressing HEK293 stable cell line (HEK293-GFP). To validate this cell line, we infected HEK293-GFP cells with *Y. pseudotuberculosis* lacking the *Yersinia* YopHEMOJT effector proteins (Δ yopHEMOJ); this strain is referred to as the Δ yop6 strain from this point forward), as several Yops modulate NF- κ B signaling (13). Approximately 40% of the cells were positive for GFP after 5 h of infection with the Δ yop6 strain at a multiplicity of infection (MOI) of 7 (Fig. 1). In contrast, *Y. pseudotuberculosis* carrying a nonfunctional T3SS (Δ yop6 Δ yopB) induced low levels of GFP expression similar to those of uninfected samples. The known T3SS inhibitor piericidin A1 significantly reduced the percentage of GFP-expressing cells in response to the Δ yop6 strain (Fig. 1). A Z-score, described in detail previously (27), is a single numerical value that accurately validates the reproducibility of high-throughput assays. Our stable cell line generated data with Z-scores ranging from 0.4 to 0.8, which is in the reliable range. These data suggest that our stable cell line can be used for high-throughput screens for T3SS inhibitors.

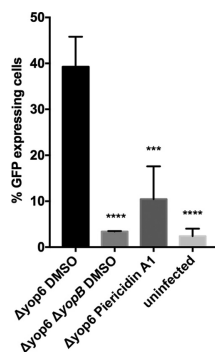


FIG 1 A newly developed NF- κ B-GFP reporter stable cell line can be used to identify chemical inhibitors of the *Yersinia* T3SS. A HEK293-based stable cell line developed for this study was infected with *Y. pseudotuberculosis* Δ yop6 (T3SS⁻) or Δ yop6 Δ yop8 (T3SS⁻), and GFP fluorescence was quantified as a readout of T3SS-induced NF- κ B activation in the presence or absence of a known T3SS inhibitor, piericidin A1. The results are representative of three independent replicates. Data were analyzed by one-way ANOVA with Dunnett's multiple comparison test. ****, $P < 0.0001$; ***, $P < 0.001$.

As part of a previous study (28), a library of 20 synthetic peptides and peptomers based on the structure of a natural product, phepropeptin D (29), were synthesized and placed in an internal screening library. These peptomers were not previously screened for any bioactivity and may have a high intrinsic potential to disrupt protein-protein interactions (30), such as those critical for assembly of a large proteinaceous structure such as the T3SS. The compounds were screened for the ability to inhibit NF- κ B activation during *Y. pseudotuberculosis* Δ yop6 infection of HEK293-GFP cells. We used 2 standard deviations below the mean for the dimethyl sulfoxide (DMSO) control as the threshold for hit calling (26). The following 8 of the 20 peptomers reduced NF- κ B-driven GFP expression at the two highest concentrations tested: EpD-1N, EpD-1'N, EpD-2N, EpD-3N, EpD-3'N, EpD-4'N, EpD-6N, and EpD-6'N (Fig. 2A and B) (Z-score, -0.5). While the "hit rate" is high, each of these eight peptomers has a single peptide-to-peptoid substitution compared to the parent compound, epiphepropeptin D (EpD), a phepropeptin D derivative containing a stereo-inversion at the proline position, and are thus structurally similar to each other (Fig. 2A).

Cyclic peptomers inhibit type III secretion in *Yersinia pseudotuberculosis*. In order to validate whether the cyclic peptomers we identified in our primary screen were indeed T3SS inhibitors, we evaluated the effects of our hits on secretion of *Y. pseudotuberculosis* effectors under T3SS-inducing conditions *in vitro*. The previously identified T3SS inhibitor piericidin A1 (26) was used as a positive control. Wild-type (WT) *Y. pseudotuberculosis* was grown in low-calcium medium in the presence or absence of one of the compounds at 60 μ M, an equivalent volume of DMSO, or 71 μ M piericidin A1, and secretion of the YopE effector protein was analyzed as a measure of general type III secretion. YopE was selected because it can easily be distinguished from other secreted proteins visible upon Coomassie blue staining (Fig. 2C; see Fig. S1 in the supplemental material) (26). *Y. pseudotuberculosis* lacking one of the T3SS structural operons (Δ yscNU) was used as a negative control. YopE secretion was reduced $\geq 70\%$ by EpD-4'N and EpD-3'N treatments ($P < 0.0001$) and $\geq 45\%$ by EpD-1N, EpD-1'N, EpD-2N, and EpD-3N treatments ($P < 0.001$) (Fig. 2D). Furthermore, the abundances of the other Yops visible upon Coomassie blue staining were also reduced upon compound treatment (Fig. 2C; Fig. S1). Given that each of the eight peptomers carries only one peptoid substitution compared to the parent compound, we hypothesized that a

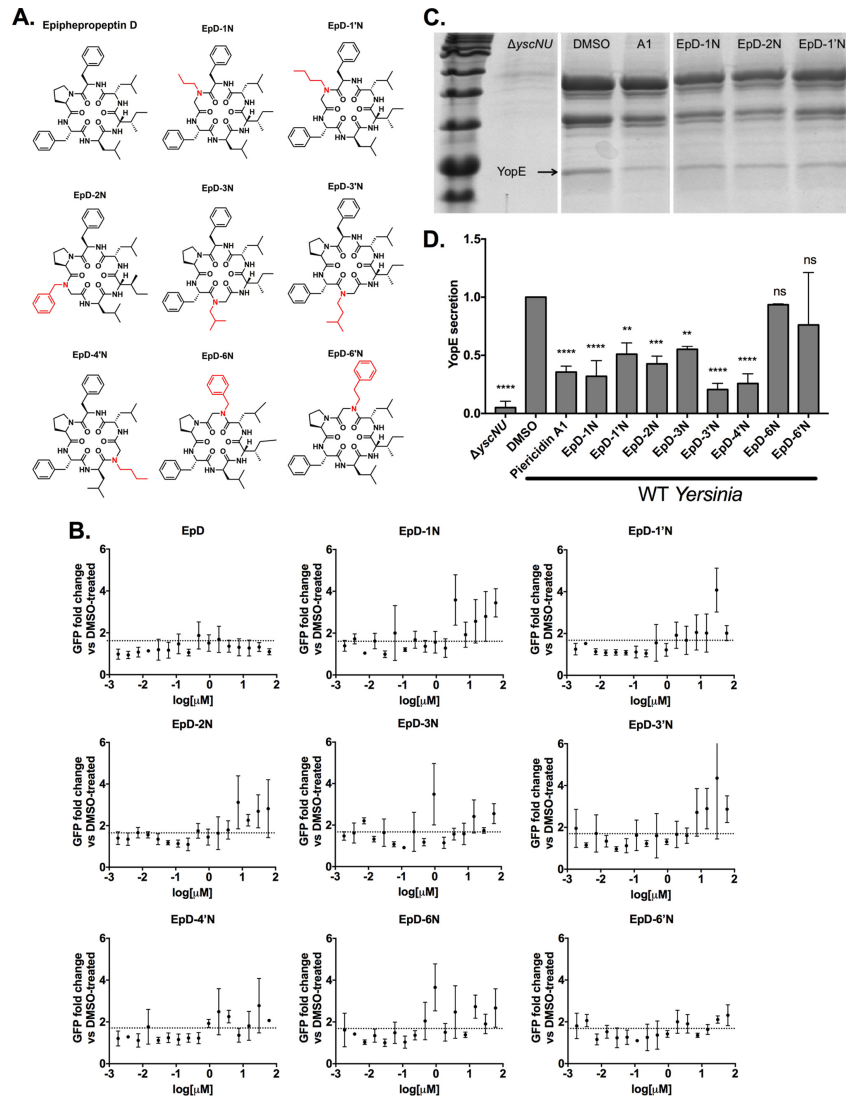


FIG 2 First-generation cyclic peptomers inhibit NF- κ B activation in infected host cells and secretion of *Yersinia* T3SS effector proteins. (A) Structures of the first-generation cyclic peptomers, each of which carries one side chain modification compared to the parental compound, epiphepropeptin D (EpD). (B) HEK293-GFP cells were infected with *Y. pseudotuberculosis* Δ yop6 in the presence or absence of the first-generation cyclic peptomers, and GFP fluorescence

(Continued on next page)

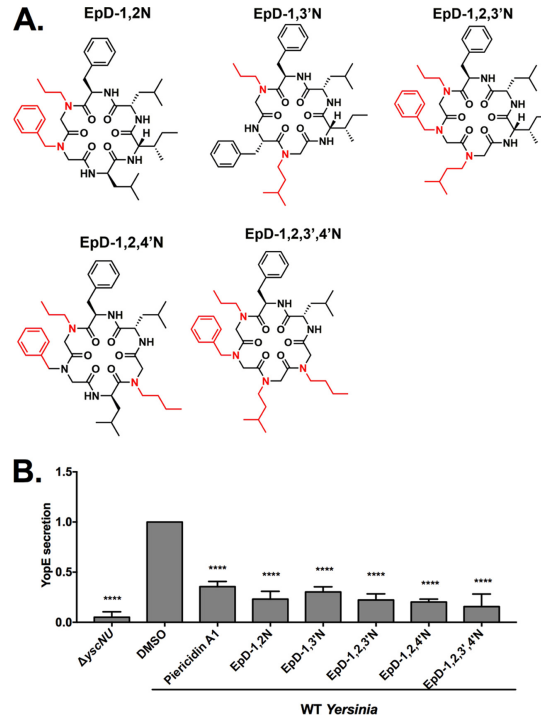


FIG 3 Second-generation cyclic peptomers inhibit secretion of *Yersinia* T3SS effector proteins. (A) Structures of the second-generation cyclic peptomers, each of which carries two, three, or four side chain modifications compared to EpD. (B) WT *Y. pseudotuberculosis* was grown under T3SS-inducing conditions with 60 μ M cyclic peptomer, 71 μ M piericidin A1, or an equivalent volume of DMSO, and secretion of T3SS cargo into the culture supernatant was assessed by precipitating secreted proteins and visualizing with Coomassie blue. Data were analyzed by one-way ANOVA with Dunnett's multiple comparison test. ****, $P < 0.0001$.

combination of peptoid substitutions may further improve the compounds' bioactivity. We synthesized second-generation peptomers with combinatorial changes at positions 1, 2, 3, and 4 on the cyclic peptide backbone (Fig. 3A). All five new compounds led to >70% reductions in secretion ($P < 0.0001$) (Fig. 3B).

To further validate that the candidate T3SS inhibitors are active in a dose-dependent manner, the eight compounds showing the greatest inhibition at 60 μ M were chosen

FIG 2 Legend (Continued)

was quantified. The fold reductions of the GFP signals in the presence of cyclic peptomers compared to the signal with DMSO are shown as averages for three independent experiments. The dotted lines represent 2 standard deviations above the DMSO control level. (C and D) WT *Y. pseudotuberculosis* was grown under T3SS-inducing conditions with 60 μ M cyclic peptomer, 71 μ M piericidin A1, or an equivalent volume of DMSO, and secretion of T3SS cargo into the culture supernatant was assessed by precipitating the secreted proteins, visualizing them with Coomassie blue (C), and quantifying the YopE effector band intensity (D). The data were analyzed by one-way ANOVA with Dunnett's multiple comparison test. ****, $P < 0.0001$; ***, $P < 0.001$; **, $P < 0.01$; ns, not significant. For panel C, the lanes containing the ladder and samples shown were separated by unrelated samples in the intervening lanes of the same gel and are therefore shown divided by white borders.

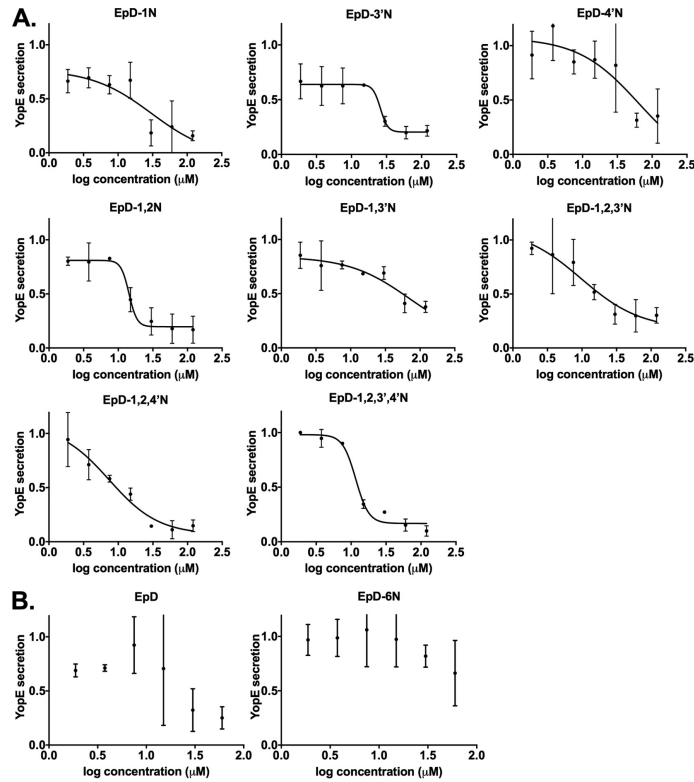


FIG 4 Cyclic peptomers inhibit type III secretion in *Yersinia pseudotuberculosis* in a dose-dependent manner. WT *Y. pseudotuberculosis* was grown under T3SS-inducing conditions with increasing concentrations of peptomers. Secretion of T3SS cargo into the culture supernatant was assessed by precipitating secreted proteins and visualizing them with Coomassie blue. YopE band intensities were quantified and normalized to that of the DMSO control. The results are from two independent experiments. Nonlinear curve fitting is shown to depict the trend of inhibition. (A) EpD-1N, EpD-3'N, EpD-4'N, EpD-1,2N, EpD-1,3'N, EpD-1,2,3'N, EpD-1,2,4'N, and EpD-1,2,3',4'N. (B) EpD and EpD-6N.

for testing at 2-fold increasing concentrations from 1.875 μM to 120 μM (Fig. 4; Table 1). EpD-1N, EpD-3'N, EpD-1,2N, EpD-1,2,3'N, EpD-1,2,4'N, and EpD-1,2,3',4'N showed a dose-response relationship and reduced secretion of YopE, to less than 40% of normal DMSO control levels, at 30 μM . Surprisingly, although the parental compound EpD did not decrease NF- κB activation in our primary screen (Fig. 2B), EpD did inhibit YopE secretion in a dose-dependent manner (Fig. 4B). However, the EpD-6N peptomer did not show dose-dependent inhibition of YopE secretion (Fig. 4B), consistent with the inability of this compound to inhibit YopE secretion at 60 μM (Fig. 2D). These data suggest that specific peptoid substitutions in the epiphepropeptin scaffold improve the bioactivity of peptomers as T3SS inhibitors.

We observed that several of the cyclic peptomers formed aggregates over time when they were added to culture media. We set out to measure the amounts of

TABLE 1 Cyclic peptomer data summary^h

Compound	YopE secretion (%) ^a		ExoU secretion (%) ^b		YopM-Bla translocation (%) ^c	Concn (μ M) with cell rounding ^d	Concn (μ M) with cell toxicity ^e	% reduction in motility ^f	Growth ^g
	60 μ M	30 μ M	60 μ M	30 μ M					
EpD-1N	30	18	17	21	62	NE	All	NE	NE
EpD-1'N	51	ND	ND	ND	ND	ND	ND	ND	ND
EpD-2N	43	ND	ND	ND	ND	ND	ND	ND	ND
EpD-3N	55	ND	ND	ND	ND	ND	ND	ND	ND
EpD-3'N	21	30	11	17	59	4	NE	NE	NE
EpD-4'N	28	82	13	84	75	2	>102	NE	NE
EpD-1,2N	21	25	19	15	54	NE	NE	NE	NE
EpD-1,3'N	36	69	21	21	51	2	NE	NE	NE
EpD-1,2,3'N	26	31	18	14	51	2	NE	20	NE
EpD-1,2,4'N	17	14	18	12	56	2	NE	NE	NE
EpD-1,2,3',4'N	16	27	14	12	65	2	NE	NE	NE
EpD-6N	94	ND	ND	ND	ND	ND	ND	ND	ND
EpD-6'N	76	ND	ND	ND	ND	ND	ND	ND	ND

^a*Yersinia* YopE secretion with 60 or 30 μ M peptomers compared to that with DMSO (100%).

^b*Pseudomonas* ExoU secretion with 60 or 30 μ M peptomers compared to that with DMSO (100%).

^cYopM-Bla translocation into CHO-K1 cells treated with 7.5 μ M peptomers, normalized to that with DMSO (100%).

^dLowest concentration of peptomers at which cell rounding in HeLa cells was statistically significantly reversed.

^eConcentration of compound showing cytotoxicity in HeLa cells by the MTT assay.

^fPercent reduction in *Yersinia* motility compared to that with DMSO (100%).

^g*Yersinia* pYV⁻ growth at 37°C over 8 h compared to that of the DMSO control.

^hNE, no effect (not significantly different from the DMSO control); ND, not determined.

monomeric peptomers in bacteriological and cell culture media. The solubility of peptomers able to inhibit type III secretion ranged from 1 to 84 μ M (Fig. S4). To determine whether cyclic peptomer aggregates were responsible for the observed T3SS-inhibitory activity, we sought to disaggregate the compounds and test their activity by adding the detergent Triton X-100 to bacterial cultures during type III secretion. Concentrations of Triton X-100 of >0.005% (vol/vol), in the absence of cyclic peptomers, led to enhanced Yop release into the culture media (Fig. S5A), perhaps as a result of cell envelope leakiness or perturbations to normal T3SS regulation with high levels of detergent. Therefore, we chose to carry out our disaggregation experiment with 0.001% (vol/vol) Triton X-100, as this concentration of detergent did not cause enhanced Yop release but has been shown to be effective at inhibiting nonspecific activity due to aggregate formation (31) and to give a decreased absorbance at 600 nm when added to cyclic peptomers (data not shown). In the presence of 0.001% Triton X-100, EpD-1,2,4'N showed activity comparable to that of the no-detergent control (Fig. 4; Fig. S5B), suggesting that peptomer aggregates that can be disrupted by 0.001% Triton X-100 are not required for T3SS-inhibitory activity.

In order to rule out nonspecific interaction with protein as the cause of the T3SS-inhibitory activity observed for the cyclic peptomers, we carried out the Yop secretion assay in the presence of increasing concentrations of bovine serum albumin (BSA). We observed no effect of BSA on secretion inhibition by EpD-1,2N, and the presence of BSA did not shift the dose-response curve for EpD-1,2N (Fig. S6). These data indicate that nonspecific protein binding does not underlie the T3SS-inhibitory activity of the cyclic peptomers.

Cyclic peptomers do not affect *Yersinia* growth or flagellar motility. To determine whether the peptomers affect type III secretion specifically or have a broader impact on *Yersinia* physiology, we monitored bacterial growth and metabolic activity following drug treatment. Active type III secretion, induced under low-calcium conditions at 37°C *in vitro*, causes growth arrest, complicating analysis of bacterial growth. Therefore, we used a strain of *Y. pseudotuberculosis* lacking the T3SS-encoding virulence plasmid pYV (*Yersinia* pYV⁻). Kanamycin was used as a positive control because it is known to inhibit *Yersinia* growth. In the presence of 60 μ M cyclic peptomers, *Yersinia* pYV⁻ grew similarly to the DMSO-treated control, while kanamycin inhibited growth (Fig. 5A). Furthermore, in the presence of a high concentration of cyclic peptomers (120

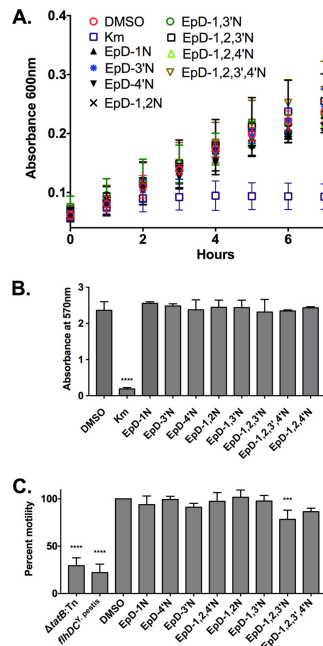


FIG 5 Cyclic peptomers do not affect *Yersinia* growth or motility. (A) *Yersinia* pYV⁻ was grown in low-calcium medium at 37°C in the presence of 60 μ M cyclic peptomer, an equivalent volume of DMSO, or kanamycin. The bacterial density over time was measured by determining the absorbance at 600 nm. (B) *Yersinia* pYV⁻ was grown in low-calcium medium at 37°C in the presence of 120 μ M cyclic peptomer, an equivalent volume of DMSO, or kanamycin for 24 h. MTT was added, and the absorbance at 570 nm was used as a readout of bacterial metabolic activity. (C) Cyclic peptomers were added to motility agar plates at 60 μ M, and the diameter of WT *Yersinia* colonies was measured as a readout of flagellar motility. Averages for three independent experiments are shown. Data were analyzed by one-way ANOVA with Dunnett's multiple comparison test. ****, $P < 0.0001$; ***, $P < 0.001$.

μ M), no significant difference in metabolic activity was detected compared to that of the DMSO-treated control, while kanamycin induced a significant reduction in metabolic activity (Fig. 5B). These results suggest that, unlike conventional antibiotics, peptomers do not inhibit bacterial replication or metabolic activity, yet they inhibit type III secretion in *Yersinia*.

The flagellar basal body, which is a T3SS, is structurally related to the injectisome T3SS (32). For *Y. enterocolitica*, the proton motive force was shown to be required for both type III secretion and motility (33). In addition, the twin-arginine translocation (Tat) secretion system is required for motility in *Y. pseudotuberculosis* and requires the proton motive force (34, 35). Therefore, compounds that affect the proton motive force or the Tat system should affect motility. To determine if the cyclic peptomers affect either of these processes, WT *Y. pseudotuberculosis* was spotted on soft motility agar with 60 μ M cyclic peptomers or an equivalent volume of DMSO. A *Y. pseudotuberculosis* mutant carrying the inactive *Y. pestis* allele of the *flhDC* flagellar master regulator genes (*flhDC*^{Y.pestis}) and a Tat mutant (*atB::Tn*) were used as negative controls. Colony diameters were measured and

normalized to that of the DMSO control (100%). At 60 μM , the cyclic peptomers did not affect *Yersinia* motility compared to that with DMSO, except for EpD-1,2,3'N, which reduced motility by 20% ($P = 0.0005$) (Fig. 5C). These results suggest that cyclic peptomers do not inhibit type III secretion by targeting the Tat secretion system, the flagellar T3SS, or the proton motive force.

In order to assess the ability of the cyclic peptomers to disrupt flagellar T3SS activity in liquid culture over a shorter period more comparable to that of the T3SS secretion conditions, we assessed the motility of *Salmonella* and *Pseudomonas* in liquid culture after 2 to 3 h of growth in the presence or absence of cyclic peptomers. These bacteria were chosen because, unlike *Yersinia*, they express flagella at 37°C (36, 37). As the bacterial culture increased in density 32-fold during this time, new flagellar synthesis should have occurred in the presence of the cyclic peptomers. However, we observed no difference in swimming distance, speed, or percentage of motile bacteria (Fig. S7). These data suggest that cyclic peptomers do not nonspecifically block the assembly or activity of the flagellar T3SS or, more broadly, the functions of proteinaceous appendages in bacteria, other than the injectisome T3SS.

Cyclic peptomers inhibit type III secretion in *Pseudomonas aeruginosa*. To determine whether the cyclic peptomers specifically blocked type III secretion in *Yersinia* or were active against the T3SS of other pathogens, we tested their bioactivity in *P. aeruginosa*. We found that the cyclic peptomers at 60 μM significantly reduced secretion of the effector protein ExoU compared to the DMSO control (Fig. 6A). In addition, these compounds showed a dose-response inhibitory effect (Fig. 6B; Table 1). At 30 μM , EpD-3'N, EpD-1,2N, EpD-1,2,3'N, EpD-1,2,4'N, and EpD-1,2,3',4'N reduced secretion of ExoU to less than 20% of that with DMSO, which was normalized to 100%. These data suggest that five cyclic peptomers, EpD-3'N, EpD-1,2N, EpD-1,2,3'N, EpD-1,2,4'N, and EpD-1,2,3',4'N, strongly inhibit type III secretion in both *Yersinia* and *Pseudomonas*.

Cyclic peptomers inhibit T3SS effector protein translocation and activity but are not toxic to host cells. To test whether the cyclic peptomers affect mammalian cell physiology, we evaluated HeLa cell metabolic activity following exposure to the compounds (Fig. 7). TPEN, a known cytotoxic compound (38–40), was used as a positive control and showed toxicity at concentrations of $>3.75 \mu\text{M}$, in agreement with previous findings (38, 39). Most cyclic peptomers were not cytotoxic to HeLa cells, except for EpD-4'N, which showed toxicity at concentrations of $>102 \mu\text{M}$. In addition, EpD-1N-treated cells displayed low absorbance in the MTT [3-(4,5-dimethyl-2-thiazolyl)-2,5-diphenyl-2H-tetrazolium bromide] assay at all concentrations, for reasons that are unclear but may reflect the compound's physical properties under these conditions. These data suggest that the majority of the cyclic peptomers are not toxic to mammalian cells.

We tested the ability of the cyclic peptomers to inhibit translocation of the *Y. pseudotuberculosis* effector YopM, translationally fused to a reporter β -lactamase (YopM-Bla), into CHO-K1 cells. Infected cells were loaded with the fluorescent substrate CCF2-AM, and green (uncleaved) versus blue (cleaved) fluorescence was monitored. All eight peptomers significantly reduced YopM-Bla translocation into CHO-K1 cells at 7.5 μM (Fig. 8A). DMSO affected the percentage of blue cells at high concentrations (Fig. S2). Thus, we chose 7.5 μM because the volume of DMSO necessary to achieve this final concentration does not exceed the maximum tolerable dose of DMSO for this assay.

We next tested the ability of the cyclic peptomers to inhibit the ability of translocated *Yersinia* effector proteins to target the host actin cytoskeleton. As a result of YopEHO activity on the actin cytoskeleton, HeLa cells become rounded following *Yersinia* infection and YopEHO translocation. HeLa cells were treated with increasing concentrations of cyclic peptomers during WT *Y. pseudotuberculosis* infection at an MOI of 40, and the total cellular area was quantified as a measure of cell rounding (Fig. 8B). EpD-3'N and EpD-1,2,4'N reversed cell rounding induced by WT *Yersinia* with increasing

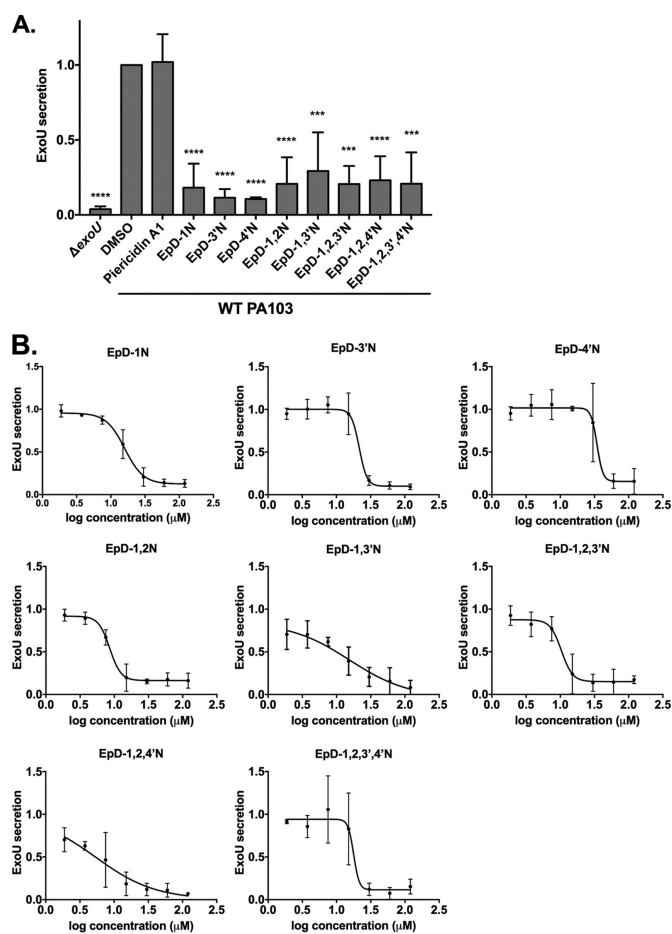


FIG 6 Cyclic peptomers inhibit type III secretion in *Pseudomonas aeruginosa*. WT *Pseudomonas* PA103 was grown under T3SS-inducing conditions with 60 μM cyclic peptomers (A), cyclic peptomers at concentrations ranging from 1.9 μM to 120 μM (B), or an equivalent volume of DMSO. Secretion of T3SS cargo into the culture supernatant was assessed by precipitating secreted proteins and visualizing them with Coomassie blue. ExoU band intensities were quantified and normalized to that of the DMSO control. Piericidin A1, which does not inhibit T3SS secretion in *P. aeruginosa*, was used as a negative control. (A) Data were analyzed by one-way ANOVA with Dunnett's multiple comparison test. ****, $P < 0.0001$; ***, $P < 0.001$. (B) The results are averages for at least two independent experiments. Nonlinear curve fitting is shown to depict the trend of inhibition.

concentrations of these compounds, starting at 3.75 μM and 1.875 μM , respectively (Fig. 8B and C). EpD-4'N, EpD-1,3'N, EpD-1,2,3'N, and EpD-1,2,3,4'N reversed cell rounding to some degree at lower concentrations but enhanced rounding at higher concentrations, indicating a possible effect on the actin cytoskeleton at the higher

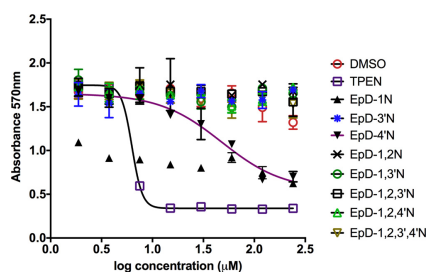


FIG 7 The majority of cyclic peptomers are not toxic to mammalian cells. HeLa cells were treated with increasing concentrations of cyclic peptomers or an equivalent volume of DMSO for 24 h. MTT was added to the culture, and the absorbance at 570 nm was used as a readout of cellular metabolism. TPEN, a known cytotoxic compound, was used as a control. Data shown are the averages for two independent biological replicates.

concentrations. EpD-1N and EpD-1,2N enhanced rounding at almost all concentrations tested, indicating an even greater off-target effect. These data suggest that while some of the cyclic peptomers may affect mammalian cell physiology, EpD-3'N and EpD-1,2,4'N inhibit the activity of Yop effector proteins on the actin cytoskeleton. This is especially important because the activity of these effectors is critical for *Yersinia* to avoid important host defense mechanisms and cause disseminated disease (41).

DISCUSSION

Here we present a HEK293 stable cell line expressing an NF- κ B-GFP reporter that enables high-throughput screening for inhibitors of the bacterial T3SS. We used this cell line to identify a novel set of T3SS inhibitors, i.e., synthetic peptomer analogs of the natural product phepropeptin. We found that a subset of these compounds inhibit type III secretion in both *Yersinia* and *Pseudomonas* as well as limit translocation of *Yersinia* effector proteins inside target host cells and, consequently, their activity on host cell processes. Importantly, the majority of these compounds do not affect bacterial growth, mammalian cell metabolism, or flagellar motility, indicating a specific effect on the T3SS.

Cyclic peptides may be particularly well suited for novel therapeutic strategies, including the targeting of virulence factors. The rich structural diversity of cyclic peptides and their larger size than that of traditional drugs may allow greater potency and specificity than those of typical small molecules (42). Oligomers of N-substituted glycine units ("peptoids") were originally conceived as synthetic peptide derivatives that possess the modularity and protein binding characteristics of peptides but avoid the pitfalls associated with the notoriously poor metabolic stability of peptides (43, 44). Peptide-to-peptoid substitutions can increase or maintain the ability of cyclic peptides to permeate eukaryotic cells while enabling greater side chain diversity than that in the pool of commercially available amino acids (45). The phepropeptins are cyclic hexapeptides isolated from *Streptomyces* sp. and previously characterized for their activity as weak proteasome inhibitors (29). It was shown previously that stereo-inversion of the Pro residue to form epiphepropeptin (EpD) significantly altered the compound conformation as determined by nuclear magnetic resonance (NMR) analysis (28). Thus, it is unlikely that the compounds described here as possessing T3SS-inhibitory activity would retain the proteasomal inhibition of the natural product. In addition, *Yersinia* and *Pseudomonas* lack a proteasome. This suggests that phepropeptin compared to EpD and its cyclic peptomer analogs has distinct bioactivities and that proteasome inhibition does not underlie the T3SS-inhibitory activity of the EpD cyclic peptomers.

Peptides as a class have rich antimicrobial activities, such as that of antimicrobial

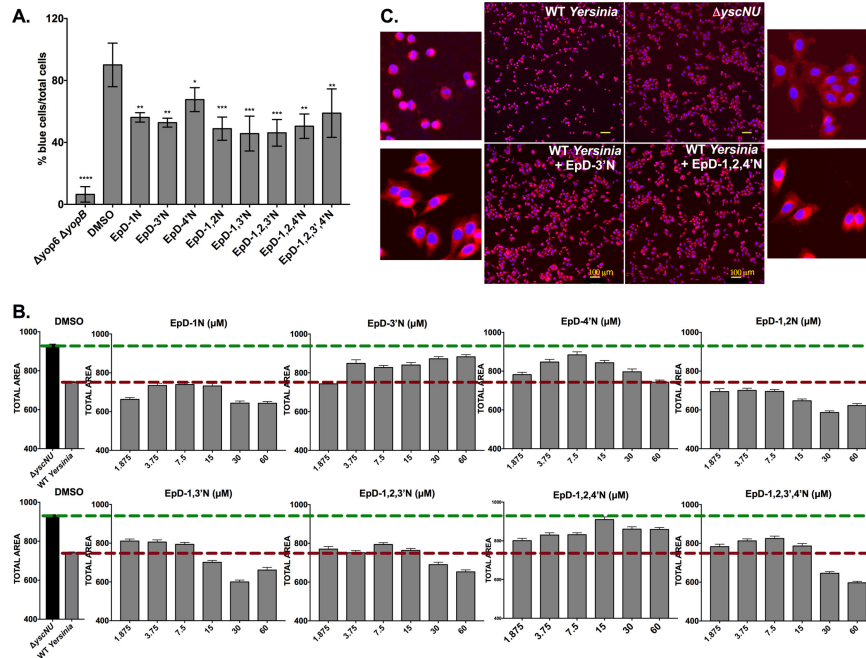
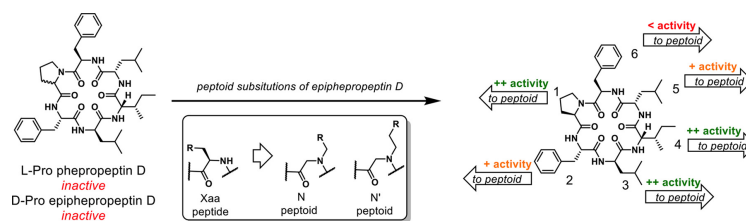


FIG 8 Cyclic peptomers block translocation of a T3SS effector protein into host cells and protect host cells from T3SS effector activity. (A) *Yersinia* carrying a Yop effector- β -lactamase fusion (Δ yop6/YopM-Bla) was used to infect CHO-K1 cells at an MOI of 5 in the presence of 7.5 μ M peptomer or an equivalent volume of DMSO. CCF2-AM was added, and the percentage of cells with cleaved CCF2-AM (blue) among the total number of cells (green) was quantified. Data shown are averages for 3 independent experiments. (B) HeLa cells were infected with WT *Yersinia* at an MOI of 40 in the presence of increasing concentrations of peptomers for 3.5 h. *Yersinia* lacking a T3SS (Δ yscNU) was used as a negative control. Total cell area was quantified as a measure of cell rounding, which is a readout of host actin cytoskeleton modulation by the *Yersinia* T3SS YopEHO effector proteins. Median total area values for all imaged cells were plotted. Data shown are averages for two independent replicates with three technical replicates each. (C) Micrographs of HeLa cells infected with the Δ yscNU mutant or WT *Yersinia* and treated with EpD-3'N, EpD-1,2,4'N, or DMSO.

peptides (AMPs), which are naturally produced by host cells to protect themselves from pathogens (46). AMPs kill a wide range of species, including fungi and viruses (46–48) as well as Gram-positive and Gram-negative bacteria, including *Listeria monocytogenes*, *Staphylococcus aureus*, *Salmonella enterica* serovar Typhimurium, *Escherichia coli*, and *Pseudomonas aeruginosa* (49). However, AMPs, which are ribosomally produced, exhibit unfavorable properties for use as antimicrobial therapies, such as susceptibility to degradation, cytotoxicity to host cells, instability with heat or enzymes, and a high cost of production (50, 51). It might be worth noting that most nonribosomal antimicrobial peptides, such as polymyxin, fusaricidin, and daptomycin, are "lipopeptides" which contain a mixture of charged residues and aliphatic tails and act by disrupting cell membrane or cell wall function (52, 53). In contrast, our peptides contain only aliphatic groups and are reminiscent of natural products that inhibit intracellular targets, such as griselimycin, which targets DnaN of *Mycobacterium tuberculosis* (54). Whether the peptomers can cross the bacterial membrane remains to be tested. Peptide analogues of a native autoinducing peptide signal in *Staphylococcus aureus* were shown to be potent at inhibiting quorum sensing and attenuating the virulence of the bacterium



Generation One

Compound	Position						YopE Secretion 60 μ M	
	1	2	3	4	5	6	N Peptoid	N' Peptoid
EpD-1N or 1'N	Naa*	AA	AA	AA	AA	AA	0.32	0.51
EpD-2N or 2'N	AA	Naa*	AA	AA	AA	AA	0.43	0.70
EpD-3N or 3'N	AA	AA	Naa*	AA	AA	AA	0.55	0.21
EpD-4'N	AA	AA	AA	Naa'	AA	AA	not tested	0.26
EpD-5'N	AA	AA	AA	AA	Naa'	AA	not tested	0.48
EpD-6N or 6'N	AA	AA	AA	AA	AA	Naa*	0.94	0.76

Naa* = N peptoid or N' peptoid, Naa' = N' peptoid, AA = amino acid

Generation Two

Position	Position						YopE Secretion 15 μ M
	1	2	3	4	5	6	
EpD-1,2N	Naa	Naa	AA	AA	AA	AA	45%
EpD-1,3'N	Naa	AA	Naa'	AA	AA	AA	68%
EpD-1,2,3'N	Naa	Naa	Naa'	AA	AA	AA	52%
EpD-1,2,4'N	Naa	Naa	AA	Naa'	AA	AA	44%
EpD-1,2,3',4'N	Naa	Naa	Naa'	Naa'	AA	AA	35%

Naa = N peptoid, Naa' = N' peptoid, AA = amino acid

FIG 9 Structure-activity relationships and structural descriptions of peptoid analogs of epiphepropeptin D. N and N' peptoids differ by a single $-CH_2$ group in the peptoid chain. The YopE secretion assay was used to evaluate potency, with the first- and second-generation sets analyzed at 60 μ M and 15 μ M, respectively. Secretion inhibition was colored to highlight potency differences between compounds.

(55). Amide-bridged peptide analogues were more enzymatically stable than the peptides while still showing moderate quorum sensing inhibition (56). Our finding provides the first evidence suggesting that peptide-peptoid derivatives (peptomers) can act as T3SS inhibitors. Furthermore, our compounds contain peptoid positions that allow for facile diversification, making further optimization of these compounds synthetically tractable.

Our results suggest that the assay for T3SS inhibition with the largest dynamic range is the secretion assay, for both *Yersinia* and *Pseudomonas* T3SS effector proteins. In the absence of a standard measurement of compound activity, such as the MIC typically determined for classical antibiotics that inhibit bacterial growth or viability, we relied mainly on the secretion assay to determine the relative potencies of cyclic peptomers. When the single peptoid substitutions are compared to the parent compound, it appears that positions 1, 3, and 4 are the most important peptoid positions for activity. Although not every peptoid substitution was tested as both the N-peptoid and the chain-elongated N'-peptoid (Fig. 9), there appears to be a preference for one side chain over the other in all matched pairs, especially for position 3, with EpD-3'N inhibiting 79% of secretion while EpD-3N inhibits only 45% of secretion at 60 μ M (Fig. 2 and Table 1),

hinting at some specificity of interaction. While the peptoids with single substitutions at positions 1, 3, and 4 display high levels of YopE secretion inhibition at 60 μM , none of them show >50% inhibition when diluted to 15 μM . When both positions 1 and 2 are replaced with a peptoid, the potency is increased compared to those for both individual substitutions and the 1,3 combination (Fig. 4 and Table 1). The peptomers containing substitutions at both positions 1 and 2 all inhibit secretion >50% at 15 μM , with EpD-1,2,4'N and EpD-1,2,3',4'N showing the most inhibition at this concentration. As several cyclic peptomers were found to perturb the host actin cytoskeleton and a subset of these disrupted mammalian cell metabolism, further derivatization is warranted to mitigate such off-target effects while improving activity. Importantly, the activities displayed by the cyclic peptomers are comparable to those of other known T3SS inhibitors, such as piericidin A1 (active at 71 μM) (26), *N*-hydroxybenzimidazole derivatives (50% inhibitory concentration [IC_{50}] in the range of 3 to 70 μM) (57), various T3SS ATPase inhibitors (IC_{50} in the range of 17 to 70 μM) (58), and the salicylidene acylhydrazide INP0010 (active at 40 μM), for which three molecular targets have been identified (59).

Aggregation effects have been attributed to nonspecific or promiscuous inhibitor activity (60). Most of the active cyclic peptomers have solubility values of <30 μM , while secretion inhibition was observed at higher concentrations. However, detergent disaggregation of compounds did not ablate T3SS-inhibitory activity, indicating that aggregate formation is not essential for T3SS inhibition. In addition, adding BSA to bacteria undergoing type III secretion in the presence of compounds did not abolish the compounds' activity, indicating that secretion inhibition was not due to nonspecific protein binding. Taken together, our data show that it is possible that both monomeric cyclic peptomers and peptomer aggregates are able to inhibit secretion. Alternatively, the active moiety, perhaps of a specific aggregate size, may be present at a range of cyclic peptomer concentrations as well as in the presence of Triton X-100. Without further testing (e.g., using dynamic light scattering), the observed T3SS inhibition in the presence of detergent and BSA does not formally rule out the possibility that some degree of aggregation plays a role in these compounds' activity. Future medicinal chemistry optimization will be aimed at improving both inhibitory potency and solubility, for example, by replacing one or more of the peptoid side chains with more polar groups.

The proton motive force is important for the *Yersinia* flagellar T3SS, as the proton motive force inhibitor carbonyl cyanide *m*-chlorophenylhydrazone (CCCP) prevents *Yersinia* motility (33, 61). Yet the majority of our compounds do not affect flagellar motility. This suggests that the cyclic peptomers do not inhibit type III secretion by perturbing the proton motive force. Since the Tat secretion system has been shown to be essential for *Yersinia* type III secretion (34), our data also indicate that the cyclic peptomers do not generally block bacterial secretion systems. Furthermore, the cyclic peptomers inhibit type III secretion in both *Yersinia* and *Pseudomonas* but do not block flagellar motility in *Yersinia*, *Pseudomonas*, or *Salmonella*. The flagellar and injectisome T3SS share eight conserved components, including an ATPase and several proteins that make up basal body membrane rings (62). However, over a dozen other T3SS components are conserved between *Yersinia* and *Pseudomonas* but are divergent or absent from the flagellar T3SS. Our data predict that the cyclic peptomers act on such a target, such as the SctF needle subunit. The activity of the cyclic peptomers is in contrast to that of the T3SS inhibitor piericidin A1, which inhibits the *Yersinia* Ysc T3SS but is inactive against the *Pseudomonas* T3SS (61). The *Pseudomonas* cell envelope is particularly exclusive to chemicals (63); the activity of the cyclic peptomers on the *Pseudomonas* T3SS suggests that these compounds either act on an extracellular T3SS component or can gain access to the *Pseudomonas* periplasm or cytoplasm. The specific mechanism of action of the cyclic peptomers will be the subject of another study.

In summary, the HEK293-GFP stable cell line and high-throughput screen reported here provide a rapid and reproducible platform for T3SS inhibitor discovery. Using this strategy, we have identified a new class of T3SS inhibitors, synthetic derivatives of the

TABLE 2 Bacterial strains used in this study

Strain	Description	Reference
<i>Y. pseudotuberculosis</i> strains		
Wild type (WT)	Strain IP2666	68
$\Delta yop6$	$\Delta yopHEMOJ$ mutant	25
$\Delta yop6 \Delta yop8$	$\Delta yopHEMOJ8$ mutant	25
$\Delta yop6/pYopM-Bla$	$\Delta yopHEMOJ8$ mutant carrying pYopM-Bla	64
$\Delta yop6 \Delta yop8/pYopM-Bla$	$\Delta yopHEMOJ8$ mutant carrying pYopM-Bla	64
$\Delta yscNU$	Deletion of <i>yscNU</i> operon	69
pYV ⁻	IP2666 cured of its virulence plasmid	69
<i>tatB::Tn</i>	$\Delta yop6$ with a <i>tatB::TnHimar1</i> insertion	This study
<i>flhDC^{C. pestis}</i>	$\Delta yop6$ with inactive <i>Y. pestis flhDC</i>	64
<i>Pseudomonas aeruginosa</i> strains		
Wild type	Strain PA103	70
$\Delta exoUT$	$\Delta exoU \Delta exoT$ mutant	71
PAO1	PAO1	72
<i>Salmonella</i> Typhimurium strains		
Wild type	Strain LT2	73
$\Delta flhDC$	TH5736 ($\Delta flhDC$ - <i>motAB-cheAW-tar</i>)	

natural product pheuropeptin, that significantly decrease type III secretion in *Y. pseudotuberculosis* and *P. aeruginosa* without affecting bacterial survival, motility, or other secretion systems, and without host cell toxicity. Future studies will focus on compound EpD-1,2,4'N, as this compound inhibited type III secretion in both *Yersinia* and *Pseudomonas* and blocked the native activity of *Yersinia* T3SS effector proteins on target host cells.

MATERIALS AND METHODS

Bacterial strains and mammalian cells used in this study. The bacterial strains and cell lines used in this study are listed in Table 2. *Y. pseudotuberculosis* was grown in 2× YT (2× yeast extract and tryptone) at 26°C with shaking at 250 rpm overnight, unless otherwise noted. The cultures were back diluted to an optical density at 600 nm (OD₆₀₀) of 0.2 in low-calcium medium (2× YT with 20 mM sodium oxalate and 20 mM MgCl₂) or M9 medium supplemented with Casamino Acids to induce the T3SS (64). Cultures were grown for 1.5 h at 26°C with shaking at 250 rpm. Compounds or DMSO was added to bacterial cultures prior to shifting to 37°C to induce T3SS synthesis. *Pseudomonas aeruginosa* was grown in Luria-Bertani medium (LB) at 37°C with shaking at 250 rpm overnight. Low-calcium medium (LB with 20 mM EGTA and 20 mM MgCl₂) was used to induce the T3SS.

HeLa (ATCC), HEK293 (ATCC), and HEK293-GFP (described below) cells were cultured in Dulbecco's modified Eagle's medium (DMEM) with 10% fetal bovine serum (FBS). CHO-K1 cells (ATCC) were cultured in F-12K medium with 10% FBS. All cell lines were incubated at 37°C with 5% CO₂.

Stable cell line generation. A promoter containing five repeats of an NF-κB enhancer element (5'-TGGGGACTTCCGC-3') (26) was cloned upstream of the GFP gene, followed by integration of the construct into the HEK293 chromosome. The primers 5'-ATTAGAGCTCTGCAATTGTTAACTTGTTT ATT-3' (forward primer; SacI restriction site is underlined) and 5'-ATTAAAGCTTTATATACCCTCTAGAGTCTCCGCG-3' (reverse primer; HindIII restriction site is underlined) were used to clone the NF-κB reporter construct (26) into the multicloning site of peTurboGFP-PRL-dest1, containing a gene encoding a destabilized variant of green fluorescent protein (TurboGFP; Evrogen, Russia). The plasmid was linearized with BsaI and transfected into HEK293 cells by use of Lipofectamine 2000 (Invitrogen). Neomycin was used to select for cells carrying the plasmid, as previously described (65). Single cells were grown in DMEM supplemented with fresh neomycin every 2 weeks until they reached confluence in 96-well plates. Monoclonal NF-κB-driven GFP-expressing HEK293 cells were tested for their NF-κB response to the *Yersinia* T3SS, and positive clones were transferred to 25-cm² and then 75-cm² flasks and cryotubes. One clone, HEK293-GFP, was selected and used for the screen described below.

NF-κB screen for T3SS inhibitors. HEK293-GFP cells were plated on poly-L-lysine-coated 384-well plates at a density of 1.2×10^4 cells/well in 25 μl FluoroBrite DMEM (Thermo Fisher Scientific). *Y. pseudotuberculosis* $\Delta yop6$ or $\Delta yop6 \Delta yop8$ (Table 2) overnight cultures were back diluted to an OD₆₀₀ of 0.2 in M9 medium supplemented with Casamino Acids and grown for 1.5 h with shaking at 250 rpm and 26°C. Bacteria were transferred to 384-well plates. Compounds were added to bacteria prior to shifting the plate to 37°C, as well as to cell monolayers prior to infection by use of a pinning robot (Janus MDT robot; PerkinElmer). After 2 h of incubation at 37°C, bacteria were added to cell monolayers at an MOI of 7 (Janus MDT robot), and the infected cell plates were incubated for 5 h at 37°C and 5% CO₂. Cells were stained with the nucleic acid dye Hoechst 33342 (Thermo Fisher Scientific) and fixed with 1% paraformaldehyde (PFA; Sigma-Aldrich) on ice for 10 min. Plates were washed with phosphate-buffered saline (PBS), and residual PFA was quenched by incubation with 0.1 M glycine for 30 min. Plates were washed

in PBS four times and imaged with a Molecular Devices Image Express instrument within 24 h. T3SS function was quantified as the percentage of GFP-expressing cells among the total number of cells (total nuclei).

Cyclic peptide synthesis. Peptides were synthesized using standard Fmoc solid-phase peptide synthesis, utilizing the submonomer approach for peptoid synthesis (66), either at room temperature or with microwave assistance. Cyclization was done in solution at a high dilution.

Loading of 2-chlorotrityl resin. Fmoc-Xaa (10 mmol) was added to a flame-dried round-bottomed flask and dried in a vacuum desiccator with phosphorous pentoxide overnight. Fifty milliliters of dry dichloromethane (DCM) was cannula transferred into the flask, followed by 2.5 ml of *N,N*-diisopropylethylamine (DIPEA) transferred via syringe. After sonication for 10 min, 5 g of 2-chlorotrityl resin was added under a stream of N_2 and allowed to shake for 4 h. The resin was capped with a 15-ml solution of 1:2:17 methanol (MeOH):DIPEA:dimethylformamide (DMF) (3 times for 15 min each). The resin was washed with DMF (3 times with 15 ml each) followed by DCM (3 times with 15 ml each). The loading value was calculated by determining the mass increase of dried, loaded resin.

Amino acid coupling at room temperature. Four equivalents of Fmoc-Xaa, 5 eq of DIPEA, and 4 eq of *O*-benzotriazol-1-yl-*N,N,N'*-tetramethyluronium hexafluorophosphate (HBTU) were added to the resin in DMF. The reaction mixture was agitated via shaking for 45 min and then drained. The resin was washed with DMF (3 times with 3 ml each) and DCM (3 times with 3 ml each). The reaction was monitored by liquid chromatography-mass spectrometry (LC-MS) and repeated until the starting material was no longer observed. For microwave conditions, a solution of 4 eq of Fmoc-Xaa, 4 eq of HBTU, and 6 eq of DIPEA in DMF was allowed to prereact for 5 min. This solution was added to the deprotected peptide on-resin and allowed to react for 10 min at 50°C under microwave heating. The solution was drained, and the resin was washed with DMF (3 times with 3 ml each) and DCM (3 times with 3 ml each). The reaction was monitored by LC-MS and repeated until the starting material was no longer observed.

Coupling of BrAcOH at room temperature. A solution of 5 eq of bromoacetic acid (BrAcOH) and 5 eq of *N,N'*-diisopropylcarbodiimide (DIC) in DMF was allowed to prereact for 10 min. This solution was added to the deprotected peptide on-resin. The reaction mixture was agitated via shaking for 45 min and then drained. The resin was washed with DMF (3 times with 3 ml each) and DCM (3 times with 3 ml each). The reaction was monitored by LC-MS and repeated until the starting material was no longer observed. For microwave conditions, a solution of 5 eq of BrAcOH and 5 eq of DIC in DMF was allowed to prereact for 10 min. This solution was added to the deprotected peptide on-resin and allowed to react for 10 min at 50°C under microwave heating. The solution was drained, and the resin was washed with DMF (3 times with 3 ml each) and DCM (3 times with 3 ml each). The reaction was monitored by LC-MS and repeated until the starting material was no longer observed.

Installation of peptoid side chain. A solution of 5 to 10 eq of the desired amine was prepared in a minimum volume of DMF. The resin containing the BrAc-peptide was swollen with DCM for 5 min prior to reaction. The amine was added, and the reaction mixture was agitated vigorously for 45 min. The solution was drained, and the resin was washed with DMF (3 times with 3 ml each) and DCM (3 times with 3 ml each). The reaction was monitored by LC-MS and repeated until the starting material was no longer observed.

Removal of the *N*-Fmoc protection group at room temperature. A solution of 2% piperidine and 2% 1,8-diazabicyclo[5.4.0]undec-7-ene (DBU) in DMF was added to the resin. The reaction mixture was agitated via shaking for 20 min and then drained. The resin was washed with DMF (3 times with 3 ml each) and DCM (3 times with 3 ml each). For microwave conditions, a solution of 2% piperidine and 2% DBU in DMF was added to the resin. The reaction mixture was allowed to react for 5 min at 50°C under microwave heating and then drained. The resin was washed with DMF (3 times with 3 ml each) and DCM (3 times with 3 ml each).

Peptide cleavage. Complete linear peptides were cleaved off the resin in 5 resin volumes of 2.5% trifluoroacetic acid (TFA) in DCM for 4 min three times, with a 5-resin-volume DCM wash between steps. Solvent was removed under N_2 , followed by dissolution in acetone or DCM and evaporation under reduced pressure. Residual TFA was removed *in vacuo* overnight.

Cyclization with COMU. Linear peptides were dissolved in 20 ml of dry acetonitrile (ACN) with 4 eq of DIPEA and added dropwise (final concentration, 1 mg crude peptide per ml) to a solution of 1:1 tetrahydrofuran (THF):ACN containing 2 eq of (1-cyano-2-ethoxy-2-oxoethylideneaminoxy)dimethylamino-morpholinocarbenium hexafluorophosphate (COMU). Reaction mixtures were stirred for 0.5 to 24 h, until complete cyclization was achieved as monitored by LC-MS. The reaction mixture was reduced *in vacuo* for purification via high-pressure liquid chromatography (HPLC).

Purification of peptides. COMU by-products were removed after solution-phase cyclization on a Biotage Isolera Prime system equipped with a KP-C₁₈-HS 12g column eluting with H₂O-acetonitrile modified with 0.1% TFA. Peptides of insufficient purity were subsequently purified on a Waters mass-directed AutoPure system equipped with an X-Bridge BEH130 5- μ m 19 \times 150 C₁₈ column eluting with H₂O-acetonitrile, modified with 0.1% formic acid or 0.1% TFA. The mass spectra of all peptides are shown in Fig. S3 in the supplemental material.

Cyclic peptide manipulation. Stock peptides were kept at 15 mM and were prediluted in DMSO prior to experiments. All the treatment and control pairs had the same DMSO volumes in all assays.

Secretion assay. Visualization of proteins secreted into the culture medium was carried out as described previously (25). Briefly, *Y. pseudotuberculosis* or *Pseudomonas aeruginosa* was grown in T3SS-inducing medium (as described above) at 37°C in the presence of peptomers or an equivalent volume of DMSO carrier for 2 h. The cultures were normalized based on bacterial density (OD₆₀₀) and then centrifuged at 13,200 rpm for 15 min. The supernatants were transferred to a new tube, mixed with

6.1 N trichloroacetic acid (TCA) to a final volume of 10%, and vortexed vigorously for 30 s. Samples were incubated on ice for 30 min and then spun down at 13,200 rpm for 15 min at 4°C. The pellet was resuspended in final sample buffer (FSB) plus 20% dithiothreitol (DTT) and boiled for 5 min prior to running in a 12.5% or 7.5% SDS-PAGE gel for *Y. pseudotuberculosis* or *Pseudomonas aeruginosa*, respectively. Quantification of the bands relative to those of DMSO-treated controls was carried out using Image Lab software (Bio-Rad). The WT *Y. pseudotuberculosis* YopE or *Pseudomonas aeruginosa* ExoJ bands in DMSO control samples were set to 1.00. Bovine serum albumin (BSA) or Triton X-100 (Sigma-Aldrich) was added to the bacterial culture at the same time as the compounds in a subset of secretion assays, as indicated in Results. Note that the amount of BSA used in the assays (32 µg/ml) approached the maximum amount of BSA possible, as more BSA resulted in BSA aggregation following TCA addition (data not shown).

Translocation assay. Translocation of T3SS effector proteins into mammalian cells was assayed as previously described (26). Briefly, 6,000 CHO-K1 cells were plated in each well of a 384-well plate in 50 µl of F-12K medium plus 10% FBS and incubated overnight at 37°C with 5% CO₂. Overnight cultures of *Y. pseudotuberculosis* encoding a T3SS effector protein translocation reporter, YopM translationally fused with a β-lactamase (Bla), were back diluted to an OD₆₀₀ of 0.2 and grown at 26°C for 1.5 h with shaking. The cultures were diluted to obtain a multiplicity of infection (MOI) of 5 and then transferred to a 384-well plate. Peptomers or DMSO alone was added to the plates containing the bacterial cultures and incubated for 1.5 h at 37°C. Immediately prior to infection, the peptomers or DMSO was added to the CHO-K1 cells. Bacteria were then transferred to cells by use of a pinning robot (Janus MDT; PerkinElmer) and incubated for 1 h at 37°C and 5% CO₂. The β-lactamase substrate CCF2-AM (Invitrogen) was added to each well, and the plate was incubated in the dark for 30 min at room temperature. Cells were fixed with 4% PFA for 20 min and then stained with the DNA dye DRAQ5 (Cell Signaling Technology) in PBS for 10 min. Plates were washed once with PBS and imaged using an ImageXpress automated microscope, and the images were analyzed using MetaXpress analysis software (Molecular Devices). Translocation was quantified as the number of YopM-Bla-positive cells (blue cells containing cleaved CCF2) divided by the total number of cells (green cells containing uncleaved CCF2).

Growth curves. Overnight cultures of *Y. pseudotuberculosis* pYV⁻ (lacking the virulence plasmid that encodes the Ysc T3SS) were back diluted to an OD₆₀₀ of 0.1 in low-calcium medium, and 100 µl was added to each well of 96-well plates. This T3SS-deficient strain was used because active type III secretion induces growth arrest in *Yersinia*. Peptomers were added to each well, to a final concentration of 60 µM, in three technical replicates. Equivalent volumes of DMSO were added to the positive-control wells, and kanamycin was used as a negative control (50 µg/ml). Bacteria were maintained at 37°C, and the OD₆₀₀ values of the cultures were measured every hour for 8 h in a plate reader (VersaMax tunable microplate reader; Molecular Devices).

Motility agar assay. Motility agar plates (1% tryptone, 0.25% agar) supplemented with peptomers at a final concentration of 60 µM or with an equivalent volume of DMSO were prepared in triplicate. Motility was analyzed by spotting 1-µl aliquots of either nonmotile *Y. pseudotuberculosis* (*fliHDC*^Δ or *tatB::Tn*) or motile bacteria (WT) onto the motility agar from overnight cultures standardized to an OD₆₀₀ of 2.5 in PBS. Plates were incubated at room temperature for 1 day. Colonies were imaged by use of a Chemidoc system (Bio-Rad), and the diameters of the colonies were determined in Image Lab (Bio-Rad) and used to calculate the percent motility relative to the motility with DMSO, which was set to 100%.

Liquid motility assay. *Salmonella* Typhimurium or *Pseudomonas aeruginosa* PAO1 was cultured in LB at 37°C with shaking at 250 rpm overnight. The cultures were then diluted to an OD of 0.025 in LB, and 30 µM peptomers or an equivalent volume of DMSO was added. An *S. Typhimurium* flagellar mutant (*ΔfliHDC*) (Table 2) was used as a negative control for motility. *S. Typhimurium* and PAO1 were filmed by use of a Hamamatsu C4742-95 digital camera and a Nikon Eclipse E600 microscope after 2 and 3 h of incubation, respectively. Ten-microliter aliquots of culture were spotted onto coverslips, and videos were taken every 1 s for 60 frames. Five videos, from the four corners and the center of the slide, were recorded for each sample. The movies were analyzed in Imares v.8 and subsequently processed in Matlab2016a and GraphPad Prism 7. The movement observed for nonmotile bacteria was due to drift of the culture on the slide during the course of the movie, as all bacteria in the negative-control culture showed drift in the same direction. Bacteria were considered motile if they traveled a distance 2 standard deviations greater than the average nonmotile bacterial drifting distance.

Cell viability. The yellow tetrazolium MTT [3-(4,5-dimethyl-2-thiazolyl)-2,5-diphenyl-2H-tetrazolium bromide] is reduced by metabolically active cells by the action of dehydrogenase enzymes, resulting in intracellular purple formazan. The MTT assay measures the cell proliferation rate, which correlates with formazan signals. To measure mammalian cell cytotoxicity in the presence of peptomers, HeLa cells were placed in 384-well plates at a density of 2,000 cells/well in triplicate and incubated at 37°C and 5% CO₂ for 24 h. Compounds were added to each well in a 2-fold dilution series, starting at 240 µM, and the cultures were incubated at 37°C and 5% CO₂ for 20 h. Ten microliters of MTT was added to each well, and plates were returned to the incubator for 4 h. Plates were washed once with PBS. Fifty microliters of ammonia-DMSO (67) was added to each well to solubilize the formazan crystals. Plates were incubated in the dark for 30 min at room temperature, and the absorbance at 570 nm was read in a plate reader (VersaMax tunable microplate reader; Molecular Devices).

To measure bacterial cell cytotoxicity in the presence of peptomers, *Y. pseudotuberculosis* pYV⁻ overnight cultures were back diluted as described above for growth curves and then treated with compounds at a final concentration of 120 µM. The cultures were incubated at 37°C for 24 h. Ten microliters of MTT reagent was added to each well, and the plate was incubated for 2 h in the dark. One hundred microliters of 0.04 N HCl-DMSO (67) was added to each well and mixed thoroughly to solubilize

the formazan crystals. Plates were read at 570 nm in a plate reader (VersaMax tunable microplate reader; Molecular Devices) within a few minutes.

Cell rounding. HeLa cells were placed in 384-well plates at a density of 2,000 cells/well, centrifuged at 1,000 rpm for 5 min, and maintained at 37°C with 5% CO₂. WT *Yersinia pseudotuberculosis*, which encodes the actin-targeting YopEHO effectors that cause cell rounding in host cells, was treated with peptomers in a 2-fold dilution series, starting at 120 μM, in low-calcium medium at 37°C for 2 h. HeLa cells were infected with WT *Yersinia* at an MOI of 40, and plates were spun at 750 rpm for 5 min and maintained at 37°C for 3 h. WT *Yersinia* treated with an equivalent amount of DMSO was used as a positive control, and the T355-deficient *ΔyycNU* mutant was used as a negative control for induction of cell rounding. Cells were stained with the plasma membrane stain CellMask deep red (Thermo Fisher Scientific) and the nuclear stain Hoechst 33342 (Thermo Fisher Scientific) for 20 min, fixed with 4% PFA (Sigma-Aldrich) for 10 min, washed with PBS, and imaged with a Molecular Devices Image Express system.

Thermodynamic solubility assay. Stocks (15 mM) of the compounds were prepared in DMSO. Each stock solution was dispensed into a 96-well plate and evaporated overnight under reduced pressure with heat (50°C). To the evaporated film/solid, 125 μl of DMEM was added to make a 2 mM solution of the target compound. This solution was sonicated for 1 h and then shaken at 37°C for 16 h. The turbid solution was passed over a 0.7-μm glass-fiber filter. The solution was diluted 1:4 in acetonitrile. The solution was centrifuged at 1,000 × g for 10 min. The supernatant (10 μl) was injected onto a Thermo Fisher Orbitrap Velos Pro instrument. A 10 μM standard was used for comparison, and the assay was done in triplicate.

Kinetic solubility assay. The kinetic solubility assay was done similarly to the thermodynamic solubility assay, except that the compounds were shaken for 2 h in the presence of 0.8% DMSO to mimic the conditions in most of our assays. The kinetic solubility assay mimics many of our assay conditions, in that compounds are predissolved in DMSO and tested after a short incubation time.

Statistical analysis. GraphPad Prism 7 (GraphPad Software, La Jolla, CA, USA) was used to calculate the means, standard errors of the means, medians, standard errors of the medians, and one-way analysis of variance (ANOVA) values shown in the figures.

SUPPLEMENTAL MATERIAL

Supplemental material for this article may be found at <https://doi.org/10.1128/AAC.00060-17>.

SUPPLEMENTAL FILE 1, PDF file, 5.1 MB.

ACKNOWLEDGMENTS

We acknowledge National Institutes of Health grant R01AI106930 (to V.A.), NIH National Human Genome Research Institute grant R25HG006836 (to J.M.), and the Vietnam Education Foundation (to H.L.) for support.

We thank Joanne Engel and Susanne Häussler for the *Pseudomonas aeruginosa* strains, Melanie Marketon for the YopM-Bla plasmid, Karen Ottemann for *Salmonella* Typhimurium strains, Benjamin Abrams for helping with spot-tracking analysis, Matthew R. Naylor for helping with the Orbitrap instrument, and Hector Ramirez for characterization of the *tatB::Tn* strain.

REFERENCES

- Coates AR, Halls G, Hu Y. 2011. Novel classes of antibiotics or more of the same? *Br J Pharmacol* 163:184–194. <https://doi.org/10.1111/j.1476-5381.2011.01250.x>.
- Levy SB, Marshall B. 2004. Antibacterial resistance worldwide: causes, challenges and responses. *Nat Med* 10:S122–S129. <https://doi.org/10.1038/nm1145>.
- Schjorring S, Krogfelt KA. 2011. Assessment of bacterial antibiotic resistance transfer in the gut. *Int J Microbiol* 2011:312956. <https://doi.org/10.1155/2011/312956>.
- Schjorring S, Struve C, Krogfelt KA. 2008. Transfer of antimicrobial resistance plasmids from *Klebsiella pneumoniae* to *Escherichia coli* in the mouse intestine. *J Antimicrob Chemother* 62:1086–1093. <https://doi.org/10.1093/jac/dkn323>.
- Duncan MC, Lirington RG, Auerbuch V. 2012. Chemical inhibitors of the type three secretion system: disarming bacterial pathogens. *Antimicrob Agents Chemother* 56:5433–5441. <https://doi.org/10.1128/AAC.00975-12>.
- Lewis K. 2013. Platforms for antibiotic discovery. *Nat Rev Drug Discov* 12:371–387. <https://doi.org/10.1038/nrd3975>.
- Kamada N, Chen GY, Inohara N, Nunez G. 2013. Control of pathogens and pathobionts by the gut microbiota. *Nat Immunol* 14:685–690. <https://doi.org/10.1038/ni.2608>.
- Baumler AJ, Sperandio V. 2016. Interactions between the microbiota and pathogenic bacteria in the gut. *Nature* 535:85–93. <https://doi.org/10.1038/nature18849>.
- Troisfontaines P, Cornelis GR. 2005. Type III secretion: more systems than you think. *Physiology* 20:326–339. <https://doi.org/10.1152/physiol.00011.2005>.
- Diepold A, Armitage JP. 2015. Type III secretion systems: the bacterial flagellum and the injectisome. *Philos Trans R Soc Lond B Biol Sci* 370:20150020. <https://doi.org/10.1098/rstb.2015.0020>.
- Notti RQ, Stebbins CE. 12 February 2016. The structure and function of type III secretion systems. *Microbiol Spectr* 4:VMBF-0004–2015. <https://doi.org/10.1128/microbiolspec.VMBF-0004-2015>.
- Matsumoto H, Young GM. 2009. Translocated effectors of *Yersinia*. *Curr Opin Microbiol* 12:94–100. <https://doi.org/10.1016/j.mib.2008.12.005>.
- Pha K, Navarro L. 2016. *Yersinia* type III effectors perturb host innate immune responses. *World J Biol Chem* 7:1–13. <https://doi.org/10.4331/wjbc.v7.i1.1>.
- Hauser AR. 2009. The type III secretion system of *Pseudomonas aeruginosa*: infection by injection. *Nat Rev Microbiol* 7:654–665. <https://doi.org/10.1038/nrmicro2199>.
- Von Pawel-Rammingen U, Telepnev MV, Schmidt G, Aktories K, Wolf-

- Watz H, Rosqvist R. 2000. GAP activity of the *Yersinia* YopE cytotoxin specifically targets the Rho pathway: a mechanism for disruption of actin microfilament structure. *Mol Microbiol* 36:737–748. <https://doi.org/10.1046/j.1365-2958.2000.01898.x>.
16. Black DS, Bliska JB. 2000. The RhoGAP activity of the *Yersinia pseudotuberculosis* cytotoxin YopE is required for antiphagocytic function and virulence. *Mol Microbiol* 37:515–527. <https://doi.org/10.1046/j.1365-2958.2000.02021.x>.
17. Guan KL, Dixon JE. 1990. Protein tyrosine phosphatase-activity of an essential virulence determinant in *Yersinia*. *Science* 249:553–556. <https://doi.org/10.1126/science.2166336>.
18. Fallman M, Persson C, Wolf-Watz H. 1997. *Yersinia* proteins that target host cell signaling pathways. *J Clin Invest* 99:1153–1157. <https://doi.org/10.1172/JCI119270>.
19. Lee WL, Grimes JM, Robinson RC. 2015. *Yersinia* effector YopO uses actin as bait to phosphorylate proteins that regulate actin polymerization. *Nat Struct Mol Biol* 22:248–255. <https://doi.org/10.1038/nsmb.2964>.
20. Mesaros N, Nordmann P, Plesiat P, Rousset-Delvallez M, Van Eldere J, Glupczynski Y, Van Laethem Y, Jacobs F, Lebecque P, Malfroot A, Tulkens PM, Van Bambeke F. 2007. *Pseudomonas aeruginosa*: resistance and therapeutic options at the turn of the new millennium. *Clin Microbiol Infect* 13:560–578. <https://doi.org/10.1111/j.1469-0691.2007.01681.x>.
21. Driscoll JA, Brody SL, Kollef MH. 2007. The epidemiology, pathogenesis and treatment of *Pseudomonas aeruginosa* infections. *Drugs* 67:351–368. <https://doi.org/10.2165/00003495-200767030-00003>.
22. Schuler G, Feltman H, Rabin SDP, Martin CG, Battle SE, Rello J, Hauser AR. 2003. Secretion of the toxin ExoU is a marker for highly virulent *Pseudomonas aeruginosa* isolates obtained from patients with hospital-acquired pneumonia. *J Infect Dis* 188:1695–1706. <https://doi.org/10.1086/379372>.
23. Livermore DM. 2002. Multiple mechanisms of antimicrobial resistance in *Pseudomonas aeruginosa*: our worst nightmare? *Clin Infect Dis* 34: 634–640. <https://doi.org/10.1086/338782>.
24. Mitchell S, Vargas J, Hoffmann A. 2016. Signaling via the NFκB system. *Wiley Interdiscip Rev Syst Biol Med* 8:227–241. <https://doi.org/10.1002/wsbm.1331>.
25. Auerbuch V, Golenbock DT, Isberg RR. 2009. Innate immune recognition of *Yersinia pseudotuberculosis* type III secretion. *PLoS Pathog* 5:e1000686. <https://doi.org/10.1371/journal.ppat.1000686>.
26. Duncan MC, Wong WR, Dupzyk AJ, Bray WM, Linington RG, Auerbuch V. 2014. An NF-κB-based high-throughput screen identifies pteridins as inhibitors of the *Yersinia pseudotuberculosis* type III secretion system. *Antimicrob Agents Chemother* 58:1118–1126. <https://doi.org/10.1128/AAC.02025-13>.
27. Zhang J-H, Chung TDY, Oldenburg KR. 1999. A simple statistical parameter for use in evaluation and validation of high throughput screening assays. *J Biomol Screen* 4:67–73. <https://doi.org/10.1177/108705719900400206>.
28. Schwochert J, Lao Y, Pye CR, Naylor MR, Desai PV, Gonzalez Valcarcel IC, Barrett JA, Sawada G, Blanco MJ, Lokey RS. 2016. Stereochemistry balances cell permeability and solubility in the naturally derived phepropeptin cyclic peptides. *ACS Med Chem Lett* 7:757–761. <https://doi.org/10.1021/acsmchemlett.6b00100>.
29. Sekizawa R, Momose I, Kinoshita N, Naganawa H, Hamada M, Muraoka Y, Iinuma H, Takeuchi T. 2001. Isolation and structural determination of phepropeptins A, B, C, and D, new proteasome inhibitors, produced by *Streptomyces* sp. *J Antibiot (Tokyo)* 54:874–881. <https://doi.org/10.7164/antibiotics.54.874>.
30. Qian Z, Dougherty PG, Pei D. 2017. Targeting intracellular protein-protein interactions with cell-permeable cyclic peptides. *Curr Opin Chem Biol* 38:80–86. <https://doi.org/10.1016/j.cbpa.2017.03.011>.
31. McGovern SL, Helfand BT, Feng B, Shoichet BK. 2003. A specific mechanism of nonspecific inhibition. *J Med Chem* 46:4265–4272. <https://doi.org/10.1021/jm030266r>.
32. Portaliou AG, Tsois KC, Loos MS, Zorzini V, Economou A. 2016. Type III secretion: building and operating a remarkable nanomachine. *Trends Biochem Sci* 41:175–189. <https://doi.org/10.1016/j.tibs.2015.09.005>.
33. Wilhelm G, Lehmann V, Krauss K, Lehnert B, Richter S, Ruckdeschel K, Heesemann J, Trulzsch K. 2004. *Yersinia enterocolitica* type III secretion depends on the proton motive force but not on the flagellar motor components MotA and MotB. *Infect Immun* 72:4004–4009. <https://doi.org/10.1128/AI.72.7.4004-4009.2004>.
34. Lavander M, Ericsson SK, Broms JE, Forsberg A. 2006. The twin arginine translocation system is essential for virulence of *Yersinia pseudotuberculosis*. *Infect Immun* 74:1768–1776. <https://doi.org/10.1128/AI.74.3.1768-1776.2006>.
35. Mould RM, Robinson C. 1991. A proton gradient is required for the transport of 2 luminal oxygen-evolving proteins across the thylakoid membrane. *J Biol Chem* 266:12189–12193.
36. Wozniak CE, Chevance FF, Hughes KT. 2010. Multiple promoters contribute to swarming and the coordination of transcription with flagellar assembly in *Salmonella*. *J Bacteriol* 192:4752–4762. <https://doi.org/10.1128/JB.00093-10>.
37. Dasgupta N, Wolfgang MC, Goodman AL, Arora SK, Jyot J, Lory S, Ramphal R. 2003. A four-tiered transcriptional regulatory circuit controls flagellar biogenesis in *Pseudomonas aeruginosa*. *Mol Microbiol* 50: 809–824. <https://doi.org/10.1046/j.1365-2958.2003.03740.x>.
38. Mendivil-Perez M, Velez-Pardo C, Jimenez-Del-Rio M. 2012. TPEN induces apoptosis independently of zinc chelator activity in a model of acute lymphoblastic leukemia and ex vivo acute leukemia cells through oxidative stress and mitochondria caspase-3- and AIF-dependent pathways. *Oxid Med Cell Longev* 2012:313275. <https://doi.org/10.1155/2012/313275>.
39. Fatfat M, Merhi RA, Rahal O, Stoyanovsky DA, Zaki A, Haidar H, Kagan VE, Gali-Muhtasib H, Machaca K. 2014. Copper chelation selectively kills colon cancer cells through redox cycling and generation of reactive oxygen species. *BMC Cancer* 14:527. <https://doi.org/10.1186/1471-2407-14-527>.
40. Adler M, Shafer H, Hamilton T, Petrari JP. 1999. Cytotoxic actions of the heavy metal chelator TPEN on NG108-15 neuroblastoma-glioma cells. *Neurotoxicology* 20:571–582.
41. Viboud G, Bliska JB. 2005. *Yersinia* outer proteins: role in modulation of host cell signaling responses and pathogenesis. *Annu Rev Microbiol* 59:69–89. <https://doi.org/10.1146/annurev.micro.59.030804.121320>.
42. Craik DJ, Fairlie DP, Liras S, Price D. 2013. The future of peptide-based drugs. *Chem Biol Drug Des* 81:136–147. <https://doi.org/10.1111/cbdd.12055>.
43. Miller SM, Simon RJ, Ng S, Zuckermann RN, Kerr JM, Moos WH. 1994. Proteolytic studies of homologous peptide and N-substituted glycine peptid oligomers. *Bioorg Med Chem Lett* 4:2657–2662. [https://doi.org/10.1016/S0960-894X\(01\)80691-0](https://doi.org/10.1016/S0960-894X(01)80691-0).
44. Simon RJ, Kania RS, Zuckermann RN, Huebner VD, Jewell DA, Banville S, Ng S, Wang L, Rosenberg S, Marlowe CK, Spelmeyer DC, Tan RY, Frankel AD, Santi DV, Cohen FE, Bartlett PA. 1992. Peptoids—a modular approach to drug discovery. *Proc Natl Acad Sci U S A* 89:9367–9371. <https://doi.org/10.1073/pnas.89.20.9367>.
45. Schwochert J, Turner R, Thang M, Berkeley RF, Ponkey AR, Rodriguez KM, Leung SSF, Khunte B, Goetz G, Limberakis C, Kalgutar AS, Eng H, Shapiro MJ, Mathiowetz AM, Price DA, Liras S, Jacobson MP, Lokey RS. 2015. Peptide to peptoid substitutions increase cell permeability in cyclic hexapeptides. *Org Lett* 17:2928–2931. <https://doi.org/10.1021/acs.orglett.5b01162>.
46. Wassing GM, Bergman P, Lindbom L, van der Does AM. 2015. Complexity of antimicrobial peptide regulation during pathogen-host interactions. *Int J Antimicrob Agents* 45:447–454. <https://doi.org/10.1016/j.ijantimicag.2014.11.003>.
47. Wang G. 2015. Improved methods for classification, prediction, and design of antimicrobial peptides. *Methods Mol Biol* 1268:43–66. https://doi.org/10.1007/978-1-4939-2285-7_3.
48. Park SC, Park Y, Hahn KS. 2011. The role of antimicrobial peptides in preventing multidrug-resistant bacterial infections and biofilm formation. *Int J Mol Sci* 12:5971–5992. <https://doi.org/10.3390/ijms12095971>.
49. Jang A, Jo C, Kang KS, Lee M. 2008. Antimicrobial and human cancer cell cytotoxic effect of synthetic angiotensin-converting enzyme (ACE) inhibitory peptides. *Food Chem* 107:327–336. <https://doi.org/10.1016/j.foodchem.2007.08.036>.
50. Ebbensgaard A, Mordhorst H, Overgaard MT, Nielsen CG, Aarestrup FM, Hansen EB. 2015. Comparative evaluation of the antimicrobial activity of different antimicrobial peptides against a range of pathogenic bacteria. *PLoS One* 10:e0144611. <https://doi.org/10.1371/journal.pone.0144611>.
51. Mader JS, Hoskin DW. 2006. Cationic antimicrobial peptides as novel cytotoxic agents for cancer treatment. *Expert Opin Invest Drugs* 15: 933–946. <https://doi.org/10.1517/13543784.15.8.933>.
52. Straus SK, Hancock REW. 2006. Mode of action of the new antibiotic for Gram-positive pathogens daptomycin: comparison with cationic antimicrobial peptides and lipopeptides. *Biochim Biophys Acta* 1758: 1215–1223. <https://doi.org/10.1016/j.bbame.2006.02.009>.
53. Horn JN, Romo TD, Pitman MC, Grossfield A. 2010. Binding of anti-

- crobal lipopeptides to lipid bilayers characterized by microsecond molecular dynamics simulations. *Biophys J* 98:81a.
54. Kling A, Lukat P, Almeida DV, Bauer A, Fontaine E, Sordello S, Zburannyi N, Herrmann J, Wenzel SC, König C, Ammerman NC, Barrio MB, Borchers K, Bordon-Pallier F, Bronstrup M, Courtemanche G, Gerlitz M, Geslin M, Hammann P, Heinz DW, Hoffmann H, Klieber S, Kohlmann M, Kurz M, Lair C, Matter H, Nuernberger E, Tyagi S, Fraisse L, Grosse JH, Lagrange S, Muller R. 2015. Targeting DnaN for tuberculosis therapy using novel griselmycins. *Science* 348:1106–1112. <https://doi.org/10.1126/science.1254490>.
 55. Tal-Gan Y, Stacy DM, Foegen MK, Koenig DW, Blackwell HE. 2013. Highly potent inhibitors of quorum sensing in *Staphylococcus aureus* revealed through a systematic synthetic study of the group-III autoinducing peptide. *J Am Chem Soc* 135:7869–7882. <https://doi.org/10.1021/ja3112115>.
 56. Tal-Gan Y, Ivancic M, Cornilescu G, Yang T, Blackwell HE. 2016. Highly stable, amide-bridged autoinducing peptide analogues that strongly inhibit the AgrC quorum sensing receptor in *Staphylococcus aureus*. *Angew Chem Int Ed Engl* 55:8913–8917. <https://doi.org/10.1002/anie.201602974>.
 57. Kim OK, Garrity-Ryan LK, Bartlett VJ, Grier MC, Verma AK, Medjanis G, Donatelli JE, Macone AB, Tanaka SK, Levy SB, Alekshun MN. 2009. N-hydroxybenzimidazole inhibitors of the transcription factor LcrF in *Yersinia*: novel antivirulence agents. *J Med Chem* 52:5626–5634. <https://doi.org/10.1021/jm9006577>.
 58. Swietnicki W, Carmany D, Retford M, Guelta M, Dorsey R, Bozue J, Lee MS, Olson MA. 2011. Identification of small-molecule inhibitors of *Yersinia pestis* type III secretion system YscN ATPase. *PLoS One* 6:e19716. <https://doi.org/10.1371/journal.pone.0019716>.
 59. Wang D, Zetterstrom CE, Gabrielsen M, Beckham KS, Tree JJ, Macdonald SE, Byron O, Mitchell TJ, Gally DL, Herzyk P, Mahajan A, Uvell H, Burchmore R, Smith BO, Elofsson M, Roe AJ. 2011. Identification of bacterial target proteins for the salicylidene acylhydrazide class of virulence-blocking compounds. *J Biol Chem* 286:29922–29931. <https://doi.org/10.1074/jbc.M111.233858>.
 60. McGovern SL, Caselli E, Grigorieff N, Shoichet BK. 2002. A common mechanism underlying promiscuous inhibitors from virtual and high-throughput screening. *J Med Chem* 45:1712–1722. <https://doi.org/10.1021/jm010533y>.
 61. Morgan JM, Duncan MC, Johnson KS, Diepold A, Lam H, Dupzyk AJ, Martin LR, Wong WR, Armitage JP, Linington RG, Auerbuch V. 2017. Pleiadin A1 blocks *Yersinia* Ysc type III secretion system needle assembly. *mSphere* 2:e00030-17. <https://doi.org/10.1128/mSphere.00030-17>.
 62. Cornelis GR. 2006. The type III secretion injectisome. *Nat Rev Microbiol* 4:811–825. <https://doi.org/10.1038/nrmicro1526>.
 63. Zgurskaya HI, Lopez CA, Gnanakaran S. 2015. Permeability barrier of Gram-negative cell envelopes and approaches to bypass it. *ACS Infect Dis* 1:512–522. <https://doi.org/10.1021/acscinfed.5b00097>.
 64. Miller HK, Kwuan L, Schwiesow L, Bernick DL, Mettert E, Ramirez HA, Ragle JM, Chan PP, Kiley PJ, Lowe TM, Auerbuch V. 2014. IscR is essential for *Yersinia pseudotuberculosis* type III secretion and virulence. *PLoS Pathog* 10:e1004194. <https://doi.org/10.1371/journal.ppat.1004194>.
 65. Ludwig DL. May 2006. Mammalian expression cassette engineering for high-level protein production. *BioProcess Int* 2006(Suppl):14–23.
 66. Zuckermann RN, Kerr JM, Kent SBH, Moos WH. 1992. Efficient method for the preparation of peptoids [oligo(N-substituted glycines)] by submonomer solid-phase synthesis. *J Am Chem Soc* 114:10646–10647. <https://doi.org/10.1021/ja00052a076>.
 67. Wang HW, Wang FQ, Tao XY, Cheng HR. 2012. Ammonia-containing dimethyl sulfoxide: an improved solvent for the dissolution of formazan crystals in the 3-(4,5-dimethylthiazol-2-yl)-2,5-diphenyl tetrazolium bromide (MTT) assay. *Anal Biochem* 421:324–326. <https://doi.org/10.1016/j.ab.2011.10.043>.
 68. Bliska JB, Guan KL, Dixon JE, Falkow S. 1991. Tyrosine phosphate hydrolysis of host proteins by an essential *Yersinia*-virulence determinant. *Proc Natl Acad Sci U S A* 88:1187–1191. <https://doi.org/10.1073/pnas.88.4.1187>.
 69. Balada-Llasat JM, Mecas J. 2006. *Yersinia* has a tropism for B and T cell zones of lymph nodes that is independent of the type III secretion system. *PLoS Pathog* 2:816–828. <https://doi.org/10.1371/journal.ppat.0020086>.
 70. Rabin SD, Hauser AR. 2005. Functional regions of the *Pseudomonas aeruginosa* cytotoxin ExoU. *Infect Immun* 73:573–582. <https://doi.org/10.1128/IAI.73.1.573-582.2005>.
 71. Rangel SM, Diaz MH, Knoten CA, Zhang A, Hauser AR. 2015. The role of ExoS in dissemination of *Pseudomonas aeruginosa* during pneumonia. *PLoS Pathog* 11:e1004945. <https://doi.org/10.1371/journal.ppat.1004945>.
 72. Stover CK, Pham XQ, Erwin AL, Mizoguchi SD, Warrenner P, Hickey MJ, Brinkman FSL, Hufnagle WO, Kowalik DJ, Lagrou M, Garber RL, Goltry L, Tolentino E, Westbrock-Wadman S, Yuan Y, Brody LL, Coulter SN, Folger KR, Kas A, Larbig K, Lim R, Smith K, Spencer D, Wong GK, Wu Z, Paulsen IT, Reizer J, Saier MH, Hancock REW, Lory S, Olson MV. 2000. Complete genome sequence of *Pseudomonas aeruginosa* PAO1, an opportunistic pathogen. *Nature* 406:959–964. <https://doi.org/10.1038/35023079>.
 73. Frye J, Karlinsey JE, Felise HR, Marzolf B, Dowidar N, McClelland M, Hughes KT. 2006. Identification of new flagellar genes of *Salmonella enterica* serovar Typhimurium. *J Bacteriol* 188:2233–2243. <https://doi.org/10.1128/JB.188.6.2233-2243.2006>.

Figure S1. Secretion of T3SS cargo into the culture supernatant was assessed by precipitating secreted proteins and visualizing with coomassie blue. Representative images of T3SS cargo from the secretion assays. WT *Y. pseudotuberculosis* was grown under T3SS-inducing conditions in the presence of A) 60 μ M peptomers or equivalent volume of DMSO or B) increasing concentration of peptomers ranging from 1.9 μ M to 120 μ M. YopE band is indicated by the arrow. C) WT *Pseudomonas* PA103 was grown under T3SS-inducing conditions in concentrations ranging from 1.9 μ M to 120 μ M, or the equivalent volume of DMSO. ExoU band is shown. NU is the Δ lysC/NU/T3SS deficient control strain.

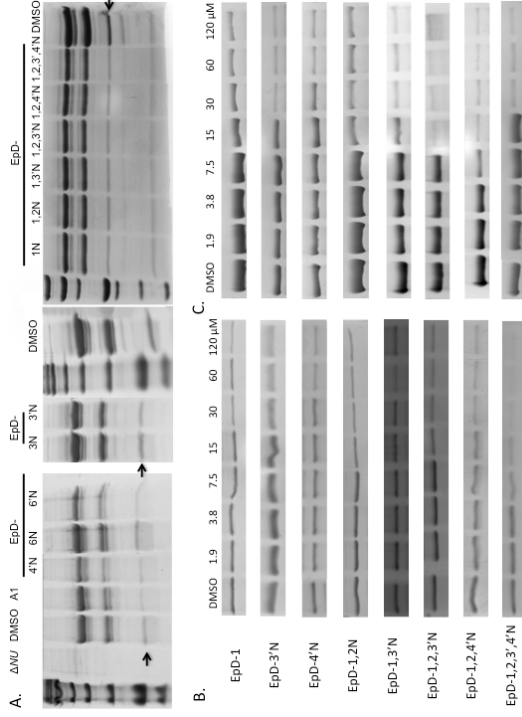


Figure S2. Translocation of *Yersinia* effector YopM to CHO-K1 cells at increasing concentration of peptomers and DMSO. Red line crosses the top plateau of the curve fit of DMSO treated samples, depicting minimal effect of DMSO on translocation, while green line crosses the bottom plateau of the curve fit of DMSO treated samples, depicting maximum effect of DMSO on translocation.

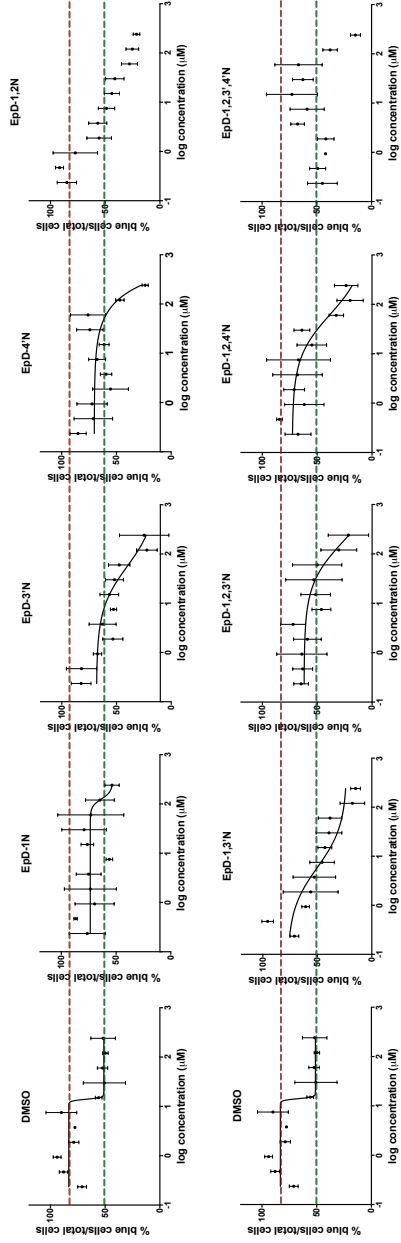
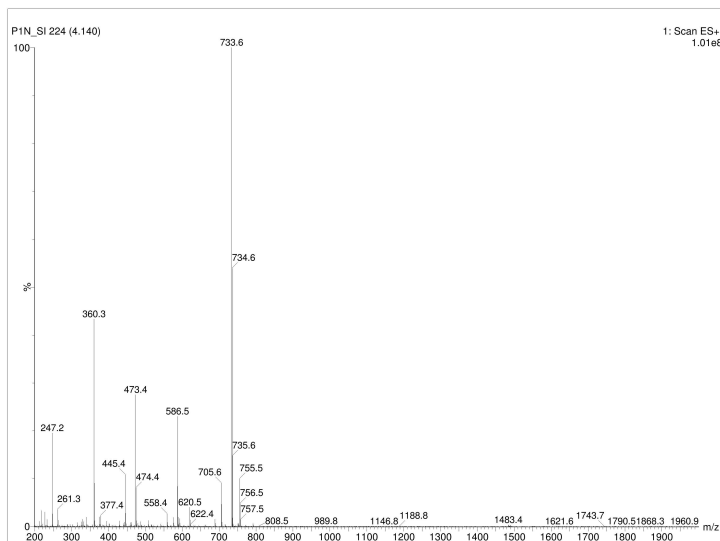
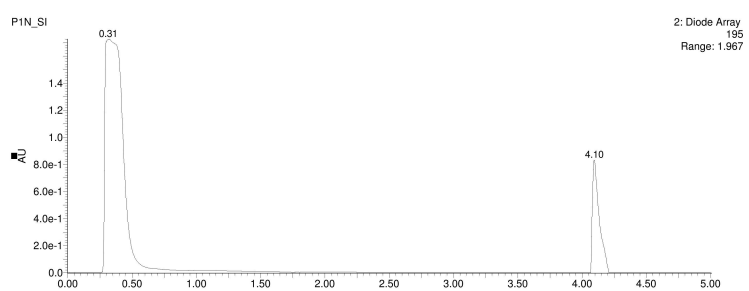
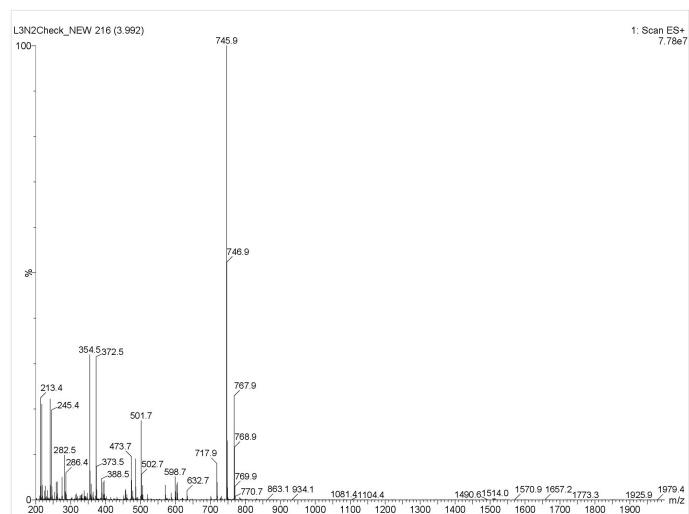
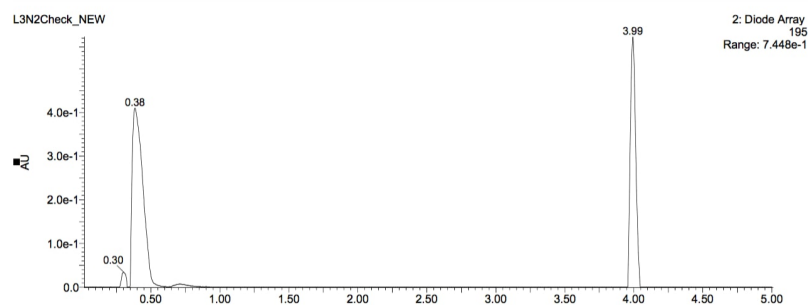


Figure S3. Reversed-phase HPLC-UV-MS spectra of select pure compounds. Compounds were eluted on gradients between H₂O modified with 0.1% formic acid and acetonitrile modified with 0.1% formic acid on a Thermo Fischer C18 Accucore 2.6 μM particle size, 50 mm x 4.6 mm on a Waters Autopure system detected with a Micromass ZQ 2000.

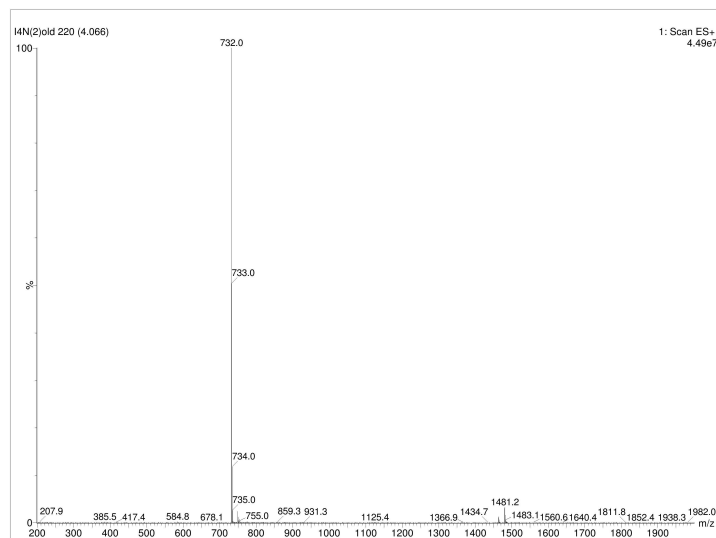
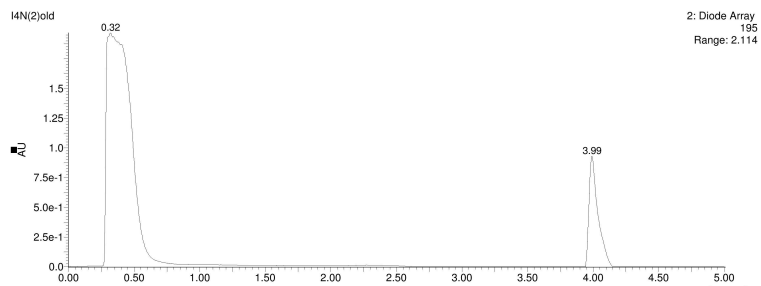
EpD-1N: C₄₁H₆₀N₆O₆[M+H]⁺ $m/z = 733.4$; found 733.6
Extracted Mass Spectrum from major peak:



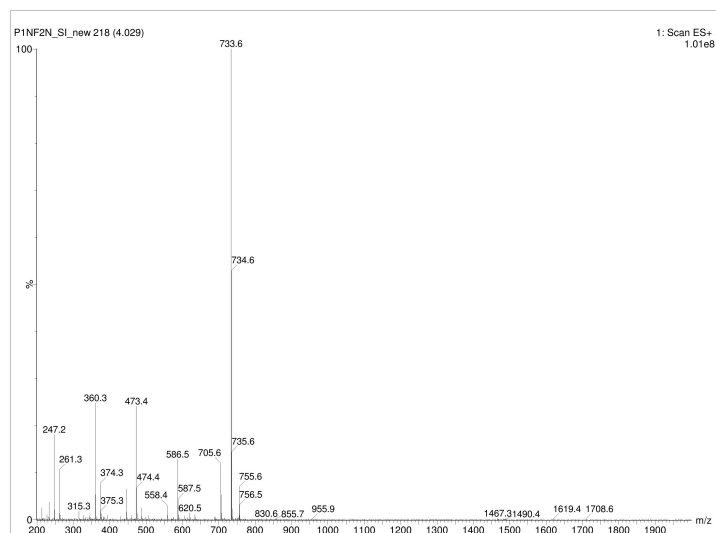
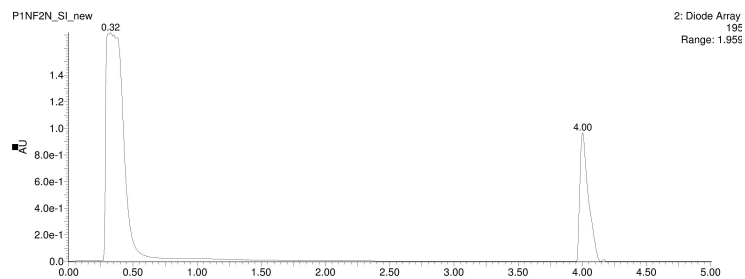
EpD-3'N: C₄₂H₆₀N₆O₆[M+H]⁺ m/z = 745.4; found 745.6
Extracted Mass Spectrum from major peak:



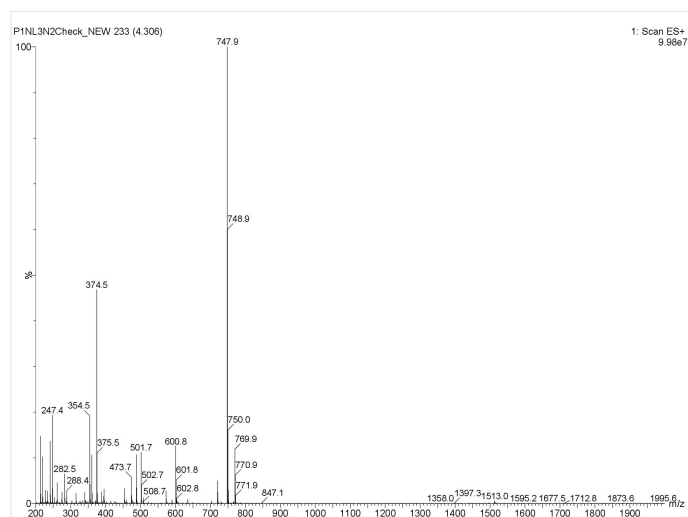
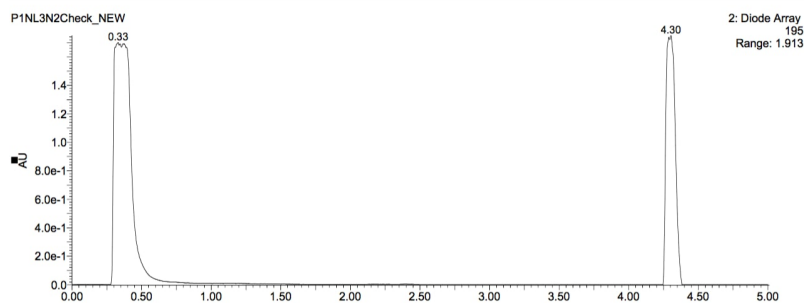
EpD-4'N C₄₁H₅₈N₆O₆[M+H]⁺ *m/z* = 731.4; found 732.0
Extracted Mass Spectrum from major peak:



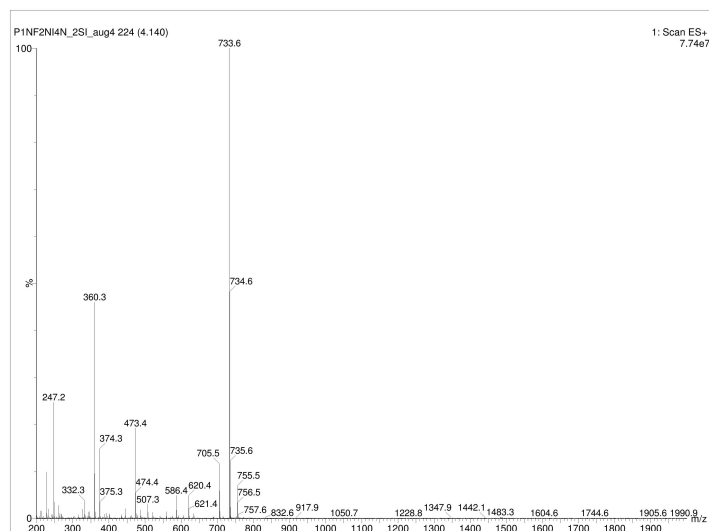
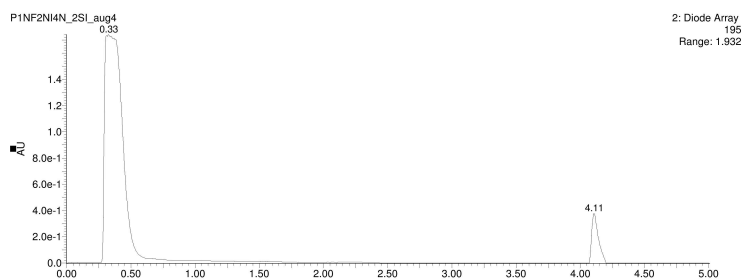
EpD-1,2N: C₄₁H₆₀N₆O₆[M+H]⁺ *m/z* = 733.4; found 733.6
Extracted Mass Spectrum from major peak:



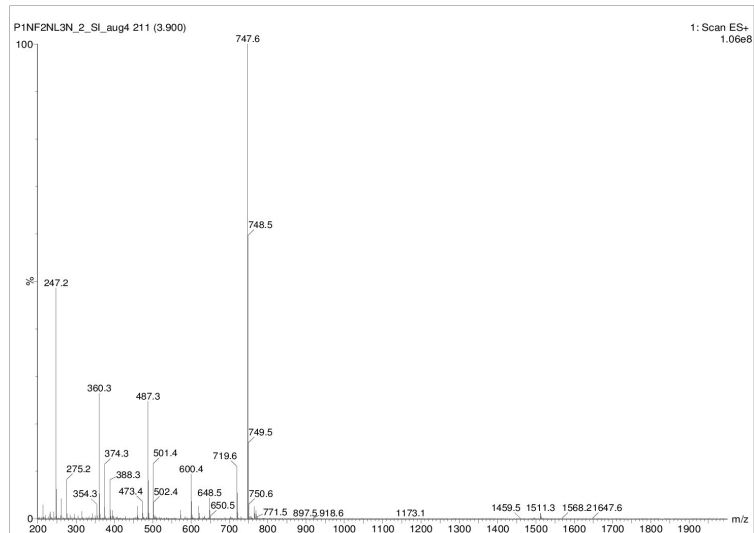
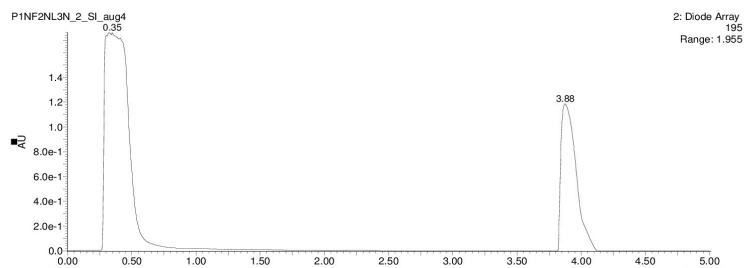
EpD-1,3'N: $C_{42}H_{62}N_6O_6[M+H]^+$ $m/z = 747.4$; found 747.6
Extracted Mass Spectrum from major peak:



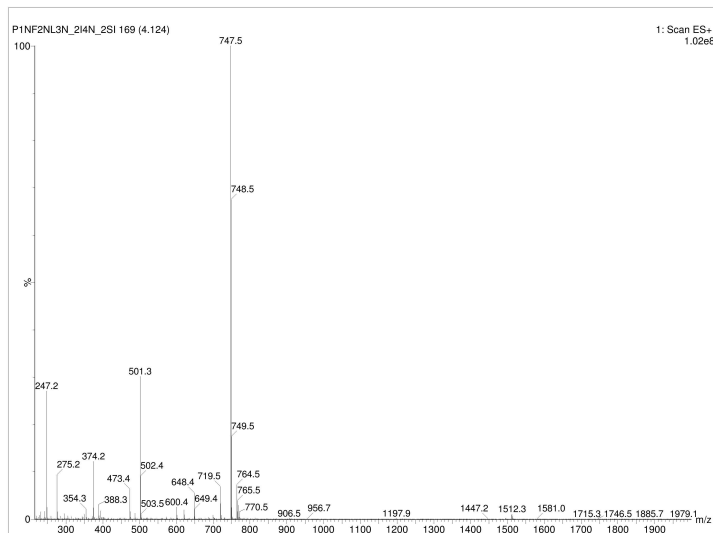
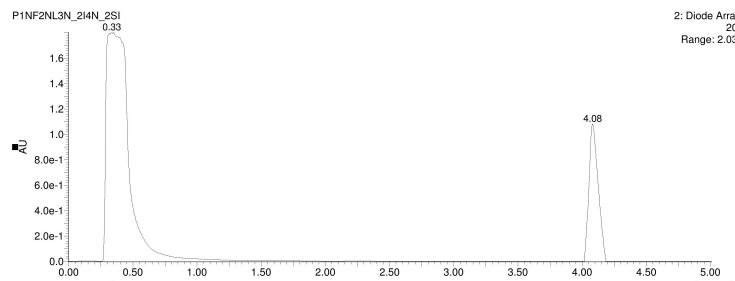
EpD-1,2,4'N: C₄₁H₆₀N₆O₆[M+H]⁺ m/z = 733.4; found 733.6
Extracted Mass Spectrum from major peak:



EpD-1,2,3'N: C₄₂H₆₂N₆O₆[M+H]⁺ *m/z* = 747.4; found 747.6
Extracted Mass Spectrum from major peak:



EpD-1,2,3',4'N: $C_{42}H_{62}N_6O_6[M+H]^+$ $m/z = 747.4$; found 747.5
Extracted Mass Spectrum from major peak:



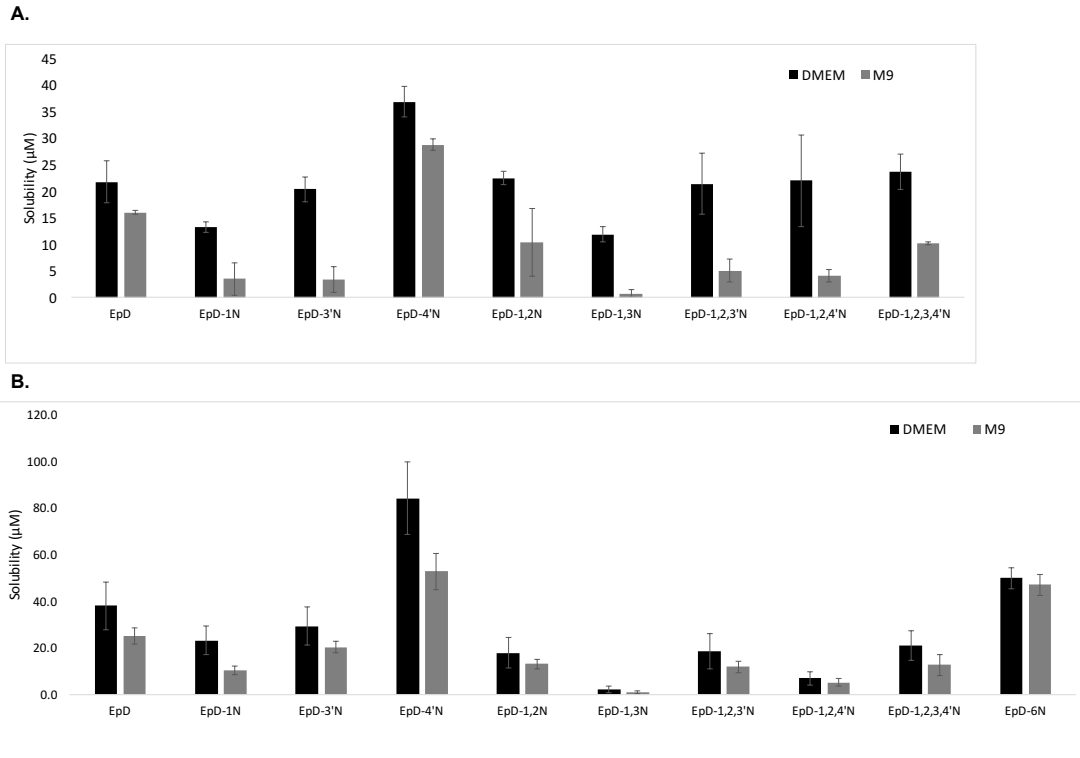
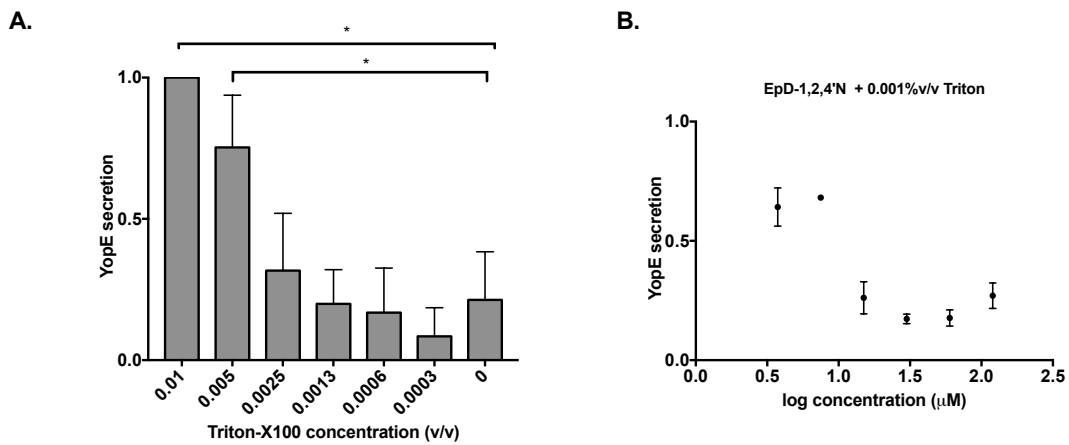


Figure S4. Solubility of peptomers determined by (A) kinetic and (B) thermodynamic solubility assay in cell culture media (DMEM) and T3SS inducing bacteriological media (M9).

Figure S5. Disaggregation of cyclic peptomer with detergent does not prevent inhibition of type III secretion. WT *Y. pseudotuberculosis* was grown under T3SS-inducing conditions and secretion of T3SS cargo into the culture supernatant assessed by precipitating secreted proteins, visualizing with coomassie blue (A) in the presence of increasing concentration of Triton X-100. Values are average of two independent replicates. T-test was done, P-value < 0.05 (*). (B) The same experiment as in A was done in the presence of increasing concentration of EpD-1,2,4'N and fixed concentration of Triton X-100 (0.001% v/v). The results are from three independent experiments.



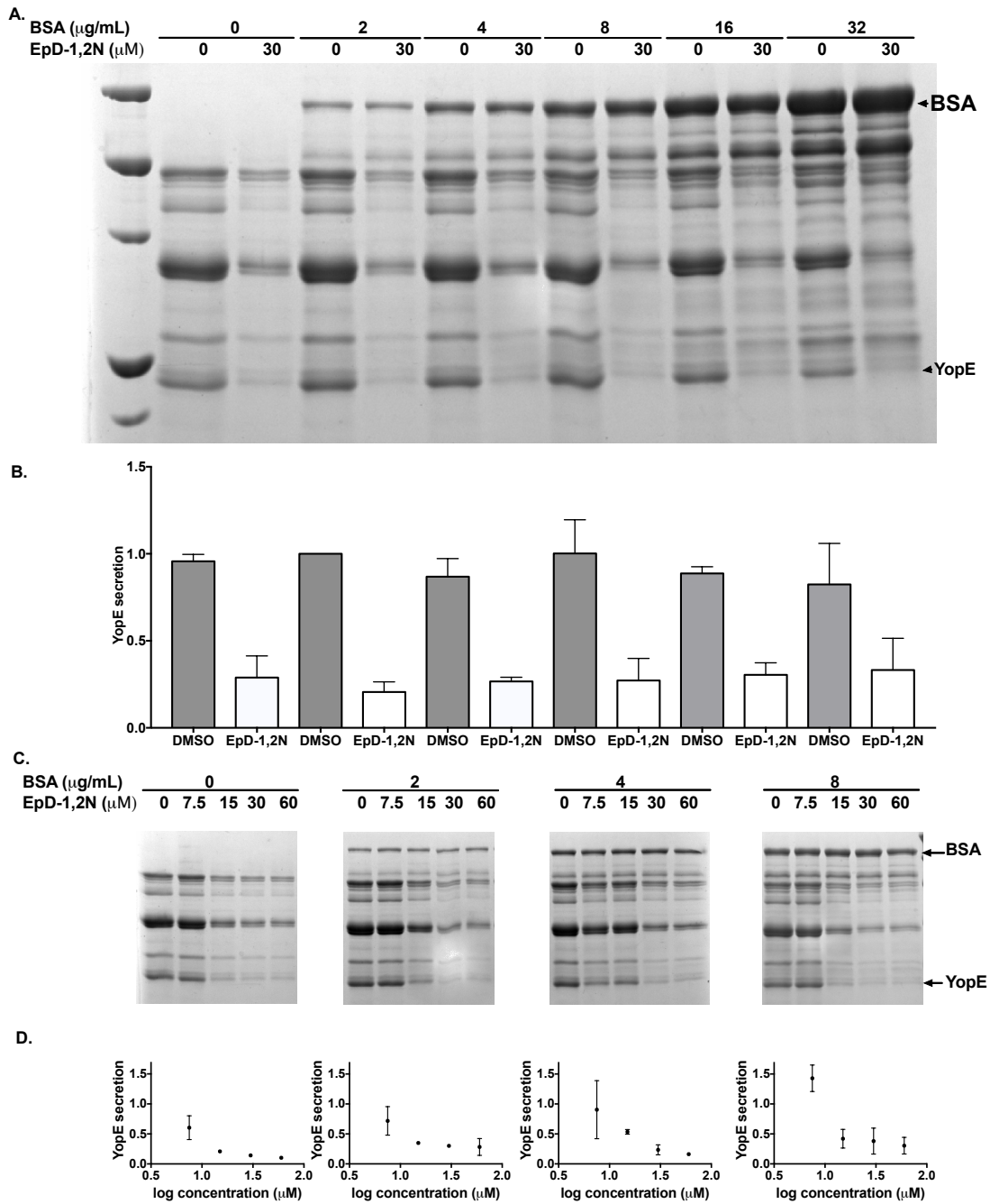


Figure S6. Addition of non-specific protein does not block cyclic peptomer inhibition of type III secretion. WT *Y. pseudotuberculosis* was grown under T3SS-inducing conditions and secretion of T3SS cargo into the culture supernatant assessed by precipitating secreted proteins, visualizing with coomassie blue. A,B) in the presence of increasing concentrations of BSA and 30 μM EpD-1,2N. C,D) in the presence of increasing concentration of EpD-1,2N with different concentration of BSA. The results are from two independent experiments.

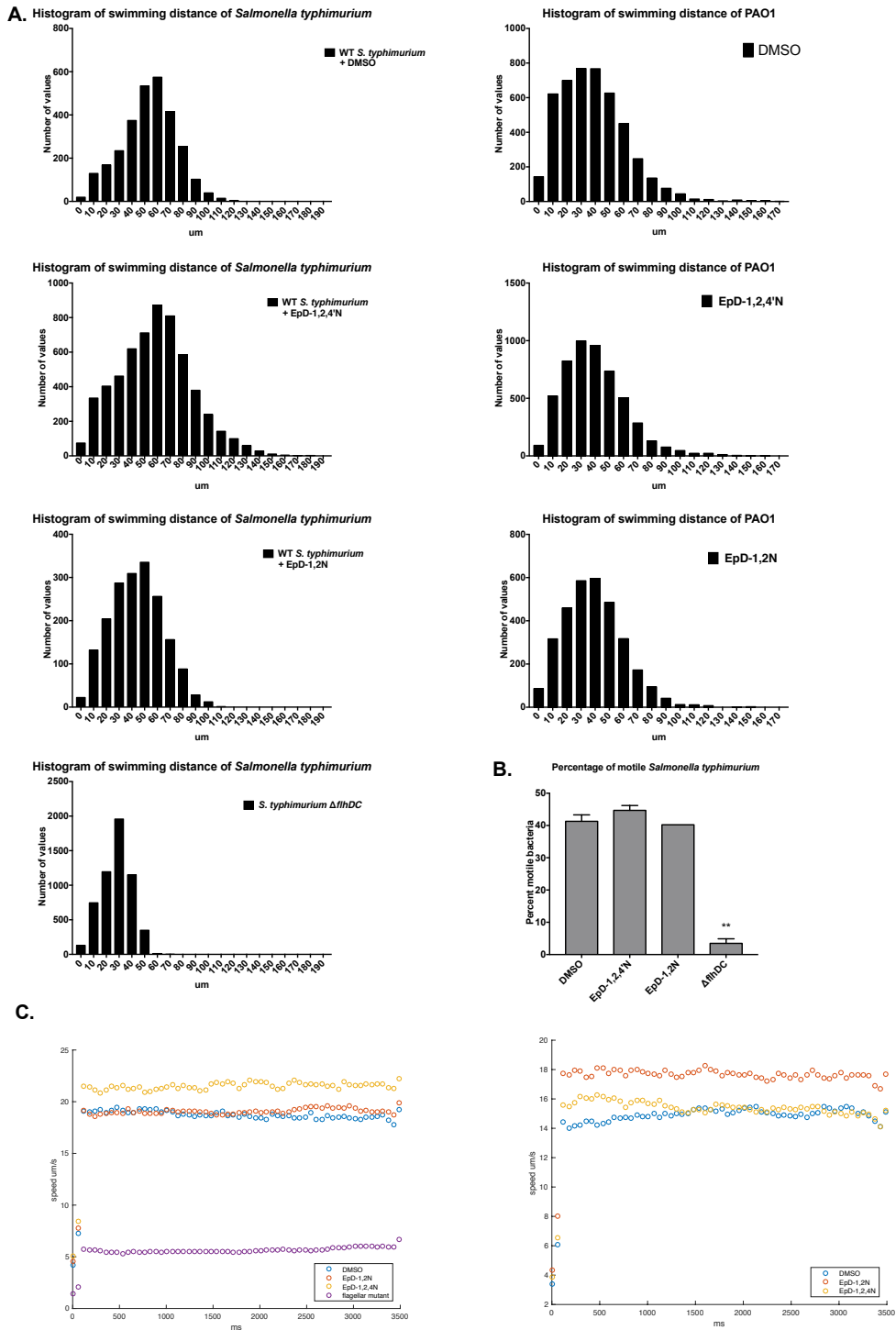


Figure S7. Motility of *Salmonella typhimurium* and *Pseudomonas aeruginosa* PAO1 in liquid media. A) Histogram of swimming distance of all bacteria. B) Percentage of motile *Salmonella typhimurium*. The data from A, where bacteria were considered motile when they traveled a distance two standard deviation greater than the average for $\Delta flhDC$. C) Spontaneous swimming speed of *Salmonella typhimurium* and *Pseudomonas aeruginosa* PAO1 over time. The results are from two independent experiments, except only one replicate was done for EpD-1,2N on *S. typhimurium*. 30 μ M of peptomers were used in the treatment. One-way ANOVA with Tukey multiple comparison was done in Graphpad, P-value < 0.01 (**)

1.2 Broad-spectrum inhibitors of the Type III secretion system

The following work was completed as a collaboration between all of the following authors:

Hanh N. Lam ^{1*}, **Tannia Lau**^{2*}, Adam Lentz¹, Jessica Sherry³, Alejandro Cabrera-Cortez², Karen Hug¹, Joanne Engel³, R. Scott Lokey², Victoria Auerbuch¹

¹Department of Microbiology and Environmental Toxicology, University of California Santa Cruz, Santa Cruz, CA 95064.

²Department of Chemistry and Biochemistry, University of California Santa Cruz, Santa Cruz, CA 95064.

³Department of Medicine, University of California San Francisco, San Francisco, CA 94143.

*Co-first authors

Summary

Expanding from previous work on cyclic peptomers and T3SS inhibition, we investigated the most potent derivative 1EpDN ($IC_{50} \sim 8\mu M$) with structure activity relationship (SAR) studies. First we synthesized six alanine scan derivatives to identify which residues are most important for activity and which sites can tolerate substitution. This information would provide us guidance for the optimization of the initial hits in terms of potency and properties. In brief, our synthetic strategy includes the EpD synthesis from C- to N-terminus starting with Fmoc-Leu-Resin, then stepwise solid-phase assembly of a linear precursors, attaching alanine and sarcosine (an alanine substitute for peptoids, N-methylglycine) in six possible positions, and upon completion the product is cyclized. Upon synthesis of the alanine/sarcosine scan library the compounds were evaluated by the Auerbuch Stone lab for bioactivity and potency. Alanine or Sarcosine replacement at any of the six positions resulted in significant loss of activity, suggesting that all side chains contribute to the activity. Next, we carried out a stereochemistry scan, in which different combinations of L- and D-amino acids at positions 3 to 6 were generated. The parent compound, 1EpDN, has **Propylamine**, and **Benzylamine** at positions 1 and 2, and **D-Leu**, **L-Ile**, **L-Leu**, and **D-Phe** at positions 3-6. While most stereoisomers had the same or reduced T3SS inhibitory activity, 4EpDN (PBLDD) showed improved activity by two fold, with an IC_{50} of $\sim 4\mu M$ compared to the parent compound 1EpDN IC_{50} of $\sim 8\mu M$. Replacement of position 1 (4EpDN 1Sar) or position 2 (4EpDN 2Sar) with sarcosine significantly reduced activity

of 4EpDN. In follow-up experiments, 4EpDN and 4EpDN 2Sar were used as an active compound and a negative control, respectively. The Auerbuch Stone lab and others investigated, 4EpDN and 4EpDN 2Sar, in *Y. pseudotuberculosis*, *Pseudomonas aeruginosa*, *Salmonella*, *Chlamydia trachomatis*, and *Y. enterocolitica*. In summary, 4EpDN inhibits three different classes of T3SS in four different pathogens. It does not inhibit the flagella T3SS of *Salmonella* or the Twin-arginine translocation (Tat) system of *Y. pseudotuberculosis* suggesting its specificity for T3SSs. Furthermore, data suggests that the compound inhibits the function and not the expression of the T3SS by reducing the assembly of the inner ring protein YscD in *Y. enterocolitica* T3SS. Also, the inhibitor significantly reduced intracellular growth of *Chlamydia trachomatis* in HeLa cells which requires the T3SS for survival. Collectively, these data suggest that cyclic peptomer 4EpDN specifically inhibits the injectisome T3SS in a variety of Gram-negative bacteria making this cyclic peptide a suitable broad-spectrum antimicrobial compound.

Abstract

Antibiotic resistant bacteria are an emerging global health threat. New antimicrobials are urgently needed. The injectisome type III secretion system (T3SS), required by dozens of Gram-negative bacteria for virulence but largely absent from non-pathogenic bacteria, is an attractive antimicrobial target. We previously identified synthetic cyclic peptomers, inspired by the natural product phepropeptin D, that inhibit protein secretion through the *Yersinia* Ysc and *Pseudomonas aeruginosa* Psc T3SSs, but do not inhibit bacterial growth. Here we describe identification of an isomer, 4EpDN, that is two-fold more potent (IC_{50} 4 μ M) than its parental compound. Furthermore, 4EpDN inhibited the *Yersinia* Ysa and the *Salmonella* SPI-1 T3SSs, suggesting that this cyclic peptomer has broad efficacy against evolutionarily distant injectisome T3SSs. Indeed, 4EpDN strongly inhibited intracellular growth of *Chlamydia trachomatis* in HeLa cells, which requires the T3SS. 4EpDN did not inhibit the unrelated Twin arginine translocation (Tat) system, nor did it impact T3SS gene transcription. Moreover, although the injectisome and flagellar T3SSs are evolutionarily and structurally related, the 4EpDN cyclic peptomer did not inhibit secretion of substrates through the *Salmonella* flagellar T3SS, indicating that cyclic peptomers broadly but specifically target the injectisome T3SS. 4EpDN reduced the number of T3SS basal bodies detected on the surface of *Y. enterocolitica*, as visualized using a fluorescent derivative of YscD, an inner membrane ring with low homology to flagellar protein FliG. Collectively,

these data suggest that cyclic peptomers specifically inhibit the injectisome T3SS from a variety of Gram-negative bacteria, possibly by preventing complete T3SS assembly.

Introduction

Antibiotic resistance is of great concern to global public health. Bacterial pathogens have evolved numerous mechanisms to survive treatment with clinically-available antibiotics (1). Alternative therapies against multidrug-resistant strains of so-called ESKAPE pathogens (*Enterococcus faecium*, *Staphylococcus aureus*, *Klebsiella pneumoniae*, *Acinetobacter baumannii*, *Pseudomonas aeruginosa*, and *Enterobacter* species) are urgently needed. Various strategies have been explored to avoid the antimicrobial apocalypse (2). One promising approach is to inhibit bacterial virulence mechanisms to disarm pathogens without affecting non-pathogenic members of the microbiota or environmental bacteria (3, 4). This approach has the potential to not only control infection but to do so in a way that preserves the integrity of the microbiome, which is beneficial for human health and is often the source of antibiotic resistance genes (5, 6).

The type III secretion system (T3SS), a needle-like injectisome apparatus, is required for virulence in many Gram-negative pathogens including *Salmonella*, *Yersinia*, *Chlamydia* and the ESKAPE pathogen, *P. aeruginosa*. The T3SS is largely absent from commensal bacteria, making it a good target for virulence blocker antimicrobials. Phylogenetic analysis suggests that T3SSs evolved from the flagellar system (7, 8). Indeed, the flagellar basal body is a secretion system, referred to as the flagellar T3SS, that secretes flagellin and other structural components into the extracellular space in order to build the flagellar filament to power motility. The flagellar and injectisome

T3SS share a number of conserved basal body and export apparatus components (9). However, the injectisome T3SS does not mediate motility, but instead delivers effector proteins into target host cells.

A number of small molecules, antibodies, and vaccines have been studied for T3SS targeted therapies (10). Despite showing promising effects on the T3SS *in vitro* and in animal models, only one antibody-based therapy has entered clinical trials. A bispecific antibody, MEDI3902, against the *P. aeruginosa* T3SS needle tip protein PcrV and the Psl exopolysaccharide is effective against both acute and chronic infection models and is in phase II clinical trials for prevention of ventilator-associated pneumonia (11, 12).

As narrow-spectrum antimicrobials require more precise diagnostics, broad-spectrum T3SS inhibitors would be more valuable clinically than those only able to target one bacterial species. In addition, most mammalian pathogens that utilize a T3SS only require their T3SS during growth within, but not outside, the host animal. However, *Chlamydiae*, which cause lung, genital, and eye infections, are obligate intracellular bacteria and their T3SS is strictly required for their growth (13). Interestingly, the *Chlamydia* T3SS belongs to its own T3SS family (7, 8). Here we identify a derivative of a synthetic cyclic peptomer family of T3SS inhibitors (14) that can inhibit the T3SS machinery of three evolutionarily distinct T3SS families used by five different bacterial species to cause human disease, including *Chlamydia trachomatis*.

Results

Structure-activity relationship study of cyclic peptomers.

Previously we identified a group of cyclic peptomers that inhibited secretion of substrates from *Y. pseudotuberculosis* and *P. aeruginosa* T3SSs, but did not inhibit bacterial growth, motility, or HeLa cell metabolism (14). The results suggested a potential for development of these cyclic peptomers as pathogen-specific virulence blockers. Based on dose response curves and concentration of half maximal inhibition (IC_{50}) of the *P. aeruginosa* T3SS, 1EpDN (previously named as EpD1,2N) was chosen for structure- activity relationship (SAR) analysis. Compounds used in SAR analysis are listed in Table 1.

We first assessed the effect of alanine replacement at each of the six positions of the parent scaffold, 1EpDN. Note that because peptoids have side chains appended to a nitrogen atom rather than carbon as in amino acids, positions 1 and 2 were synthesized with N-methylglycine, also known as sarcosine (Sar), as the peptoid equivalent of alanine (Ala). Ala or Sar replacement at any of the six positions resulted in significant loss of activity, suggesting that all side chains contribute to the activity (Fig. S1). Next, we carried out a stereochemistry scan, in which different combinations of L- and D-amino acids at positions 3 to 6 were generated. The parent compound, 1EpDN, has **P**ropylamine, and **B**enzylamine at positions 1 and 2, and **D**-Leu, **L**-Ile, **L**-Leu, and **D**-Phe at positions 3-6. For the stereochemistry scan, we will refer to 1EpDN as

PBDLLD. While most stereoisomers had the same or reduced T3SS inhibitory activity, 4EpDN (PBLDD) showed improved activity, with an IC_{50} of $\sim 4\mu M$ compared to the parent compound IC_{50} of $\sim 8\mu M$ (Fig. 1A-B). Replacement of position 1 (4EpDN 1Sar) or position 2 (4EpDN 2Sar) with Sar significantly reduced activity of 4EpDN (Fig. 2A-B). 4EpDN and 4EpDN 2Sar were used as an active compound and a negative control, respectively, in most follow-up experiments.

Cyclic peptomers inhibit secretion of T3SS substrates from the Inv-Mxi-Spa T3SS family, but does not inhibit secretion through the flagellar T3SS. Based on phylogenetic analysis of core T3SS proteins, T3SSs were classified into seven families (7, 8). However, T3SSs have many highly conserved structural components (9). T3SS genes are typically encoded on virulence plasmids or pathogenicity islands, indicative of horizontal gene transfer (15); therefore, phylogeny of T3SSs does not follow organismal phylogeny. We previously showed that cyclic peptomers inhibited the Ysc T3SS family found in *P. aeruginosa* and *Yersinia* (Fig. 1-2) (14). In order to test whether cyclic peptomers are active against other T3SS families, we evaluated the effect of cyclic peptomers on the Inv-Mxi-Spa T3SS in *Y. enterocolitica* and *Salmonella enterica* serovar Typhimurium.

The *Y. enterocolitica* Ysa system, a chromosomally encoded T3SS, is distinct from the *Yersinia* Ysc T3SS and contributes to *Y. enterocolitica* colonization of the terminal ileum and gastrointestinal system associated tissues (16, 17). A *Y. enterocolitica* mutant

that lacks expression of the Ysa T3SS ($\Delta ysaT$) was used as a negative control, while a mutant lacking the Ysc T3SS ($\Delta yscL$) (18) was used to evaluate the effect of compounds specifically on the Ysa system. Secretion of the Ysa effector protein YspF was quantified. 4EpDN inhibited secretion of YspF in a dose dependent manner, while 4EpDN 2Sar did not affect its secretion (Fig. 3). Together, these results suggest that cyclic peptomers are active against both the Ysc and Ysa T3SSs in *Yersinia*.

In order to evaluate whether the cyclic peptomers are active against T3SSs distinct from the Ysc T3SS outside the *Yersinia* genus, we tested cyclic peptomer efficacy in *Salmonella*. *Salmonella* employs two T3SSs during infection, with the SPI-1 T3SS belonging to the Inv-Mxi-Spa T3SS family (7, 8). Inhibition of SPI-1 T3SS effector protein SipC and SipA (19-21) secretion by 4EpDN was observed at $\sim 1 \mu\text{M}$ and $\sim 1.4 \mu\text{M}$, respectively, while 4EpDN 2Sar showed inhibition of SipC and SipA secretion only at concentrations greater than $30 \mu\text{M}$ (Fig. 4). In order to test whether inhibition of secretion by the cyclic peptomers in *Salmonella* could be affected by aggregation of the compounds, we also evaluated secretion in the presence of detergent. The presence of Tween-20 (0.003%, Fig. S2) did not reduce activity of 4EpDN (Fig. 4), suggesting that aggregation of cyclic peptomers does not affect its activity.

As 4EpDN inhibited both the Ysc and Inv-Mxi-Spa T3SS families, we tested whether this cyclic peptomer could inhibit the flagellar T3SS, which is the most distantly related T3SS based on previous phylogenetic analysis (7). Conveniently, *Salmonella* expresses

the SPI-1 and its flagellar system under the same conditions *in vitro* (rich media). This allowed us to investigate effects of cyclic peptomers on both the SPI-1 T3SS and flagellar systems under the same culture conditions. Because of the conservation between the injectisome and flagellar T3SSs, flagellar substrates can be secreted through both systems. Therefore, secretion of flagellar substrates (FliC and FliD) was quantified in both WT and Δ SPI-1 strains to distinguish secretion through both the SPI-1 T3SS and flagellar system (WT strain) or only through the flagellar system (Δ SPI-1 strain). 4EpDN inhibited FliC and FliD secretion in WT *Salmonella* at concentrations of $\geq 60 \mu\text{M}$ and $\geq 3.75 \mu\text{M}$, respectively (Fig. S3), consistent with the ability of the SPI-1 T3SS being able to secrete flagellar substrates. However, 4EpDN only inhibited FliC and FliD secretion at high concentrations ($\geq 60 \mu\text{M}$) in the Δ SPI-1 mutant, with unfavorable dose response curves compared to WT *Salmonella*. This suggests that the inhibitory effect of 4EpDN on FliD secretion in the WT strain was mainly through inhibition of its secretion through the SPI-1 T3SS. 4EpDN 2Sar had no significant effect on FliC secretion or FliD secretion. These data suggest that the cyclic peptomer 4EpDN does not significantly inhibit substrate secretion through the flagellar T3SS in *Salmonella* but strongly inhibits the SPI-1 T3SS under the same conditions.

Cyclic peptomers affect the T3SS basal body.

The T3SS basal body must be assembled prior to T3SS substrate secretion (22-24). In *Yersinia*, the T3SS basal body component YscD is an inner ring protein that is conserved among injectisome T3SSs, but has low sequence homology with the flagellar

ortholog FliG (9). Absence of YscD at the inner membrane prevents assembly of other T3SS machinery (YscL, YscK, YscQ) (23, 25), and secretion of T3SS substrates (26). We used a *Y. enterocolitica* strain expressing a YscD allele translationally fused with EGFP to visualize the effect of compounds on YscD assembly (23). 4EpDN caused reduction in the number of YscD puncta, although not to the levels seen under non-T3SS inducing conditions (high Ca^{2+}), while the inactive isomer 4EpDN 2Sar had no effect (Fig. 5). These data suggest that cyclic peptomers affect the assembly or stability of the T3SS basal body, ultimately dampening secretion of effector proteins.

Cyclic peptomers do not inhibit T3SS gene expression.

As cyclic peptomers inhibit substrate secretion and basal body assembly on the bacterial membrane, we evaluated the effect of cyclic peptomers on T3SS gene expression, as this step occurs prior to T3SS assembly. Interestingly, 1EpDN did not inhibit transcription of *exoT* while phenoxyacetamide MBX1641 did (Fig. 6A). Expression of the *dsbA* gene, whose product was shown to be required for expression of the T3SS (27), was unchanged following either cyclic peptomer or the phenoxyacetamide treatment (Fig. 6A). Similarly, 4EpDN did not affect expression of the effectors *exoS* and *exoT* in a strain of *P. aeruginosa* lacking all known efflux pumps (28) (Fig. 6B). In contrast, MBX1641 strongly reduced expression of both *exoS* and *exoT* in this strain. These data suggest that cyclic peptomers do not block T3SS activity by blocking T3SS expression.

In *P. aeruginosa*, secretion and transcription are coupled through a negative regulator ExsE (29). Secretion of ExsE allows transcription of T3SS genes by the *Pseudomonas* regulator ExsA (29). We evaluated the impact of cyclic peptomers on secretion of ExsE and the effector ExoS by Western Blot. Both 1EpDN and 4EpDN significantly reduced the amount of secreted ExoS, with a concomitant accumulation of ExoS in the bacterial cytosol (Fig. 7). In contrast, we did not observe any decrease in secreted ExsE and could not detect any cytosolic ExsE (data not shown). These data suggest that cyclic peptomers block effector protein secretion but not secretion of T3SS regulators. Cyclic peptomers do not inhibit secretion through the Twin-arginine translocation (Tat) system. In order to determine if cyclic peptomers inhibit the activity of secretion systems completely unrelated to the T3SS, we sought to assess the impact of cyclic peptomers on the Twin arginine translocation (Tat) system in *Y. pseudotuberculosis*. The Tat system translocates fully folded substrates across the inner membrane, while the T3SS translocates partially unfolded substrates across the inner, outer, and target host cell membranes (30). To monitor Tat secretion system activity, a reporter strain expressing an IPTG-inducible β -lactamase TEM-1 domain fused to the signal peptide of the SufI Tat substrate (31) was constructed. Following IPTG induction, β -lactamase confers resistance to the β -lactam peptidoglycan-targeting antibiotic penicillin G when the SufI- β -lactamase reporter has successfully translocated into the periplasm (Fig. 8A). The presence of known Tat inhibitors, Bay 11-7082 or N-phenylmaleimide (32), strongly reduced growth of bacteria after four and six hours, while growth of bacterial

cultures treated with cyclic peptomers were similar to the DMSO control (Fig. 8B,C). These results suggested that 4EpDN does not inhibit the Tat secretion system.

Cyclic peptomers block *Chlamydia* infection.

Our data point to the cyclic peptomer 4EpDN being able to inhibit multiple T3SS injectisome families but not other secretion systems, indicating a broad yet specific activity. In order to evaluate whether this cyclic peptomer can disarm virulence, we chose to examine the effect of this compound on the *Chlamydia* infection, as this pathogen requires the T3SS for infection and growth within human cells. The *Chlamydial* life cycle involves two major bacterial forms: the extracellular infectious Elementary Bodies (EBs), and the intracellular replicative Reticulate Bodies (RBs). Upon entry, EBs discharge preloaded T3SS effectors and are taken up into a membrane-bound compartment (the inclusion) where they differentiate into RBs, secrete additional T3SS effectors and replicate, and then re-differentiate into EBs. Initial stages of infection were assessed by quantifying the number of inclusions/cell at 24 hpi in the presence of 9 μ M cyclic peptomers or DMSO; a decrease in inclusion number or size suggests inhibition of binding, entry, EB-RB differentiation, or replication. Production of infectious progeny, which assays RB-EB re-differentiation (including production of pre-packaged effectors) and/or release of EBs, was assayed by collecting EBs at 48 hpi, and infecting fresh monolayers for 24 hpi, and then quantifying inclusion formation. INP0400, a known T3SS inhibitor was used as a control (33). 4EpDN but not 4EpDN 2Sar decreased primary inclusion formation

~50% but inhibited formation of infectious progeny ~98%, without affecting host cell viability as assayed by LDH release (Fig. 9). Together, these results suggest that 4EpDN may predominantly inhibit production or secretion of pre-packaged *C. trachomatis* effectors rather than those made during RB replication.

In this study we further developed cyclic peptomers as T3SS inhibitors and investigated their effects on various virulence mechanisms and pathogens. A newly synthesized cyclic peptomer derivative, 4EpDN, exhibited an IC₅₀ in the low μ M range. 4EpDN inhibits secretion through the T3SS of a number of pathogens including the nosocomial ESKAPE pathogen *Pseudomonas aeruginosa*, enteropathogenic *Yersinia*, *Salmonella* and the obligate intracellular pathogen *Chlamydia trachomatis*. 4EpDN does not inhibit secretion from two other secretion systems – the flagellar T3SS and the Tat secretion system. Cyclic peptomers do not inhibit T3SS gene expression, but affect localization of the T3SS basal body component YscD, indicating disruption of normal T3SS assembly. These data suggest that cyclic peptomers specifically inhibit the injectisome T3SS in a broad spectrum of pathogens.

Structure activity relationship analysis resulted in a T3SS inhibitor with an IC₅₀ in the low μ M range.

Through alanine and stereochemistry scans, we identified 4EpDN, a cyclic peptomer with an IC₅₀ of 4 μ M, as inhibiting secretion of T3SS effector proteins in *P. aeruginosa* and 1 μ M in inhibiting the *Salmonella* SPI-1 T3SS. Compared to previously published

T3SS inhibitors (Table 2), this low μM activity is encouraging. The only published T3SS inhibitors with comparable IC_{50} are the phenoxyacetamides (MBX 2359 and its optimized derivatives), which inhibit *P. aeruginosa* T3SS secretion at 1-3 μM (28). Stereoisomers of 1EpDN showed a wide range of potencies, suggesting that differences in their three dimensional structures affect their biological activity. 9EpDN is a true enantiomer of 1EpDN with an IC_{50} of $\sim 13 \mu\text{M}$, a lower potency than the 1EpDN parental compound of $\sim 8 \mu\text{M}$. Importantly, the activity of these isomers do not positively correlate with solubility (Fig. S4), indicating that the observed activity is due to a specific molecular reaction rather than a non-specific biophysical effect due to aggregation. Furthermore, the presence of nonionic detergent did not affect activity of compounds (Fig. 4). Moreover, 4EpDN is potent at concentrations significantly lower than its solubility (Table S1). These data suggest that 4EpDN is an active cyclic peptomer with specific T3SS inhibitory activity.

Cyclic peptomers act as broad-spectrum, but specific, inhibitors of the injectisome T3SS.

Secretion of protein substrates through the injectisome T3SS, the flagellar system, and the Tat secretion system require the proton motive force (34-36). Although cyclic peptomers inhibited secretion from the injectisome T3SS, they did not inhibit the Tat system and only weakly inhibited flagellar substrate secretion, suggesting that the proton motive force is unaffected, as we previously suggested (14), and that the cyclic peptomers do not inhibit bacterial secretion in general. The 4EpDN cyclic peptomer

demonstrated efficacy against the T3SSs of *P. aeruginosa*, *Y. pseudotuberculosis*, *Y. enterocolitica*, *Salmonella enterica* Typhimurium, and *Chlamydia trachomatis*, with an IC₅₀ in the range of 1 μM (for the *Salmonella* SPI-1 T3SS) to ~16 μM (for the *Y. pseudotuberculosis* Ysa T3SS) (Table 2). Based on phylogenetic analysis of core T3SS proteins, T3SSs group into seven T3SS families, five of which contain T3SSs from human pathogens (37). 4EpDN has efficacy against T3SSs from three of these T3SS families: the Ysc (Ysc and Psc), Inv-Mxi-Spa (SPI-1 and Ysa), and *Chlamydiales*. Interestingly, the flagellar ATPase from *E. coli* falls at the root of the phylogenetic tree (38), distinct from other T3SS families. As 4EpDN impacted secretion through the flagellar T3SS significantly less than through the injectisome T3SS in the same bacterial species and under the same culture and experimental conditions, we reason that the pathway targeted by cyclic peptomers is common to all injectisome T3SSs but absent from the flagellar system.

Cyclic peptomers decrease cell envelope localization of the T3SS basal body protein YscD and inhibit secretion of T3SS effector proteins, but do not inhibit T3SS gene expression.

The T3SS is a complex system made of ~20 different proteins and is assembled in a hierarchical manner prior to secretion of effector proteins (22, 39). Our study showed that 4EpDN inhibited secretion of T3SS effector proteins in *Yersinia*, *Pseudomonas*, and *Salmonella* and blocked *Chlamydial* growth, which requires translocation of T3SS effector proteins in human cells. Importantly, 4EpDN did not decrease expression of

T3SS genes in *Pseudomonas* or *Salmonella* (Fig. 6, Fig. S5), suggesting that cyclic peptomers do not act at the level of T3SS gene expression. However, the T3SS of *Yersinia*, *Pseudomonas*, *Salmonella*, and *Chlamydia* share a number of orthologous basal body components that, if targeted, could lead to disruption of effector protein secretion. Interestingly, 4EpDN reduced localization of the inner membrane ring protein YscD to the *Yersinia* cell envelope (Fig 3), indicating a perturbation to T3SS assembly or stability. Surprisingly, the effect of 4EpDN on the T3SS did not significantly impact secretion of the *Pseudomonas* regulator ExsE. In *P. aeruginosa*, ExsA is the key positive transcriptional regulator of genes encoding the T3SS machinery and substrates. ExsE leads to sequestration of ExsA, preventing it from inducing T3SS gene expression through a complex partner switching pathway (29, 40, 41). Under secreting conditions, ExsE, a T3SS substrate, is secreted, enabling release of ExsA and thereby allowing increased transcription of T3SS genes (29). However, we did not detect a decrease in ExsE secretion in the presence of cyclic peptomers, in contrast to the marked decrease in effector protein secretion. These results are consistent with the data showing that 4EpDN did not inhibit T3SS gene expression in *P. aeruginosa*, as ExsE mediates elevation of gene expression in response to secretion. It is not completely clear why the cyclic peptomers inhibited secretion of effector substrates and ExsE differently, although the small size of ExsE compared to other effectors such as ExoU (~8.7 kDa versus 74 kDa) may be a factor.

Cyclic peptomers strongly inhibit *Chlamydia* primary and secondary infection.

4EpDN strongly inhibited *Chlamydia* from infecting HeLa cells during primary infection, and furthermore prevented *Chlamydia* from infecting subsequent host cells (Fig. 9). This highlights the potential of cyclic peptomers to prevent the spread of *Chlamydia* infection. *Chlamydia* relies on its T3SS effector proteins to interact with host factors, such as the actin cytoskeleton, Golgi network, endoplasmic reticulum, and microtubule network, to mediate invasion and intracellular growth (42). It is possible that compounds that inhibit these host pathways could interfere with *Chlamydial* growth (43-45). However, microscopic analysis of many cellular structures in HeLa cells in the presence of 4EpDN did not show any gross changes to the actin cytoskeleton, Golgi network, endoplasmic reticulum, or microtubule network at the concentration used in our *Chlamydia* infection, 9 μ M (Fig. S6). *C. trachomatis* infection may cause infertility in female patients and eye damage, in addition to lung infections (13). Antibiotics, such as β -lactam antibiotics, are a common way to treat *Chlamydia* infection, but the chance of recurrence is high (46, 47). Current vaccine development efforts are underway but multiple challenges remain (48). There is increased demand for drugs against *Chlamydia* due to antibiotic resistance (49). The strong efficacy of cyclic peptomers highlights their potential for development as an anti-*Chlamydial* drug.

Discussion

In this study we further developed cyclic peptomers as T3SS inhibitors and investigated their effects on various virulence mechanisms and pathogens. A newly synthesized cyclic peptomer derivative, 4EpDN, exhibited an IC_{50} in the low μM range. 4EpDN inhibits secretion through the T3SS of a number of pathogens including the nosocomial ESKAPE pathogen *Pseudomonas aeruginosa*, enteropathogenic *Yersinia*, *Salmonella* and the obligate intracellular pathogen *Chlamydia trachomatis*. 4EpDN does not inhibit secretion from two other secretion systems – the flagellar T3SS and the Tat secretion system. Cyclic peptomers do not inhibit T3SS gene expression, but affect localization of the T3SS basal body component YscD, indicating disruption of normal T3SS assembly. These data suggest that cyclic peptomers specifically inhibit the injectisome T3SS in a broad spectrum of pathogens.

Structure activity relationship analysis resulted in a T3SS inhibitor with an IC_{50} in the low μM range.

Through alanine and stereochemistry scans, we identified 4EpDN, a cyclic peptomer with an IC_{50} of 4 μM , as inhibiting secretion of T3SS effector proteins in *P. aeruginosa* and 1 μM in inhibiting the *Salmonella* SPI-1 T3SS. Compared to previously published T3SS inhibitors (Table 2), this low μM activity is encouraging. The only published T3SS inhibitors with comparable IC_{50} are the phenoxyacetamides (MBX 2359 and its optimized derivatives), which inhibit *P. aeruginosa* T3SS secretion at 1-3 μM (28). Stereoisomers of 1EpDN showed a wide range of potencies, suggesting that differences

in their three dimensional structures affect their biological activity. 9EpDN is a true enantiomer of 1EpDN with an IC_{50} of $\sim 13 \mu\text{M}$, a lower potency than the 1EpDN parental compound of $\sim 8 \mu\text{M}$. Importantly, the activity of these isomers do not positively correlate with solubility (Fig. S4), indicating that the observed activity is due to a specific molecular reaction rather than a non-specific biophysical effect due to aggregation. Furthermore, the presence of nonionic detergent did not affect activity of compounds (Fig. 4). Moreover, 4EpDN is potent at concentrations significantly lower than its solubility (Table S1). These data suggest that 4EpDN is an active cyclic peptomer with specific T3SS inhibitory activity.

Cyclic peptomers act as broad-spectrum, but specific, inhibitors of the injectisome T3SS.

Secretion of protein substrates through the injectisome T3SS, the flagellar system, and the Tat secretion system require the proton motive force (34-36). Although cyclic peptomers inhibited secretion from the injectisome T3SS, they did not inhibit the Tat system and only weakly inhibited flagellar substrate secretion, suggesting that the proton motive force is unaffected, as we previously suggested (14), and that the cyclic peptomers do not inhibit bacterial secretion in general. The 4EpDN cyclic peptomer demonstrated efficacy against the T3SSs of *P. aeruginosa*, *Y. pseudotuberculosis*, *Y. enterocolitica*, *Salmonella enterica* Typhimurium, and *Chlamydia trachomatis*, with an IC_{50} in the range of $1 \mu\text{M}$ (for the *Salmonella* SPI-1 T3SS) to $\sim 16 \mu\text{M}$ (for the *Y. pseudotuberculosis* Ysa T3SS) (Table 2). Based on phylogenetic analysis of core T3SS

proteins, T3SSs group into seven T3SS families, five of which contain T3SSs from human pathogens (37). 4EpDN has efficacy against T3SSs from three of these T3SS families: the Ysc (Ysc and Psc), Inv-Mxi-Spa (SPI-1 and Ysa), and *Chlamydiales*. Interestingly, the flagellar ATPase from *E. coli* falls at the root of the phylogenetic tree (38), distinct from other T3SS families. As 4EpDN impacted secretion through the flagellar T3SS significantly less than through the injectisome T3SS in the same bacterial species and under the same culture and experimental conditions, we reason that the pathway targeted by cyclic peptomers is common to all injectisome T3SSs but absent from the flagellar system.

Cyclic peptomers decrease cell envelope localization of the T3SS basal body protein YscD and inhibit secretion of T3SS effector proteins, but do not inhibit T3SS gene expression.

The T3SS is a complex system made of ~20 different proteins and is assembled in a hierarchical manner prior to secretion of effector proteins (22, 39). Our study showed that 4EpDN inhibited secretion of T3SS effector proteins in *Yersinia*, *Pseudomonas*, and *Salmonella* and blocked *Chlamydial* growth, which requires translocation of T3SS effector proteins in human cells. Importantly, 4EpDN did not decrease expression of T3SS genes in *Pseudomonas* or *Salmonella* (Fig. 6, Fig. S5), suggesting that cyclic peptomers do not act at the level of T3SS gene expression. However, the T3SS of *Yersinia*, *Pseudomonas*, *Salmonella*, and *Chlamydia* share a number of orthologous basal body components that, if targeted, could lead to disruption of effector protein

secretion. Interestingly, 4EpDN reduced localization of the inner membrane ring protein YscD to the *Yersinia* cell envelope (Fig 3), indicating a perturbation to T3SS assembly or stability.

Surprisingly, the effect of 4EpDN on the T3SS did not significantly impact secretion of the *Pseudomonas* regulator ExsE. In *P. aeruginosa*, ExsA is the key positive transcriptional regulator of genes encoding the T3SS machinery and substrates. ExsE leads to sequestration of ExsA, preventing it from inducing T3SS gene expression through a complex partner switching pathway (29, 40, 41). Under secreting conditions, ExsE, a T3SS substrate, is secreted, enabling release of ExsA and thereby allowing increased transcription of T3SS genes (29). However, we did not detect a decrease in ExsE secretion in the presence of cyclic peptomers, in contrast to the marked decrease in effector protein secretion. These results are consistent with the data showing that 4EpDN did not inhibit T3SS gene expression in *P. aeruginosa*, as ExsE mediates elevation of gene expression in response to secretion. It is not completely clear why the cyclic peptomers inhibited secretion of effector substrates and ExsE differently, although the small size of ExsE compared to other effectors such as ExoU (~8.7 kDa versus 74 kDa) may be a factor.

Cyclic peptomers strongly inhibit *Chlamydia* primary and secondary infection.

4EpDN strongly inhibited *Chlamydia* from infecting HeLa cells during primary infection, and furthermore prevented *Chlamydia* from infecting subsequent host cells

(Fig. 9). This highlights the potential of cyclic peptomers to prevent the spread of *Chlamydia* infection. *Chlamydia* relies on its T3SS effector proteins to interact with host factors, such as the actin cytoskeleton, Golgi network, endoplasmic reticulum, and microtubule network, to mediate invasion and intracellular growth (42). It is possible that compounds that inhibit these host pathways could interfere with *Chlamydial* growth (43-45). However, microscopic analysis of many cellular structures in HeLa cells in the presence of 4EpDN did not show any gross changes to the actin cytoskeleton, Golgi network, endoplasmicreticulum, or microtubule network at the concentration used in our *Chlamydia* infection, 9 μ M (Fig. S6). *C. trachomatis* infection may cause infertility in female patients and eye damage, in addition to lung infections (13). Antibiotics, such as β -lactam antibiotics, are a common way to treat *Chlamydia* infection, but the chance of recurrence is high (46, 47). Current vaccine development efforts are underway but multiple challenges remain (48). There is increased demand for drugs against *Chlamydia* due to antibiotic resistance (49). The strong efficacy of cyclic peptomers highlights their potential for development as an anti-*Chlamydial* drug.

Materials and Methods

Bacterial strains and culture conditions. The bacterial strains and cell lines used in this study are listed in Table 3. All cultures were grown with shaking at 250 rpm unless otherwise noted. *Y. pseudotuberculosis* was grown in 2xYT (2x yeast extract and tryptone) at 26°C overnight. To induce the T3SS, the cultures were subcultured to an optical density at 600 nm (OD₆₀₀) of 0.2 into low-calcium medium (2xYT with 20 mM sodium oxalate and 20 mM MgCl₂). *Y. enterocolitica* was grown in BHI (brain heart infusion) medium at 26°C overnight. The Ysc T3SS in *Y. enterocolitica* was induced using low-calcium BHI (BHI with 20 mM sodium oxalate and 20 mM MgCl₂). The Ysa T3SS was induced as described previously (50) using ‘L media’ (1% Tryptone, 0.5% Yeast extract) with 290 mM NaCl at 26°C. *P. aeruginosa* and *S. enterica* were grown in Luria-Bertani (LB) medium overnight at 37°C. For *P. aeruginosa*, the T3SS was induced using low-calcium medium (LB with 5 mM EGTA and 20 mM MgCl₂). SPI-1 T3SS secretion was assessed after subculturing into fresh LB at 37°C unless noted. HeLa cells (ATCC) were cultured in Dulbecco’s modified Eagle’s medium (DMEM) with 10% fetal bovine serum (FBS). All cell lines were incubated at 37°C with 5% CO₂.

Preparation of bacteria for T3SS induction. Visualization of secreted proteins was carried out as described previously (25). Briefly, *Y. pseudotuberculosis*, *P. aeruginosa*, or *S. enterica* was grown in T3SS-inducing medium (as described above) in the

presence of cyclic peptomers or an equivalent volume of DMSO at 37°C, 2 hrs for *Y. pseudotuberculosis* Ysc T3SS, 3 hrs for *P. aeruginosa*, 4 hrs for *S. enterica*, or at 26°C for 6 hrs for the *Y. enterocolitica* Ysa T3SS. The cultures were normalized to bacterial density (OD₆₀₀) and then centrifuged for 15 min at 14,800 rpm. The supernatants were transferred to new tubes and mixed with trichloroacetic acid (TCA) to a final volume of 10% by vortexing vigorously for 30 s. Samples were incubated on ice for 1 hr and then spun down at 4°C for 15 min at 13,200 rpm. The supernatants were carefully removed, and pelleted proteins washed with acetone and spun down at 4°C for 15 min at 13,200 rpm for a total of three washes. The pellet was then resuspended in final sample buffer (FSB) and 20% dithiothreitol (DTT) and boiled for 15 min prior to SDS-PAGE. Tween- 20 was added to the bacterial culture at the same time as the compounds in *S. enterica* secretion assays at 0.003% (v/v).

T3SS secretion cargo quantification. Image Lab software (Bio-Rad) was used to quantify T3SS cargo protein bands relative to those of DMSO-treated controls. The WT *Y. pseudotuberculosis* YopE, *P. aeruginosa* ExoU, or *S. enterica* SipA, SipC, FliC and FliD bands in DMSO control samples were set to 1.00. To evaluate type III secretion of ExoS and ExsE in *P. aeruginosa*, Western blots against T3SS cargo were carried out, using a PVDF membrane (Millipore), blocking in 5% non-fat milk for 2 hrs at room temperature, and incubated at 4°C overnight with gentle shaking. Blots were washed three times for 5 minutes each in Phosphate-Buffered Saline with 0.1% Tween® 20 (PBST). Horseradish Peroxidase conjugated secondary antibody was then

incubated for 1 hr at room temperature. Signals were detected with Luminol Kit after washing. ExoS-Bla, ExsE and SipC was visualized using β -lactamase (MA120370, Fisher Scientific) (7.5% gel), anti-ExsE antibody courtesy of Timothy Yahr (20% gel) and anti-SipC (ABIN335178, antibodies-online Inc.)(10% gel), respectively.

YscD visualization assay. *Y. enterocolitica* expressing YscD-EGFP was cultured overnight in BHI supplemented with nalidixic acid (35 $\mu\text{g}/\text{mL}$) and diaminopimelic acid (50 $\mu\text{g}/\text{mL}$), at 26°C with shaking (23), followed by subculture into low calcium BHI medium (20mM NaOX, 20mM MgCl_2 , 0.4% Glycerol) with nalidixic acid and diaminopimelic acid to OD_{600} of 0.2 for 1.5 hrs. Compounds or an equivalent volume of DMSO was added prior to inducing the T3SS. After 3 hrs at 37°C with shaking, cells were pelleted and resuspended in PBS, spotted onto a 0.1% agarose pad, and imaged live at 63X/1.4 oil magnification using a Zeiss AxioImager widefield microscope. Analysis of YscD puncta was carried out in Imaris 8 using spot tracking analysis with the same arbitrary threshold to call bacterial cell and puncta for all samples.

mRNA quantification. Overnight *P. aeruginosa* (PA103 or PA01) cultures were subcultured and shifted to T3SS inducing conditions (see above) in the presence of 60 μM 1EpDN, 60 μM 1EpDN 2Sar, or 50 μM MBX1641. Samples were taken after 3 hrs of induction. Overnight *Salmonella* cultures were subcultured into fresh LB with 0.3 M NaCl at 37°C in the presence of 9 μM 4EpDN, 4EpDN 2Sar, or equivalent DMSO. Samples were taken after 2 hrs and 4 hrs of induction. Samples were stored in RNeasy Protect reagent (Qiagen) and processed within a week. Total RNA was isolated

using an RNAeasy Kit (Qiagen), according to the manufacturer's instructions, followed by two rounds of Turbo DNase (ThermoFisher scientific) treatment. A total of 2 µg of RNA was used to make cDNA and qPCR reactions were run with SYBR Green PCR master mix (Applied Biosystems). DNA helicase (*dnaB*) and 16S rRNA genes were used as a reference for *P. aeruginosa* and *Salmonella* samples, respectively. Two to three technical replicates were averaged for each sample. Primers used are listed in Table S2. Results were analyzed using Bio-Rad CFX software.

Tat translocation assay. To make Tat targeting constructs, plasmid pMMB67EH (ATCC 37622) was digested with KpnI. TEM1 of β-lactamase was PCR amplified from *yopH*-Bla (courtesy of Melanie Marketon) using primers oHL210 and oHL217 (Table S2) and *sufI* signal peptide DNA was PCR amplified from genomic DNA of *Y. pseudotuberculosis* with primers oHL218 and oHL219 (Table S2). The digested pMMB67EH, TEM1 and *sufI* signal peptide DNA were assembled into a plasmid (*sufI*-Bla) using Gibson assembly.

WT *Yersinia* or *tatB::Tn* carrying *sufI*-Bla was grown in 2 x YT supplemented with 15µg/mL gentamicin at 26°C with shaking. Overnight cultures were subcultured to OD₆₀₀ of 0.1 and grown for 1.5hr at 26°C with shaking. 5 mM IPTG was added to the culture for 0.5 hrs to allow for expression and translocation of SufI-Bla. Penicillin G (25µg/mL) was added to the cultures. Cultures were then treated with cyclic peptomers or DMSO and OD₆₀₀ measured every hour up to 8hrs.

***Chlamydia* infection and imaging.** Primary Infections: HeLa cell monolayers were infected with *C. trachomatis*, Serovar L2 at an MOI of one in the presence of one of the following compounds at 9 μ M: (a) DMSO, (b) 4EpDN, or (c) 4EpDN 2Sar. Cells were incubated for 24 hrs in the presence of the above compounds at 37°C, and then fixed with 4% Paraformaldehyde (PFA). Cells were stained for IncA (*Chlamydia* inclusion membrane marker), DNA, and MOMP (*Chlamydia* major outer membrane protein). The percentage of cells infected (i.e. stained positively for the listed *Chlamydia* markers) in the presence of the compounds was quantified using confocal microscopy. 10 randomly selected fields of view were measured per experiment. Data represents three biological replicates. Secondary Infections: HeLa cell monolayers were infected with *C. trachomatis*, Serovar L2 at an MOI of 1.0 in the presence of one of the following compounds at 9 μ M: (a) DMSO, (b) 4EpDN, or (c) 4EpDN 2Sar. Cells were incubated for 48 hrs in the presence of the above compounds at 37°C. Infected cells were then lysed, and the lysate was applied to fresh HeLa monolayers to enumerate infectious particles. These secondary infections were fixed in 4% PFA at 24 hpi, and were stained against MOMP and DNA. Infectious units per mL (IFU/mL) were calculated by averaging the number of infected cells in each of 10 randomly selected fields of view at 60X magnification on a confocal microscope, and multiplying this by the appropriate dilution and area factors. Data represents four biological replicates.

Cytological Profiling (CP). Briefly, HeLa cells were cultured and seeded into 384-well at 2,500 cells/well. After 48 hrs, compounds were added using a Janus MDT robot

(PerkinElmer). Two stain sets were used; Stain set 1: Hoechst, EdUrhodamine, anti-Phosphohistone H3, and GM130, Stain Set 2: Hoechst, FITC-alpha tubulin, rhodamine-phalloidin, and Calnexin. For stain set 1, cells were incubated with 20 μ M EdU rhodamine for 1 hr prior to fixing in 4% formaldehyde solution in PBS for 20 min. Cells were then washed with PBS and permeabilized with 0.5 % Triton-X in PBS for 10 min before blocking with 2 % BSA in PBS solution for at least 1 hr. Following this, cells were incubated with primary antibodies overnight at 4°C. The following day, excess primary antibody was washed off with PBS and Alexa-488 and Alexa-647 secondary antibodies and Hoechst solution were incubated for 1 hr. Plates were washed with PBS and preserved with 0.1% sodium azide in PBS solution prior to imaging. For stain set 2, cells were fixed with a 4 % formaldehyde solution in PBS for 20 min. Cells were then washed with PBS and permeabilized with 0.5 % Triton-X in PBS for 10 min before blocking with 2 % BSA in PBS solution for at least 1 hr. Following this, cells were incubated with primary antibodies overnight at 4°C. After blocking, the cells were washed, and incubated with FITC conjugated anti-alpha tubulin antibody and rhodamine- phalloidin overnight at 4°C. The following day the cells were washed and then incubated with secondary Alexa-647 and Hoechst stain for 1 hr. Plates were washed with PBS and preserved with 0.1% sodium azide in PBS solution prior to imaging. Two images per well were captured with an ImageXpress Micro XLS automated epifluorescent microscope (Molecular Devices, Sunnyvale). Images were then processed as described (51). Briefly, initial image processing was performed using MetaXpress image analysis software, using built-in morphometry metrics, the

multiwavelength cell scoring, transfluor, and micronuclei modules. Custom written scripts were used to compare the treated samples with the DMSO control wells, and then to convert each feature to a “histogram difference” (HD) score. This produced a 452-feature vector CP fingerprint. Compound treatment wells were labeled as dead if the cell count for the treatment well was < 10% of the median cell count in the treatment plate. In addition to the CP fingerprint, feature cell counts (nuclei, EdU S-phase, and phospho-histone H3) were used to determine effects of compounds on HeLa cell replication.

Synthesis of cyclic peptomers

Cyclic peptide synthesis. Peptides were synthesized using standard Fmoc solid-phase peptide synthesis, utilizing the submonomer approach for peptoid synthesis (52), either at room temperature or with microwave assistance. Cyclization was done in solution at a high dilution. Fmoc-Xaa (10 mmol) was added to a flame-dried round-bottomed flask and dried in a vacuum desiccator with phosphorous pentoxide overnight. 50 ml of dry dichloromethane (DCM) was cannula transferred into the flask, followed by 2.5 ml of N,N-diisopropylethylamine (DIPEA) transferred via syringe. After sonication for 10 min, 5g of 2-chlorotriyl resin was added under a stream of nitrogen and allowed to shake for 4hrs. The resin was capped with a 15 ml solution of 1:2:17 methanol (MeOH):DIPEA:dimethylformamide (DMF) (3 times for 15 min each). The resin was washed with DMF (3 times with 15 ml each) followed by DCM (3 times with 15 ml

each). The loading value was calculated by determining the mass increase of dried, loaded resin.

Amino acid coupling at room temperature. Four equivalents (eq) of Fmoc-Xaa, 8 eq of DIPEA, and 4 eq of 1-[Bis(dimethylamino)methylene]-1H-1,2,3-triazolo[4,5-b]pyridinium 3-oxidehexafluorophosphate, Hexafluorophosphate Azabenzotriazole Tetramethyl Uronium (HATU) were added to the resin in DMF. The reaction mixture was agitated via shaking for 45 min and then drained. The resin was washed with DMF (3 times with 3 ml each) and DCM (3 times with 3 ml each). The reaction was monitored by liquid chromatography-mass spectrometry (LC-MS) and repeated until the starting material was no longer observed. For microwave conditions, a solution of 4 eq of Fmoc-Xaa, 4 eq of HATU, and 6 eq of DIPEA in DMF was allowed to prereact for 5 min. This solution was added to the deprotected peptide on-resin and allowed to react for 10 min at 50°C under microwave heating. The solution was drained, and the resin was washed with DMF (3 times with 3 ml each) and DCM (3 times with 3 ml each). The reaction was monitored by LC-MS and repeated until the starting material was no longer observed.

Coupling of BrAcOH at room temperature. A solution of 10 eq of bromoacetic acid (BrAcOH) and 5 eq of N,N'-diisopropylcarbodiimide (DIC) in DMF was allowed to react for 10 min. This solution was added to the deprotected peptide on-resin. The reaction mixture was agitated via shaking for 45 min and then drained. The resin was

washed with DMF (3 times with 3 ml each) and DCM (3 times with 3 ml each). The reaction was monitored by LC-MS and repeated until the starting material was no longer observed. The reaction was monitored by LC-MS and repeated until the starting material was no longer observed.

Peptoid side chain addition. A solution of 5 eq of the desired amine was prepared in a minimum volume of DMF. The resin containing the BrAc-peptide was swollen with DCM for 5 min prior to reaction. The amine was added, and the reaction mixture was agitated via shaking for 3 to 20 hrs. The solution was drained, and the resin was washed with DMF (3 times with 3 ml each) and DCM (3 times with 3 ml each). The reaction was monitored by LC-MS and repeated until the starting material was no longer observed.

Removal of the N-Fmoc protection group at room temperature. A solution of 2% piperidine and 2% 1,8-diazabicyclo[5.4.0]undec-7-ene (DBU) in DMF was added to the resin. The reaction mixture was agitated via shaking for 20 min and then drained. The resin was washed with DMF (3 times with 3 ml each) and DCM (3 times with 3 ml each). For microwave conditions, a solution of 2% piperidine and 2% DBU in DMF was added to the resin. The reaction mixture was allowed to react for 5 min at 50°C under microwave heating and then drained. The resin was washed with DMF (3 times with 3 ml each) and DCM (3 times with 3 ml each).

Peptide cleavage. Complete linear peptides were cleaved off the resin in 5 resin volumes of 2.5% trifluoroacetic acid (TFA) in DCM for 4 min, three times, with a 5-resin-volume DCM wash between steps. Solvent was removed under N₂, followed by dissolution in acetone or DCM and evaporation under reduced pressure. Residual TFA was removed in vacuo overnight.

Cyclization with COMU. Linear peptides were dissolved in 20 ml of dry acetonitrile (ACN) with 4 eq of DIPEA and added dropwise (final concentration, 1 mg crude peptide per ml) to a solution of 1:1 tetrahydrofuran (THF)-ACN containing 2 eq of (1-cyano-2-ethoxy-2-oxoethylideneaminoxy)dimethylamino-morpholinocarbenium hexafluorophosphate (COMU). Reaction mixtures were stirred for 0.5 to 24 hrs, until complete cyclization was achieved as monitored by LC-MS. The reaction mixture was reduced in vacuo for purification via high pressure liquid chromatography (HPLC).

Purification of peptides. COMU by-products were removed after solution-phase cyclization on a Biotage Isolera Prime system equipped with a SNAP Ultra-C18 30g column eluting with H₂O-acetonitrile modified with 0.1% TFA. The mass spectra of all peptides are shown in Fig. S7 in the supplemental material.

Proton NMR of peptides. Peptides were analyzed through nuclear magnetic resonance (NMR) spectroscopy measured in ppm and were obtained on a 500 MHz spectrometer

using CDCl_3 (7.26) as an internal standard for ^1H NMR. Identity of compounds for SAR study was confirmed by LCMS and ^1H -NMR (Fig. S7).

Kinetic Solubility. A 15 mM stock of the compounds in DMSO was prepared. 125 μL of M9 and DMEM (no antibiotics) was dispensed into 96 v-bottom plate. One microliter of 15mM stock compound was added to make a solution of 120 μM final concentration with 0.8% DMSO. The solution was shaken at 37°C for ~ 2 hrs. The solution was passed over a 0.7 μM glass fiber filter. Then the solution was diluted 1:4 in acetonitrile to crash out any proteins. The solution was centrifuged at $500 \times g$ for 10 minutes. Avoiding the pellet, 10 μL of supernatant was added to a fresh plate with 90 μL of acetonitrile. The final dilution 40 times lower. 10 μL of 40x dilution of solution was injected on the Orbi-trap. A 1 μM standard was used for the ratiometric comparison and the assay was done in triplicate.

Cyclic peptide manipulation. Stock peptides were stored at 15 mM at -70°C and were prediluted in DMSO prior to experiments. All treatment and control pairs, in all assays, had the same DMSO volumes.

Statistical analysis. GraphPad Prism 8 (GraphPad Software, La Jolla, CA, USA) was used to calculate the mean, standard error of the mean, median, standard error of median, and one-way ANOVA values shown.

Acknowledgements

The authors acknowledge the National Institutes of Health grant R01AI141511 (to V.A. and R.S.L.) and K99AI139281 (to H.L.) for support. We thank Benjamin Abrams (University of California, Santa Cruz) for technical support on the YscD spot tracking analysis. We thank Timothy Yahr for the anti-ExsE antibody.

**1.2 FIGURES FOR:
Broad spectrum inhibitors of the T3SS**

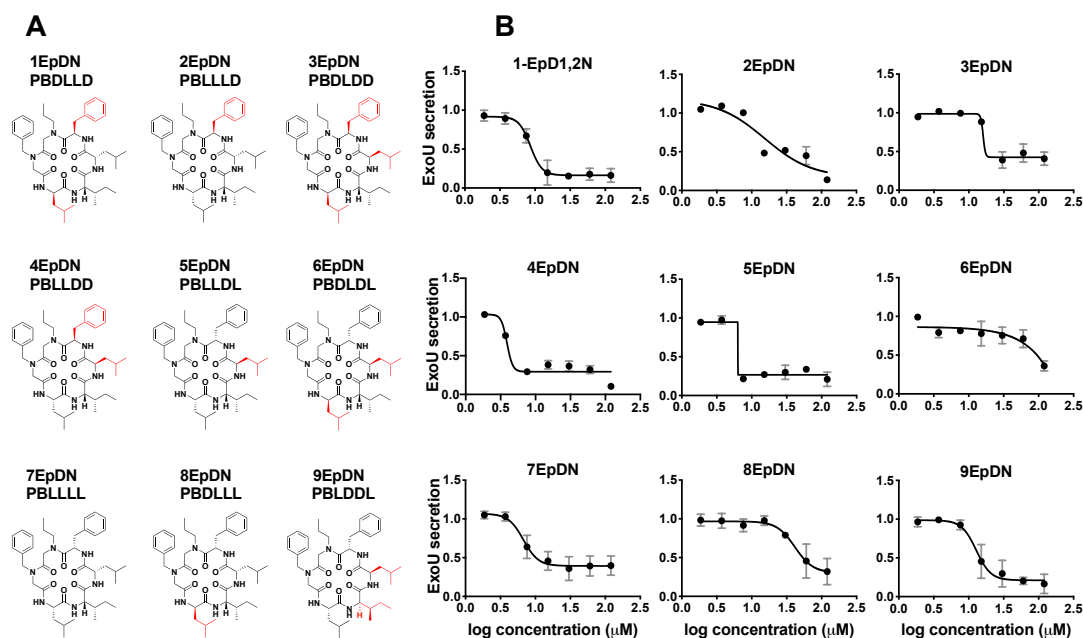


Figure 1: Stereochemistry scan of cyclic peptomers results in a more potent derivative, 4EpDN.

(A) Structures of 1EpDN stereoisomers. Isomers were generated from different combination of four side chains at position 3 to 6. Numbers preceding compounds were used to distinguish the different isomers and the conformation of the four side chains. D-amino acid side chain is shown in red. (B) WT *P. aeruginosa* PA103 was grown under T3SS-inducing conditions with increasing concentrations of cyclic peptomer isomers. Secretion of T3SS cargo into the culture supernatant was assessed by precipitating secreted proteins and visualizing them with Coomassie blue. ExoU band intensities were quantified and normalized to that of the DMSO control. The results are from at least two independent experiments. Nonlinear curve fitting is shown to depict the trend of inhibition.

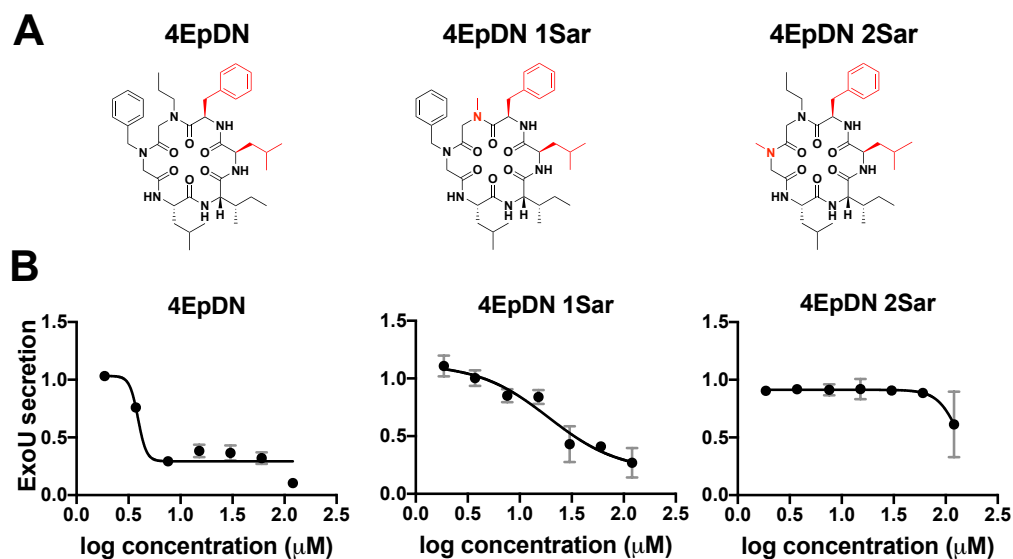


Figure 2: Sarcosine replacement of 4EpDN at position 1 or 2 eliminates activity. (A) Structures of 4EpDN and its derivatives, 4EpDN 1Sar and 4EpDN 2Sar. D-amino acid side chain is shown in red. (B) WT *P. aeruginosa* PA103 was grown under T3SS-inducing conditions with increasing concentrations of compounds. Secretion of T3SS cargo into the culture supernatant was assessed on SDS-PAGE gel. ExoU band intensities were visualized with Coomassie blue, quantified and normalized to that of the DMSO control. The results are from at least two independent experiments.

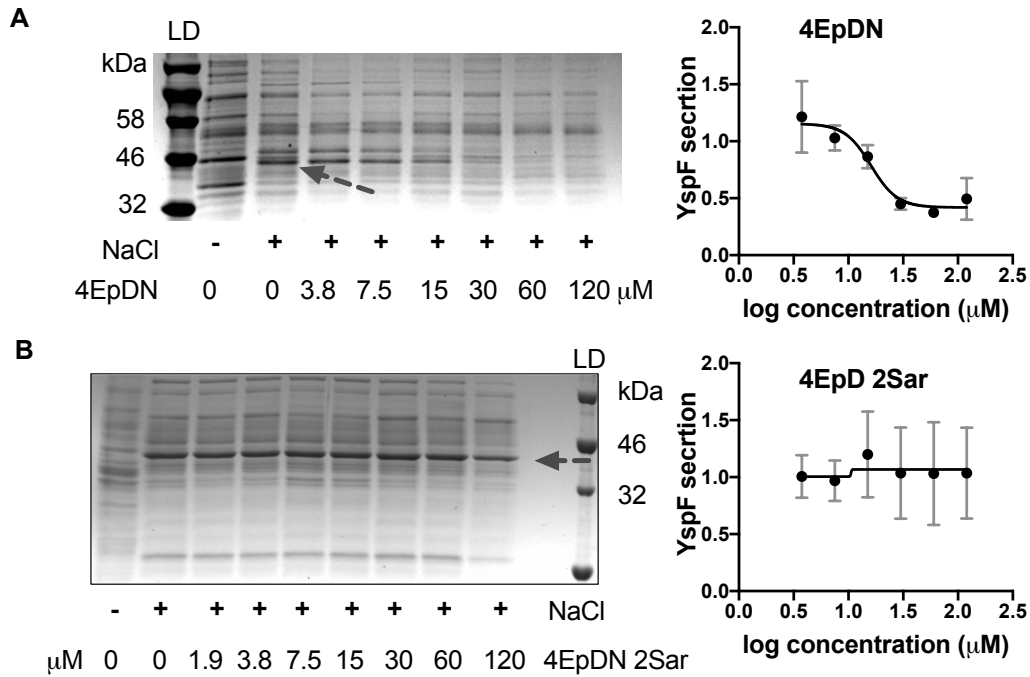


Figure 3: Effect of cyclic peptomers on secretion of *Yersinia* Ysa T3SS substrates.

Y. enterocolitica serotype O:8 was grown under T3SS-inducing conditions with increasing concentrations of cyclic peptomer isomers, 4EpDN (**A**) and 4EpDN 2Sar (**B**). Secretion of T3SS cargo into the culture supernatant was assessed by precipitating secreted proteins and visualizing them with Coomassie blue. YspF band intensities were quantified and normalized to that of the DMSO control. Representative gel images and quantification of YspF are shown. The results are from two independent experiments.

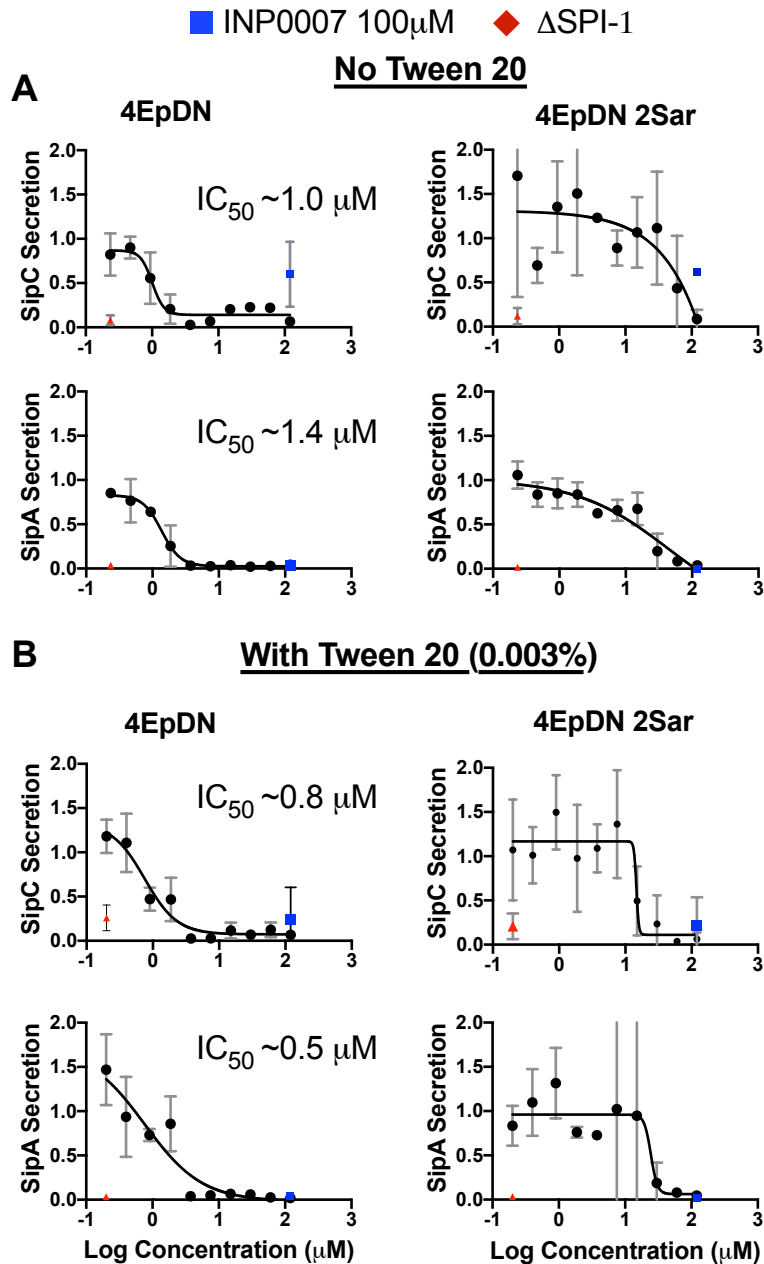


Figure 4: Cyclic peptomers inhibit the *Salmonella* SPI-1 T3SS.

Salmonella enterica Typhimurium was grown with increasing concentrations of cyclic peptomer isomers. Secretion of SPI-1 T3SS cargo into the culture supernatant was assessed by precipitating secreted proteins and visualizing them with Coomassie blue. SipA and SipC band intensities were quantified and normalized to that of the DMSO control. The experiments were carried out without the detergent Tween 20 (A), or with Tween 20 (B). A Δ SPI-1 *Salmonella* mutant and INP0007, a known SPI-1 inhibitor (60), were used as controls. The results are from at least two independent experiments.

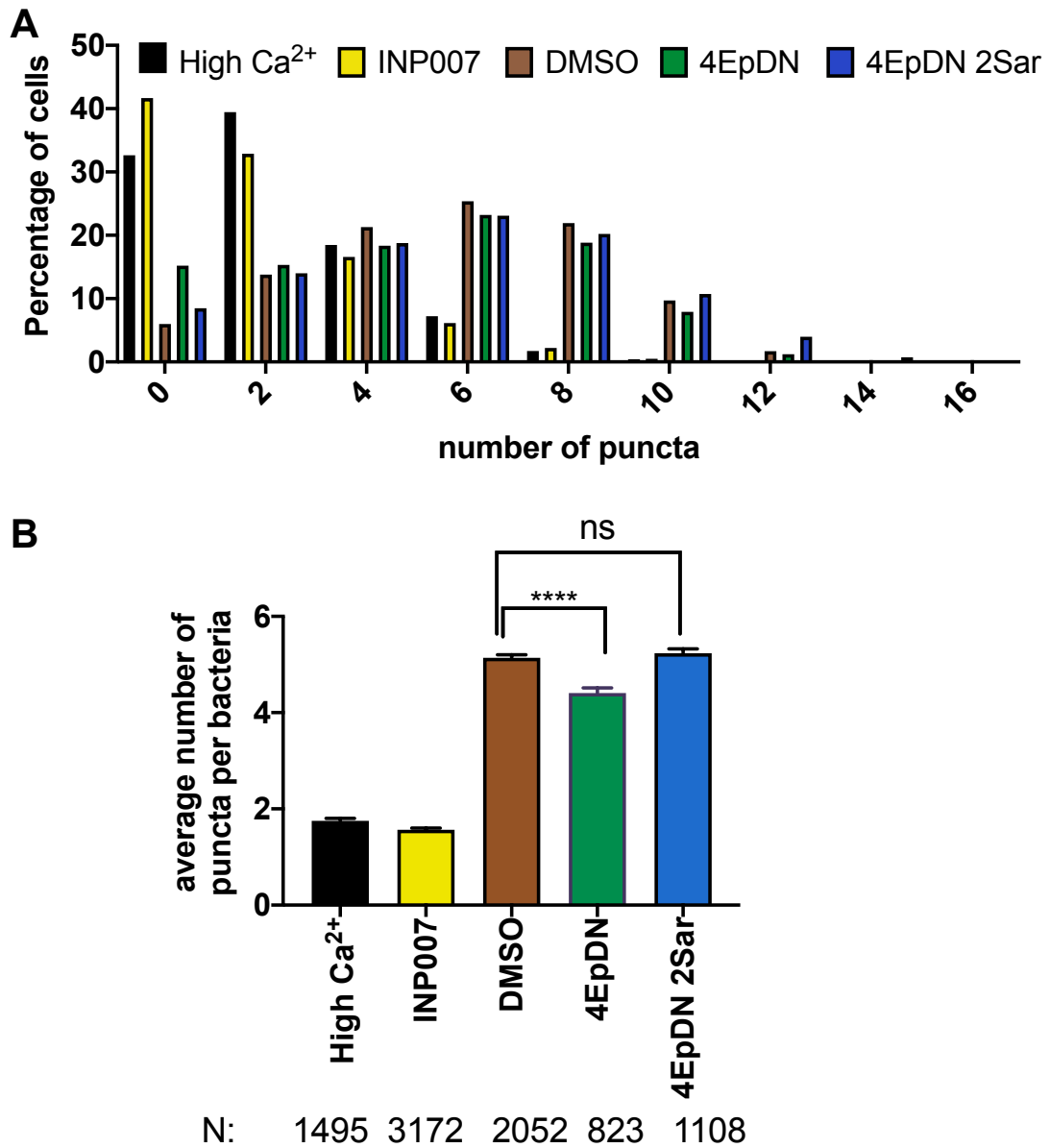


Figure 5: The cyclic peptomer 4EpDN disrupts localization of the Yersinia T3SS basal body component YscD.

Y. enterocolitica expressing YscD-EGFP was grown under T3SS inducing condition (low Ca²⁺) in the presence of 9 μ M cyclic peptomers, 50 μ M INP007, or DMSO. High Ca²⁺ media was used as a non-secreting control. **(A)** Histogram showing the frequency of YscD puncta/cell. **(B)** Average number of puncta/cell after treatment \pm standard error of the mean. Data represents three independent experiments. One-way ANOVA with Dunnett's multiple-comparison test was used. ****, P < 0.0001; ns: not significant

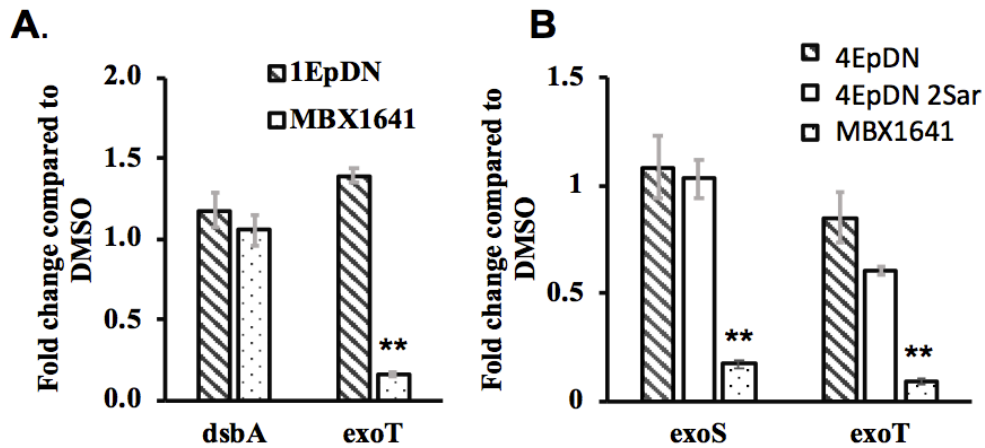


Figure 6: Cyclic peptomers do not affect transcription of T3SS genes in *P. aeruginosa*.

P. aeruginosa PA103 (A) or PA01 (B) was grown in low calcium media in the presence of 60 μ M cyclic peptomers or DMSO. Samples were collected 3 hrs after induction for qPCR analysis. The phenoxyacetamide MBX1641 (53), a known T3SS inhibitor predicted to inhibit type III secretion by binding to the T3SS needle subunit (28), was used as a control. Data were from three replicates, analyzed by one-way ANOVA with Dunnett's multiple-comparison test. **, P < 0.01

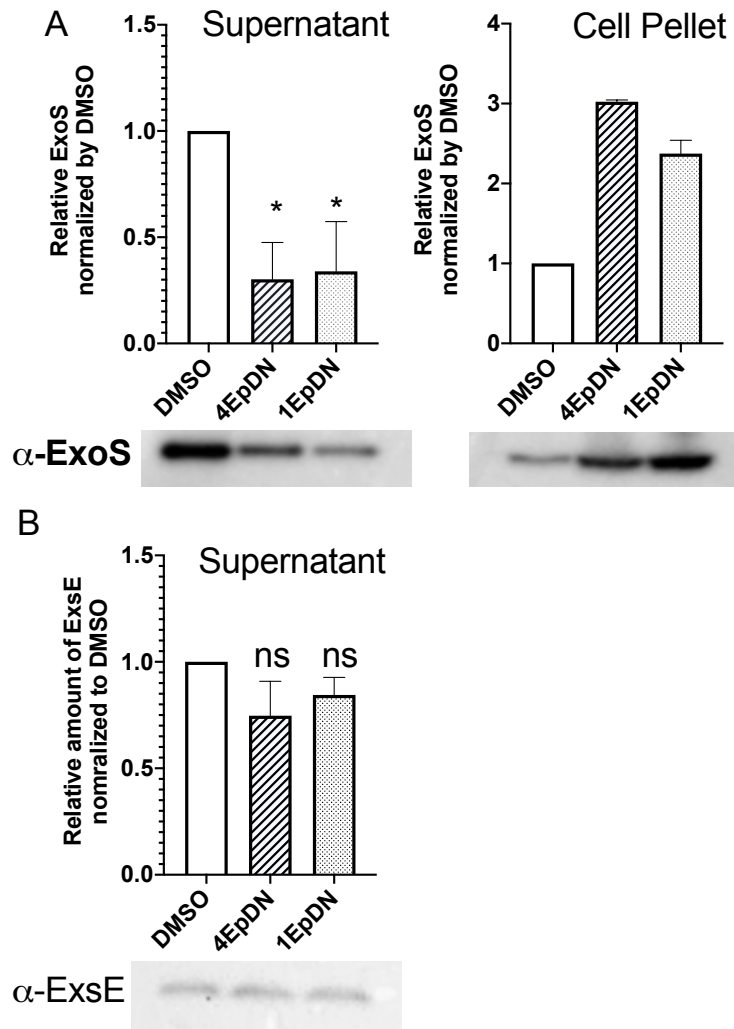


Figure 7: The cyclic peptomer 4EpDN inhibits secretion of the effector protein ExoS, but not the regulator ExsE.

PAO1 carrying ExoS-Bla was grown in T3S inducing condition on the presence of 60 μ M cyclic peptomers or DMSO. **A.** Secretion of ExoS into the culture supernatant and synthesis of ExoS in the cell pellets were assessed by Western Blot using a β -lactamase antibody. **B.** In the same samples, Western blot was carried out for ExsE. ExsE in the supernatant was observed and quantified while ExsE in the cell pellets was undetectable. Data were from at least two independent experiments. One-way ANOVA with Dunnett's multiple-comparison test was used. *, $P < 0.05$; ns: not significant, compared to DMSO.

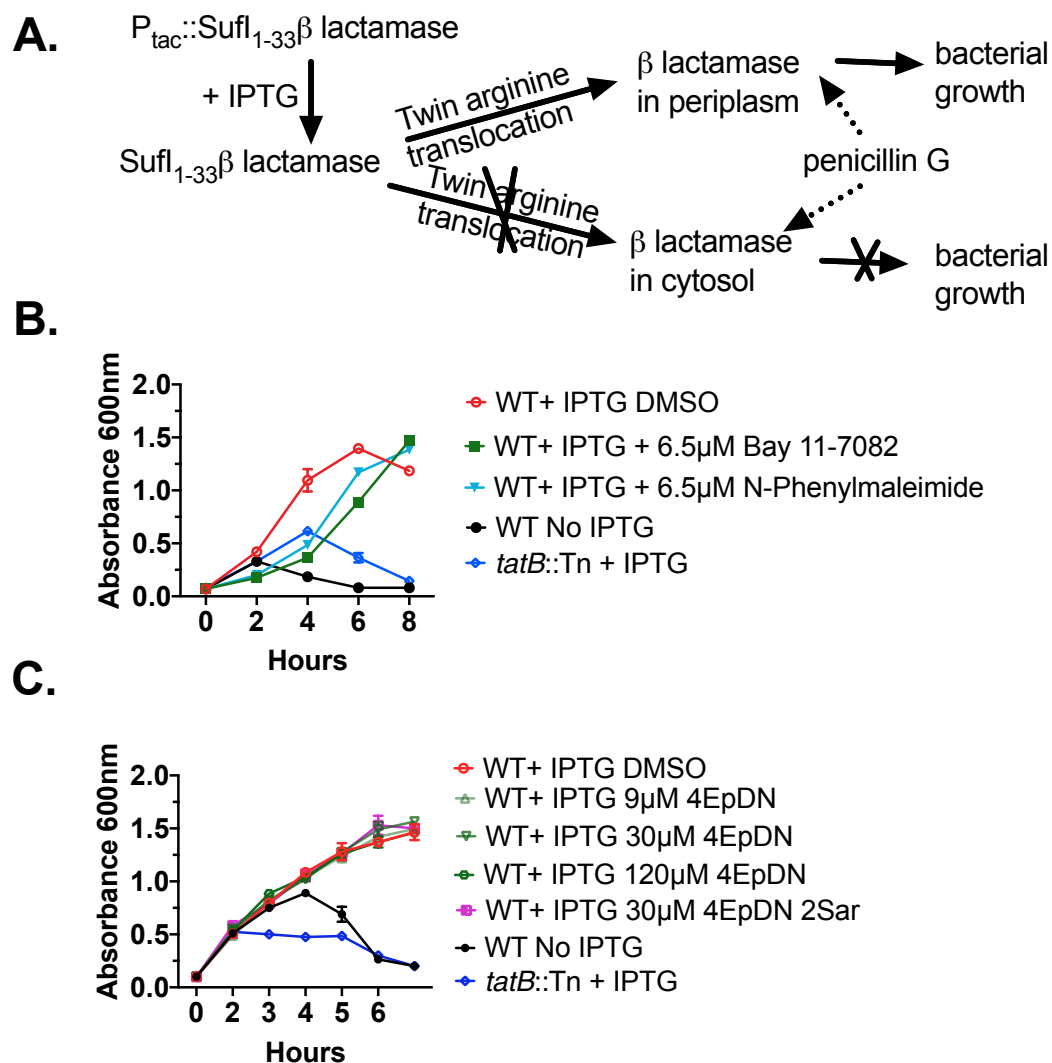


Figure 8: Cyclic peptomers do not affect the twin arginine translocation (Tat) system.

Y. pseudotuberculosis expressing a SufI- β -lactamase Tat secretion reporter incubated in the presence of penicillin G will only grow if the Tat secretion system remains functional. **(B)** *Y. pseudotuberculosis* SufI- β -lactamase reporters were treated with the Tat inhibitors Bay 11-7082, N-Phenyl maleimide, or DMSO, and culture optical density was measured. WT refers to bacteria expressing a functional Tat secretion system. A mutant strain with a transposon insertion in the *tatB* gene serves as a control **(C)** The same assay as in **(B)** was repeated in the presence of cyclic peptomers or DMSO. The result was from two independent replicates.

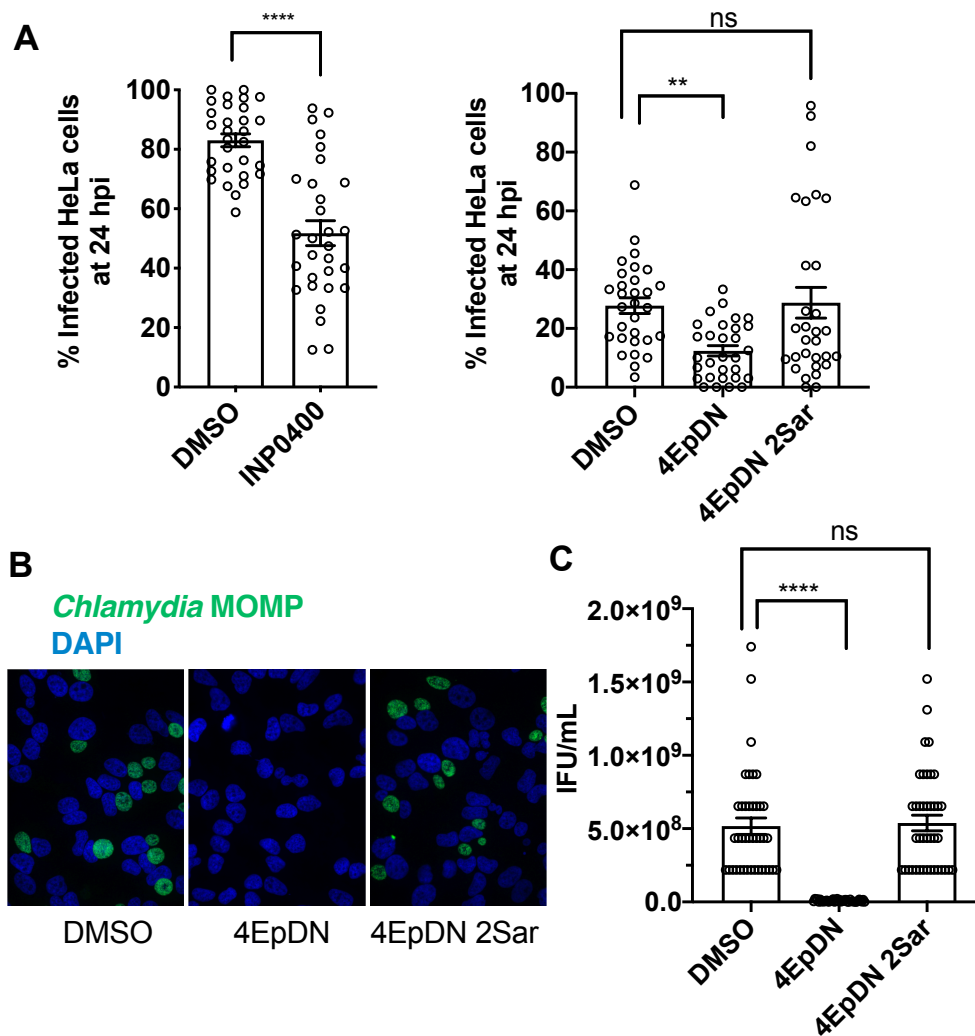


Figure 9: The cyclic peptomer 4EpDN inhibits *Chlamydia* infection

(A) HeLa cells were infected with *C. trachomatis* L2 at a multiplicity of infection (MOI) of three (left hand panel) or one (right hand panel) in the presence of 9 μ M cyclic peptomers, 30 μ M INP0400, or DMSO. Cells were stained for the *Chlamydia* major outer membrane protein (MOMP) and nucleic acids (DAPI), and imaged after 24 hrs of infection to determine the number of infected cells (primary infection). (B-C) Infectious elementary bodies (EB) were harvested after 48hrs of HeLa cell infection in the presence of inhibitors and used to infect fresh HeLa cells without applying inhibitors (secondary infection). After 24 hrs, cells were imaged as in (A). Representative images (B) and infectious units/mL (C) are shown from three to four independent experiments. One-way ANOVA with Dunnett’s multiple-comparison test was used. **, $P < 0.01$, ****, $P < 0.0001$, ns: not significant.

Table 1: Compounds synthesized and used in this study

Simplified Name	Full Name/ side chain identity (1-6)	Exact Mass	Reference
1EpDN	EpD-1,2N / Propylamine, Benzylamine, D-Leu, L-Ile, L-Leu, and D-Phe (PBDLLD)	732.46	(14)
1EpDN 1Sar	EpD1,2N 1Sar / Sarcosine, Benzylamine, D-Leu, L-Ile, L-Leu, and D-Phe (SarBDLLD)	704.43	This study
1EpDN 2Sar	EpD1,2N 2Sar / Propylamine, Sarcosine, D-Leu, L-Ile, L-Leu, and D-Phe (PSarDLLD)	656.43	This study
1EpDN 3Ala	EpD-1,2N 3Ala / Propylamine, Benzylamine, D-Ala, L-Ile, L-Leu, and D-Phe (PB,D-Ala,LLD)	690.41	This study
1EpDN 4Ala	EpD-1,2N 4Ala / Propylamine, Benzylamine, D-Leu, L-Ala, L-Leu, and D-Phe (PBD,L-Ala,LD)	690.41	This study
1EpDN 5Ala	EpD-1,2N 5Ala / Propylamine, Benzylamine, D-Leu, L-Ile, L-Ala, and D-Phe (PBDL,L-Ala,D)	690.41	This study
1EpDN 6Ala	EpD-1,2N 6Ala / Propylamine, Benzylamine, D-Leu, L-Ile, L-Leu, and D-Ala (PBDL,L,D-Ala)	656.43	This study
2EpDN	2-EpD1,2N / Propylamine, Benzylamine, L-Leu, L-Ile, L-Leu, and D-Phe (PBLLLD)	732.46	This study
3EpDN	3-EpD1,2N / Propylamine, Benzylamine, D-Leu, L-Ile, D-Leu, and D-Phe (PBDLDD)	732.46	This study
4EpDN	4-EpD1,2N / Propylamine, Benzylamine, L-Leu, L-Ile, D-Leu, and D-Phe (PBLDD)	732.46	This study
5EpDN	5-EpD1,2N / Propylamine, Benzylamine, L-Leu, L-Ile, D-Leu, and L-Phe (PBLDDL)	732.46	This study
6EpDN	6-EpD1,2N / Propylamine, Benzylamine, D-Leu, L-Ile, D-Leu, and L-Phe (PBDLDL)	732.46	This study
7EpDN	7-EpD1,2N / Propylamine, Benzylamine, L-Leu, L-Ile, L-Leu, and L-Phe (PBLLLL)	732.46	This study
8EpDN	8-EpD1,2N / Propylamine, Benzylamine, D-Leu, L-Ile, L-Leu, and L-Phe (PBDLLL)	732.46	This study
9EpDN	9-EpD1,2N / Propylamine, Benzylamine, L-Leu, D-Ile, D-Leu, and L-Phe (PBLDDL) (Enantiomer of 1EpDN)	732.46	This study
4EpDN 1Sar	4-EpD1,2N 1Sar / Sarcosine, Benzylamine, L-Leu, L-Ile, D-Leu, and D-Phe (SarBLDD)	704.43	This study
4EpDN 2Sar	4-EpD1,2N 2Sar / Propylamine, Sarcosine, L-Leu, L-Ile, D-Leu, and D-Phe (PSarLLDD)	656.43	This study

Table 2: Efficacy of cyclic peptomers and other type III secretion system inhibitors.

Species/T3SS family ^a	PA	Ysc	Ysa	SPI-1	EPEC /EHEC	<i>Chlamydia</i>	PS	fliC	Ref.
	Psc/Ysc		Inv-Mxi-Spa		Ssa-Esc	Chlamydiales	Hrc1	fla	
4EpDN	3.9 ExoU ^b	~7.5 YopE ^b	16.1 YspF ^b	1 SipAC ^b		~9 ^c		NE ^d	This study
4EpDN 2Sar	139.5 ExoU ^b			~30 SipAC ^b		X		NE ^d	This study
1EpDN	8.2 ExoU ^b	14.3 YopE ^b							(14)
MBX1641 Phe [*]	10 ExoS ^b					~10 ^c			(53)
MBX2359 Phe MBX2401 Phe	2.5 ExoS ^b 1.2 ExoS ^b								(28)
Hydroxybenzimidazoles	~3.5 ExsA ^e	~3.9 LcrF ^e							(54)
INP1750 HQ [*]	~80 ^c	12.4 YopEe EC ₅₀				25 MIC ^c		~80	(55, 56)
INP1767 HQ		14.6 YopE ^c EC ₅₀				12.5 MIC ^c			(55)
INP1855 HQ	~60 ^c	6.3 YopE ^c EC ₅₀				3.13 MIC ^c		~30	(55, 57)
INP0341 SAH [*]	~80 ^c					~20 ^c			(56, 58)
INP0400 SAH						~20 ^c			(58)
INP0403 SAH				~100 SipAC ^b					(59, 60)
INP0007 SAH		~50 YopE ^b		~100 SipAC ^b					(60, 61)
C2, C4 SAH		~20; ~5 Yops ^b							(62)
ME0052 SAH		~20 Yops ^b							(63)
INP0010 SAH C1 SAH		~50 YopE ^b ~50 Yops ^b							(64)
ME0055 SAH (INP0031)					~20 LEE genes ^e				(65)
RCZ12 SAH RCZ20 SAH					~25 EspD ^b				(66)
INP0401 SAH 5277768 SAH							~50 hrp ^e		(67)
Compound 3	13 ExoS ^b	6 YopE ^b							(53)
C20	~60 ^c	~60 YopE ^f							(68)
Compound D	~60 ExoU ^e	~60 YopE ^b							(69)
Salicylideneanilide					15 EspB ^b				(70)

Piercidin A1, Mer-A 2026B		~36; ~9 YopM ^f						(71)
N-arylbzylamines						~50 IncA ^f		(72)
Baicalin Flavonoid				3.6 SopE2 ^b		0.5mM ^c		(73, 74)
Licoflavonol				~50 SipC ^b				(75)
Epigallocatechin gallate		~16µg/ml 1 Yops ^b		~12µg/ml Sips ^b	~16µg/ml EspB ^b			(76)
Sanguinarine chloride				~5 SipA ^{br}				(77)
Obovatol				19.8 ^c				(78)
Thymol				~0.2 mM SipA ^f				(79)
TTS29 thiazolidinone		~380 Yops ^b	~380 Ysps ^b	~100 Sips ^b			~380 ^c	(80)
WEN05-03					~100 ^c			(81)
Fluorothiazinon (also CL-55)	~20µg/ml ExoT ^b ExoY ^b			~10mg/kg ^c		~25 ^c		(82-84)
(-)-Hopeaphenol	~50 ExoS ^b	3.3 YopD ^b				~25 ^c		(85)
Resveratrol oligomers							~100 hrpA ^c	(86)
Paeonol				~95 Sips ^b				(87)
Syringaldehyde				~180 Sips ^b				(88)
Fusaric acid				53.5 SipC ^b				(89)
Cytosporone B				6.25 SipC ^b			NE ^d	(90)
Aurodox					0.5 ug/mL EspABCD _b			(91)
W1227933, W1774182						25 IncA ^f		(72)
BCD03							67.3 ^b	(92)
α-tocopherol	~10 ^c ExoY ^f							(93)
Cinnamaldehyde				~100 ^c SipAB ^c				(94)

^a Species/T3SS family: PA: *Pseudomonas aeruginosa*, Ysc: *Yersinia pseudotuberculosis* Ysc, Ysa: *Yersinia enterocolitica* Ysa, SPI-1: *Salmonella enterica* Typhimurium SPI-1, SPI-II: *Salmonella enterica* Typhimurium SPI-II, EPEC/EHEC: Enteropathogenic *E. coli*/Enterohemorrhagic *E. coli*, PS: *Pseudomonas syringae*, Fla: flagella. Empty square denotes activity not tested.

^b IC₅₀ (in µM, unless otherwise indicated) measured using the indicated organism/T3SS

family/effector protein in a culture-based secretion assay. If IC₅₀ data is not available, either the lowest known inhibitory concentration (indicated by “~”), EC₅₀ (half maximal effective concentration), or MIC (minimal inhibitory concentration) are shown.

^c IC₅₀ (in μM) measured using cell-based, infection assays.

^d No effect observed

^e IC₅₀ (in μM) measured using a biochemical assay (i.e.-binding assay, enzymatic assay, qPCR).

^f IC₅₀ (in μM) measured using translocation assay.

* Phe: Phenoxyacetamide. HQ: hydroxyquinoline. SAH: Salicylidene acylhydrazides.

Table 3: Bacterial strains used in this study

Strain	Description	References
<i>Y. pseudotuberculosis</i> strains		
Wild type	<i>Y. pseudotuberculosis</i> IP2666	(95)
<i>tatB</i> ::Tn - Bla	IP2666 Δ <i>YopHEMOJ</i> <i>tatB</i> ::TnHimar1 insertion; carrying 30aa _{sufl} :: β -lactamase TEM1	This study
Wild type - Bla	IP2666 carrying 30aa _{sufl} :: β -lactamase TEM1	This study
<i>Pseudomonas aeruginosa</i> strains		
Wild type	<i>P. aeruginosa</i> PA103	(96)
Δ <i>exoUT</i>	PA103 Δ <i>exoU</i> / Δ <i>exoT</i>	(97)
PAO1 efflux pump mutant	PAO1 Δ (<i>mexAB-oprM</i>) <i>nfxB</i> Δ (<i>mexCD-oprJ</i>) Δ (<i>mexEF-oprN</i>) Δ (<i>mexJKL</i>) Δ (<i>mexXY</i>) Δ <i>opmH362</i> ::pGSV3-Spr - <i>exoT</i> '- <i>aacC1</i> ::miniCTXexoS(E379A/E381A)- <i>blaM</i>	(28)
<i>Yersinia enterocolitica</i>		
Wild type	<i>Y. enterocolitica</i> 8081 serotype O:8	(98)
pYV40-EGFP- <i>yscD</i>	<i>Y. enterocolitica</i> serotype O9 strain E40	(23)

carrying EGFP-yscD

Salmonella enterica Typhimurium strains

WT *S. enterica* Typhimurium SL1344 (99)

Δ *fliC* SL1344 Δ *fliC* (99)

Escherichia coli

E. coli DH5 α *E. coli* DH5 α carrying 30aa_{suff}: β -
lactamase TEM1 This study

Chlamydia trachomatis *C. trachomatis* serovar L2 (Joanne Engle)

**1.2 SUPPORTING INFORMATION FOR:
Broad-spectrum inhibitors of the Type III secretion system**

Hanh N. Lam ^{1*}, **Tannia Lau**^{2*}, Adam Lentz¹, Jessica Sherry³, Alejandro Cabrera-Cortez², Karen Hug¹, Joanne Engel³, R. Scott Lokey², Victoria Auerbuch¹

¹Department of Microbiology and Environmental Toxicology, University of California Santa Cruz, Santa Cruz, CA 95064.

²Department of Chemistry and Biochemistry, University of California Santa Cruz, Santa Cruz, CA 95064.

³Department of Medicine, University of California San Francisco, San Francisco, CA 94143.

*Co-first authors

Table S1: Solubility of cyclic peptomers

Compounds	Solubility (μM)			IC ₅₀
	PBS	DMEM	M9	
1EpDN 3Ala	180	ND ^a	ND ^a	>1000*
1EpDN 4Ala	75	ND ^a	ND ^a	>1000*
1EpDN 5Ala	127	ND ^a	ND ^a	>1000*
1EpDN 6Ala	125	ND ^a	ND ^a	>1000*
1EpDN	14-17	ND ^a	ND ^a	8.2
2EpDN	12	ND ^a	ND ^a	15.3
3EpDN	18	ND ^a	ND ^a	16
4EpDN	13	12	10	3.9
5EpDN	13	ND ^a	ND ^a	6.3
6EpDN	1	ND ^a	ND ^a	>1000*
7EpDN	26	ND ^a	ND ^a	6.7
8EpDN	1	ND ^a	ND ^a	41.5
9EpDN	10	ND ^a	ND ^a	12.8
4EpDN 1Sar	ND ^a	6	4	19
4EpDN 2Sar	ND ^a	61	61	~139.5

* >1000 indicates IC₅₀ could not be calculated

^a: Not Determined (ND)

Table S2. Primers used in this study

Name	Sequence	Description
oHL364	TACTGGAAACGGTGGCTAATAC	16S Forward for <i>Salmonella</i> qPCR
oHL365	TACCTCACCAACAAGCTAATCC	16S Reverse for <i>Salmonella</i> qPCR
oHL362	GCCAACGACGGTGAAACTA	fliC Forward for <i>Salmonella</i> qPCR
oHL363	GCCGTATCGCTGACCTTATATT	fliC Reverse for <i>Salmonella</i> qPCR
oHL346	ACGACTCATAATTGGCGATAC	hilA Forward for <i>Salmonella</i> qPCR
oHL347	CTGCGATAATCCCTTCACGATAG	hilA Reverse for <i>Salmonella</i> qPCR
oHL348	GGCGTCTCTATGCACTTATC	hilD Forward for <i>Salmonella</i> qPCR
oHL349	GCAGGAAAGTCAGGCGTATAG	hilD Reverse for <i>Salmonella</i> qPCR
oHL350	GCAGCAAATTATTACGCCTTCTC	invF Forward for <i>Salmonella</i> qPCR
oHL351	CTGGTTGACTGAGCGAGTAAAT	invF Reverse for <i>Salmonella</i> qPCR
oHL352	ATGCGTTGTCCGGTAGTATTT	sipC Forward for <i>Salmonella</i> qPCR
oHL353	TTAAGCGCGCCTCTTTCA	sipC Reverse for <i>Salmonella</i> qPCR
oHL354	TCTTGTTATGCAGGAGGTGATG	sipA Forward for <i>Salmonella</i> qPCR
oHL355	GTCAACAAGGTGCGTAAGATTG	sipA Reverse for <i>Salmonella</i> qPCR
BQ89	CATGACCATCGCCTGATCTT	dnaB Forward for <i>P. aeruginosa</i> qPCR
BQ90	GTTGTCCTTCCTTCTCCAAC	dnaB Reverse for <i>P. aeruginosa</i> qPCR

oHL258	ATGCGGTAATGGACAAGGTC	exoT Forward for <i>P. aeruginosa</i> qPCR
oHL259	ACTCGCCGTTGGTATAGAGA	exoT Reverse for <i>P. aeruginosa</i> qPCR
oHL282	CCGGCAGATGTCCATTTTC	DsbA Forward for <i>P. aeruginosa</i> qPCR
oHL283	CTCGACACCCATGCTTTC	DsbA Reverse for <i>P. aeruginosa</i> qPCR
BQ91	CTCTACACCGGCATTCACTAC	exoS Forward for <i>P. aeruginosa</i> qPCR
BQ92	CATACCTTGGTTCGATCAGCTT	exoS Reverse for <i>P. aeruginosa</i> qPCR
oHL210	agcgaattcgagctcgggtaccATGTCACTCAGTC GTCGC	Forward primer for 33 amino acid of <i>sufI</i> N terminus
oHL217	tttctgggtgAGGTTGCTGAGTACTACTAG	Reverse primer for 33 amino acid of <i>sufI</i> N terminus
oHL218	tcagcaacctCACCCAGAAACGCTGGTG	Forward primer for β -lactamase gene
oHL219	tctagaggatccccgggtaccTTACCAATGCTTA ATCAGTGAGG	Reverse primer for β -lactamase gene

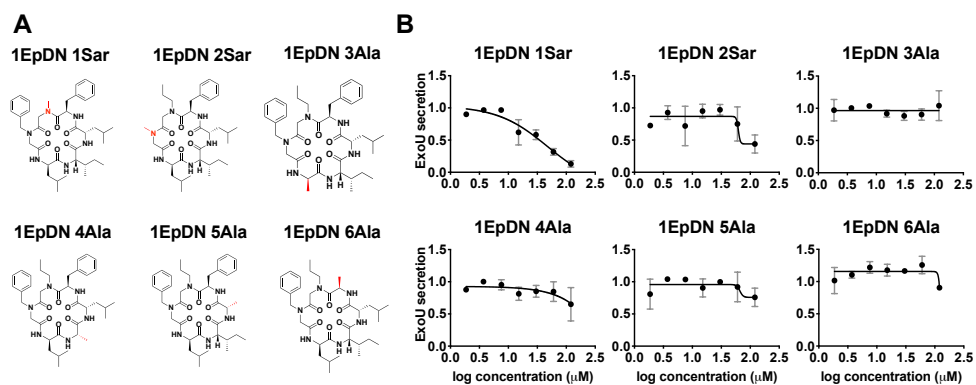


Figure S1: 1EpDN alanine/Sarcosine scan suggests peptoid sidechains are important for biological activity.

(A) Structures of 1EpDN alanine derivatives. D-form of sidechain is shown in red. **(B)** WT *P. aeruginosa* PA103 was grown under T3SS-inducing conditions with increasing concentrations of cyclic peptomers. Secretion of T3SS cargo into the culture supernatant was assessed by precipitating secreted proteins and visualizing them with Coomassie blue. ExoU band intensities were quantified and normalized to that of the DMSO control. The results are from at least two independent experiments. Nonlinear curve fitting is shown to depict the trend of inhibition.

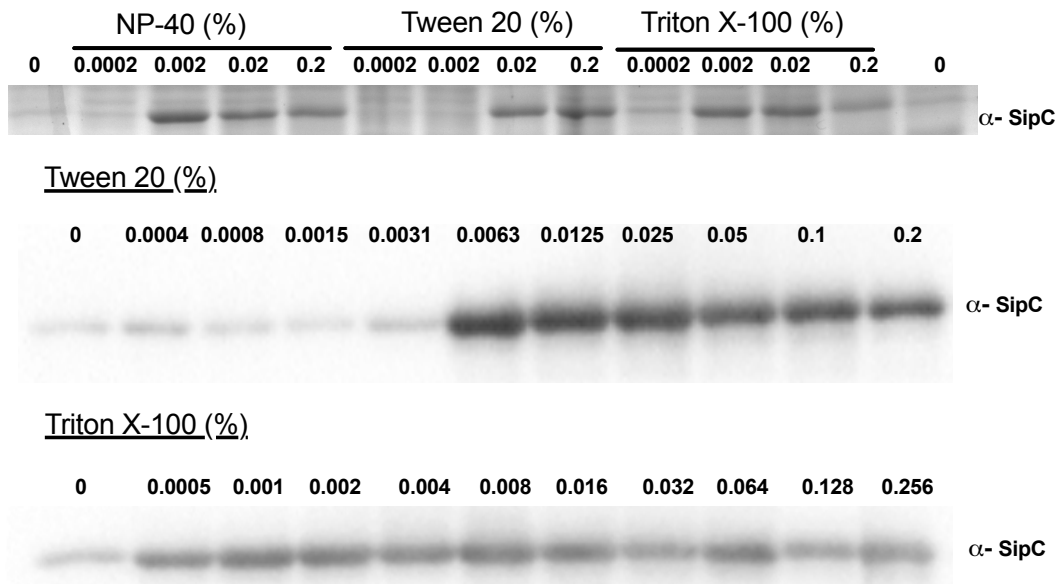


Figure S2: Secretion of *Salmonella* T3SS substrate in the presence of non-ionic detergents.

(A) *Salmonella enterica* Typhimurium was grown in LB with increasing concentrations of NP-40, Tween 20, or Triton X-100. Secretion of SPI-1 T3SS effector SipC into the culture supernatant was assessed by precipitating secreted proteins and visualizing them with Coomassie blue. **(B)** Secretion of SipC in the presence of increasing concentrations of Tween 20 or Triton X-100 was detected by Western Blot. 0.003% Tween-20 is the highest concentration of Tween-20 that resulted in little effect on secretion of SipC.

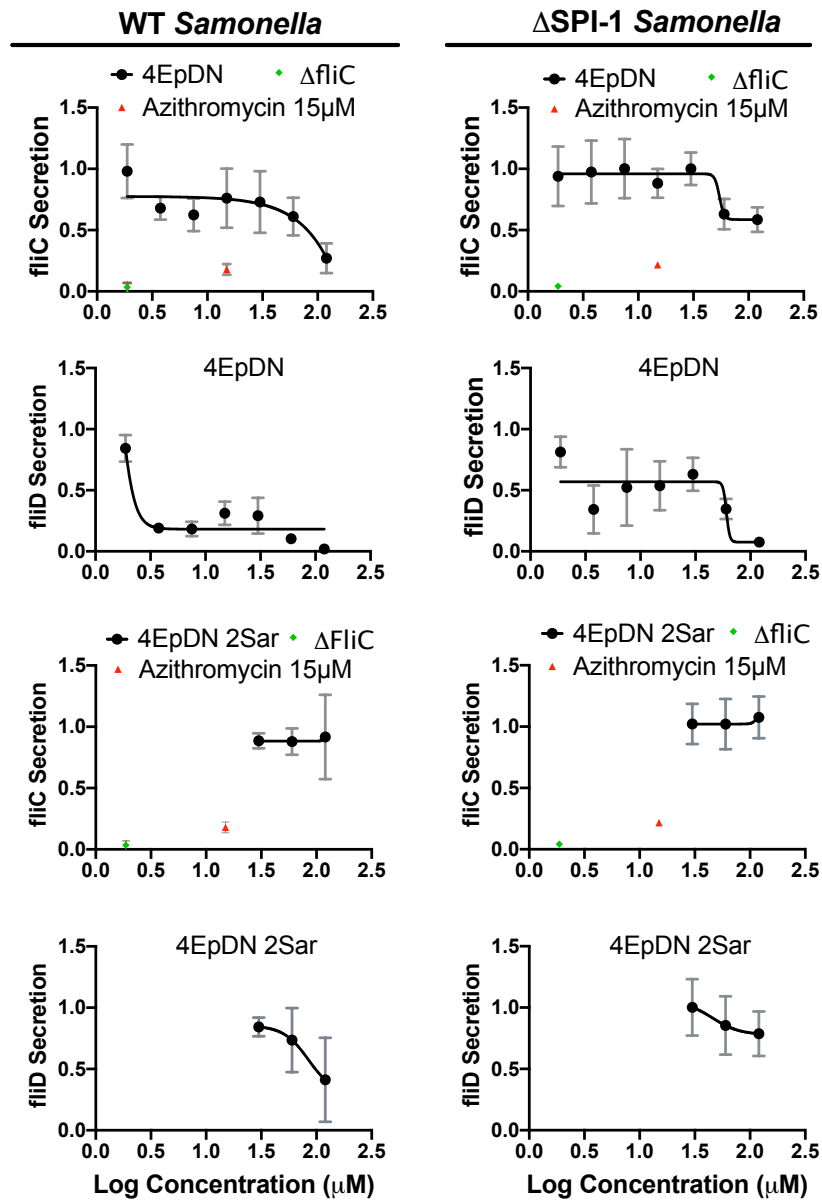


Figure S3: Cyclic peptomers do not affect secretion of flagellar proteins.

Salmonella enterica Typhimurium was grown in LB with increasing concentrations of cyclic peptomers. Secretion of flagellar structural proteins FliC and FliD were assessed by precipitating the secreted proteins and visualizing them with Coomassie blue. A $\Delta fliC$ mutant and azithromycin (100), which inhibits flagellin secretion, were used as controls. The SPI-1 mutant and WT *Salmonella* were both tested, as flagella substrates can be secreted through both flagellar and SPI-1 T3SS systems.

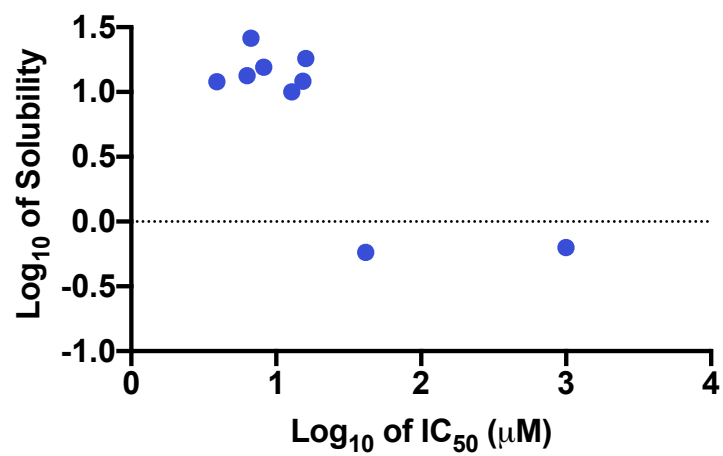


Figure S4: Relationship between solubility and activity of cyclic peptomers.
IC₅₀ of stereoisomers and their solubility (table S1) were plotted on a log₁₀ scale. Average solubility was used when the solubility was measured in different conditions.

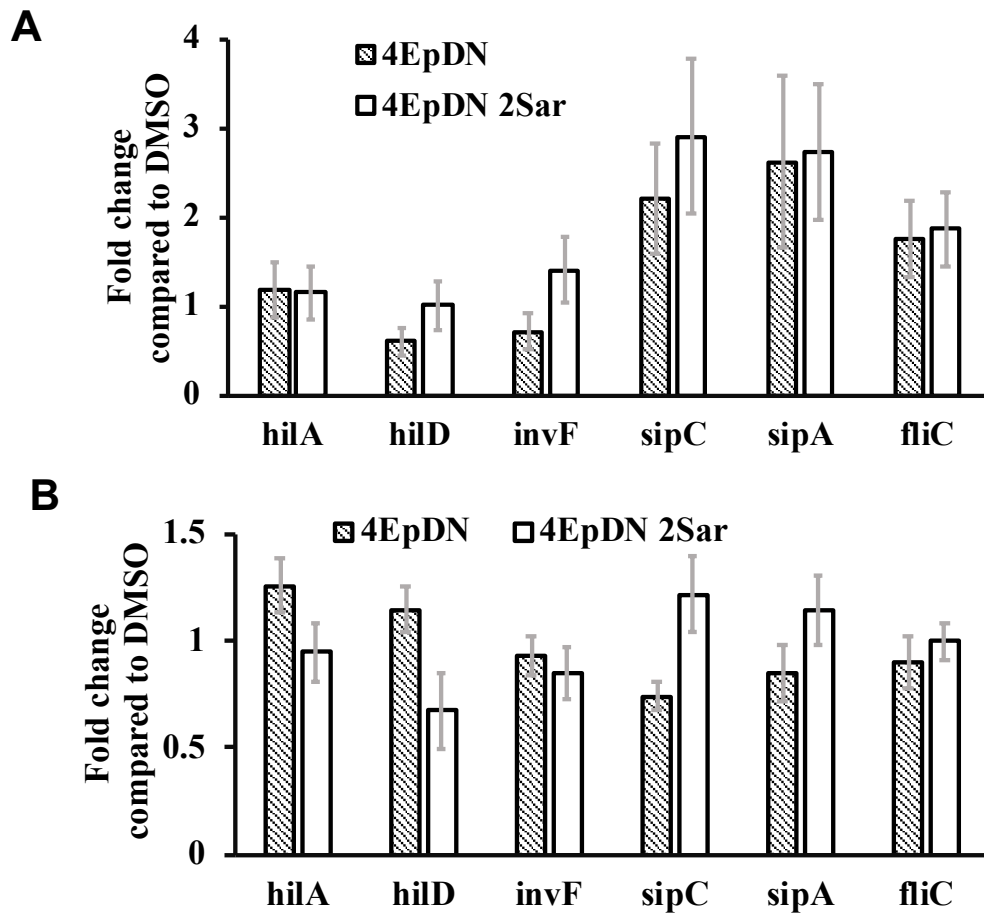


Figure S5: Cyclic peptomers do not affect transcription of T3SS genes in *Salmonella*.

Salmonella enterica Typhimurium was grown in LB with 300 mM NaCl in the presence of 9 μ M cyclic peptomers or DMSO. Samples were taken 2 hrs (A) and 4 hrs (B) after addition of compounds at 37°C and expression of flagellar (*fliC*) and injectisome T3SS (*hilA*, *hilD*, *invF*, *sipC*, *sipA*) genes were assessed using qPCR. Data are from two replicates, analyzed by one-way ANOVA showing no significant difference between control and treatment

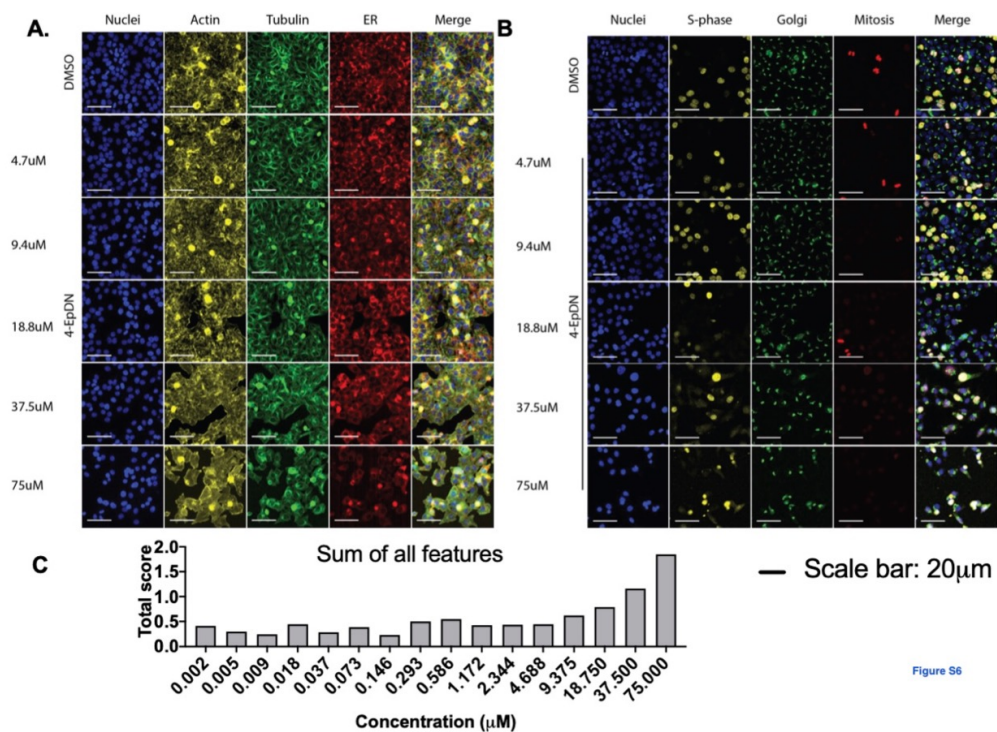


Figure S6

Figure S6: Effect of cyclic peptomers on HeLa cells.

HeLa cells were incubated with compounds for 48 hrs. Cells were then stained with: **(A)** Stain Set 1-Hoechst, FITC-alpha tubulin, rhodamine-phalloidin (actin), and Calnexin (ER induced protein); or **(B)** Stain set 2-Hoechst, EdU-rhodamine (S-phase detection), anti-Phosphohistone H3 (mitosis marker), and GM130 (Golgi matrix protein). Representative images of cells treated with different concentrations of 4EpDN or DMSO are shown. **(C)** Quantification of all cell features for 4EpDN-treated cells. The total CP score is the square root of sum of square of the difference between treatment and DMSO for all measured features.

Figure S7: Characterization of cyclic peptomers.

Structures, SMILES, exact/mass molecular weight, LCMS Spectra, and ¹H-NMR Spectra are shown.

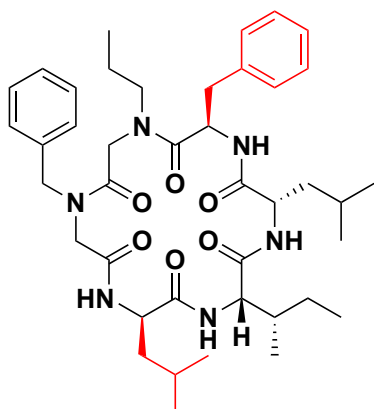
Compounds

- | | |
|----------------|----------------|
| 1. 1EpDN | 12. 1EpDN 4Ala |
| 2. 2EpDN | 13. 1EpDN 3Ala |
| 3. 3EpDN | 14. 1EpDN 1Sar |
| 4. 4EpDN | 15. 1EpDN 2Sar |
| 5. 5EpDN | 16. 4EpDN 1Sar |
| 6. 6EpDN | 17. 4EpDN 2Sar |
| 7. 7EpDN | |
| 8. 8EpDN | |
| 9. 9EpDN | |
| 10. 1EpDN 6Ala | |
| 11. 1EpDN 5Ala | |

OrbiTrap LCMS Purity Check:

- | |
|------------|
| 4EpDN |
| 4EpDN 2Sar |

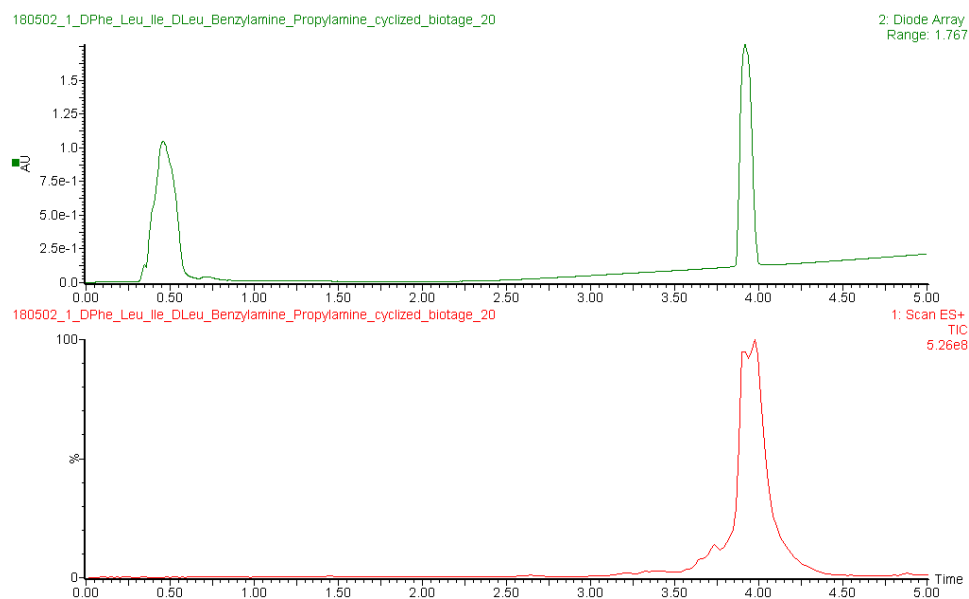
**1EpDN
PBDLLD**

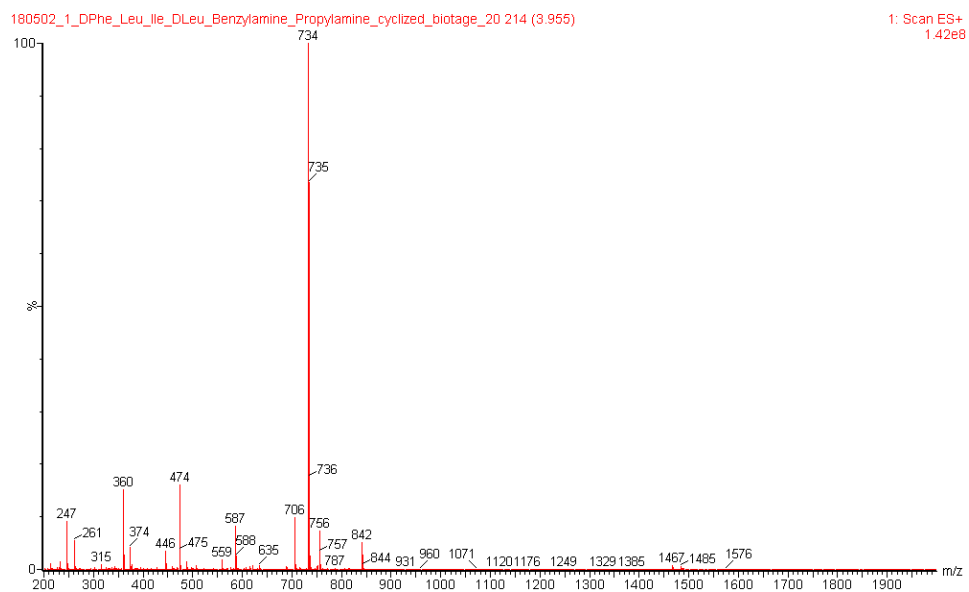


Exact Mass: 732.46
Molecular Weight: 732.97

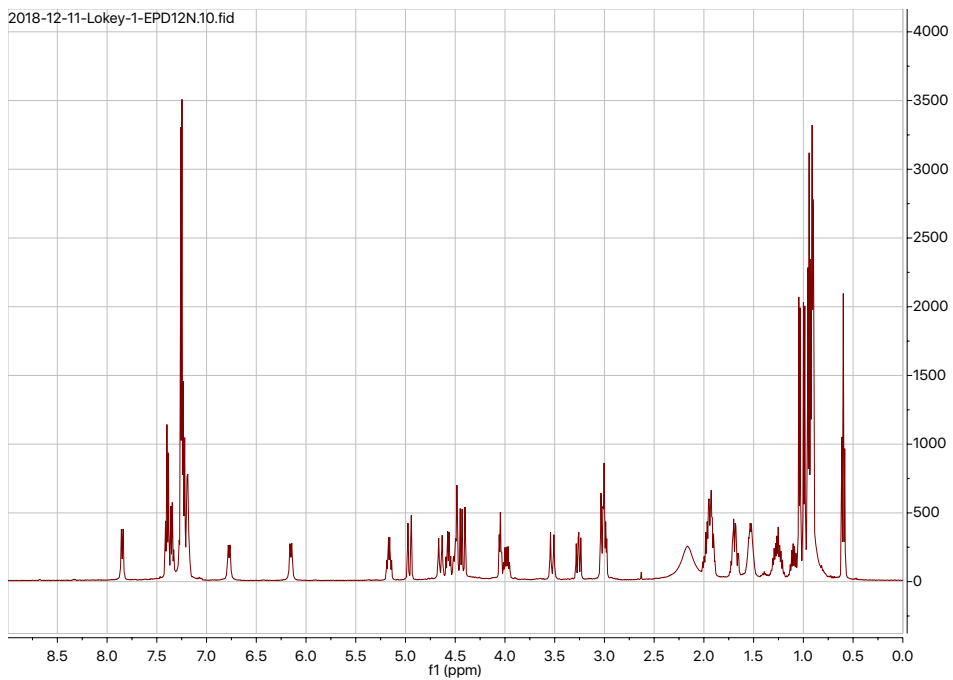
SMILES:

O=C([C@H](CC(C)C)NC([C@@]([C@@H](C)CC)([H])N1)=O)N[C@@H](C(N(C)C(N(CC2=CC=CC=C2)CC(N[C@H](CC(C)C)C1=O)=O)=O)CCC)=O)CC3=CC=C=C3

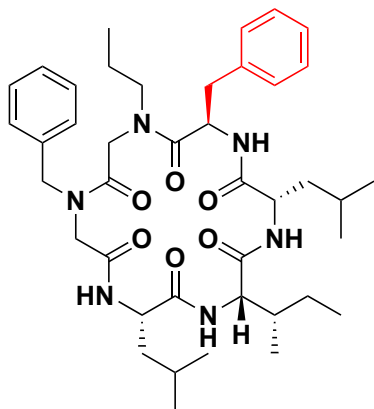




1EpDN (^1H NMR, 500 MHz, CDCl_3)



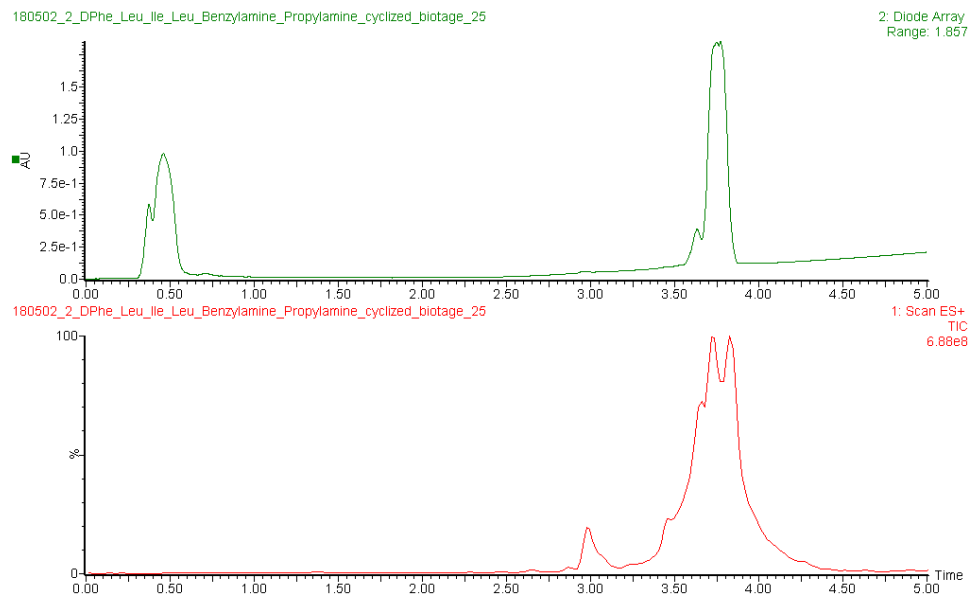
**2EpDN
PBLLLD**

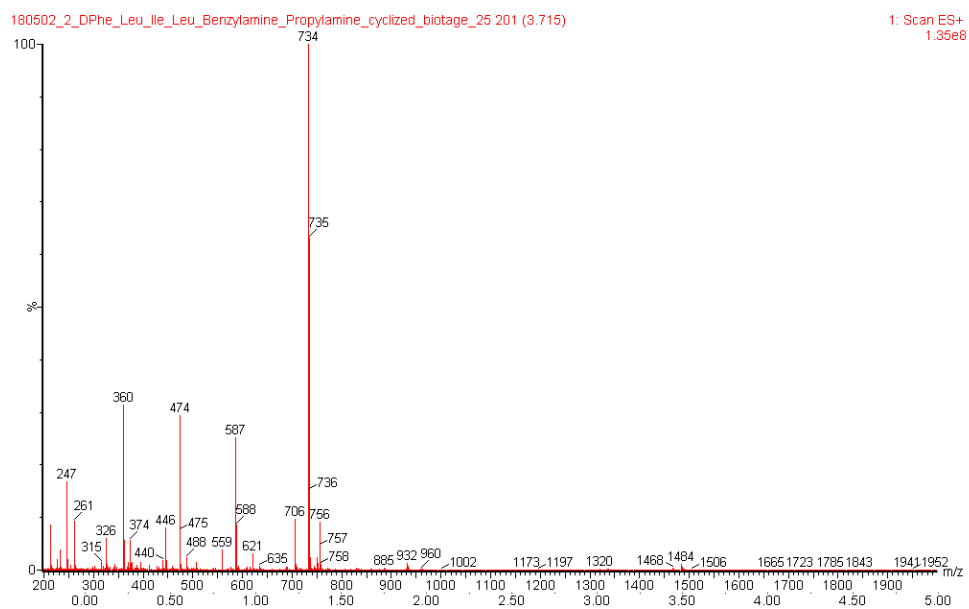


Exact Mass: 732.46
Molecular Weight: 732.97

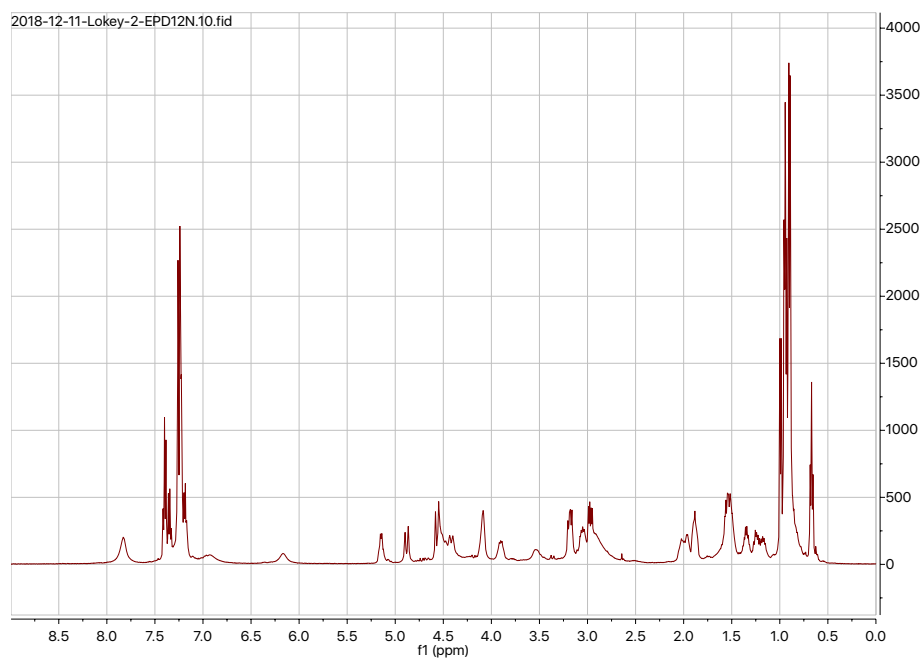
SMILES:

O=C([C@H](CC(C)C)NC([C@@]([C@@H](C)CC)([H])N1)=O)N[C@@H](C(N(C)C(N(CC2=CC=CC=C2)CC(N[C@@H](CC(C)C)C1=O)=O)=O)CCC)=O)CC3=CC=CC=C3

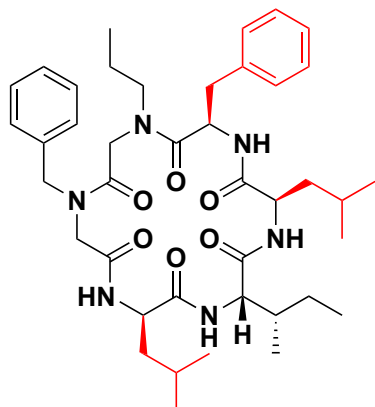




2EpDN (^1H NMR, 500 MHz, CDCl_3)



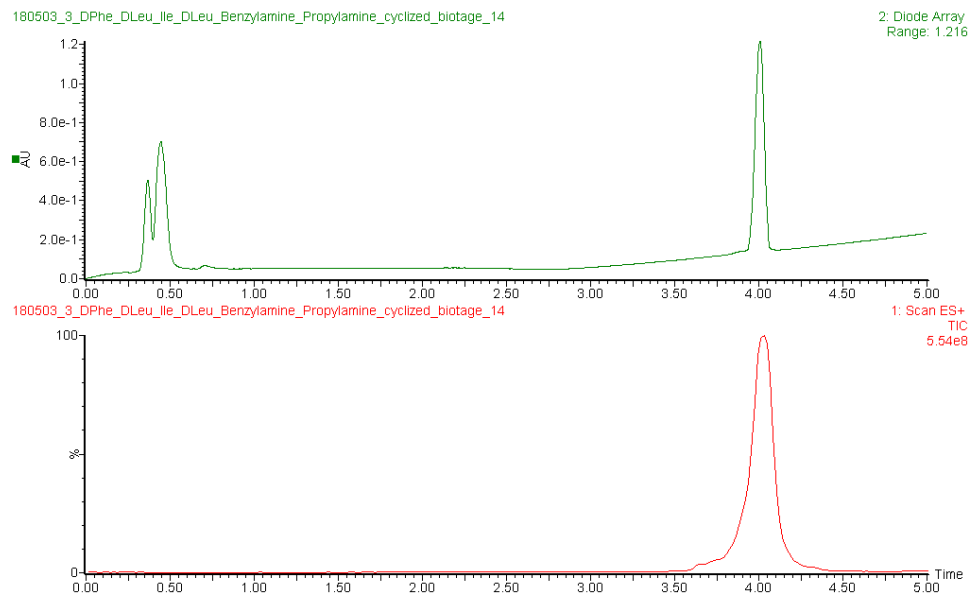
**3EpDN
PBDLDD**

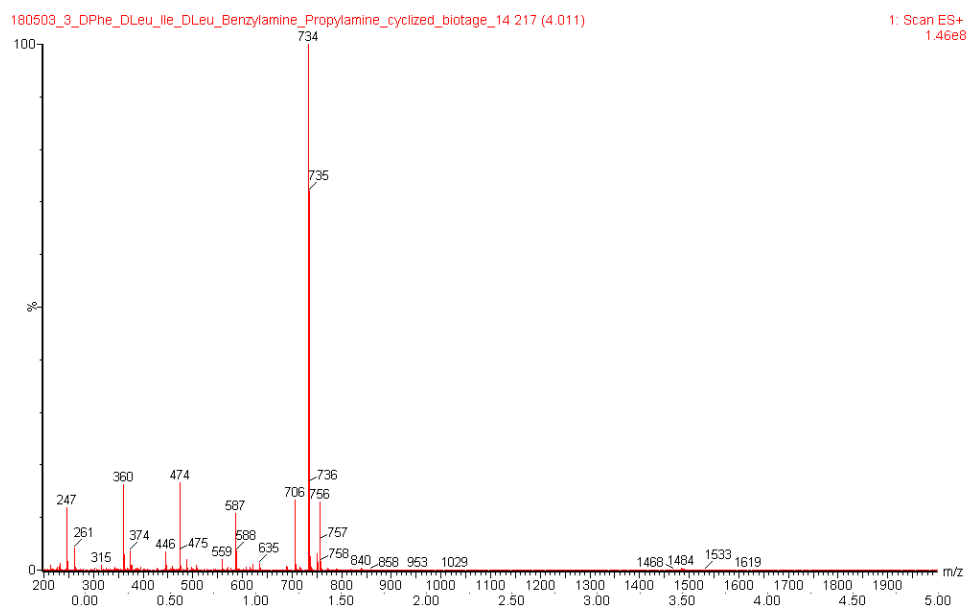


Exact Mass: 732.46
Molecular Weight: 732.97

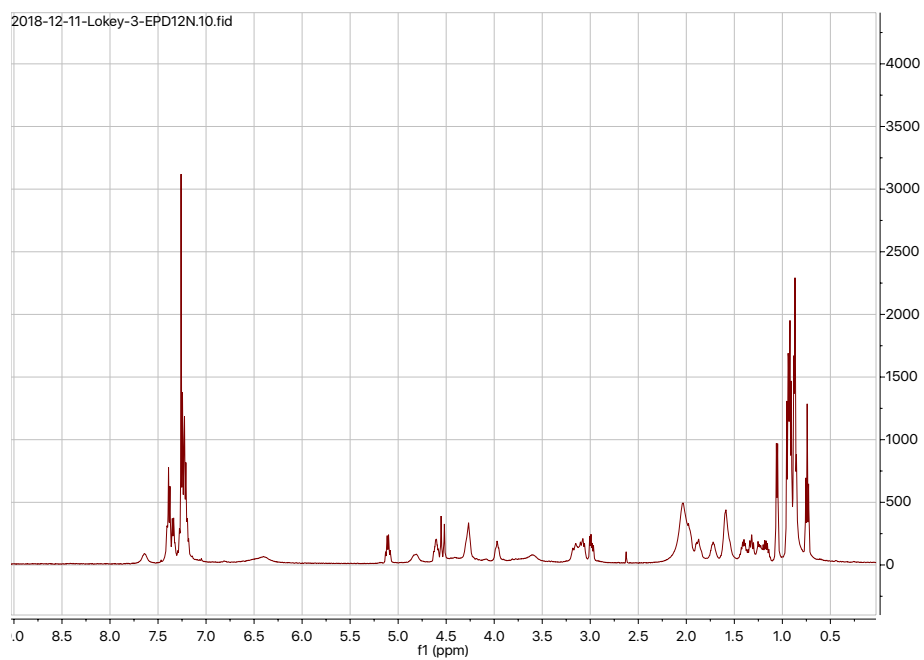
SMILES:

O=C([C@@H](CC(C)C)NC([C@@]([C@@H](C)CC)([H])N1)=O)N[C@@H](C(N(CC(N(CC2=CC=CC=C2)CC(N[C@H](CC(C)C)C1=O)=O)=O)CCC)=O)CC3=CC=CC=C3

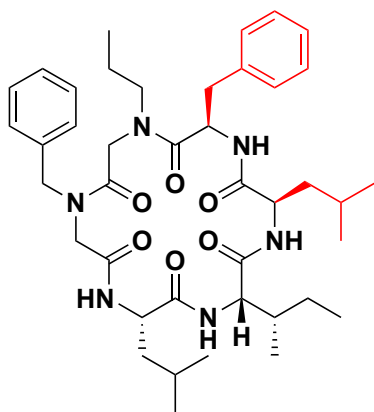




3EpDN (^1H NMR, 500 MHz, CDCl_3)



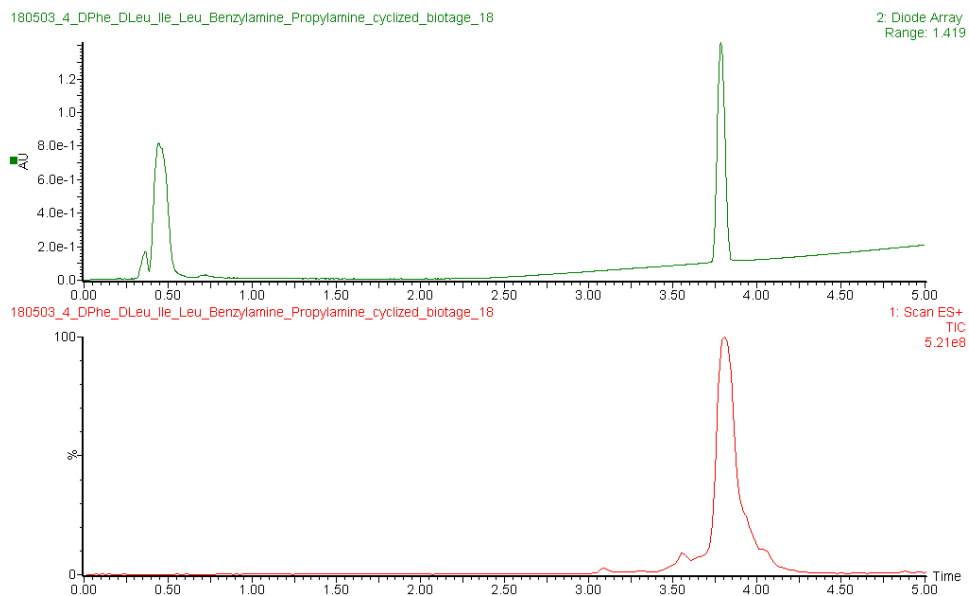
**4EpDN
PBLDD**

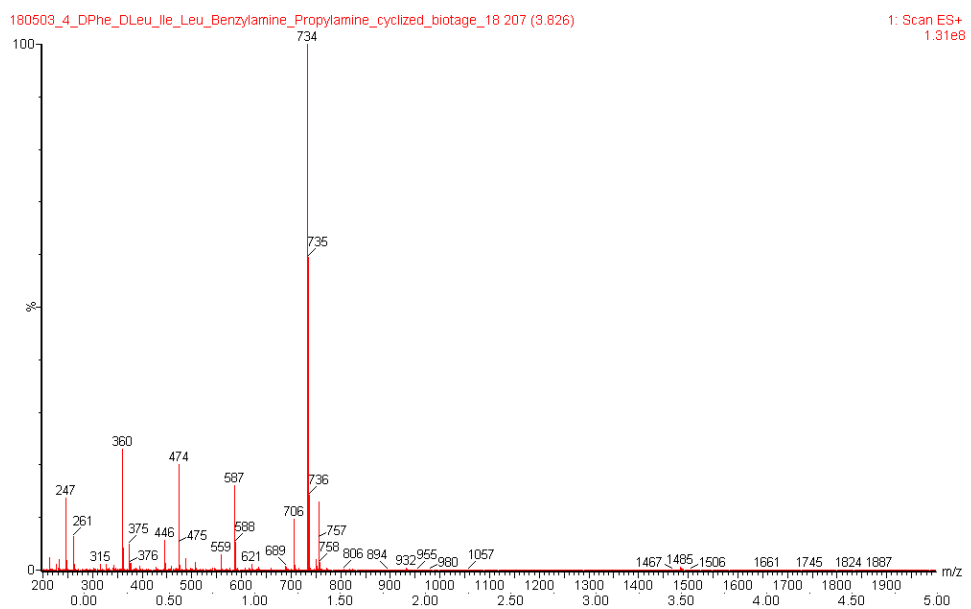


Exact Mass: 732.46
Molecular Weight: 732.97

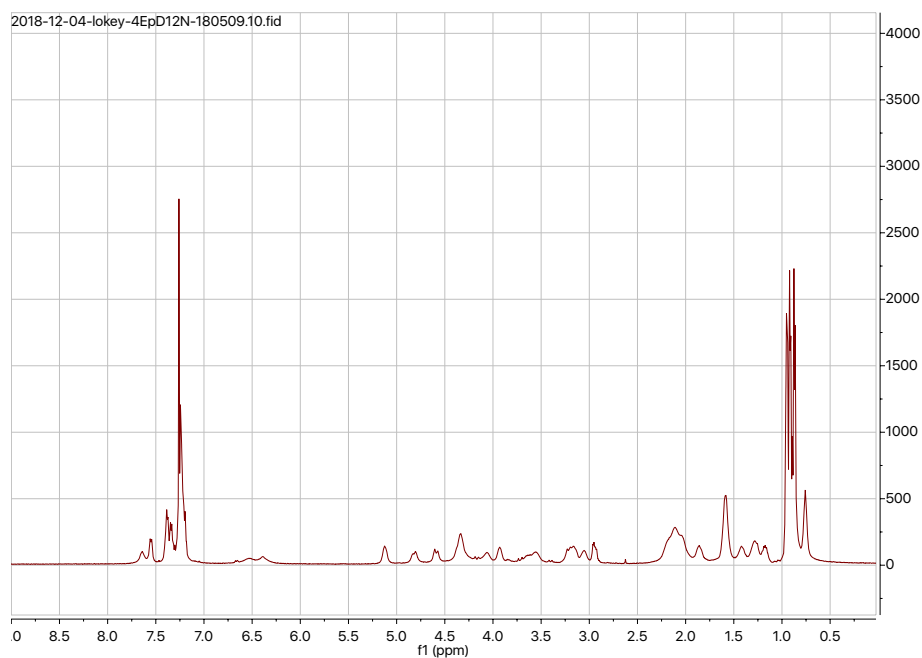
SMILES:

O=C([C@@H](CC(C)C)NC([C@@]([C@@H](C)CC)([H])N1)=O)N[C@@H](C(N(CC(N(CC2=CC=CC=C2)CC(N[C@@H](CC(C)C)C1=O)=O)=O)CCC)=O)CC3=C=C=CC=C3

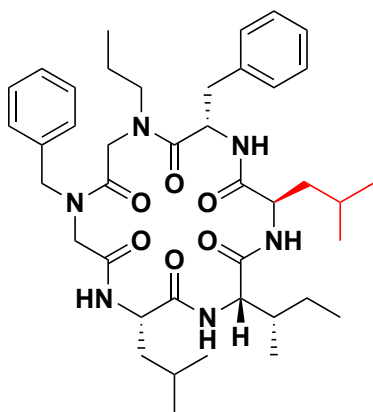




4EpDN (^1H NMR, 500 MHz, CDCl_3)



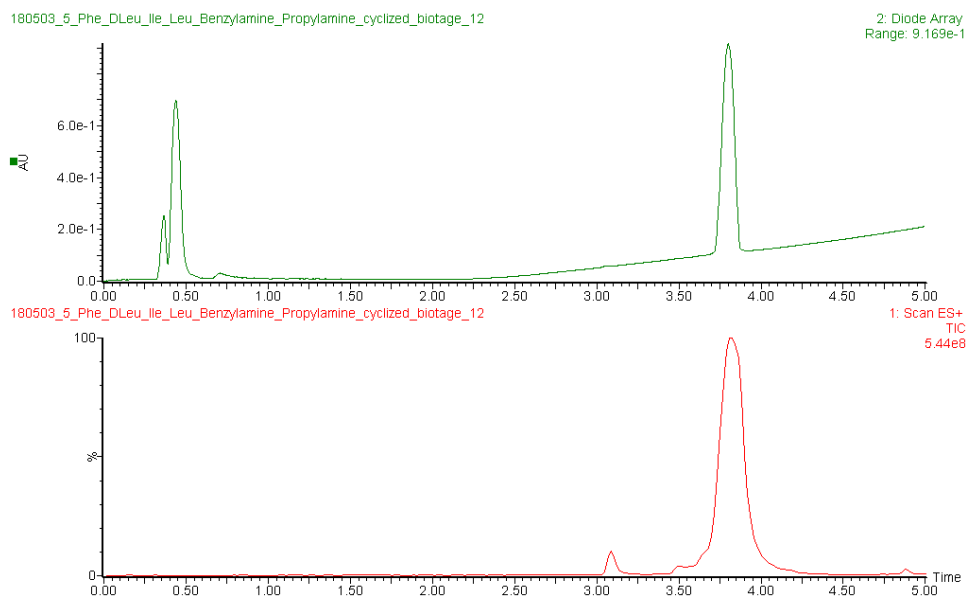
**5EpDN
PBLLDL**

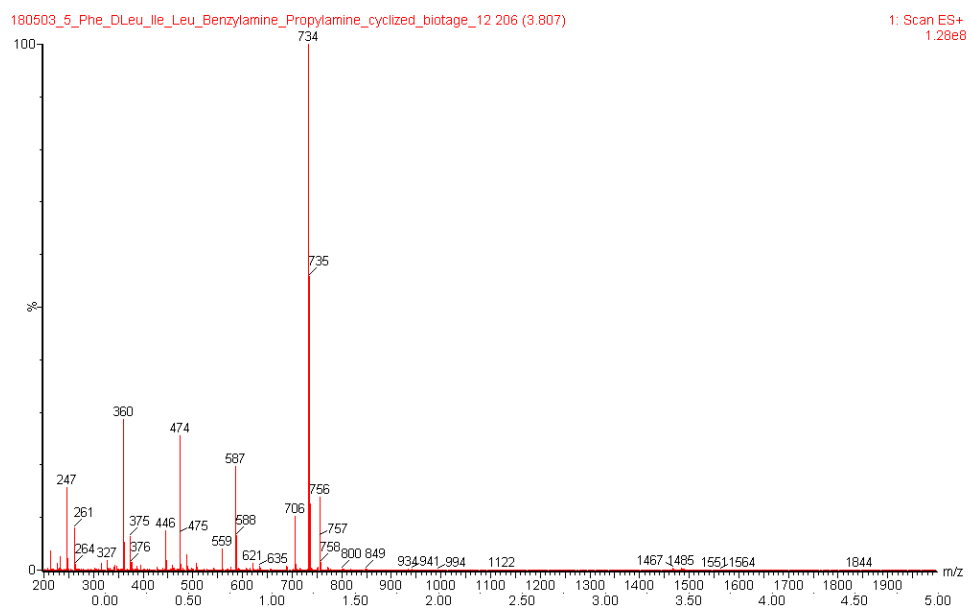


Exact Mass: 732.46
Molecular Weight: 732.97

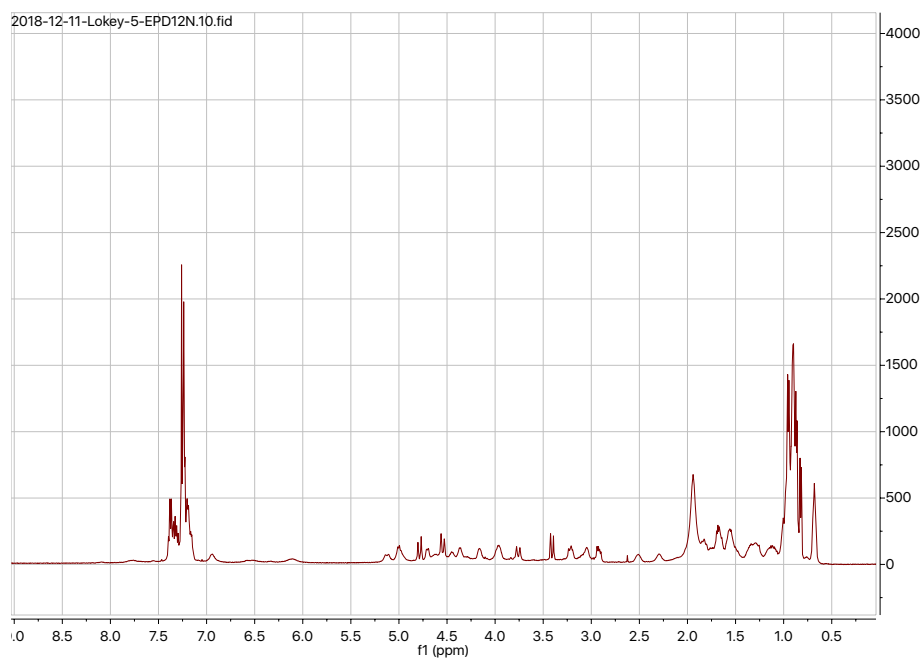
SMILES:

O=C([C@@H](CC(C)C)NC([C@@])([C@@H](C)CC)([H])N1)=O)N[C@H](C(N(C)C(N(CC2=CC=CC=C2)CC(N[C@@H](CC(C)C)C1=O)=O)=O)CCC)=O)CC3=CC=CC=C3

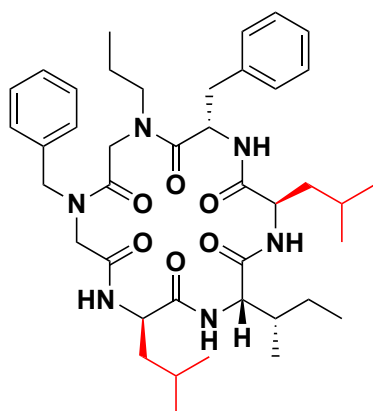




5EpDN (^1H NMR, 500 MHz, CDCl_3)



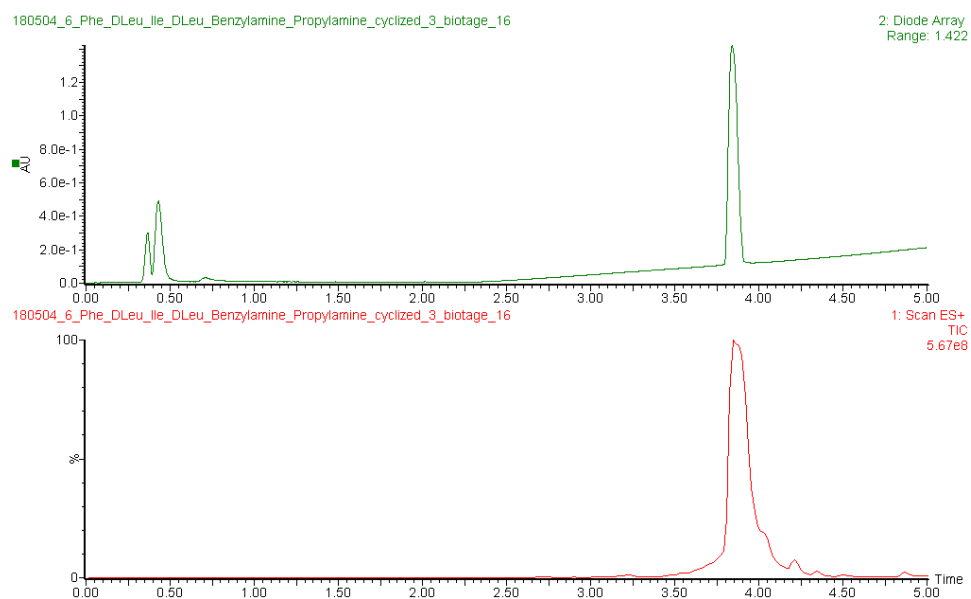
**6EpDN
PBDLDL**

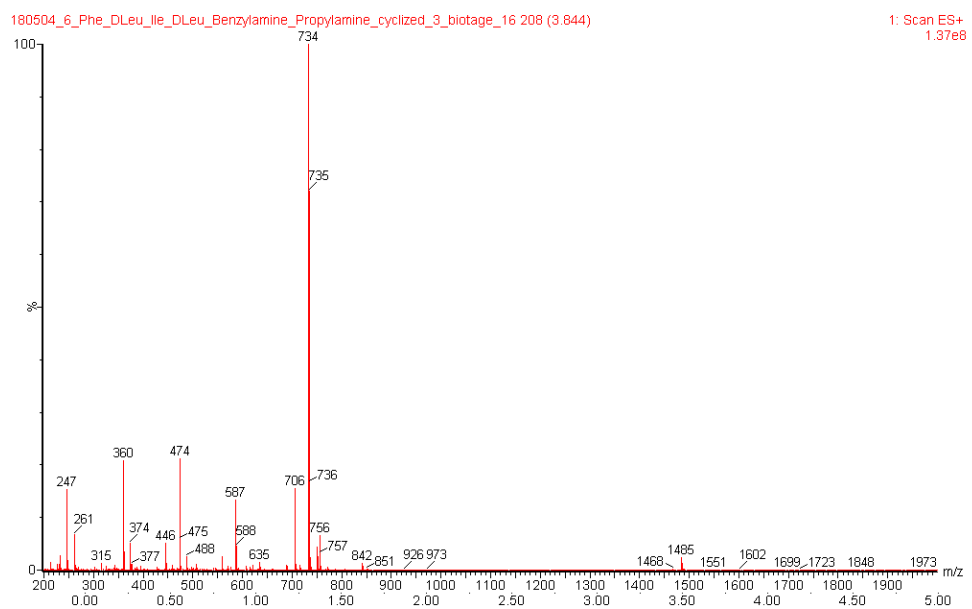


Exact Mass: 732.46
Molecular Weight: 732.97

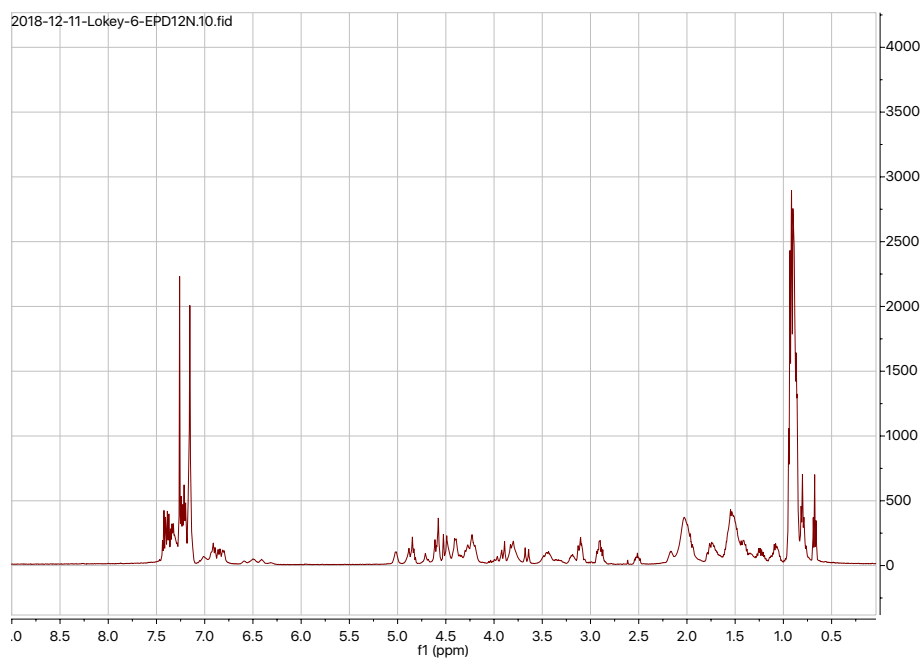
SMILES:

O=C([C@@H](CC(C)C)NC([C@@])([C@@H](C)CC)([H])N1)=O)N[C@H](C(N(C(C(N(CC2=CC=CC=C2)CC(N[C@H](CC(C)C)C1=O)=O)=O)CCC)=O)CC3=CC=C(C=C3

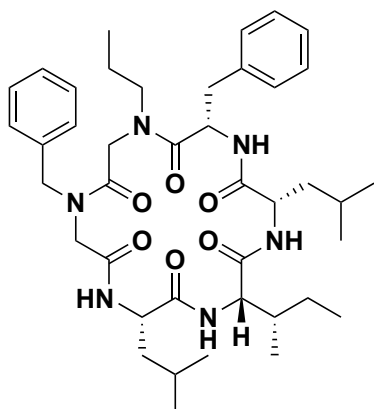




6EpDN (^1H NMR, 500 MHz, CDCl_3)



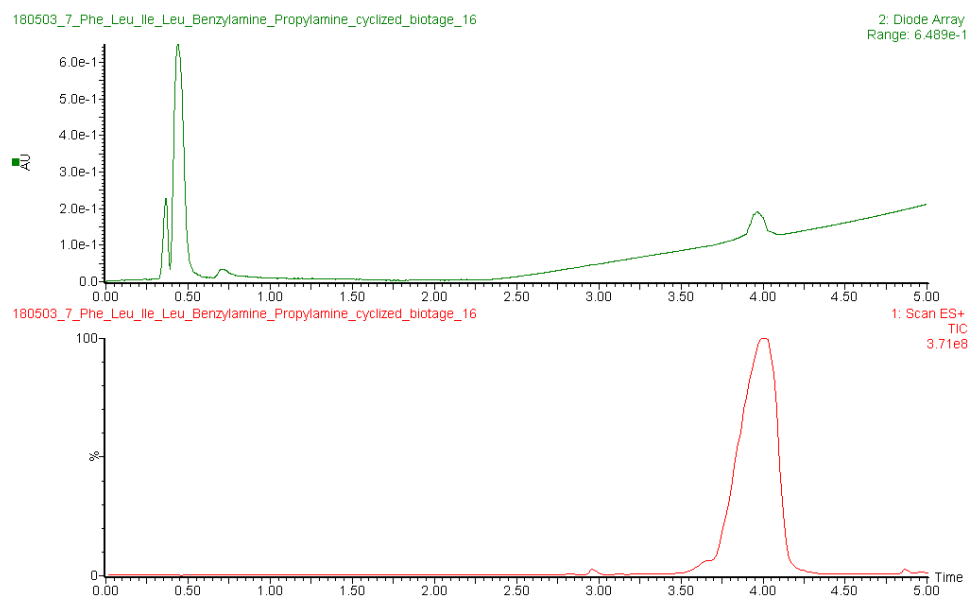
**7EpDN
PBLLLL**

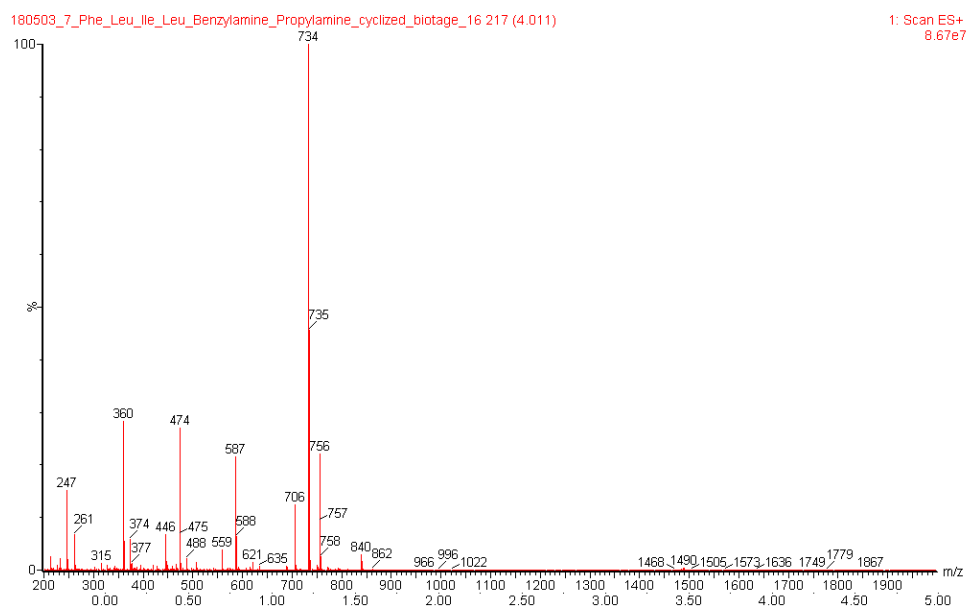


Exact Mass: 732.46
Molecular Weight: 732.97

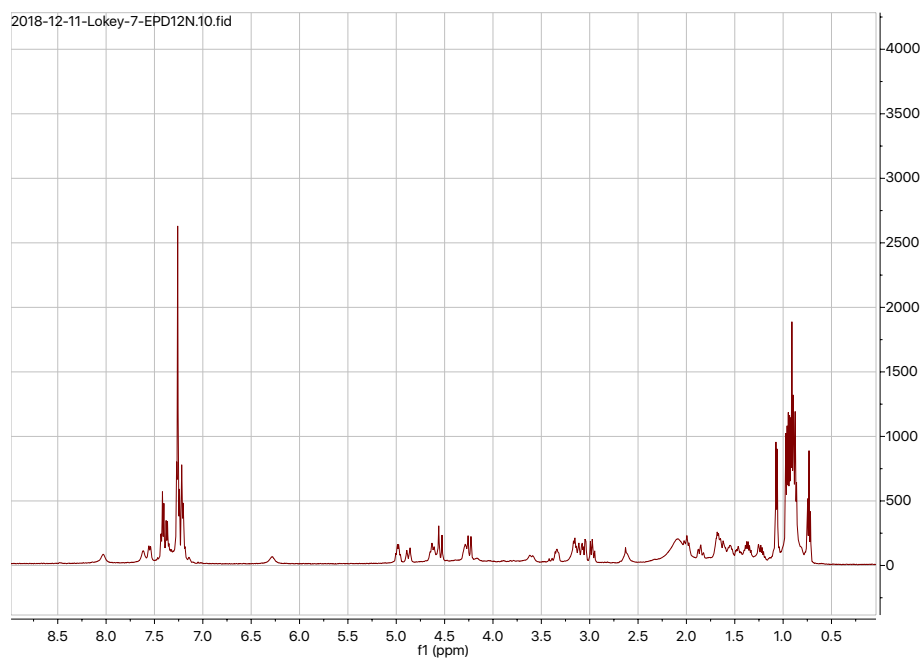
SMILES:

O=C([C@H](CC(C)C)NC([C@@]([C@@H](C)CC)([H])N1)=O)N[C@H](C(N(CC(N(CC2=CC=CC=C2)CC(N[C@@H](CC(C)C)C1=O)=O)=O)CCC)=O)CC3=CC=C=C=C3

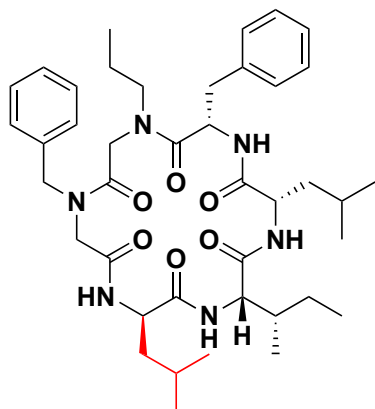




7EpDN (^1H NMR, 500 MHz, CDCl_3)



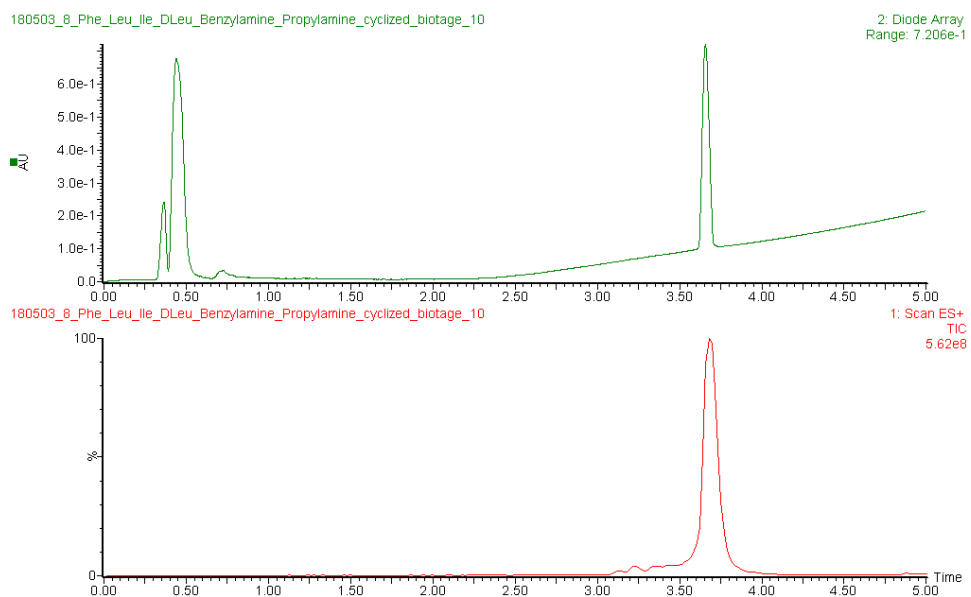
**8EpDN
PBDLLL**

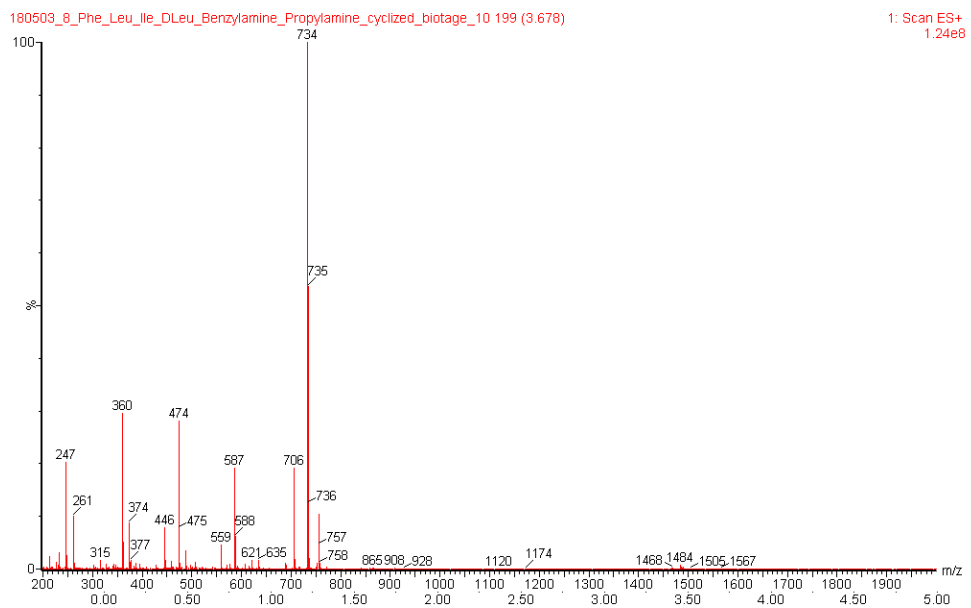


Exact Mass: 732.46
Molecular Weight: 732.97

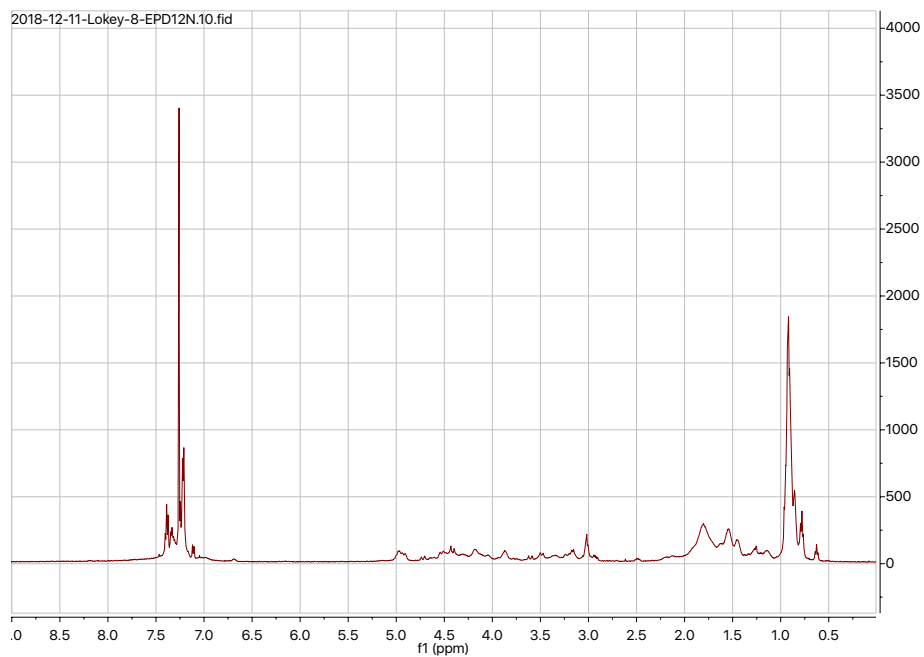
SMILES:

O=C([C@H](CC(C)C)NC([C@@]([C@@H](C)CC)([H])N1)=O)N[C@H](C(N(CC(N(CC2=CC=CC=C2)CC(N[C@H](CC(C)C)C1=O)=O)=O)CCC)=O)CC3=CC=CC=C3

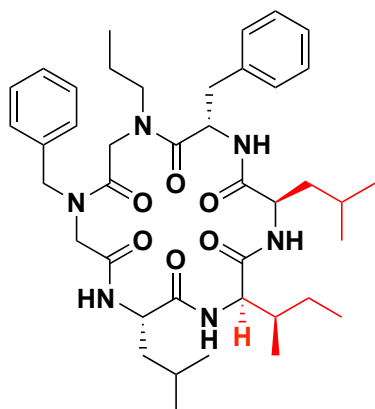




8EpDN (^1H NMR, 500 MHz, CDCl_3)



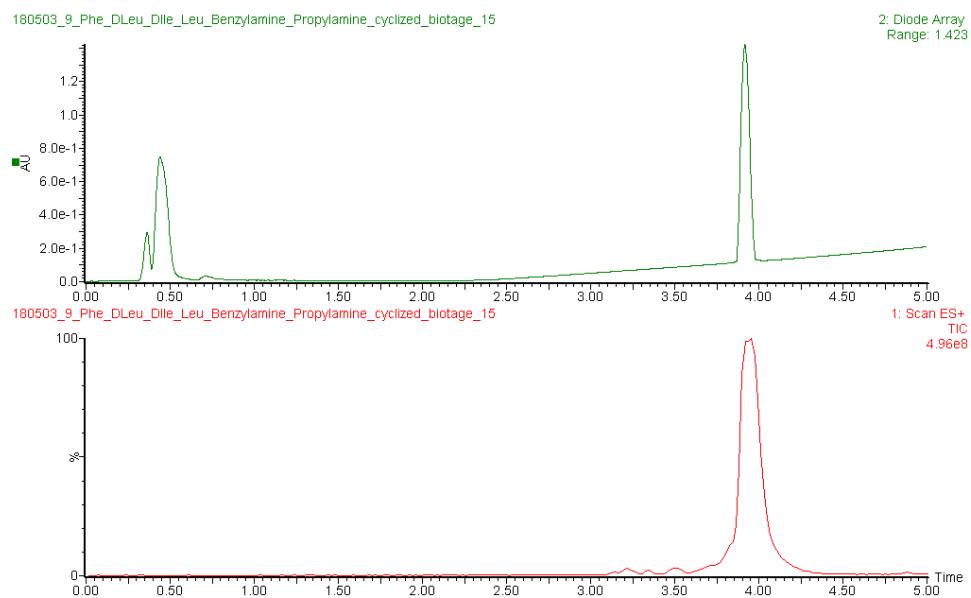
**9EpDN
PBLDDL**

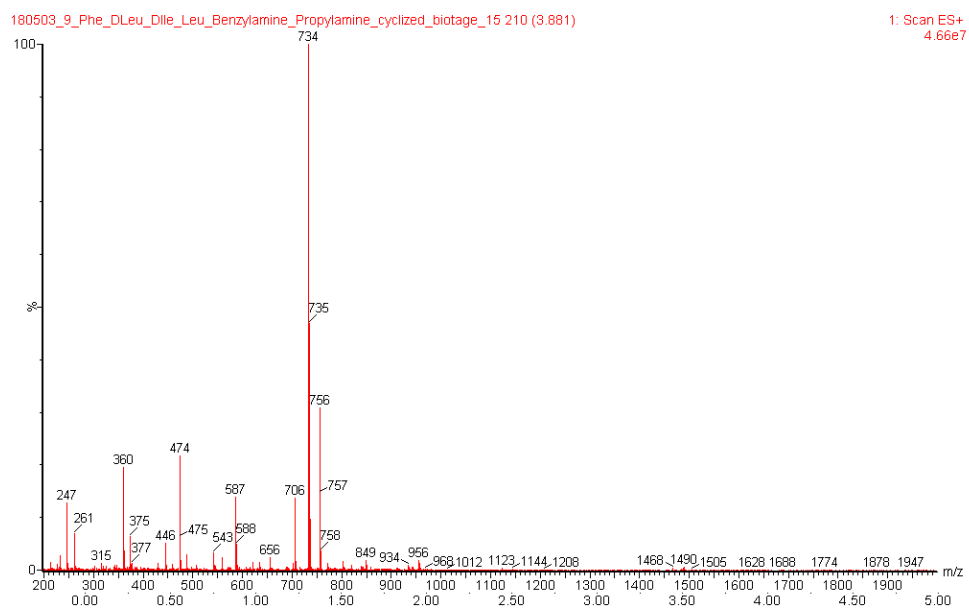


Exact Mass: 732.46
Molecular Weight: 732.97

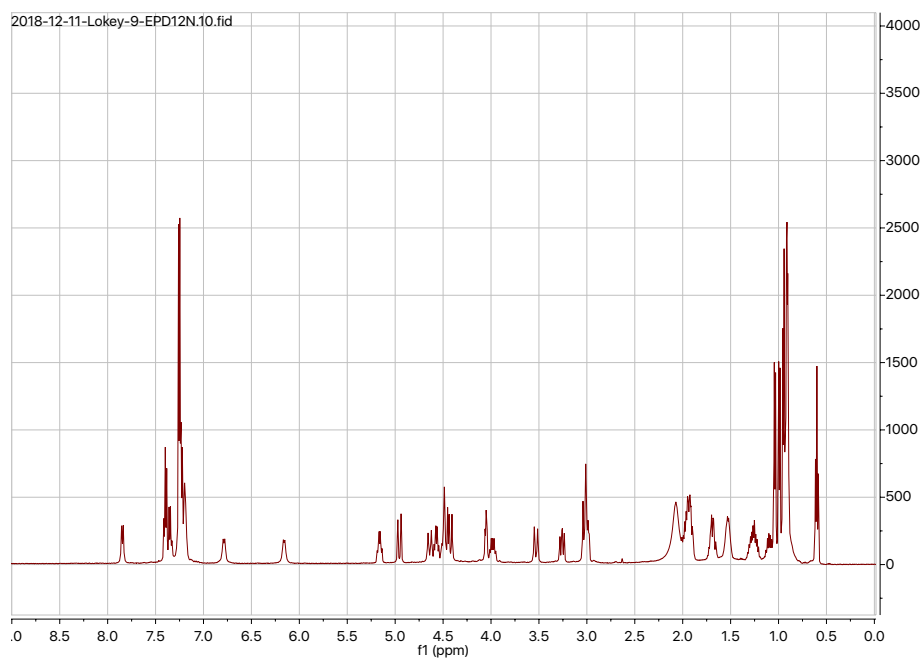
SMILES:

O=C([C@@H](CC(C)C)NC([C@]([C@H](C)CC)([H])N1)=O)N[C@H](C(N(CC(N(CC2=CC=CC=C2)CC(N[C@@H](CC(C)C)C1=O)=O)=O)CCC)=O)CC3=CC=CC=C3

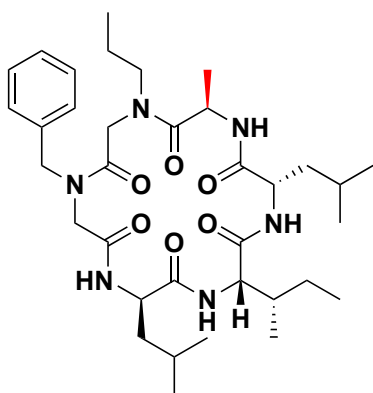




9EpDN (^1H NMR, 500 MHz, CDCl_3)



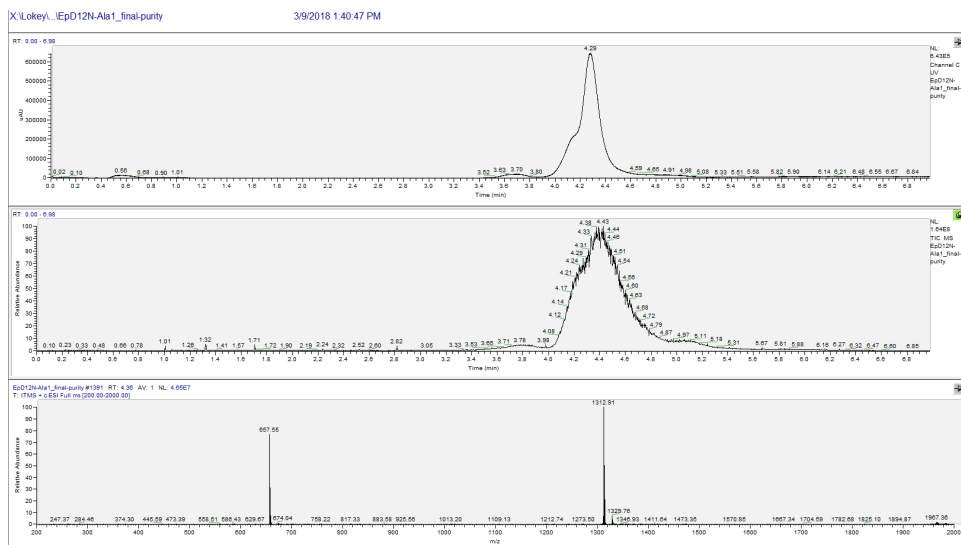
1EpDN 6A1a



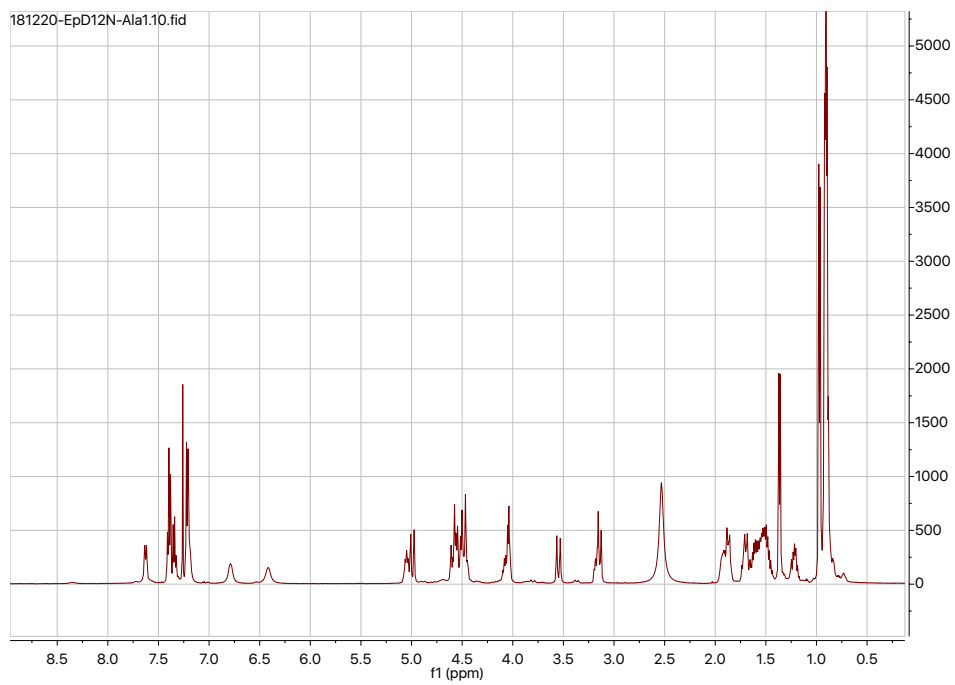
Exact Mass: 656.43
Molecular Weight: 656.87

SMILES:

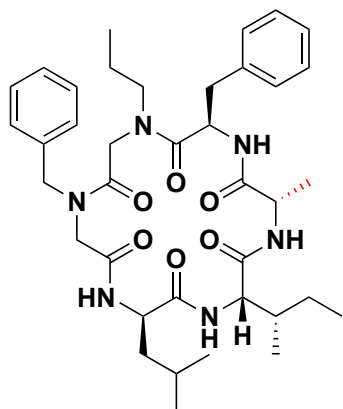
O=C([C@H](CC(C)C)NC([C@@]([C@@H](C)CC)([H])N1)=O)N[C@@H](C(N(C(C(N(CC2=CC=CC=C2)CC(N[C@H](CC(C)C)C1=O)=O)=O)CCC)=O)C



1EpDN 6Ala (^1H NMR, 500 MHz, CDCl_3)



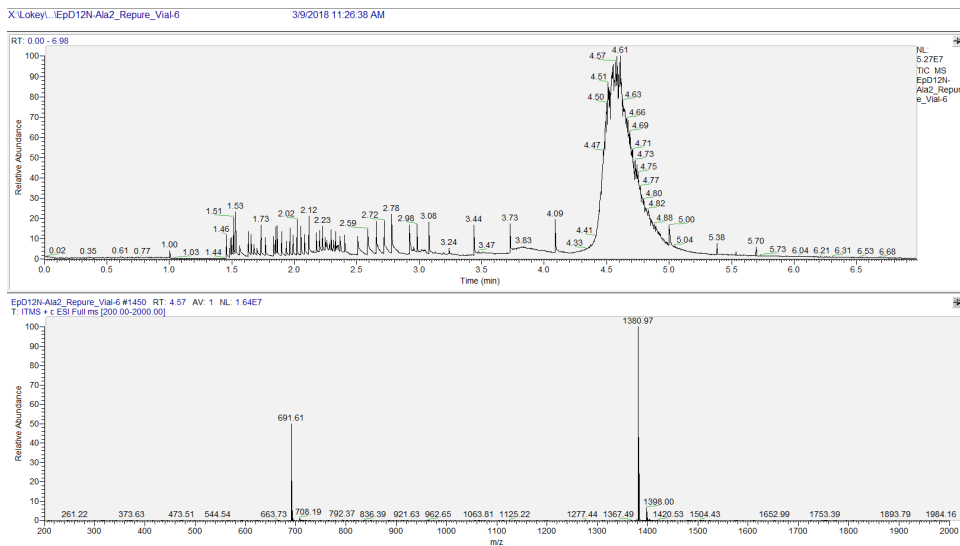
1EpDN 5A1a



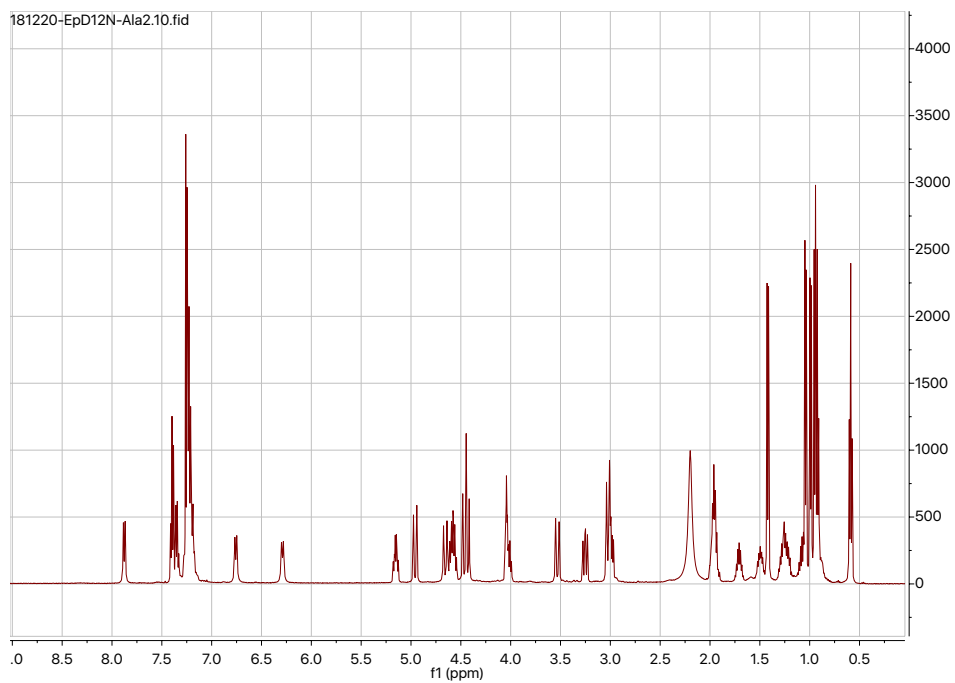
Exact Mass: 690.41
Molecular Weight: 690.89

SMILES:

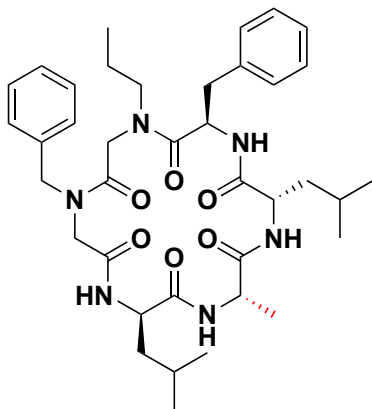
C[C@@H](C(N[C@@H](C(N(CC(N(CC1=CC=CC=C1)CC(N[C@H](CC(C)C)C2=O)=O)=O)CCC)=O)CC3=CC=CC=C3)=O)NC([C@@])([C@@H](C)CC)([H])N2=O



1EpDN 5Ala (^1H NMR, 500 MHz, CDCl_3)



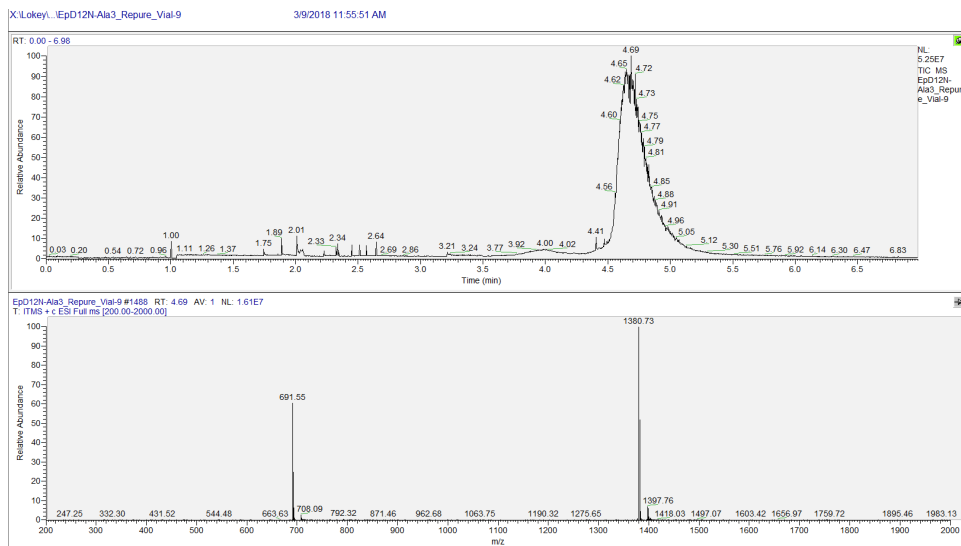
1EpDN 4A1a



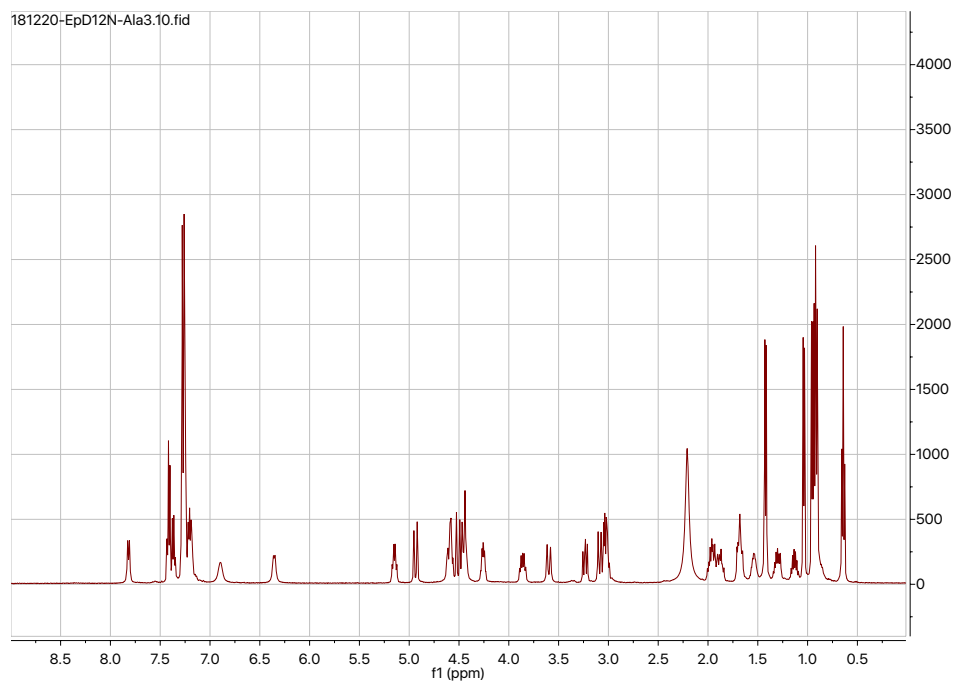
Exact Mass: 690.41
Molecular Weight: 690.89

SMILES:

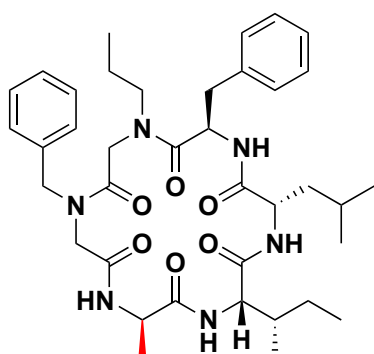
O=C([C@H](CC(C)C)NC([C@H](C)N1)=O)N[C@@H](C(N(CC(N(CC2=CC=CC=C2)CC(N[C@H](CC(C)C)C1=O)=O)=O)CCC)=O)CC3=CC=CC=C3



EpDN 4Ala (^1H NMR, 500 MHz, CDCl_3)



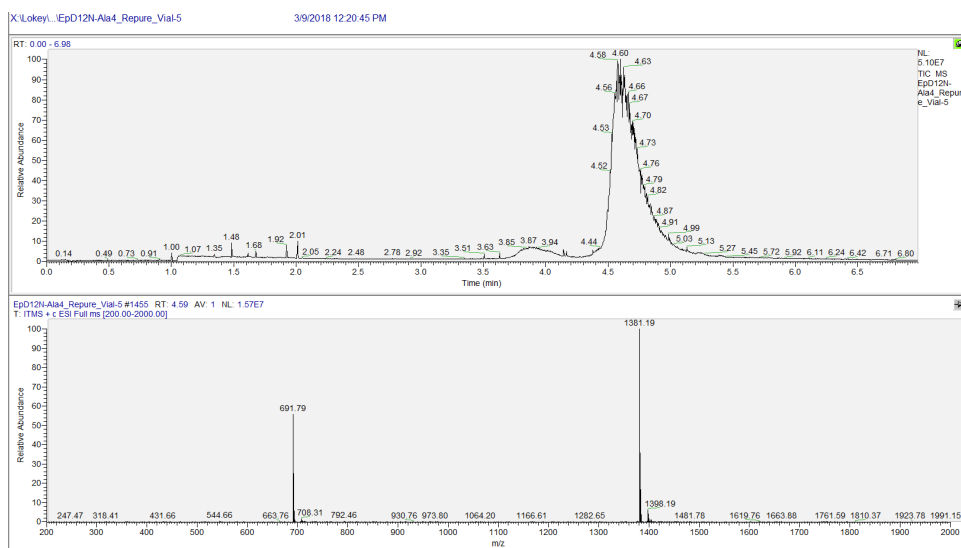
1EpDN 3Ala



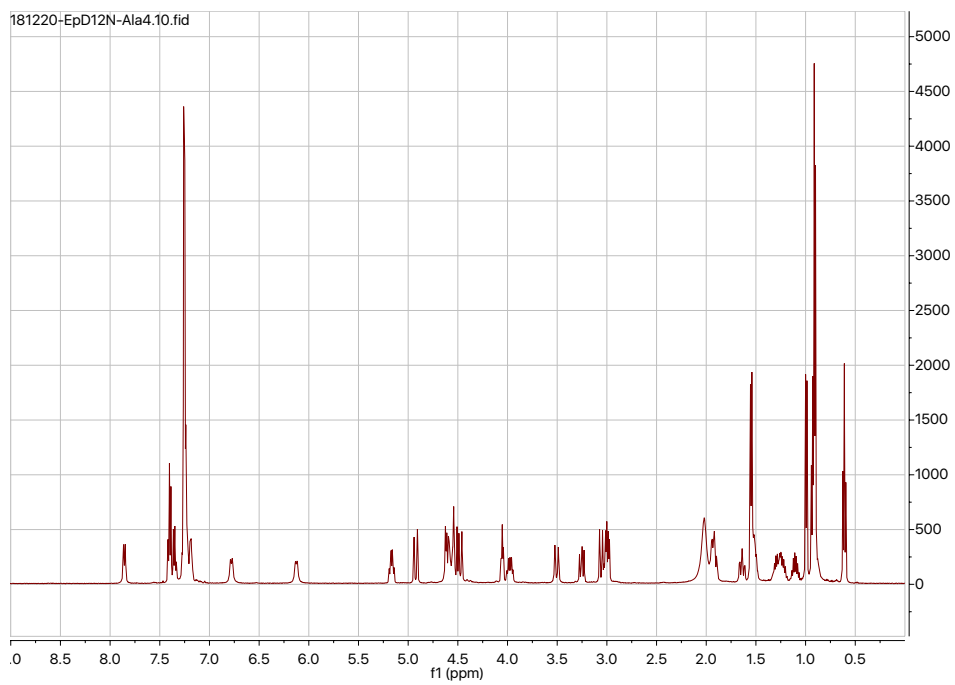
Exact Mass: 690.41
Molecular Weight: 690.89

SMILES:

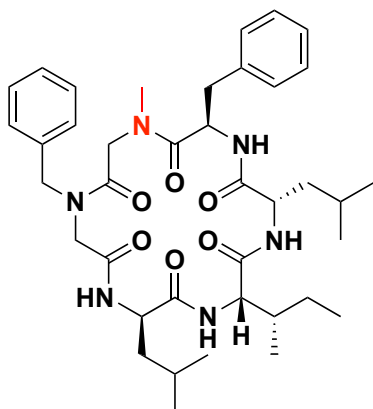
O=C([C@H](CC(C)C)NC([C@@]([C@@H](C)CC)([H])N1)=O)N[C@@H](C(N(C(C(N(CC2=CC=CC=C2)CC(N[C@H](C)C1=O)=O)=O)CCC)=O)CC3=CC=CC=C3



1EpDN 3Ala (^1H NMR, 500 MHz, CDCl_3)



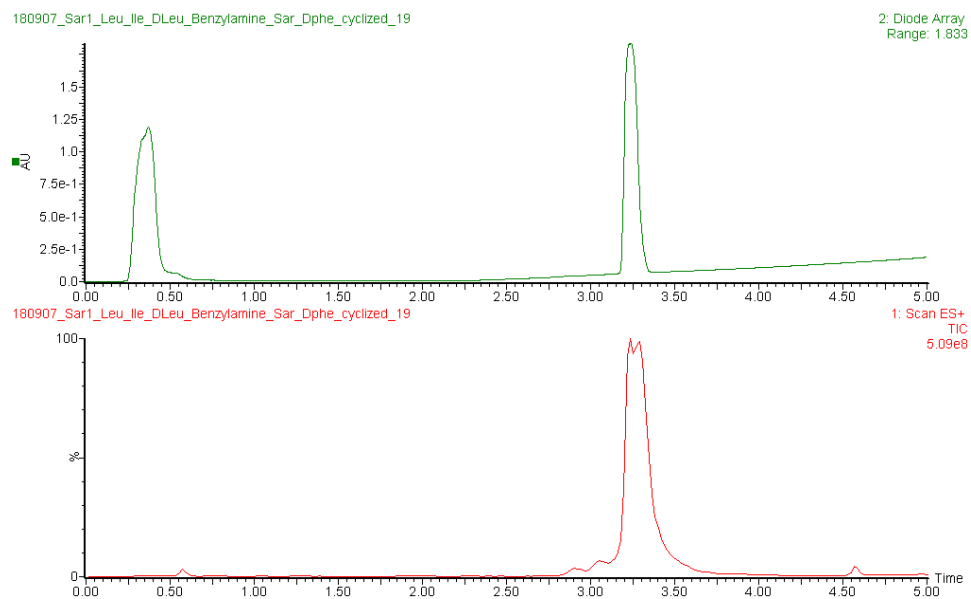
1EpDN 1Sar

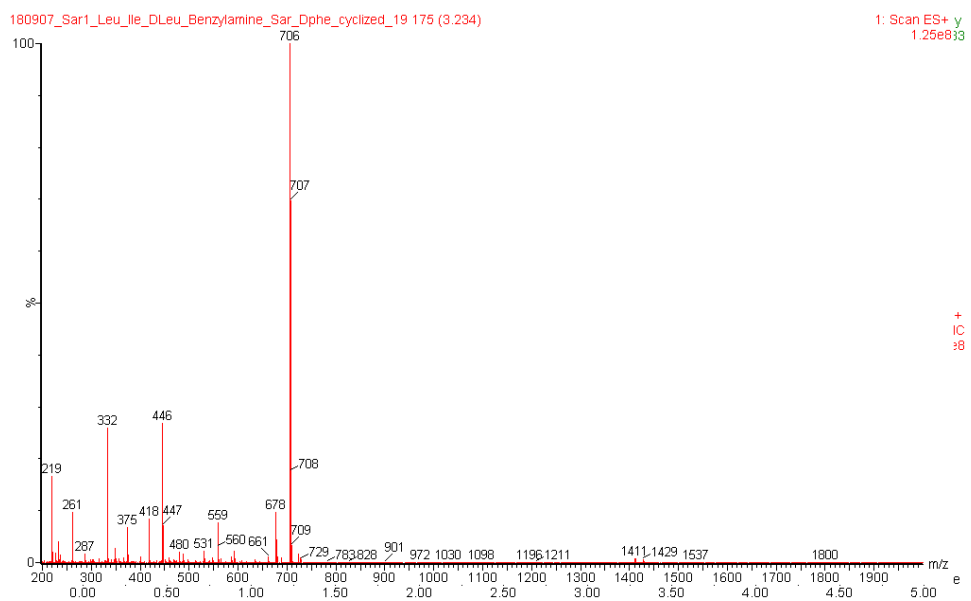


Exact Mass: 704.43
Molecular Weight: 704.91

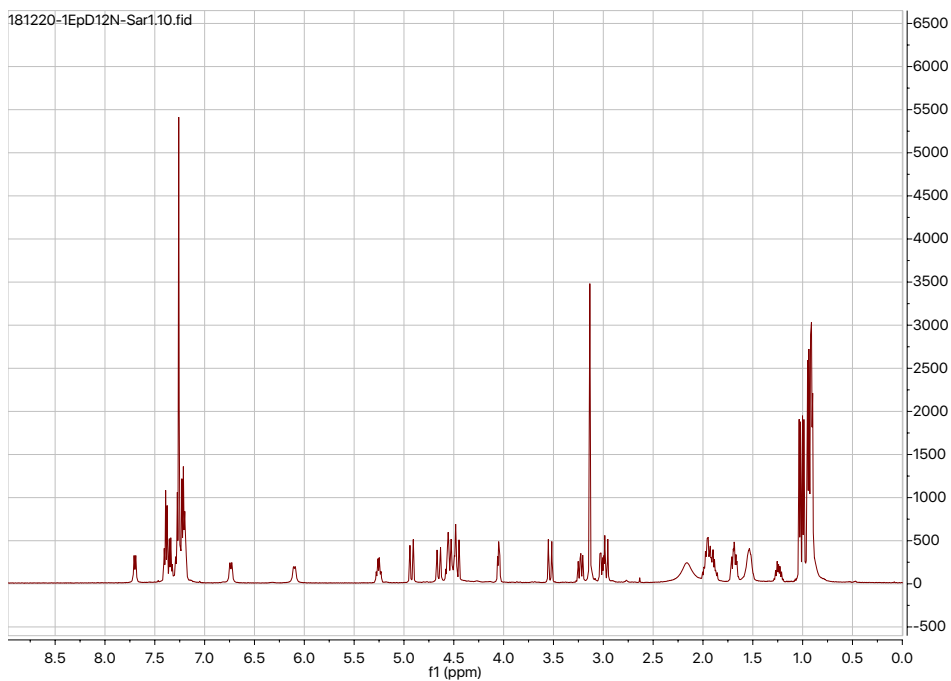
SMILES:

O=C([C@H](CC(C)C)NC([C@@]([C@@H](C)CC)([H])N1)=O)N[C@@H](C(N(C)C(N(CC2=CC=CC=C2)CC(N[C@H](CC(C)C)C1=O)=O)=O)C=O)CC3=CC=CC=C3

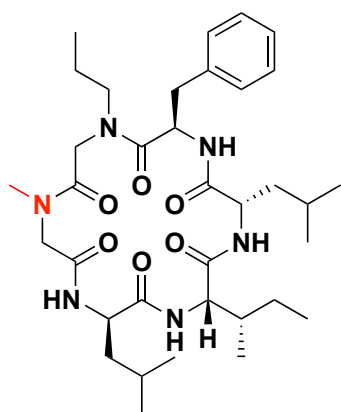




1EpDN 1Sar (^1H NMR, 500 MHz, CDCl_3)



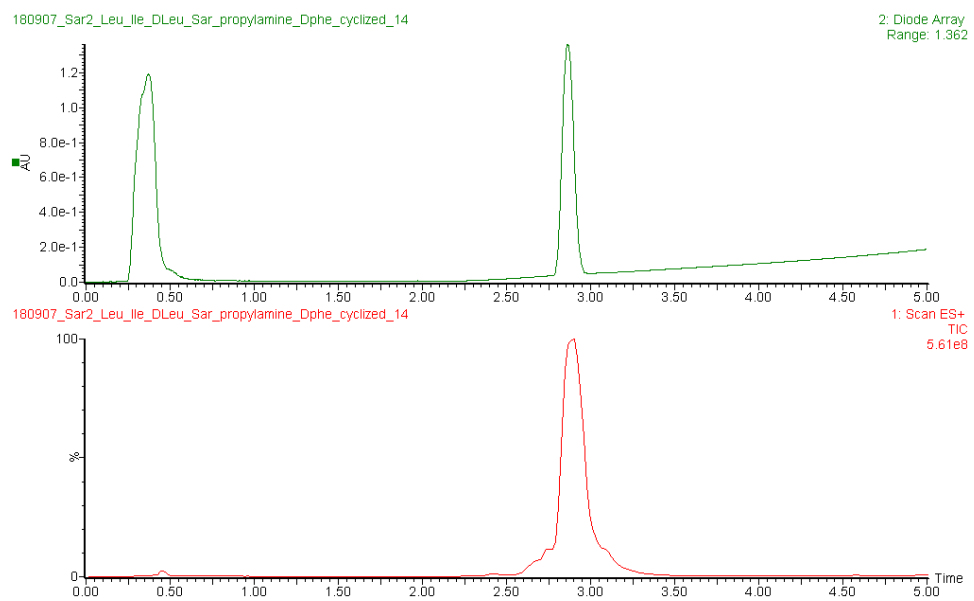
1EpDN 2Sar

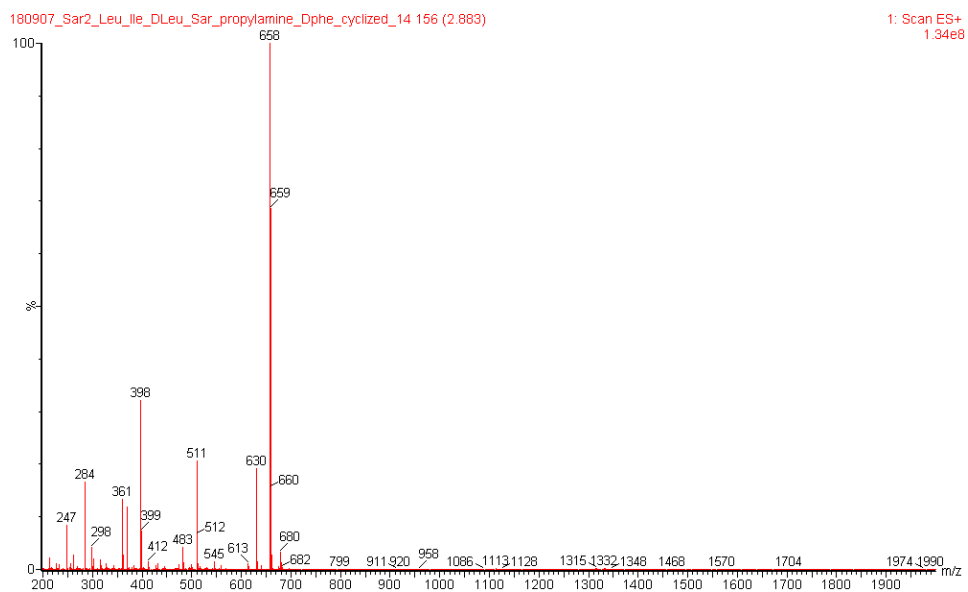


Exact Mass: 656.43
Molecular Weight: 656.87

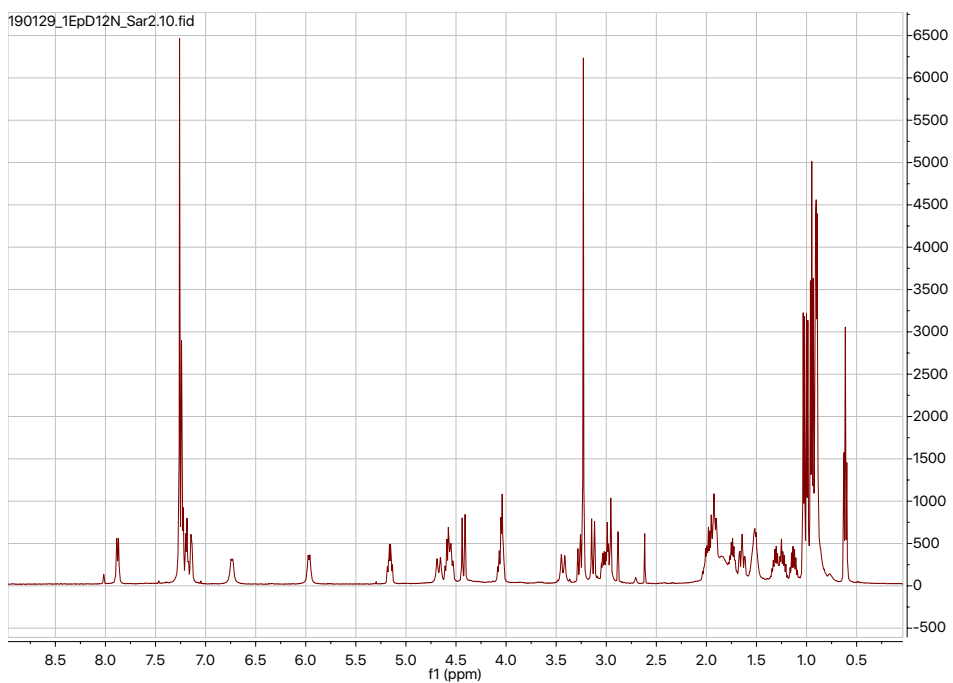
SMILES:

```
O=C([C@H](CC(C)C)NC([C@@]([C@@H](C)CC)([H])N1)=O)N[C@@H](C(N(C)C(N(C)CC(N[C@H](CC(C)C)C1=O)=O)=O)CCC)=O)CC2=CC=CC=C2
```

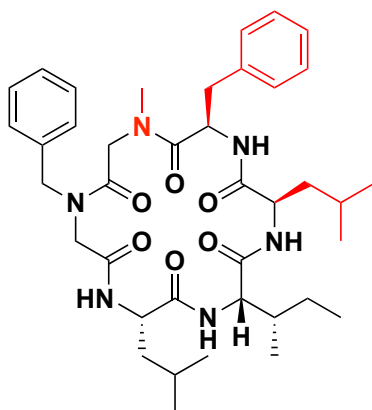




1EpDN 2Sar (^1H NMR, 500 MHz, CDCl_3)



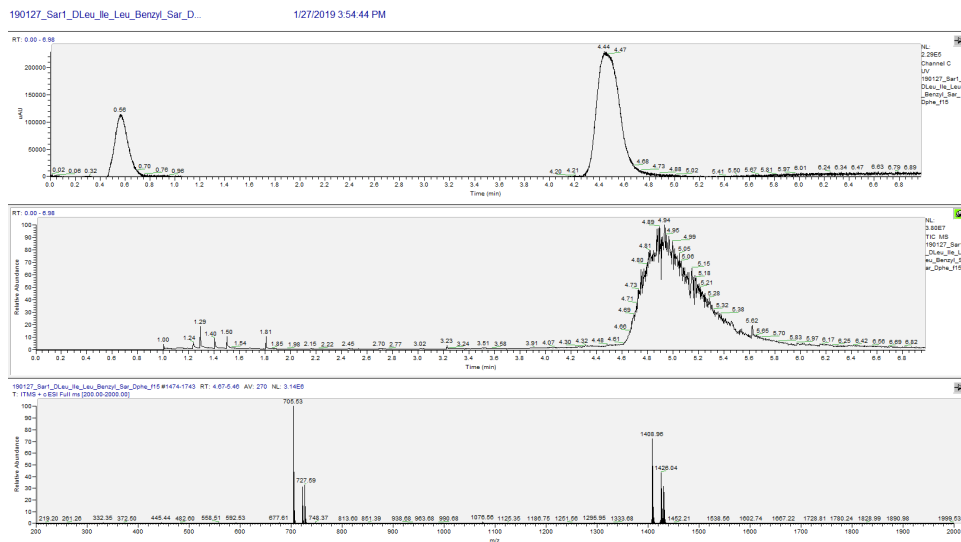
4EpDN 1Sar



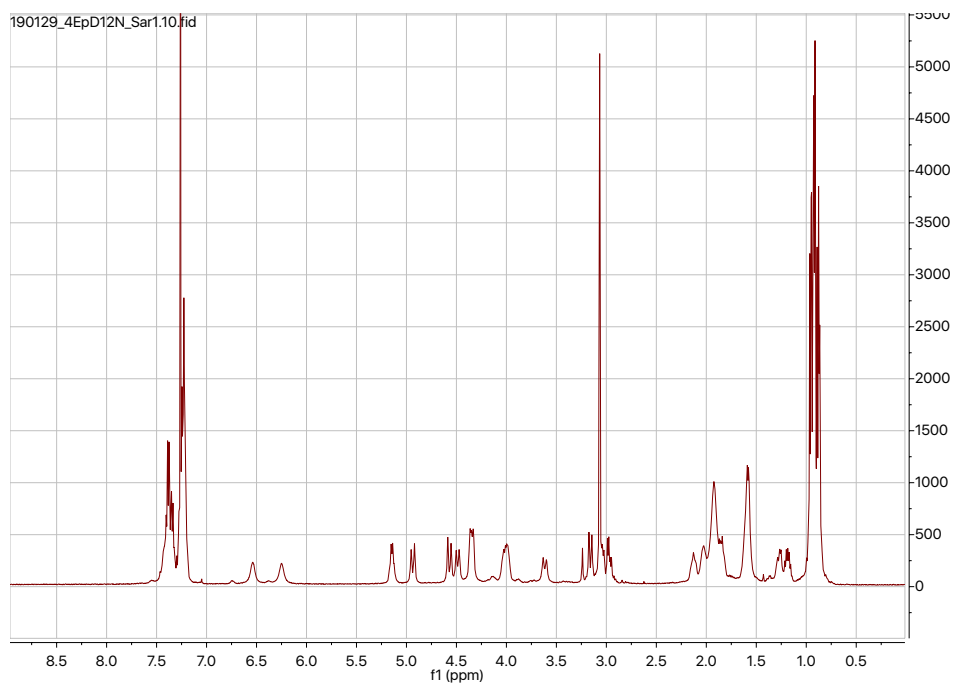
Exact Mass: 704.43
Molecular Weight: 704.91

SMILES:

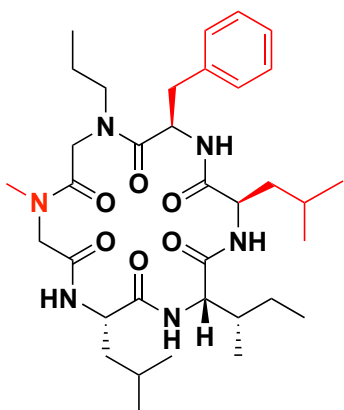
O=C([C@@H](CC(C)C)NC([C@@]([C@@H](C)CC)([H])N1)=O)N[C@@H](C(N(CC(N(CC2=CC=CC=C2)CC(N[C@@H](CC(C)C)C1=O)=O)=O)C)=O)CC3=CC=CC=C3



4EpDN 1Sar (^1H NMR, 500 MHz, CDCl_3)



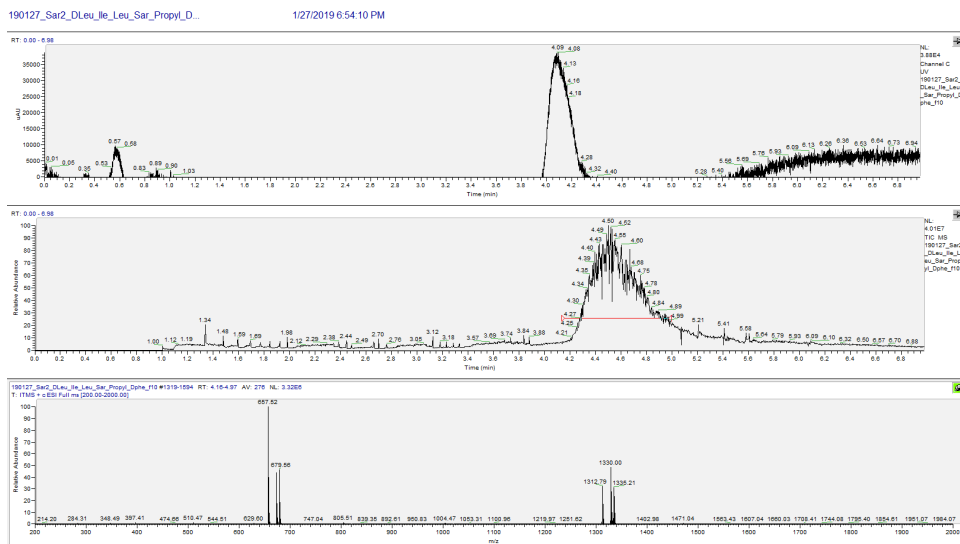
4EpDN 2Sar



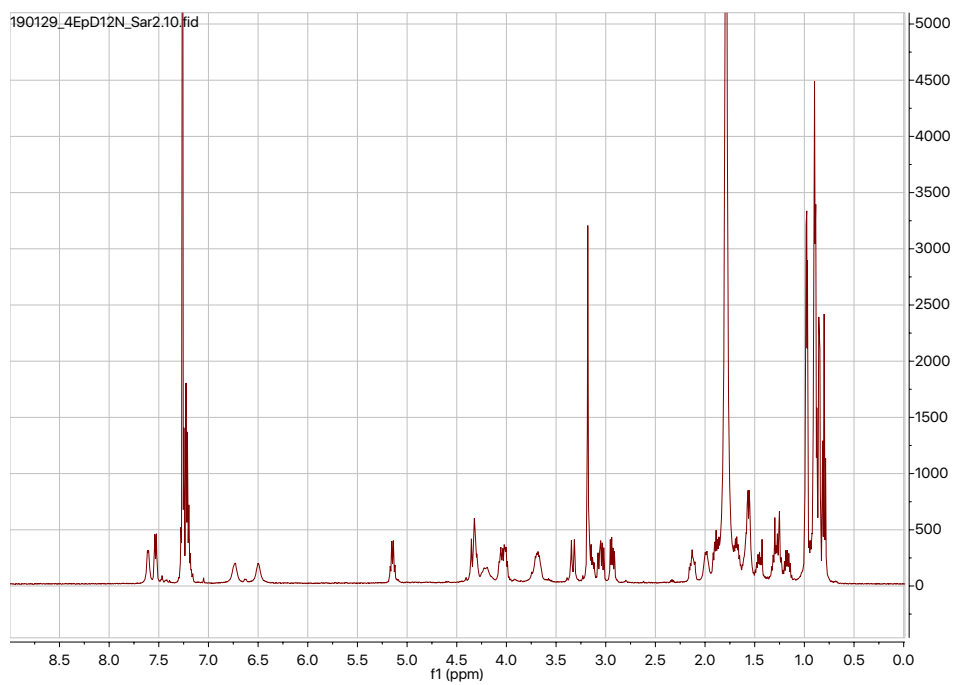
Exact Mass: 656.43
Molecular Weight: 656.87

SMILES:

O=C([C@@H](CC(C)C)NC([C@@]([C@@H](C)CC)([H])N1)=O)N[C@@H](C(N(C(C(N(C)CC(N[C@@H](CC(C)C)C1=O)=O)=O)CCC)=O)CC2=CC=CC=C2

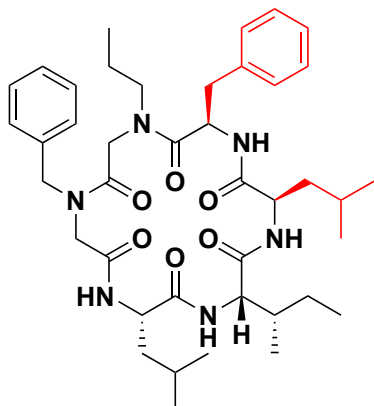


4EpDN 2Sar (¹H NMR, 500 MHz, CDCl₃)



Purity confirmed for samples sent to UCSF

4EpDN
PBLDD

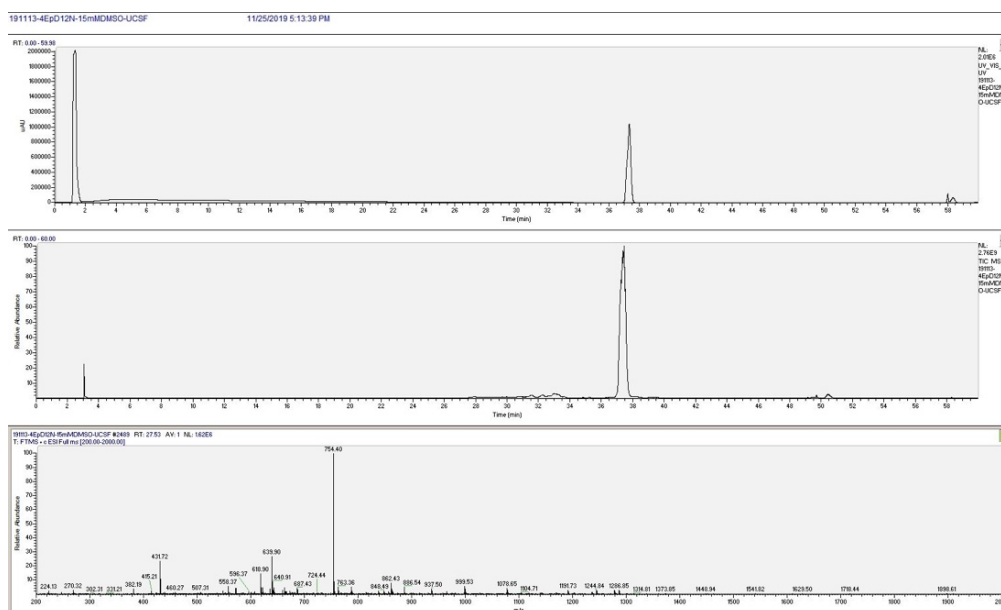


Exact Mass: 732.46
Molecular Weight: 732.97

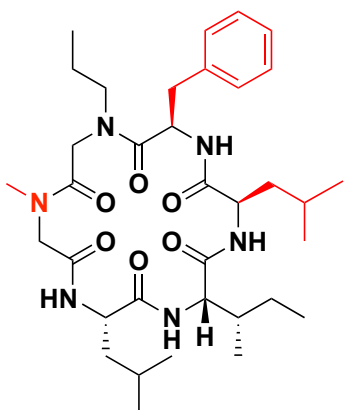
SMILES:

```
O=C([C@@H](CC(C)C)NC([C@@]([C@@H](C)CC)([H])N1=O)N[C@@H](C(N(CC(N(CC2=CC=CC=C2)CC(N[C@@H](CC(C)C)C1=O)=O)=O)CCC)=O)CC3=C  
C=CC=C3
```

30-100% acetonitrile gradient, long column, 1hr



4EpDN 2Sar

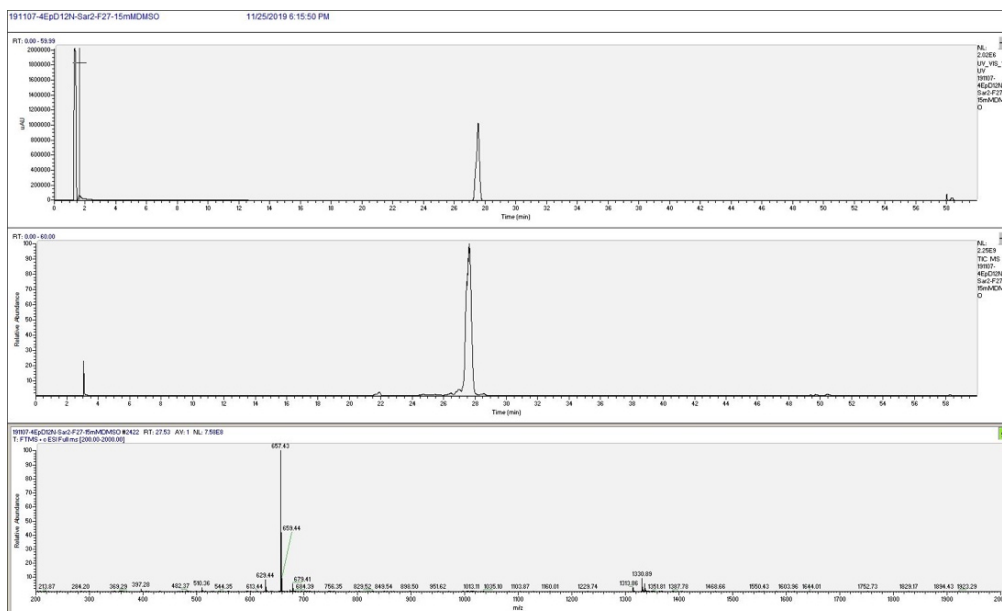


Exact Mass: 656.43
Molecular Weight: 656.87

SMILES:

```
O=C([C@@H](CC(C)C)NC([C@@])([C@@H](C)CC)([H])N1)=O)N[C@@H](C(N(CC(N(C)CC(N[C@@H](CC(C)C)C1=O)=O)=O)CCC)=O)CC2=CC=CC=C2
```

30-100% acetonitrile gradient, long column, 1hr



References

1. Santajit S, Indrawattana N. 2016. Mechanisms of Antimicrobial Resistance in ESKAPE Pathogens. *Biomed Res Int* 2016:2475067.
2. Ma YX, Wang CY, Li YY, Li J, Wan QQ, Chen JH, Tay FR, Niu LN. 2020. Considerations and Caveats in Combating ESKAPE Pathogens against Nosocomial Infections. *Adv Sci (Weinh)* 7:1901872.
3. Duncan MC, Linington RG, Auerbuch V. 2012. Chemical inhibitors of the type three secretion system: disarming bacterial pathogens. *Antimicrob Agents Chemother* 56:5433-41.
4. Calvert MB, Jumde VR, Titz A. 2018. Pathoblockers or antivirulence drugs as a new option for the treatment of bacterial infections. *Beilstein J Org Chem* 14:2607-2617.
5. Relman DA, Lipsitch M. 2018. Microbiome as a tool and a target in the effort to address antimicrobial resistance. *Proc Natl Acad Sci U S A* 115:12902- 12910.
6. Mohajeri MH, Brummer RJM, Rastall RA, Weersma RK, Harmsen HJM, Faas M, Eggersdorfer M. 2018. The role of the microbiome for human health: from basic science to clinical applications. *Eur J Nutr* 57:1-14.
7. Abby SS, Rocha EP. 2012. The non-flagellar type III secretion system evolved from the bacterial flagellum and diversified into host-cell adapted systems. *PLoS Genet* 8:e1002983.
8. Diepold A, Armitage JP. 2015. Type III secretion systems: the bacterial flagellum and the injectisome. *Philos Trans R Soc Lond B Biol Sci* 370.
9. Diepold A, Wagner S. 2014. Assembly of the bacterial type III secretion machinery. *FEMS Microbiol Rev* 38:802-22.
10. Fasciano AC, Shaban L, Mecsas J. 2019. Promises and Challenges of the Type Three Secretion System Injectisome as an Antivirulence Target. *EcoSal Plus* 8.
11. Tabor DE, Oganessian V, Keller AE, Yu L, McLaughlin RE, Song E, Warrenner P, Rosenthal K, Esser M, Qi Y, Ruzin A, Stover CK, DiGiandomenico A. 2018. *Pseudomonas aeruginosa* PcrV and Psl, the Molecular Targets of Bispecific Antibody MEDI3902, Are Conserved Among Diverse Global Clinical Isolates. *J Infect Dis* 218:1983-1994.

12. DiGiandomenico A, Keller AE, Gao C, Rainey GJ, Warrener P, Camara MM, Bonnell J, Fleming R, Bezabeh B, Dimasi N, Sellman BR, Hilliard J, Guenther CM, Datta V, Zhao W, Gao C, Yu XQ, Suzich JA, Stover CK. 2014. A multifunctional bispecific antibody protects against *Pseudomonas aeruginosa*. *Sci Transl Med* 6:262ra155.
13. Ha**cker G. 2018. *Biology of chlamydia*. Springer, Cham, Switzerland.
14. Lam H, Schwochert J, Lao Y, Lau T, Lloyd C, Luu J, Kooner O, Morgan J, Lokey S, Auerbuch V. 2017. Synthetic cyclic peptomers as type III secretion system inhibitors. *Antimicrob Agents Chemother* doi:10.1128/AAC.00060-17.
15. Gophna U, Ron EZ, Graur D. 2003. Bacterial type III secretion systems are ancient and evolved by multiple horizontal-transfer events. *Gene* 312:151-63.
16. Bent ZW, Branda SS, Young GM. 2013. The *Yersinia enterocolitica* Ysa type III secretion system is expressed during infections both in vitro and in vivo. *Microbiologyopen* 2:962-75.
17. Venecia K, Young GM. 2005. Environmental regulation and virulence attributes of the Ysa type III secretion system of *Yersinia enterocolitica* biovar 1B. *Infect Immun* 73:5961-77.
18. Young BM, Young GM. 2002. Evidence for targeting of Yop effectors by the chromosomally encoded Ysa type III secretion system of *Yersinia enterocolitica*. *J Bacteriol* 184:5563-71.
19. Hallstrom KN, McCormick BA. 2016. The type three secreted effector SipC regulates the trafficking of PERP during *Salmonella* infection. *Gut Microbes* 7:136-45.
20. Singh PK, Kapoor A, Lomash RM, Kumar K, Kamerkar SC, Pucadyil TJ, Mukhopadhyay A. 2018. *Salmonella* SipA mimics a cognate SNARE for host Syntaxin8 to promote fusion with early endosomes. *J Cell Biol* 217:4199-4214.
21. Lilic M, Galkin VE, Orlova A, VanLoock MS, Egelman EH, Stebbins CE. 2003. *Salmonella* SipA polymerizes actin by stapling filaments with nonglobular protein arms. *Science* 301:1918-21.
22. Deng W, Marshall NC, Rowland JL, McCoy JM, Worrall LJ, Santos AS, Strynadka NCJ, Finlay BB. 2017. Assembly, structure, function and regulation of type III secretion systems. *Nat Rev Microbiol* 15:323-337.

23. Diepold A, Amstutz M, Abel S, Sorg I, Jenal U, Cornelis GR. 2010. Deciphering the assembly of the *Yersinia* type III secretion injectisome. *EMBO J* 29:1928- 40.
24. Diepold A. 2019. Assembly and Post-assembly Turnover and Dynamics in the Type III Secretion System. *Curr Top Microbiol Immunol* doi:10.1007/82_2019_164.
25. Diepold A, Sezgin E, Huseyin M, Mortimer T, Eggeling C, Armitage JP. 2017. A dynamic and adaptive network of cytosolic interactions governs protein export by the T3SS injectisome. *Nat Commun* 8:15940.
26. Kudryashev M, Stenta M, Schmelz S, Amstutz M, Wiesand U, Castano-Diez D, Degiacomi MT, Munnich S, Bleck CK, Kowal J, Diepold A, Heinz DW, Dal Peraro M, Cornelis GR, Stahlberg H. 2013. In situ structural analysis of the *Yersinia enterocolitica* injectisome. *Elife* 2:e00792. Ha UH, Wang Y, Jin S. 2003. DsbA of *Pseudomonas aeruginosa* is essential for multiple virulence factors. *Infect Immun* 71:1590-5.
27. Bowlin NO, Williams JD, Knoten CA, Torhan MC, Tashjian TF, Li B, Aiello D, Meccas J, Hauser AR, Peet NP, Bowlin TL, Moir DT. 2014. Mutations in the *Pseudomonas aeruginosa* needle protein gene *pscF* confer resistance to phenoxyacetamide inhibitors of the type III secretion system. *Antimicrob Agents Chemother* 58:2211-20.
28. Rietsch A, Vallet-Gely I, Dove SL, Mekalanos JJ. 2005. ExsE, a secreted regulator of type III secretion genes in *Pseudomonas aeruginosa*. *Proc Natl Acad Sci U S A* 102:8006-11.
29. Green ER, Meccas J. 2016. Bacterial Secretion Systems: An Overview. *Microbiol Spectr* 4.
30. Avican U, Doruk T, Ostberg Y, Fahlgren A, Forsberg A. 2017. The Tat Substrate *SufI* Is Critical for the Ability of *Yersinia pseudotuberculosis* To Cause Systemic Infection. *Infect Immun* 85.
31. Bageshwar UK, VerPlank L, Baker D, Dong W, Hamsanathan S, Whitaker N, Sacchetti JC, Musser SM. 2016. High Throughput Screen for *Escherichia coli* Twin Arginine Translocation (Tat) Inhibitors. *PLoS One* 11:e0149659.
32. Muschiol S, Bailey L, Gylfe A, Sundin C, Hultenby K, Bergstrom S, Elofsson M, Wolf-Watz H, Normark S, Henriques-Normark B. 2006. A small-molecule inhibitor of type III secretion inhibits different stages of the infectious cycle of *Chlamydia trachomatis*. *Proc Natl Acad Sci U S A* 103:14566-71.

33. Lee PC, Rietsch A. 2015. Fueling type III secretion. *Trends Microbiol* 23:296- 300.
34. Paul K, Erhardt M, Hirano T, Blair DF, Hughes KT. 2008. Energy source of flagellar type III secretion. *Nature* 451:489-92.
35. Lee PA, Tullman-Ercek D, Georgiou G. 2006. The bacterial twin-arginine translocation pathway. *Annu Rev Microbiol* 60:373-95.
36. Troisfontaines P, Cornelis GR. 2005. Type III secretion: More systems than you think. *Physiology* 20:326-339.
37. Auvray F, Ozin AJ, Claret L, Hughes C. 2002. Intrinsic membrane targeting of the flagellar export ATPase FliI: interaction with acidic phospholipids and FliH. *J Mol Biol* 318:941-50.
38. Wagner S, Grin I, Malmshaimer S, Singh N, Torres-Vargas CE, Westerhausen S. 2018. Bacterial type III secretion systems: a complex device for the delivery of bacterial effector proteins into eukaryotic host cells. *FEMS Microbiol Lett* 365.
39. McCaw ML, Lykken GL, Singh PK, Yahr TL. 2002. ExsD is a negative regulator of the *Pseudomonas aeruginosa* type III secretion regulon. *Molecular Microbiology* 46:1123-1133.
40. Urbanowski ML, Lykken GL, Yahr TL. 2005. A secreted regulatory protein couples transcription to the secretory activity of the *Pseudomonas aeruginosa* type III secretion system. *Proceedings of the National Academy of Sciences of the United States of America* 102:9930-9935.
41. Elwell C, Mirrashidi K, Engel J. 2016. Chlamydia cell biology and pathogenesis. *Nat Rev Microbiol* 14:385-400. Al-Zeer MA, Al-Younes HM, Kerr M, Abu-Lubad M, Gonzalez E, Brinkmann V, Meyer TF. 2014. Chlamydia trachomatis remodels stable microtubules to coordinate Golgi stack recruitment to the chlamydial inclusion surface. *Mol Microbiol* 94:1285-97.
42. Derre I. 2015. Chlamydiae interaction with the endoplasmic reticulum: contact, function and consequences. *Cell Microbiol* 17:959-66.
43. Kumar Y, Valdivia RH. 2008. Actin and intermediate filaments stabilize the Chlamydia trachomatis vacuole by forming dynamic structural scaffolds. *Cell Host Microbe* 4:159-69.

44. Klockner A, Buhl H, Viollier P, Henrichfreise B. 2018. Deconstructing the Chlamydial Cell Wall. *Curr Top Microbiol Immunol* 412:1-33.
45. Miller KE. 2006. Diagnosis and treatment of Chlamydia trachomatis infection. *Am Fam Physician* 73:1411-6.
46. Phillips S, Quigley BL, Timms P. 2019. Seventy Years of Chlamydia Vaccine Research - Limitations of the Past and Directions for the Future. *Front Microbiol* 10:70.
47. Krupp K, Madhivanan P. 2015. Antibiotic resistance in prevalent bacterial and protozoan sexually transmitted infections. *Indian J Sex Transm Dis AIDS* 36:3-8.
48. Young BM, Young GM. 2002. YplA is exported by the Ysc, Ysa, and flagellar type III secretion systems of *Yersinia enterocolitica*. *J Bacteriol* 184:1324-34.
49. Woehrmann MH, Bray WM, Durbin JK, Nisam SC, Michael AK, Glassey E, Stuart JM, Lokey RS. 2013. Large-scale cytological profiling for functional analysis of bioactive compounds. *Mol Biosyst* 9:2604-17.
50. Ronald N. Zuckermann JMK, Stephen B. H. Kent and Walter H. Moos. 1992. Efficient method for the preparation of peptoids [oligo(N-substituted glycines)] by submonomer solid-phase synthesis. *Journal of the American Chemical Society* 114:2.
51. Aiello D, Williams JD, Majgier-Baranowska H, Patel I, Peet NP, Huang J, Lory S, Bowlin TL, Moir DT. 2010. Discovery and characterization of inhibitors of *Pseudomonas aeruginosa* type III secretion. *Antimicrob Agents Chemother* 54:1988-99.
52. Kim OK, Garrity-Ryan LK, Bartlett VJ, Grier MC, Verma AK, Medjanis G, Donatelli JE, Macone AB, Tanaka SK, Levy SB, Alekshun MN. 2009. N-Hydroxybenzimidazole Inhibitors of the Transcription Factor LcrF in *Yersinia*: Novel Antivirulence Agents. *Journal of Medicinal Chemistry* 52:5626-5634.
53. Enquist PA, Gylfe A, Hagglund U, Lindstrom P, Norberg-Scherman H, Sundin C, Elofsson M. 2012. Derivatives of 8-hydroxyquinoline--antibacterial agents that target intra- and extracellular Gram-negative pathogens. *Bioorg Med Chem Lett* 22:3550-3.

54. Anantharajah A, Buyck JM, Sundin C, Tulkens PM, Mingeot-Leclercq MP, Van Bambeke F. 2017. Salicylidene Acylhydrazides and Hydroxyquinolines Act as Inhibitors of Type Three Secretion Systems in *Pseudomonas aeruginosa* by Distinct Mechanisms. *Antimicrob Agents Chemother* 61. Anantharajah A, Faure E, Buyck JM, Sundin C, Lindmark T, Mecsas J, Yahr TL, Tulkens PM, Mingeot-Leclercq MP, Guery B, Van Bambeke F. 2016. Inhibition of the Injectisome and Flagellar Type III Secretion Systems by INP1855 Impairs *Pseudomonas aeruginosa* Pathogenicity and Inflammasome Activation. *J Infect Dis* 214:1105-16.
55. Slepentin A, Enquist PA, Hagglund U, de la Maza LM, Elofsson M, Peterson EM. 2007. Reversal of the antichlamydial activity of putative type III secretion inhibitors by iron. *Infect Immun* 75:3478-89.
56. Layton AN, Hudson DL, Thompson A, Hinton JC, Stevens JM, Galyov EE, Stevens MP. 2010. Salicylidene acylhydrazide-mediated inhibition of type III secretion system-1 in *Salmonella enterica* serovar Typhimurium is associated with iron restriction and can be reversed by free iron. *FEMS Microbiol Lett* 302:114-22.
57. Hudson DL, Layton AN, Field TR, Bowen AJ, Wolf-Watz H, Elofsson M, Stevens MP, Galyov EE. 2007. Inhibition of type III secretion in *Salmonella enterica* serovar Typhimurium by small-molecule inhibitors. *Antimicrob Agents Chemother* 51:2631-5.
58. Morgan JM, Lam HN, Delgado J, Luu J, Mohammadi S, Isberg RR, Wang H, Auerbuch V. 2018. An Experimental Pipeline for Initial Characterization of Bacterial Type III Secretion System Inhibitor Mode of Action Using Enteropathogenic *Yersinia*. *Front Cell Infect Microbiol* 8:404.
59. Kauppi AM, Nordfelth R, Uvell H, Wolf-Watz H, Elofsson M. 2003. Targeting bacterial virulence: inhibitors of type III secretion in *Yersinia*. *Chem Biol* 10:241-9.
60. Wang D, Zetterstrom CE, Gabrielsen M, Beckham KS, Tree JJ, Macdonald SE, Byron O, Mitchell TJ, Gally DL, Herzyk P, Mahajan A, Uvell H, Burchmore R, Smith BO, Elofsson M, Roe AJ. 2011. Identification of bacterial target proteins for the salicylidene acylhydrazide class of virulence-blocking compounds. *J Biol Chem* 286:29922-31.
61. Nordfelth R, Kauppi AM, Norberg HA, Wolf-Watz H, Elofsson M. 2005. Small- molecule inhibitors specifically targeting type III secretion. *Infect Immun* 73:3104-14.

62. Tree JJ, Wang D, McNally C, Mahajan A, Layton A, Houghton I, Elofsson M, Stevens MP, Gally DL, Roe AJ. 2009. Characterization of the effects of salicylidene acylhydrazide compounds on type III secretion in *Escherichia coli* O157:H7. *Infect Immun* 77:4209-20.
63. Zambelloni R, Connolly JPR, Huerta Uribe A, Burgess K, Marquez R, Roe AJ. 2017. Novel compounds targeting the enterohemorrhagic *Escherichia coli* type three secretion system reveal insights into mechanisms of secretion inhibition. *Mol Microbiol* 105:606-619.
64. Yang F, Korban SS, Pusey PL, Elofsson M, Sundin GW, Zhao Y. 2014. Small-molecule inhibitors suppress the expression of both type III secretion and amylovoran biosynthesis genes in *Erwinia amylovora*. *Mol Plant Pathol* 15:44-57.
65. Harmon DE, Davis AJ, Castillo C, Mecsas J. 2010. Identification and characterization of small-molecule inhibitors of Yop translocation in *Yersinia pseudotuberculosis*. *Antimicrob Agents Chemother* 54:3241-54.
66. Jessen DL, Bradley DS, Nilles ML. 2014. A type III secretion system inhibitor targets YopD while revealing differential regulation of secretion in calcium-blind mutants of *Yersinia pestis*. *Antimicrob Agents Chemother* 58:839-50.
67. Gauthier A, Robertson ML, Lowden M, Ibarra JA, Puente JL, Finlay BB. 2005. Transcriptional inhibitor of virulence factors in enteropathogenic *Escherichia coli*. *Antimicrob Agents Chemother* 49:4101-9.
68. Duncan MC, Wong WR, Dupzyk AJ, Bray WM, Linington RG, Auerbuch V. 2014. An NF-kappaB-based high-throughput screen identifies piericidins as inhibitors of the *Yersinia pseudotuberculosis* type III secretion system. *Antimicrob Agents Chemother* 58:1118-26.
69. Grishin AV, Luyksaar SI, Kapotina LN, Kirsanov DD, Zayakin ES, Karyagina AS, Zigangirova NA. 2018. Identification of chlamydial T3SS inhibitors through virtual screening against T3SS ATPase. *Chem Biol Drug Des* 91:717-727.
70. Hao H, Aixia Y, Lei F, Nancai Y, Wen S. 2010. Effects of baicalin on *Chlamydia trachomatis* infection in vitro. *Planta Med* 76:76-8.
71. Tsou LK, Lara-Tejero M, RoseFigura J, Zhang ZJ, Wang YC, Yount JS, Lefebre M, Dossa PD, Kato J, Guan F, Lam W, Cheng YC, Galan JE, Hang HC. 2016. Antibacterial Flavonoids from Medicinal Plants Covalently Inactivate Type III Protein Secretion Substrates. *J Am Chem Soc* 138:2209-18.

72. Guo Z, Li X, Li J, Yang X, Zhou Y, Lu C, Shen Y. 2016. Licoflavonol is an inhibitor of the type three secretion system of *Salmonella enterica* serovar Typhimurium. *Biochem Biophys Res Commun* 477:998-1004.
73. Nakasone N, Higa N, Toma C, Ogura Y, Suzuki T, Yamashiro T. 2017. Epigallocatechin gallate inhibits the type III secretion system of Gram-negative enteropathogenic bacteria under model conditions. *FEMS Microbiol Lett* 364.
74. Zhang Y, Liu Y, Wang T, Deng X, Chu X. 2018. Natural compound sanguinarine chloride targets the type III secretion system of *Salmonella enterica* Serovar Typhimurium. *Biochem Biophys Rep* 14:149-154.
75. Choi WS, Lee TH, Son SJ, Kim TG, Kwon BM, Son HU, Kim SU, Lee SH. 2017. Inhibitory effect of obovatol from *Magnolia obovata* on the *Salmonella* type III secretion system. *J Antibiot (Tokyo)* 70:1065-1069.
76. Zhang Y, Liu Y, Qiu J, Luo ZQ, Deng X. 2018. The Herbal Compound Thymol Protects Mice From Lethal Infection by *Salmonella* Typhimurium. *Front Microbiol* 9:1022.
77. Felise HB, Nguyen HV, Pfuetzner RA, Barry KC, Jackson SR, Blanc MP, Bronstein PA, Kline T, Miller SI. 2008. An inhibitor of gram-negative bacterial virulence protein secretion. *Cell Host Microbe* 4:325-36.
78. Bzdzion L, Krezel H, Wrzeszcz K, Grzegorek I, Nowinska K, Chodaczek G, Swietnicki W. 2017. Design of small molecule inhibitors of type III secretion system ATPase EscN from enteropathogenic *Escherichia coli*. *Acta Biochim Pol* 64:49-63.
79. Nesterenko LN, Zigangirova NA, Zayakin ES, Luyksaar SI, Kobets NV, Balunets DV, Shabalina LA, Bolshakova TN, Dobrynina OY, Gintsburg AL. 2016. A small-molecule compound belonging to a class of 2,4-disubstituted 1,3,4- thiadiazine-5-ones suppresses *Salmonella* infection in vivo. *J Antibiot (Tokyo)* 69:422-7.
80. Zigangirova NA, Kost EA, Didenko LV, Kapotina LN, Zayakin ES, Luyksaar SI, Morgunova EY, Fedina ED, Artyukhova OA, Samorodov AV, Kobets NV. 2016. A small-molecule compound belonging to a class of 2,4-disubstituted 1,3,4- thiadiazine-5-ones inhibits intracellular growth and persistence of *Chlamydia trachomatis*. *J Med Microbiol* 65:91-98.

81. Sheremet AB, Zigangirova NA, Zayakin ES, Luyksaar SI, Kapotina LN, Nesterenko LN, Kobets NV, Gintsburg AL. 2018. Small Molecule Inhibitor of Type Three Secretion System Belonging to a Class 2,4-disubstituted-4H-[1,3,4]-thiadiazine-5-ones Improves Survival and Decreases Bacterial Loads in an Airway *Pseudomonas aeruginosa* Infection in Mice. *Biomed Res Int* 2018:5810767.
82. Zetterstrom CE, Hasselgren J, Salin O, Davis RA, Quinn RJ, Sundin C, Elofsson M. 2013. The resveratrol tetramer (-)-hopeaphenol inhibits type III secretion in the gram-negative pathogens *Yersinia pseudotuberculosis* and *Pseudomonas aeruginosa*. *PLoS One* 8:e81969.
83. Kang JE, Jeon BJ, Park MY, Yang HJ, Kwon J, Lee DH, Kim BS. 2020. Inhibition of the type III secretion system of *Pseudomonas syringae* pv. tomato DC3000 by resveratrol oligomers identified in *Vitis vinifera* L. *Pest Manag Sci* 76:2294-2303.
84. Lv Q, Li S, Wei H, Wen Z, Wang Y, Tang T, Wang J, Xia L, Deng X. 2020. Identification of the natural product paeonol derived from peony bark as an inhibitor of the *Salmonella enterica* serovar Typhimurium type III secretion system. *Appl Microbiol Biotechnol* 104:1673-1682.
85. Lv Q, Chu X, Yao X, Ma K, Zhang Y, Deng X. 2019. Inhibition of the type III secretion system by syringaldehyde protects mice from *Salmonella enterica* serovar Typhimurium. *J Cell Mol Med* 23:4679-4688.
86. Li J, Sun W, Guo Z, Lu C, Shen Y. 2014. Fusaric acid modulates Type Three Secretion System of *Salmonella enterica* serovar Typhimurium. *Biochem Biophys Res Commun* 449:455-9.
87. Li J, Lv C, Sun W, Li Z, Han X, Li Y, Shen Y. 2013. Cytosporone B, an inhibitor of the type III secretion system of *Salmonella enterica* serovar Typhimurium. *Antimicrob Agents Chemother* 57:2191-8.
88. Kimura K, Iwatsuki M, Nagai T, Matsumoto A, Takahashi Y, Shiomi K, Omura S, Abe A. 2011. A small-molecule inhibitor of the bacterial type III secretion system protects against in vivo infection with *Citrobacter rodentium*. *J Antibiot (Tokyo)* 64:197-203.

89. Ma YN, Chen L, Si NG, Jiang WJ, Zhou ZG, Liu JL, Zhang LQ. 2019. Identification of Benzyloxy Carbonimidoyl Dicyanide Derivatives as Novel Type III Secretion System Inhibitors via High-Throughput Screening. *Front Plant Sci* 10:1059. Wagener BM, Anjum N, Evans C, Brandon A, Honavar J, Creighton J, Traber MG, Stuart RL, Stevens T, Pittet JF. 2020. Alpha-tocopherol Attenuates the Severity of *Pseudomonas aeruginosa*-induced Pneumonia. *Am J Respir Cell Mol Biol* doi:10.1165/rcmb.2019-0185OC.
90. Liu Y, Zhang Y, Zhou Y, Wang T, Deng X, Chu X, Zhou T. 2019. Cinnamaldehyde inhibits type three secretion system in *Salmonella enterica* serovar Typhimurium by affecting the expression of key effector proteins. *Vet Microbiol* 239:108463.
91. Bliska JB, Guan KL, Dixon JE, Falkow S. 1991. Tyrosine Phosphate Hydrolysis of Host Proteins by an Essential *Yersinia*-Virulence Determinant. *Proceedings of the National Academy of Sciences of the United States of America* 88:1187-1191.
92. Rabin SD, Hauser AR. 2005. Functional regions of the *Pseudomonas aeruginosa* cytotoxin ExoU. *Infect Immun* 73:573-82.
93. Rangel SM, Diaz MH, Knoten CA, Zhang A, Hauser AR. 2015. The Role of ExoS in Dissemination of *Pseudomonas aeruginosa* during Pneumonia. *PLoS Pathog* 11:e1004945.
94. Portnoy DA, Moseley SL, Falkow S. 1981. Characterization of plasmids and plasmid-associated determinants of *Yersinia enterocolitica* pathogenesis. *Infect Immun* 31:775-82.
95. Winter SE, Winter MG, Poon V, Keestra AM, Sterzenbach T, Faber F, Costa LF, Cassou F, Costa EA, Alves GE, Paixao TA, Santos RL, Baumler AJ. 2014. *Salmonella enterica* Serovar Typhi conceals the invasion-associated type three secretion system from the innate immune system by gene regulation. *PLoS Pathog* 10:e1004207.
96. Matsui H, Eguchi M, Ohsumi K, Nakamura A, Isshiki Y, Sekiya K, Kikuchi Y, Nagamitsu T, Masuma R, Sunazuka T, Omura S. 2005. Azithromycin inhibits the formation of flagellar filaments without suppressing flagellin synthesis in *Salmonella enterica* serovar typhimurium. *Antimicrob Agents Chemother* 49:3396-403.

CHAPTER 2

Anti-inflammatory Drug Discovery using High Content Image-Based Screening

Summary

Chapter 2 summarizes my goals to develop a complex yet robust high content image-based screening platform that utilizes morphologically distinct macrophages with and without endotoxin lipopolysaccharide (LPS) to: 1) improve sub-category mechanism of action (MOA) clustering using cytological profiling techniques and 2) identify anti-inflammatories using supervised deep learning approaches. Millions of people worldwide are affected by diseases and conditions related to the immune system. Unfortunately, the current supply of approved anti-inflammatory medicine is very limited and only treats a small fraction of inflammatory diseases; many of these treatments also cause severe side-effects with long-term use. Nearly half of the drugs on the market today are natural products and natural product derivatives. The long-term objective of my research is to continue efforts toward the discovery of diverse chemical compounds and their mechanism of action (MOA) to inspire the next generation of novel therapeutics. We approached this objective by utilizing known bioactive chemical libraries, new advanced technologies to allow for improved high-content phenotypic screens, and computational tools for data processing and analysis. In collaboration with natural product chemists (John MacMillan and Roger Linington), we have access to unique libraries of natural botanical and marine product extracts. The Lokey lab has shown that a high-content image-based screening platform called, cytological profiling (CP) in HeLa cells is a valuable tool to give insights about the potential MOA of lead compounds at the primary screening stage based on a limited

staining set that probes the cell cycle, organelles, and the cytoskeleton (Woehrmann et al., 2013) (Schulze et al., 2013) (Ochoa, Bray, Lokey, & Linington, 2015) (Hight et al., 2019). This technique utilizes automated fluorescence microscopy and computer-aided image segmentation algorithms to extract large quantities of morphological information from cells' images. As a result, hundreds of morphological features that describe cellular size, shape, and pixel intensities of various stains are aggregated into a collection of feature vectors generating a 'fingerprint' for each test compound's effect are clustered based on their similarity. This unsupervised method is used to predict the biological activity or MOA of a query compound on the basis of "guilt by association" method. Thereby assigning a mechanistic class to a compound with a similar feature profile to an annotated reference compound. Although this technique has been useful to predict the MOA of unknown compounds, it is limited to clustering up to 20-40 MOA classes (Cox et al., 2020). Therefore, limiting the ability only to identify ~30% of compound target classes. In Chapter 2.1 our studies comparing HeLa and Raw264.7 (with and without LPS) feature datasets confirm this limitation. Also, we briefly describe our attempts to screen with bone marrow derived macrophages (BMDMs) and compare HeLa CP and Raw264.7 CP for their ability to cluster compounds based on feature similarity and MOA classes. Furthermore, in Chapter 2.2 we utilize supervised convolutional deep learning neural network (DNN) approaches using raw images to identify compounds that reverse the LPS-stimulated phenotype in Raw264.7 macrophages to identify anti-inflammatory drug leads. The selected hit compounds from the HCS deep learning approach exhibited promising immunomodulatory effects

based on lowered pro-inflammatory cytokines measurements. Overall, this HCS deep learning screening approach is relevant for anti-inflammatory drug discovery. Finally, in Chapter 2.3 we briefly describe how we overcome challenging image viewing accessibility with a costume-built online image viewing database available to the public via website <https://immunocp.pbsci.ucsc.edu/experiment>. This online resources allows for quick and easy inspection of images from our HCS screen.

References

- Cox, M. J., Jaensch, S., Van de Waeter, J., Cougnaud, L., Seynaeve, D., Benalla, S., . . . Gohlmann, H. W. H. (2020). Tales of 1,008 small molecules: phenomic profiling through live-cell imaging in a panel of reporter cell lines. *Sci Rep*, *10*(1), 13262. doi:10.1038/s41598-020-69354-8
- Hight, S. K., Kurita, K. L., McMillan, E. A., Bray, W., Clark, T. N., Shaikh, A. F., . . . MacMillan, J. B. (2019). High-Throughput Functional Annotation of Natural Products by Integrated Activity Profiling. doi:10.1101/748129
- Ochoa, J. L., Bray, W. M., Lokey, R. S., & Linington, R. G. (2015). Phenotype-Guided Natural Products Discovery Using Cytological Profiling. *J Nat Prod*, *78*(9), 2242-2248. doi:10.1021/acs.jnatprod.5b00455
- Schulze, C. J., Bray, W. M., Woerhmann, M. H., Stuart, J., Lokey, R. S., & Linington, R. G. (2013). "Function-first" lead discovery: mode of action profiling of natural product libraries using image-based screening. *Chem Biol*, *20*(2), 285-295. doi:10.1016/j.chembiol.2012.12.007
- Woerhmann, M. H., Bray, W. M., Durbin, J. K., Nisam, S. C., Michael, A. K., Glassey, E., . . . Lokey, R. S. (2013). Large-scale cytological profiling for functional analysis of bioactive compounds. *Mol Biosyst*, *9*(11), 2604-2617. doi:10.1039/c3mb70245f

2.1 Macrophage cytological profiling and anti-inflammatory drug discovery

The following work was completed as a collaboration between all of the following authors:

Tannia A. Lau, Walter M. Bray, and R. Scott Lokey

Department of Chemistry and Biochemistry, University of California Santa Cruz,
Santa Cruz, California.

Reprint

Tannia A. Lau, Walter M. Bray, R. Scott Lokey. "Macrophage Cytological Profiling and Anti-Inflammatory Drug Discovery," *ASSAY and Drug Development Technologies*, January 2019; 17, 14-16. doi.org/10.1089/adt.2018-894

Macrophage Cytological Profiling and Anti-Inflammatory Drug Discovery

Tannia A. Lau, Walter M. Bray, and R. Scott Lokey

Department of Chemistry and Biochemistry, University of California Santa Cruz, Santa Cruz, California.

Tannia Lau from the Department of Chemistry and Biochemistry, University of California Santa Cruz, was awarded First Place Poster award at the annual Society of Biomolecular Imaging and Informatics (SBI²) meeting held in Boston, September 2018.

ABSTRACT

Millions of people are affected by diseases and conditions related to the immune system. Unfortunately, our current supply of approved anti-inflammatory medicine is very limited and only treats a small fraction of inflammatory diseases. Nearly half of the drugs on the market today are natural products and natural product derivatives. The long-term objective of my research is to continue efforts toward the discovery of diverse chemical compounds and their mechanism of action (MOA) to inspire the next generation of novel therapeutics. This project approaches this objective by creating a robust platform for the in-depth phenotypic profiling of complex natural product samples with respect to their effect on pathways related to the innate immune response. This approach has the potential to elucidate the MOAs of novel natural products relevant to inflammation and accelerate the pace of drug discovery in this therapeutic area.

Keywords: imaging, immunology, natural products, activation, assay

INTRODUCTION

Natural products are rich sources for anti-inflammatory agents. There are numerous studies quantifying their effects in cell-based model systems as well as whole organisms.¹⁻⁵ Therefore, understanding anti-inflammatory effects of commonly used natural products in folk medicine is warranted. This research will provide a platform for the chemical characterization and mode of action prediction for bioactive natural products in complex mixtures directly from primary screens. Natural products remain a rich source of structural and chemical diversity that is unsurpassed by any synthetic libraries.⁶ Al-

though, there are ~200,000 compounds in the Dictionary of Natural Products, only a small percentage has received biological evaluation to define their mechanism of action (MOA) against prokaryotic or eukaryotic targets.⁷ This lack of biological information is due to at least in part to the fact that there are no well-established high-throughput screening methods for the direct prediction of compound MOA. To address this gap, we utilize cytological profiling (CP), a technology that broadly characterizes the effects of compounds on cells and has the ability to classify cellular phenotypes into clusters of compounds with distinct MOAs.^{8,9} CP is a high-content image-based screen to quantify the phenotypic effects of compounds on mammalian cells by capturing hundreds of cellular features using automated fluorescence microscopy. Utilizing biologically relevant fluorescent markers and computer-aided image segmentation and feature extraction provides detailed quantitative phenotypic profiles on individual cells. The aggregate of processed features gives rise to a "fingerprint" for each compound followed by hierarchical clustering. It is possible to predict the MOAs of unknown compounds^{10,11} by comparing the generated fingerprint to the fingerprints from a training library of ~3000 compounds with known mechanisms of action. Cell images are substantially richer in data compared with single readout, target-based, or cell reporter approaches.¹²⁻¹⁴ Our rationale is to create a system that inverts the natural product drug discovery process, with compound modes of action being determined at the first stage of project selection, rather than as the final step in the drug discovery process.

THE TECHNICAL CHALLENGE

There are currently few general methods for the broad biological characterization of natural products. Current biological annotation tools include the NCI 60-cell line program (National Institutes of Health), which is typically limited to the evaluation of pure compounds with proven efficacy in *in vitro* models; and the Connectivity Map (Broad Institute), which provides genome-wide transcriptional expression data for the set of ~1300 compounds under a variety of experimental conditions and time points. Although powerful, neither of these tools is appropriate for the large-scale analysis of complex natural product libraries, due to the cost and logistical complexities of acquiring data on large (>10,000) screening libraries. By contrast, CP has the

capacity to evaluate many thousands of samples (including crude extracts, prefractions, high performance liquid chromatography fractions, and pure compounds), and is configured to incorporate new data on a rolling basis, with the resolution and accuracy of MOA predictions improving as the size of the data set increases.

Current CP methods utilize cancer cell lines and cytological stains that recognize cell cycle, organelle, and cytoskeletal features.^{9,15–24} Although powerful to query MOAs, many compounds such as bioactive lipids (known to cause pro- and anti-inflammatory effects) and kinase inhibitors show no phenotype in the HeLa cervical cancer cell line using the current stain set. Our original application of CP in HeLa cells revealed that only ~30% of the reference library showed any discernable phenotypic effect (up to 10 μ M and upon 24-h treatment). Thus, compounds that engage and inhibit specific signaling pathways involved in disease states such as inflammation may not give rise to a cytological profile in a resting cancer cell. To address this issue, we will harness the phenotypic plasticity of macrophages under proinflammatory stimulus to uncover new bioactivities in compounds that showed minimal effect in resting cells. Lipopolysaccharide (LPS) is a general name for a class of molecules with a lipid A core that is found in the outer membrane of gram-negative bacteria. LPS initiates the innate immune response by binding Toll-like receptor 4, activating a cascade of intracellular inflammatory signaling pathways.²⁵ Although this response is advantageous as a protection against bacterial infection, it can lead to an uncontrolled release of cytokines and rapid death by septic shock. We hypothesize that LPS-stimulated macrophages, which show a dramatic visual phenotype compared with unstimulated cells, could provide an opportunity for capturing more diverse phenotypes and will improve the ability to distinguish MOA subcategories in CP. Improving CP in this manner could be an effective approach to diversifying our current selection of anti-inflammatories.

IMMUNO-CP: A METHOD TO SCREEN FOR NOVEL THERAPEUTICS FROM NATURAL PRODUCTS TO IDENTIFY ANTI-INFLAMMATORIES

Our laboratory has shown that CP in HeLa cells is a valuable tool to give insights about the potential MOA of lead compounds at the primary screening stage based on a limited staining set that probes the cell cycle, organelles, and the cytoskeleton. Current CP methods utilize cancer cell lines; however, these cell lines exhibit limited phenotypic/functional characteristics in comparison with activated macrophage cells, which exhibit dramatic changes in their form and physiology under inflammatory conditions. We hypothesize that expand-

MACROPHAGE CYTOLOGICAL PROFILING

ing the cell line from HeLa to macrophages with an addition of proinflammatory stimuli, LPS, will improve the ability to assign biological functions to natural product extracts. We have optimized murine macrophage-like RAW264.7 cell conditions with proinflammatory, LPS, and introduced drugs from our known bioactive compound libraries. We have shown the feasibility to apply RAW264.7 macrophages to the CP platform that exhibit measurable differences in cellular features between +LPS and -LPS macrophages. Preliminary data show significant phenotype changes with proinflammatory responses to LPS. We expect that with the addition of the LPS stimulus, we will refine the ability of CP to cluster compounds that engage and inhibit specific signaling pathways involved in a diseased inflammation state, not seen in resting cells.

Furthermore, we will develop and implement a high-throughput high-content screen for compounds that reverse the LPS-induced phenotype in macrophages as potential drug leads against septic shock. We will screen for small molecule inhibitors of the LPS-induced activation of macrophages. In a preliminary test of this assay, we screened 360 compounds from a library of drugs and inhibitors with annotated MOAs (SelleckChem). RAW264.7 cells were incubated with dimethyl sulfoxide (DMSO) controls and 360 compounds and \pm LPS for a total reaction time of 24 h. We found that compounds BMS-536924, AG-1024, and genistein affect downstream actin rearrangements and appear to reverse the LPS phenotypic to features similar to the DMSO control. Compounds of interest are those that are highly potent (at least in the low- to mid-nanomolar range) and selective, and have desirable pharmacokinetic properties. Further image analysis tools and pipelines using CellProfiler Analyst²⁶ will be developed to detect the reversal of the inflammatory LPS phenotype using supervised machine learning. I will train a classifier to recognize the -LPS phenotype using DMSO-treated field-of-view-level images. Then the trained and annotated model will be used to automatically detect the -LPS phenotypes in the +LPS samples treated with compound. Compounds that show a reversal of the LPS phenotype will be scored as positive (by matching the phenotypes to unstimulated cells) and carried forward for proinflammatory cytokine assays and viability tests.

FUTURE DIRECTIONS

We will screen the unique collection of botanical and marine natural products against the Immuno-CP assay. We anticipate that training the \pm LPS macrophages with the annotated chemical libraries and fitting the natural product extract fingerprints to those clusters will dramatically improve our ability to identify MOAs and potential anti-inflammatory therapeutic leads. Furthermore, extracts that

LAU, BRAY, AND LOKEY

cluster with known compounds tend to have the similar chemical components or derivatives that give rise to that same phenotype. Therefore, it is possible to reduce rediscovery of known compounds in complex extracts. The presence of a unique CP fingerprint from the natural product extracts could suggest that there are multiple bioactive compounds in a prefraction or there is a unique compound that does not act by any of the commonly encountered MOA. Follow-up studies on natural product compounds of interest will be done to verify their MOA. The natural products that have unique fingerprints will be identified by assay-guided fractionation of the corresponding extracts and deconvolution or structure elucidation of the bioactive component.

We will utilize LPS-stimulated macrophages to capture bioactive compounds that are involved in pathways related to the innate immune response and build a database toward assigning biological functions to natural product extracts. These contributions are significant because they will resolve fundamental technological barriers for the prediction of MOA in complex natural product mixtures and provide new tools to continue the discovery of biologically relevant diverse compounds with unique chemical space. The establishment of a robust high-content macrophage CP pipeline will illuminate the path for the discovery of new and novel anti-inflammatory therapeutics from natural products in an efficient, cost-effective, and high-throughput manner to combat immune-related conditions such as sepsis.

DISCLOSURE STATEMENT

No competing financial interests exist.

REFERENCES

- Sun Q, Zhu J, Cao F, Chen F: Anti-inflammatory properties of extracts from *Chimonanthus nitens* Oliv. leaf. *PLoS One* 2017;12:e0181094.
- Chen CL, Zhang DD: Anti-inflammatory effects of 81 Chinese herb extracts and their correlation with the characteristics of traditional Chinese medicine. *Evid Based Complement Altern Med* 2014;2014:1-8.
- Zong Y, Sun L, Liu B, et al.: Resveratrol inhibits LPS-induced MAPKs activation via activation of the phosphatidylinositol 3-kinase pathway in murine RAW 264.7 macrophage cells. *PLoS One* 2012;7:e44107.
- Mahdi JM: The historical analysis of aspirin discovery, its relation to the willow tree and antiproliferative and anticancer potential. *Cell Prolif* 2006;39:147-155.
- Wilson MA, Shukitt-Hale B, Kalt W, Ingram DK, Joseph JA, Wolkow CA: Blueberry polyphenols increase lifespan and thermotolerance in *Caenorhabditis elegans*. *Aging Cell* 2006;5:59-68.
- Harvey A: Natural products in drug discovery. *Drug Discovery Today* 2008;13:894-901.
- Hu Y, Chen J, Hu G, et al.: Statistical research on the bioactivity of new marine natural products discovered during the 28 years from 1985 to 2012. *Mar Drugs* 2015;13:202-221.
- Adams CL, Kutsy V, Coleman DA, et al.: Compound classification using image-based cellular phenotypes. In: *Measuring Biological Responses with Automated Microscopy*, Ingelse J (ed.), pp. 440-468. Elsevier Masson SAS, San Diego, CA, 2006.
- Periman ZE, Slack MD, Feng Y, Mitchison TJ, Wu LF, Altschuler SJ: Multidimensional drug profiling by automated microscopy. *Science* 2004;306:1194-1198.
- Ochoa JL, Bray WM, Lokey RS, Linington RG: Phenotype-guided natural products discovery using cytological profiling. *J Nat Prod* 2015;78:2242-2248.
- Schulze CJ, Bray WM, Woerhmann MH, Stuart J, Lokey RS, Linington RG: "Function first" lead discovery: mode of action profiling of natural product libraries using image-based screening. *Chem Biol* 2013;285-295.
- Swinney DC, Anthony J: How were new medicines discovered? *Nat Rev Drug Discovery* 2011;10:507-519.
- Shoemaker RH: The NCI60 human tumour cell line anticancer drug screen. *Nat Rev Cancer* 2006;6:813-823.
- Vichai V, Kirtikara K: Sulforhodamine B colorimetric assay for cytotoxicity screening. *Nat Protoc* 2006;1:1112-1116.
- Bray MA, Singh S, Han H, et al.: Cell painting, a high-content image-based assay for morphological profiling using multiplexed fluorescent dyes. *Nat Protoc* 2016;11:1757-1774.
- Kremb S, Voolstra CR: High-resolution phenotypic profiling of natural products-induced effects on the single-cell level. *Sci Rep* 2017;7:44472.
- Kang J, Hsu CH, Wu Q, et al.: Improving drug discovery with high-content phenotypic screens by systematic selection of reporter cell lines. *Nat Biotechnol* 2016;34:70-77.
- Kurita KL, Glassey E, Linington RG: Integration of high-content screening and untargeted metabolomics for comprehensive functional annotation of natural product libraries. *Proc Natl Acad Sci USA* 2015;112:11999-12004.
- Gustafsdottir SM, Ljosa V, Sokolnicki KL, et al.: Multiplex cytological profiling assay to measure diverse cellular states. *PLoS One* 2013;8:e80999.
- Woerhmann MH, Bray WM, Durbin JK, et al.: Large-scale cytological profiling for functional analysis of bioactive compounds. *Mol Biosyst* 2013;9:2604-2617.
- Sunmiya E, Shimogawa H, Sasaki H, et al.: Cell-morphology profiling of a natural product library identifies bisbromamide and mirraenamamide A as actin filament stabilizers. *ACS Chem Biol* 2011;6:425-431.
- Sutherland JJ, Low J, Blosser W, Dowless M, Engler TA, Stancato LF: A robust high-content imaging approach for probing the mechanism of action and phenotypic outcomes of cell-cycle modulators. *Mol Cancer Ther* 2011;10:242-254.
- Young DW, Bender A, Hoyt J, et al.: Integrating high-content screening and ligand-target prediction to identify mechanism of action. *Nat Chem Biol* 2008;4:59-68.
- Feng Y, Mitchison TJ, Bender A, Young DW, Tallarico JA: Multi-parameter phenotypic profiling: using cellular effects to characterize small-molecule compounds. *Nat Rev Drug Discov* 2009;8:567-578.
- Lu YC, Yeh WC, Ohashi PS: LPS/TLR4 signal transduction pathway. *Cytokine* 2008;42:145-151.
- Dao D, Fraser AN, Hung J, Ljosa V, Singh S, Carpenter AE: CellProfiler Analyst: interactive data exploration, analysis, and classification of large biological image sets. *Bioinformatics* 2016;32:3210-3212.

Address correspondence to:

Tannia A. Lau, BS
Department of Chemistry and Biochemistry
University of California Santa Cruz
Santa Cruz, CA 95064

E-mail: talau@ucsc.edu

Abbreviations Used

CP = cytological profiling
LPS = lipopolysaccharide
MOA = mechanism of action

Abstract

The Lokey lab has shown that Cytological Profiling (CP) in HeLa cells is a valuable tool to give insights about the potential mechanism of action (MOA) of lead compounds at the primary screening stage based on a limited staining set that probes the cell cycle, organelles, and the cytoskeleton. However, further improvements that need to be addressed are resolving sub-category target class clustering, identifying anti-inflammatories, and building a database toward assigning biological functions to natural product extracts. To address this, I proposed to develop a high-content screen that utilizes pro-inflammatory lipopolysaccharide (LPS)-stimuli and immunologically relevant primary bone marrow-derived macrophages (BMDMs) to improve the resolution of biological annotation and capture bioactive compounds that are involved in pathways related to the innate immune response.

Introduction

Classical CP approaches utilize cancer cell lines and are blind to mechanisms that are not constitutively active under standard cell culture conditions. Applying a stimulus to cells can activate pathways that are normally quiescent. By screening compounds in parallel under stimulated and non-stimulated conditions, we can capture phenotypes related to pathways that, under non-stimulus conditions, would otherwise not be engaged. The HeLa cells exhibit limited phenotypic/functional characteristics in comparison to activated Raw264.7 and BMDM cells, which demonstrate dramatic changes in their form and physiology under inflammatory conditions (**Fig. 1**). We

hypothesize that expanding the cell line from HeLa (cervical cancer) to primary macrophages with an addition of pro-inflammatory stimuli, LPS will improve indistinguishable MOA sub-categories in CP.

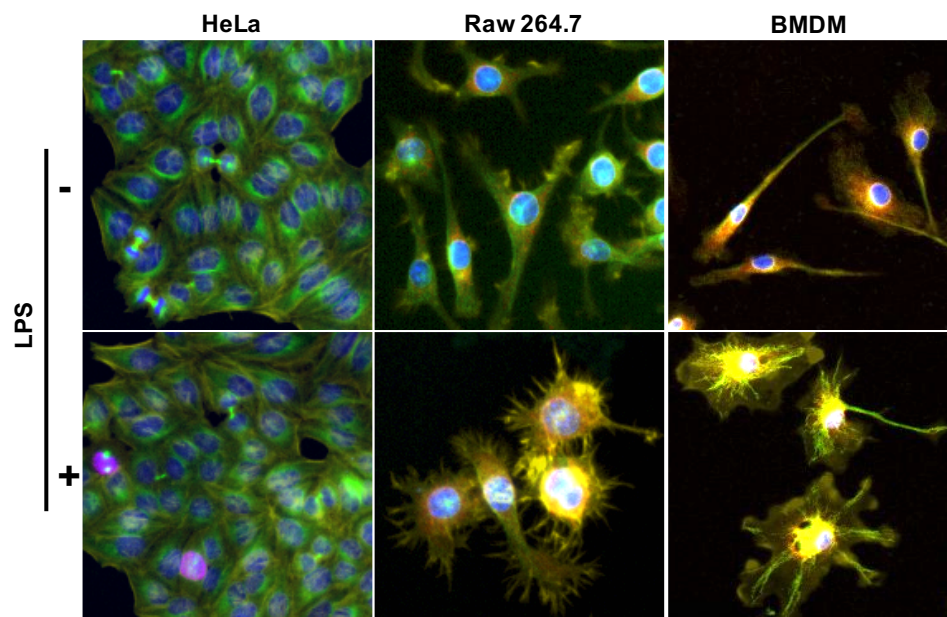


Figure 1. HeLa cells exhibit limited biological features compared to macrophages, Raw264.7 , and primary bone marrow derived macrophages (BMDM), under LPS inflammatory stimuli.

+/- 50ng/mL LPS for 24hrs, image overlay. cells are probed for nuclei (Hoescht, blue), microtubules (anti-tubulin, green), actin (phalloidin, yellow). HeLa: mitosis (anti-pHH3, red) and macrophages -endoplasmic reticulum (calnexin, red).

We optimized BMDM conditions with pro-inflammatory, LPS, and introduce drugs from our known bioactive compound library in a 384 well plate format. However, due to inconsistent results with the unstimulated controls we moved to Raw264.7 macrophages for primary screening purposes. We utilized cytological profiling techniques (Woehrmann et al., 2013) to compare HeLa and Raw264.7 cells, with and without LPS, with the idea of improving the ability to capture more phenotypes that

would reveal more mechanisms of action classes. Our analysis involved a two sample, one-sided Kolmogorov–Smirnov test (KS-test) to assess the ability of the two cell lines to cluster MOA classes and the CP-score to analyze bioactivity of natural product fractions (NPFs). We predicted that this strategy would expand the coverage of CP and permits extension into a variety of new target areas. However, the results are modest for the Raw264.7 datasets compared to HeLa as we reveal 11 new target classes and 43 bioactive natural product fractions not seen in HeLa.

Results and Discussion

Optimization of BMDM conditions: BMDMs not suitable for large HCS

Preliminary studies showed the feasibility to apply murine Raw264.7 macrophages to the CP platform. However, Abelson murine leukemia virus transformed macrophage cell line from a Balb/c mouse does not fully recapitulate normal macrophage physiology. Therefore, we applied primary mouse macrophages from C57BL6 wild type mice in our screening platform. Pilot experiments for HCS utilizing bone marrow derived macrophages (BMDMs) were promising. We confirmed dramatic morphological changes upon stimulation with 50ng/mL of LPS (TLR4/TLR2, *E.coli*055:B5) and LPS-EB Ultrapure (TLR4, *E.coli*0111:B4) in comparison to unstimulated BMDMs (**Fig.2**). To focus on specific activity along the TLR4 pathway we decided to continue with LPS-EB Ultrapure for future experiments.

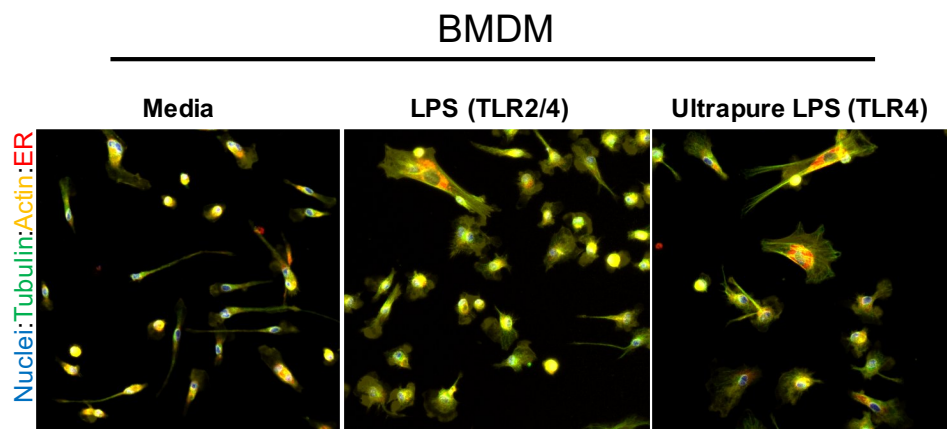


Figure 2. Primary BMDMs stimulated with LPS (TLR4/TLR2) and LPS-EB Ultrapure (TLR4) exhibit dramatic morphological changes in comparison to unstimulated BMDMs.

50ng/mL LPS for 24hrs, image overlay for **nuclei** (Hoechst, blue), **microtubules** (anti-tubulin, green), **actin** (phalloidin, yellow), **endoplasmic reticulum** (calnexin, red).

In addition, we optimized the screening assay to work with previously frozen BMDMs instead of collecting fresh primary monocytes (derived into macrophages with L929 supernatant) from mouse bone marrow for every screen. Initially, we tried to grow the BMDMs in a 10cm² tissue culture dish with M-CSF supplemented media after thawing the cells, then after two days plating the cells in a 384 well plate. However, this reduced viability and the LPS stimulatory function of the BMDMs. Therefore, direct plating of the BMDMs (after thawing) into the 384 well plates worked best. After optimizing these critical high throughput screening aspects and running a chemical screen (with the inflammation informer set SP20299), we learned that these cells were extremely prone to stimulation, possibly by adventitious LPS in the tubing or media. It turns out that BMDMs are very difficult to maintain in their unstimulated state, and so these cells, while they are a good model of innate immunity, were not be the best choice for the primary screen. So we continued with the transformed Raw264.7 cell line, which is more robust toward activation and is therefore a better cell line for the initial high-throughput screen.

Cytological profiling comparison for HeLa and Raw264.7 +/- LPS

Utilizing Raw264.7 cells and ultrapure LPS we followed through with the full screen of 2,259 from SelleckChem [25uM], 160 from the MCE inflammation set [25uM and 5uM], 628 marine microbial extracts from MacMillan and Linington collections [50ug/mL], and 320 synthetic cyclic peptides from the Lokey library [37.5uM]. The stain sets for this screen are, ss1: nuclei, Golgi, actin, pHH3 and ss2: nuclei, tubulin, EdU, and mitochondria with the respective channels: DAPI, FITC, TRITC, and Cy5. In comparison to existing HeLa legacy data [50uM] we replaced the endoplasmic reticulum stain with MitoTracker DeepRed FM and included Golgi.

HeLa CP outperforms Raw264.7 CP to associate target classes

To assess the ability of each dataset to identify significant associations within the SelleckChem library target classes, we used the KS-test to determine in-class and out-of-class associations. We compare all of the p-values for each target class across all of the datasets and show that HeLa identified more target classes as significantly self-associated than Raw264.7, Raw264.7+LPS, and the Raw264.7 +/- LPS datasets merged (Raw264.7_merge) (**Fig. 3A**). The datasets are also represented as Venn diagrams for comparison of the cell types. In **Figure 3D** we reveal 11 new target classes (**Table 1**) with the Raw264.7 +/- LPS dataset not seen in HeLa. In summary, HeLa CP outperforms Raw264.7 CP to associate target classes by two fold according to the KS-test.

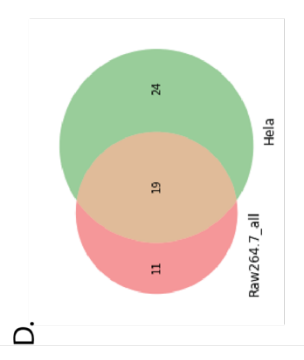
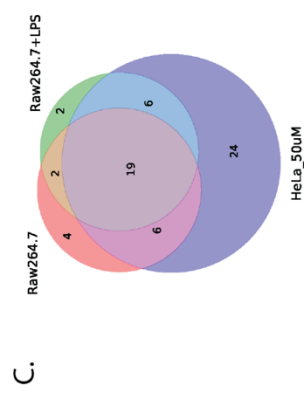
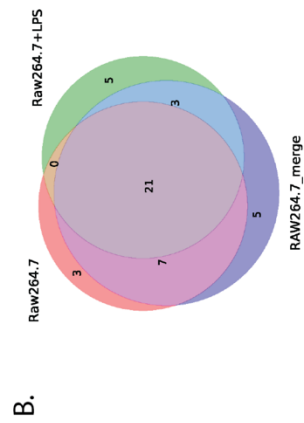
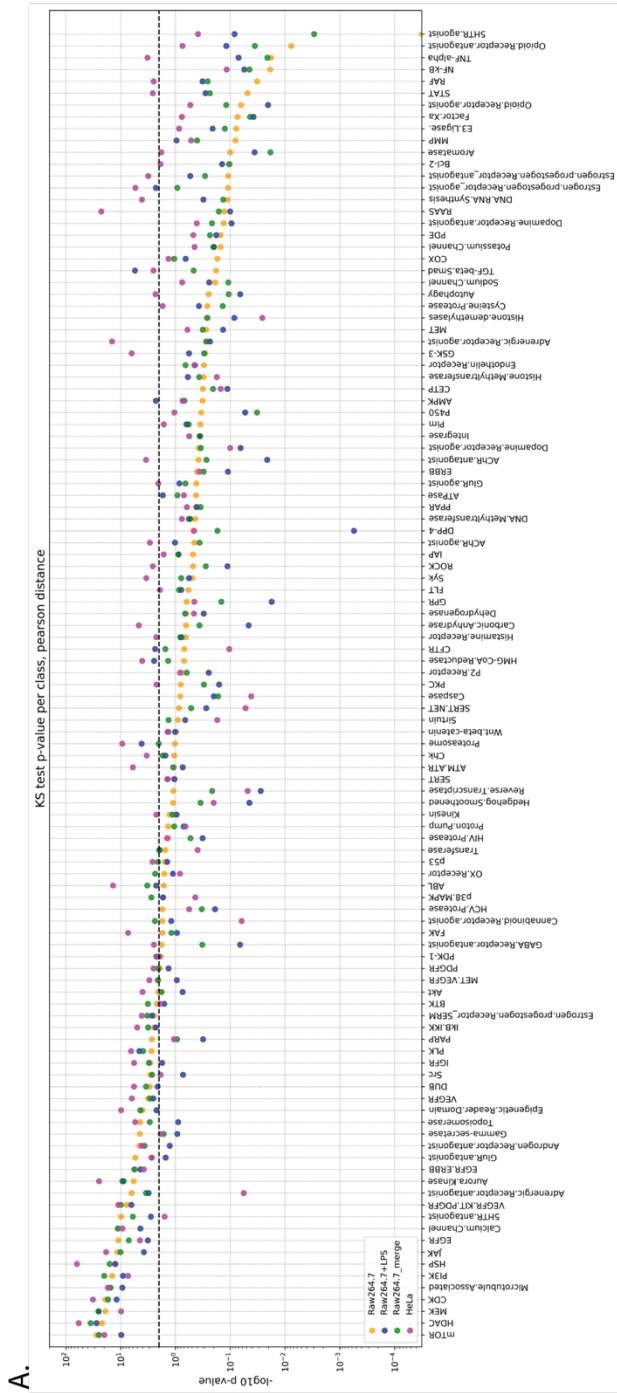


Figure 3. Comparison of in-class target annotation vs out-of-class annotation KS-test p-values <0.01 in Raw264.7 and HeLa cells for SelleckChem

A. Dot plot comparing the p-value on a $-\log_{10}$ scale in Raw264.7 and HeLa datasets, using Pearson distance as the similarity metric by target class annotation. The significance threshold is represented by the horizontal line ($p=0.01$) **B.** Venn diagram of unique or shared target classes between Raw264.7 cells and Raw264.7 stimulated with LPS and both datasets combined Raw264.7_merge reveal **44 target total drug classes out of 111 total.** **C.** Comparison of Raw264.7 +/- LPS to HeLa reveal **8 target classes unique to Raw264.7 cells** **D.** Raw264.7_all (Raw264.7 cells and Raw264.7 stimulated with LPS and both datasets combined Raw264.7_merge) reveal **11 new target drug classes** not seen in HeLa. The HeLa CP outperforms Raw264.7_all nearly two-fold.

Table 1. List of unique and shared target drug classes for Raw264.7_all and HeLa.

Raw264.7_all vs. HeLa SelleckChem annotations Pearson KS Test: Target Drug Classes

RAW_all	HeLa	RAW_all & HeLa
PARP	Histamine.Receptor	PI3K
Gamma-secretase	AChR.antagonist	HDAC
Src	Adrenergic.Receptor.agonist	CDK
BTK	DNA.RNA.Synthesis	JAK
CFTR	RAAS	mTOR
AMPK	RAF	HSP
p38.MAPK	GSK-3	Aurora.Kinase
Cannabinoid.Receptor.agonist	PDGFR	Calcium.Channel
OX.Receptor	ATM.ATR	MEK
Adrenergic.Receptor.antagonist	GluR.agonist	EGFR
5HTR.antagonist	AChR.agonist	Microtubule.Associated
	Estrogen.progestogen.Receptor_antagonist	VEGFR
	Kinesin	VEGFR.KIT.PDGFR
	p53	EGFR.ERBB
	PKC	Epigenetic.Reader.Domain
	STAT	DUB
	Syk	IkB.IKK
	Autophagy	PLK
	Carbonic.Anhydrase	Estrogen.progestogen.Receptor_SERM
	FAK	
	ROCK	
	TNF-alpha	
	Chk	
	GABA.Receptor.antagonist	

Bioactive natural product fraction comparisons based on CP-Score

Furthermore, we compare active natural product fractions (NPFs) based on the CP-score (**Fig. 4**). The CP-score is a measure of phenotypic strength calculated by taking the vector magnitude square root of the sum of the square for all of the histogram difference feature scores (Woehrmann et al., 2013). Plotting of the rank-ordered CP vector magnitudes for all treated instances yield an elbow plot where distinct phenotypes emerge at the elbow (threshold) (**Fig.4A**). NPFs that fall below the cutoff correspond to relatively featureless instances. Amongst all of the NPFs, Raw264.7 cells reveal ~33% and HeLa ~38% of NPF instances with distinct features (**Fig. 4B-C**). However, HeLa still out performs Raw264.7 by double in regards to distinct phenotypes based on the CP-score. We look closer at the CP-scores of the cells treated with NPFs from the MacMillan and Linington libraries. The MacMillan library reveals more active NPFs with the HeLa cells (**Fig. 4D**) whereas, the Linington Library has almost equal active NPFs between Raw264.7 and HeLa cells (**Fig. 4E**).

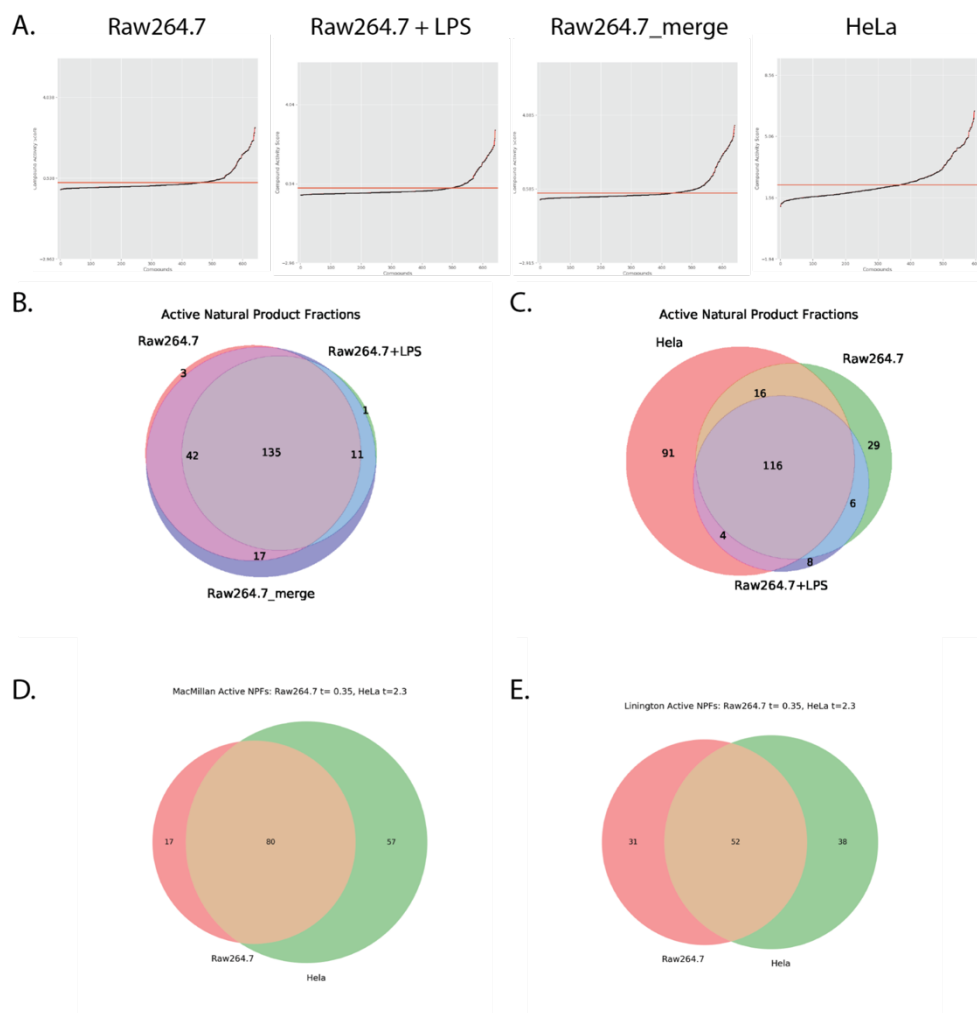


Figure 4. Comparison of Active Natural Product Fractions based on CP Score.

A. Elbow plots with threshold for Raw264.7, +LPS = 0.35, _merge = 0.4, and HeLa = 2.3. **B.** Comparison of Raw264.7 cells +/- LPS and with merged datasets (_merge), **209 NPFs** were active out of 628 total NPFs. **C.** Comparison of Raw264.7/LPS to HeLa. **270 total NPFs** were active out of 596, 179 were detected with Raw264.7 and 227 with HeLa cells. Raw264.7 cells and +LPS reveal **43** total active NPFs not seen in HeLa. **D-E.** Comparison of Raw264.7 and HeLa NPF activity score between individual NPF libraries.

Conclusion

Taken together, we optimized BMDMs for high-throughput image-based screening however, we had complications keeping the BMDMs unstimulated and had issues with batch-to-batch variation. For this to work, I recommend designating specific multi-drop tubing for the BMDMs and to freeze down a large batch of BMDMs. Given the sensitivity of the BMDMs, I suggest to perform this approach only for small screens (<600 compounds). Furthermore, we conclude that both the KS-test and CP-score analyses reveal that HeLa CP performs better than the Raw264.7 +/-LPS CP. Although, the results are not as dramatic as we predicted for the Raw264.7 datasets, we continue our efforts to identify compounds that reverse the LPS-phenotype for anti-inflammatory drug discovery using supervised deep learning approaches.

2.2 High-content image-based screening and deep learning for the detection of anti-inflammatory drug leads

The following work was completed as a collaboration between all of the following authors:

Tannia A. Lau*¹, Elmar Mair², Scott Lokey¹

¹Department of Chemistry and Biochemistry, University of California Santa Cruz, Santa Cruz, CA 95064.

²No Affiliation, Santa Cruz, CA 95060

Abstract

We developed a high-content image-based screen that utilizes the pro-inflammatory stimulus lipopolysaccharide (LPS) and murine macrophages (Raw264.7) with the goals of identifying anti-inflammatory drug leads. We screened 2,419 bioactive compounds with annotated mechanisms of action (MOA) and 628 marine microbial extracts to identify compounds that reverse the LPS-induced phenotype in macrophages. We utilize a limited staining set of seven probes for cell cycle (S-phase, mitosis), organelles (nuclei, Golgi, mitochondria), and the cytoskeleton (actin, tubulin). The generated images were used to train a deep neural network classifier on unstimulated and LPS-stimulated macrophage controls. We ran ablation studies on different image sizes and convolutional deep neural network (DNN) architectures. Those that performed best were the models trained on full images which hints that context is more important than details for this classification task. Furthermore, we determined that all stains contain valuable information since the best classification performance is achieved when combining all features in a respective model architecture. From the primary deep learning hit list, we selected a subset for multiplex cytokine expression follow-up from different mechanistic classes that included, MEK1/2, IRAK-4, I-BET, and TLR4 inhibitors. These hits reveal various cytokine expression profiles but overall dampen the inflammation response. In summary, this deep learning morphological assay identified compounds that modulate the innate immune response to LPS and is relevant for accelerating the pace of drug discovery in this therapeutic area.

Introduction

Sepsis is one of the predominant diseases of microbial and viral origin, causing profound morbidity and mortality. The very high incidence (3 cases per 1000 people) and death rate (200,000 – 300,000 deaths each year in the U.S.) in sepsis make it a major health crisis facing the nation as well as the world (CDC, 2017). Lipopolysaccharide (LPS) is a conserved lipoprotein from gram negative bacteria that initiates the innate immune response by binding Toll-like receptor 4 (TLR4), and activating a cascade of intracellular inflammatory signaling pathways (Lu, Yeh, & Ohashi, 2008). While this response is advantageous as a protection against foreign pathogens and substances, an overwhelming response can lead to an excessive release of cytokines, multiple organ failure, and septic shock. Unfortunately, there are currently no effective treatments for acute, LPS-mediated induction of septic shock. Therefore, the development of a screening assay to identify anti-inflammatories is critical for the discovery of the next generation of novel therapeutics.

Screening for anti-inflammatory drugs has traditionally been complicated because of the complexity of the immune response and existing therapies span various MOA classes such as nonsteroidal anti-inflammatories, glucocorticoids, anti-cytokine biologics, statins, HDAC, kinase inhibitors, and many more (Dinarello, 2010). However, industry preferred high throughput screening (HTS) approaches report on simple readouts for cell viability, target binding, and enzyme activity. These assays do not capture cellular complexity and limits discovery to a specific biological target and the inability to detect off target effects. Whereas, multiplex assays such as

transcriptomics, proteomics, and metabolic profiling provide rich multiplexed information, but are low throughput due to cost. Another high throughput multi-dimensional profiling technique that is more affordable (but requires specialized equipment) is high content image-based profiling. This technique combines automated fluorescence microscopy and computer-aided image segmentation to extract large quantities of morphological information from images of cells to characterize the effects of test compounds. This whole cell-based morphological assay bypasses the need for a validated target allowing for this technique to be an attractive approach for anti-inflammatory discovery.

Several studies using HCS assays for pathogenic and immunomodulating drug discovery measured human and mouse macrophages based on their functional morphology and immune responses. Studies that identified inhibitors of *Mycobacterium tuberculosis* proliferation (Christophe, Ewann, Jeon, Cechetto, & Brodin, 2010) and *Leishmania* parasite infection (Siqueira-Neto et al., 2012) in macrophages was accomplished without the knowledge of a specific target. Another study identified activators and inhibitors of innate signaling through IRF3 and NFkB pathways by measuring protein translocation using primary human CD14 monocytes (Koch et al., 2018). The unique morphological differences of functionally polarized macrophages enabled identification of compounds that reverse a tumor-associated macrophages (TAMs) to polarize into an inflammatory M1 macrophage resulting in anti-tumor activity (Hu et al., 2021). Furthermore, machine learning approaches have been used to distinguish functionally diverse macrophage populations (monocytes,

naive, M1, and M2) from human peripheral blood mononuclear cells (PBMCs) based on their morphology with an accuracy of 90% (Rostam, Reynolds, Alexander, Gadegaard, & Ghaemmaghami, 2017).

In this study, we developed a supervised convolutional deep learning neural network (DNN) classifier to identify compounds that reverse the LPS-stimulated phenotype by training on unstimulated and LPS-stimulated morphological feature changes in murine Raw264.7 macrophages, in order to identify compounds with an immunomodulatory effect (**Fig. 1**). Deep learning models replace manual, user-defined feature extraction with a neural network algorithm. The automated image processing and analysis ensure consistent interpretation of the results without human bias. The discoveries from this screen could provide new lead therapeutic candidates against septic shock and other inflammatory diseases. The resulting active compounds could also be used as chemical tools in the study of innate immunity.

Workflow to identify anti-inflammatory hits using deep learning

The Raw264.7 cells were plated into 384-well plates and pre-treated with compound for 4h or vehicle control DMSO then stimulated with +/- 50ng/mL LPS for a total of 24h. We collected well-based images exposed to a collection of 2,419 MOA annotated bioactive compounds and 628 marine microbial extracts. For every sample, we imaged four sites per well at 20x for a total of eight stains, ss1: nuclei, Golgi, actin, pHH3 and ss2: nuclei, tubulin, s-phase, mitochondria. We trained our DNN models using varying image resolutions and sizes on unstimulated controls and LPS-stimulated Raw264.7

cells probed with a limited stain set that captures cell cycle events, organelles, and cytoskeleton features. Then we ran DNN models and input formats against the entire dataset of 3,047 test compounds and LPS-stimulated cells. In order to eliminate false positives from the primary hits we performed a dose-response assay using HCS with the addition of iNOS as a readout for inflammatory activity. Test compounds that reverse the LPS-stimulated phenotype and reduced iNOS expression were selected for 32-plex cytokine assay follow-up. Our goal is to utilize this assay for anti-inflammatory drug discovery.

Results and Discussion

Measured morphological feature changes between unstimulated and LPS-stimulated Raw264.7 cells

The plasticity of macrophages under pro-inflammatory conditions exhibits various dramatic cellular feature changes in comparison to unstimulated vehicle control cells (**Fig. 2A**). Under non-stimulating conditions the cells appear circular or elliptical shaped in contrast to the LPS-stimulated cells which appear flattened and enlarged with extensive filopodia protrusions (**Fig. 2B**). The principal component analysis (PCA) plots represent a multiplex of selected features based on a correlation matrix that validate feature separation between the LPS-stimulated and the unstimulated cell features for both stain sets (Omta et al., 2016) (**Fig. 2C**). In addition, the cytological profile fingerprint represents feature changes of LPS-stimulated features relative to the unstimulated features as an aggregate of 375 extracted features describing cell size, shape, feature counts, and pixel intensities (Woehrmann et al., 2013). (**Fig. 2D**). Taken together, our studies suggest that the morphological features of the controls are well separated and validate the ability to distinguish an unstimulated and LPS-stimulated cell phenotype.

LPS stimulation causes dramatic actin and microtubule cytoskeleton reorganization such as filopodia extensions and flattening/spreading of the cell in response to enhanced activities such as migration, phagocytosis, and antigen presentation capacities (Eswarappa, Pareek, & Chakravorty, 2008) (Isowa, Keshavjee, & Liu,

2000) (Hanania et al., 2012). Other reasons for these cytoskeleton rearrangements include the ability to form multinucleated giant cells by cell-cell fusion initiated by actin-based protrusions formed at the leading edge (Faust et al., 2019), and microtubule stabilization allows for efficient secretion of chemokine matrix metalloproteinase (MMP-9) (Hanania et al., 2012). Activation of macrophages by LPS increases energy demand and induces mitochondrial fission/fragmentation events that deliver small fragmented mitochondria to energy-demanding areas. This organelle is highly versatile and has the ability to change in density and shape through fission and fusion events (Kapetanovic et al., 2020) (Kasahara et al., 2011) (Correa-da-Silva, Pereira, de Aguiar, & de Moraes-Vieira, 2018) (Ramond, Jamet, Coureuil, & Charbit, 2019). An increase in the activation of MyD88 and TRIF signaling pathways for the production and secretion of cytokines requires the Golgi apparatus. This critical organelle has the ability to modify and deliver proteins and lipids to secretory vesicles, lysosomes, or the cell surface. Upon infection there is an increase of Golgi tubules and budding events (Zi Zhao Lieu, 2008) (Tao, Yang, Zhou, & Gong, 2020). To engage in a rapid pro-inflammatory response metabolic reprogramming shifts away from homeostatic proliferation of primary murine bone marrow derived macrophages (BMDMs) in the presence of LPS (L. Liu et al., 2016) (Vadiveloo, Keramidaris, Morrison, & Stewart, 2001). However, Raw264.7 cells retain its ability to proliferate under inflammatory stimulus because we notice increased cell cycle activity represented by phospho-histone H3 (pHH3) and 5-ethyny-2'-deoxyuridine (EdU) for mitotic and S-phase events, respectively (Fig. 2D). This might be a characteristic unique to this Abelson

murine leukemia virus macrophage-like cell line (Wu et al., 2013). In summary, validation of significant morphological changes using image feature based extraction methods and literature supported morphological feature changes gives us confidence to train a neural network on the control images.

Supervised deep learning parameters: input format and DNN model

In our experiment, each plate has a set of controls which consist of the same number of unstimulated and LPS-stimulated control wells. We used these images to train a deep neural network based classifier. While we acknowledge that the distribution represented by the images of the controls might differ from the distribution of the compound treated sample images, we assume that the sample images will also contain features which allow us to discriminate between LPS-stimulated cells and compound treated cells that reverse the LPS-stimulated phenotype. Hence, such a classifier should hint us on compounds with properties that reverse the LPS-stimulated phenotypes. In order to approach the DNN based classifier method on raw input images we need to understand the best parameters for optimal classifier performance. To address this, we performed two ablation studies 1) determine image resolution and size parameters and 2) determine the complexity of the DNN for optimal classification.

Deep learning models are known to be computationally expensive and are, in general, trained on rather small images with side lengths of a few hundred pixels. The images we recorded have been magnified by a factor of 20x and have a side length of 1080 pixels. One question we try to answer is which level of detail is necessary to reliably

differentiate the controls for training purposes. We want to understand what information is important such as the details (high resolution) or context (full image less pixels). In our experiments we compare four different image modifications as illustrated in **Figure 3A**. To address the details question, we test high resolution images by cropping the input image with a side length of 1080 px into sixteen 270 px (c270) and four 540 px (c540) images. Then we test the context question, by utilizing the full sized image of 1080 px but at a low resolution and resized the image to 270 px (r1080) and cropping the image into four 540 px and resized those images to 270 px (cr540).

Next we asked, could we use a simple custom built 3-layer deep model or do we need a complex EfficientNet neural network for classification (Tan & Le, 2020). Also, how much information do we really need to use for the classifications, is a single stain set enough or does both stain sets have equally valuable information? We designed a Single Tower Model (STM) that analyzes individual stain sets separately (ss1 and ss2) (**Fig.3B**) and a Combined Tower Model (CTM), a Siamese network that brings together both image stain sets (ss1+ss2) in a single head (**Fig.3C**). The models are designed with only three convolutional layers, with 16, 32, and 64 channels respectively and 3 x 3 pixel convolutions, followed by a dropout (rate=0.2) and two fully connected layers. As an activation function we use the Rectified Linear Unit (ReLU) and a sigmoid function for the final classification. Since the phenotype expressions are at cell level the convolutional network doesn't need to capture a lot of image area. That insight inspired us to aim for a shallow architecture. In addition, reducing the model depth comes with several advantages, like faster training and reduced risk of over fitting. As

a baseline deep learning model we used a EfficientNet B3, a backbone feature extraction architecture identified by neural architecture search for image classification and compared it to our own models (**Fig.3D**).

Training a deep neural network classifier on images of unstimulated and LPS-stimulated macrophage controls.

In our study, we compare the accuracy of the 4 image resolution inputs (**Fig. 4A**) and the single tower model (**Fig. 3B**) trained on individual stain sets (ss1 and ss2), the combination of the stain sets (ss1+ss2) in the Siamese model (**Fig. 3C**), as well as EfficientNet on the individual stain sets (**Fig. 3D**). We determined that input 1080px resized to 270px (r1080) shows the best performance classifying the controls for all of the deep learning models and closely followed by the 1080px cropped to 540px and resized to 270px (**Fig. 4A**). Therefore, hinting that image context, not details are important for classification. The customized combined tower model (CTM) with both stain sets shows high accuracy amongst all of the input image resolutions (**Fig. 4B**). Suggesting that both image stain sets are important for the accuracy of classification. Furthermore, a training size of at least 1,000 images is necessary to train classifiers for unstimulated and LPS-stimulated macrophages with ~99% accuracy. The overall ROC-AUC scores to evaluate the performance of our training models and image resolutions are optimal with a AUC value of 0.9 - 1 suggesting the ability to distinguish between the unstimulated and LPS-stimulated phenotype (**Fig. 4C**). The reliable classifier CTM (ss1+ss2) performed best, closely followed by EM/STM(ss2) and EM/STM(ss1). Stain set #2 (ss2) performs slightly better than stain set #1 (ss1) amongst all of the input formats and DNN models. One thing to note is that ss1 images have fewer cells than the ss2 images, which could be an element to the performance of this stain set, however, achieving a good classifier performance resolved with larger training sizes.

Deep learning primary hits

We narrow in on the resulting primary hits based on the classification accuracy of models CTM (ss1+ss2), EM(ss1), and EM(ss2) using the input format 'resized 1080' and the largest classification training size of 5,632 images. The binary classification model assigns the unstimulated class 0 and the LPS-stimulated class 1. The goal is to classify images with similar phenotypical expressions as the unstimulated controls and, hence, we specified all classifications between 0 and 0.1 to be 'hits'. The CTM model resulted in a total of 326 hits, EM(ss1) 69 hits, and EM(ss2) 65 hits. The two EfficientNet models have 31 hits in common between each other and 68 hits between the CTM and EMs (**Fig.5**). The more complex EfficientNet models are pre-trained with a large visual database for visual object recognition called ImageNet, which makes them less prone to over-fitting. This might explain their lower hits count compared to CTM.

The largest compound class revealed by the deep learning primary hits were inhibitors of PI3K/mTOR and MAPK/MEK. Other classes included histamine receptor, interleukin related, JAK, STAT, and many other drug classes including natural products (**Fig. 5B**). Several of these classes are known for their anti-inflammatory effects in various inflammatory disease contexts. Compound hits for EM with two or more similar annotated target classes reveal unique target classes associated with each stain set (**Fig. 5C**). Unique to each stain set are ss1: histamine receptor, JAK, SPHK, and synthetic cyclic peptides, and, for ss2: only EGFR. Those in common between the two stain sets are TLR, Ikk, STAT, mTOR, Syk, MEK, and natural products. However,

individual stain sets perform better at detecting certain classes. For example, ss1 detects more target classes such as Ikk, STAT, mTOR, and MEK, whereas, ss2 detects more classes for PI3k, Syk, and natural products.

Selected deep learning hits that reverse the LPS-stimulated Raw264.7 phenotype

From the primary deep learning hit list (**SI Table 1**), we visually inspected the images of the hits to confirm the reversal of the LPS phenotype. A selection of samples that exhibit the unstimulated phenotype in the primary screen were prioritized for additional follow-up studies that included dose-response and cytokine assays. We selected a subset that represents different mechanistic classes and based on literature precedent could be modulating the innate immune response. In order to eliminate false positives, we performed a dose-response assay using HCS with the addition of iNOS as a readout for inflammation on thirteen primary deep learning hits and four non-deep learning hits (three annotated as anti-inflammatory and one ROCK inhibitor) (**SI Table 3**). Unlike the unstimulated phenotype, the ROCK inhibitor causes a dramatic elongated thin morphology (Y. Liu et al., 2016) also known as a hummingbird phenotype as seen in endothelial cells infected by *Helicobacter pylori* (Bourzac, Botham, & Guillemin, 2007). There are studies showing that this elongated morphology polarizes macrophages to an anti-inflammatory M2 macrophage which are characterized by increased IL-10 expression (McWhorter, Davis, & Liu, 2015). Therefore, we investigate this thin elongated morphology inducing compound as a possible anti-inflammatory phenotype outside of the phenotypes of our training set.

One compound (TAK-242) reduced iNOS counts to baseline levels whereas, six compounds (PD032901, U0126, I-BET-762, Bay 11-7085, AZD2014, and Rapamycin) modestly reduced iNOS counts in a dose-dependent manner (**SI Fig. 1**). A visual inspection for the reversal of the LPS phenotype omitted all of the non-deep learning hits and seven other compounds. Six out of thirteen, exhibited the LPS-reversal in the primary screen at 25uM and again at 5uM in the dose-response assay (**Fig. 6A-B**). These hits represent target classes, MEK1/2, IRAK-4, I-BET, and TLR4, with the addition of ROCK and are prioritized for cytokine expression follow up (**Table 1**).

Quantitative analysis of inflammatory cytokines released from drug treated

LPS-stimulated Raw264.7 cells

To confirm the anti-inflammatory cytokine suppression activity of the deep learning hits in response to +/- LPS stimulation, 32 cytokines were assessed. Among 32 cytokines examined, 22 cytokines were enhanced by LPS-stimulation: IL-1 α , IL-2, IL-3, IL-4, IL-5, IL-6, IL-9, IL-12(P70), IL-17A, IFN- γ , IP-10, KC, LIF, GM-CSF, G-CSF, MCP-1, MIP-1 α , MIP-1 β , MIP-2, RANTES, TNF- α , and VEGF. Whereas, the other 10 cytokines, IL-1 β , IL-5, IL-7, IL-10, IL-12(P40), IL-13, IL-15, LIX, eotaxin, and MIG were notably low or undetectable in the culture supernatant of the treated samples (raw data, **SI Fig. 2**). Overall, the drug treated samples exhibit minimal changes in cytokine expression levels. In comparison to the test compound and LPS treated cytokine profiles, the test compounds elicit variable cytokine expression levels (**Fig. 7**)

The most effective pro-inflammatory cytokine inhibitor TLR4 inhibitor (TAK-242) exhibits overall cytokine expression levels similar to the unstimulated control. This class of drug modulates the immune response by blocking membrane bound TLR4 receptors from recruiting adaptor molecules that lead to a downstream signaling cascade and pro-inflammatory cytokine expression. There are several *in-vitro* and *in-vivo* studies in septic shock models demonstrating the effectiveness of TAK-242 in suppressing pro-inflammatory cytokine expression and improving survival rates (Kuzmich et al., 2017). Unfortunately, clinical trials for sepsis with TLR4 antagonists did not improve survival rates for patients with severe sepsis (Opal et al., 2013) (Marshall, 2014). Failure of these trials was attributed to trial design, patient population diversity, lack of specific biomarkers to monitor, and unknown types of infection. There could have been various other TLR pathogens from gram-positive bacteria and viruses that led to systemic inflammatory syndrome other than TLR4. However, there are several other clinical trials for the use of TLR4 antagonists to treat other inflammatory diseases such as diabetes, rheumatoid arthritis, hepatitis, and neuropathic pain (Anwar, Shah, Kim, & Choi, 2019) (Bhattacharyya et al., 2018) (Ono et al., 2020) (Ding & Liu, 2019) (Samarpita, Kim, Rasool, & Kim, 2020).

Another effective cytokine suppressor (except for VEGF) among the hits was an interleukin-1 receptor-associated kinase 4 (IRAK-4) inhibitor called "IRAK-4 Inhibitor 1". IRAK-4 is a central element in the early signal transduction of Toll-like and interleukin-1 receptors that enables the activation of immune related signal transduction pathways, NFkB and MAPK (Nobutaka Suzuki, 2002). IRAK-4 inhibition

impairs many MyD88-dependent pro-inflammatory genes while the TRIF-dependent pathway can still trigger transcriptional activation of IRAK-4 independent genes to cooperatively regulate IRF3 and NFkB activities in response to LPS (Koziczak-Holbro, Gluck, Tschopp, Mathison, & Gram, 2008). Studies *in-vitro* and *in-vivo* show that inhibiting IRAK-4 improves survival in response to multiple TLR agonist (Mages, Dietrich, & Lang, 2007) (Park et al., 2015). Several clinical trials utilizing IRAK-4 inhibitors are addressing inflammatory diseases such as, rheumatoid arthritis, inflammatory bowel disease, atopic dermatitis, and B-cell lymphoma. (Wiese, Manning-Bennett, & Abuhelwa, 2020) (Mullard, 2020) (Park et al., 2013). Furthermore, IRAK-4 deficient patients are resistant to viruses, fungi, parasites, and many bacteria but suffer from pyogenic infections (Picard et al., 2003) suggesting that blocking of IRAK-4 kinase activity is beneficial for chronic inflammatory diseases. Even though IRAK-4 kinase activity does not influence all LPS-regulated events, it still allows type I IFN responses by several other TLR pathways, allowing for the ability to still defend against most viruses and bacteria.

One of the largest target class revealed from the primary hits were MEK inhibitors. Extracellular stimuli such as growth factors, mitogens, cytokines, and stress activate mitogen-activated protein kinases (MAPK). Effector molecules downstream are MEK1/2-ERK, MEK3/6-p38, and MEK4/7-JNK that induce the translocation of nuclear transcription factors to facilitate gene expression play a central role to control cellular proliferation, development, inflammatory responses, motility, and survival (Cargnello & Roux, 2011). Generally, MEK1/2 inhibitors are used for various

oncology treatments (Chappell et al., 2011) (Cheng & Tian, 2017), however, there is some evidence that suggests that MEK1/2 inhibitors have broader functionality in relation to inflammation (Jaffee et al., 2000). Inhibition of MEK1/2 pathway in *in-vitro* and *in-vivo* have demonstrated effectiveness to regulate inflammatory responses to LPS (Shi-Lin, Yuan, Zhan, Luo-Jia, & Chao-Yang, 2015) (Li et al., 2015) (Smith, Mayeux, & Schnellmann, 2016). Studies have demonstrated their effectiveness for the treatment of autoimmune diseases such as collagen induced arthritis, rheumatoid arthritis, and lung diseases (Jaffee et al., 2000) (Long, Eddy, et al., 2017) (Shi-Lin et al., 2015) (Bergqvist et al., 2020). In our hands, most of the cytokines were reduced in the presence of MEK1/2 inhibitors (MEK162, PD0325901, and U0126) except for IP-10, KC, and RANTES. MEK1/2 inhibitors effectively suppress MyD88-dependent MEK1/2-ERK1/2 MAPK pathway pro-inflammatory cytokine expression. However, alternate signaling through the TRIF-dependent pathway still induces the expression of chemokines such as RANTES, IP-10, and KC. Although these inhibitors do not fully reduce all LPS induced pro-inflammatory mediators, MEK inhibitors have been shown to enhance IFN responses (Yang & Ding, 2019), increase bacterial killing (Kurian et al., 2019) (Long, Gong, Eddy, Liles, & Manicone, 2017), and reduce viral replication (Baturcam et al., 2019) while dampening the inflammation response.

Modest cytokine expression levels are visible with the bromodomain inhibitor (I-BET-762) notably the TNF- α cytokine expression levels are unaffected by the inhibitor but other pro-inflammatory cytokines such as IL-6 and IFN- γ are reduced. These bromodomain extra terminal (BET) proteins are important epigenetic regulators for the

expression of multiple inflammatory genes. Synthetic BET (I-BET) inhibitors interfere with the recognition of acetylated histones by nuclear proteins that initiate mRNA transcription and support mRNA elongation. As a result, the initial first wave of inflammatory gene expression is reduced affecting pro-inflammatory cytokines such as, IL-6 and INF- γ but not TNF- α and promoting survival to septic shock (Nicodeme et al., 2010) (Belkina, Nikolajczyk, & Denis, 2013). Therefore, demonstrating I-BET inhibitors as an important epigenetic immunomodulator to LPS. I-BET inhibitors for inflammation suppression is supported by a broad range of anti-inflammatory activities such as bone loss, asthma, atherosclerosis, and spinal cord injury (Tough, Tak, Tarakhovsky, & Prinjha, 2016) (Meng et al., 2014) (Maksylewicz et al., 2019) (Perry, Durham, Austin, Adcock, & Chung, 2015) (Sanchez-Ventura, Amo-Aparicio, Navarro, & Penas, 2019) (Wang et al., 2020) (Rudman et al., 2018) (Bhattacharya, Piya, & Borthakur, 2018) (Cochran, Conery, & Sims, 2019).

We investigated the ROCK inhibitor for its dramatic elongated morphology that resemble the M2 anti-inflammatory macrophages. However, Y-27632 did not fully dampen the pro-inflammatory cytokine response in comparison to the other inhibitors, although there were reduced levels of cytokines such as IL-12p70, IL-2, IL-4, GM-CSF, and IL-9. This ROCK inhibitor acts on the RhoA GTPase and actin cytoskeleton causing a reduction in podosomes, motility, and phagocytosis (Y. Liu et al., 2016) limiting inflammatory cell infiltration and shown to reduce renal fibrosis, diabetic nephropathy, and acute lung injury (Nagatoya et al., 2002) (Rao et al., 2017) (Tasaka

et al., 2005). Further exploration of this phenotype in future inflammation screens are warranted.

Conclusion

The primary focus of this research was to develop a HCS screen in macrophages using a convolutional deep learning neural network classifier to identify anti-inflammatory drug leads. We investigated morphological feature changes in the presence of pro-inflammatory endotoxin LPS and determined image resolution and DNN model parameters for reliable classification based on raw images of unstimulated and LPS-stimulated macrophages. Primary hits were further examined in a HCS dose-response assay with an iNOS probe and hits that exhibited the reversal of the LPS phenotype continued on for a multiplex cytokine analysis.

This drug discovery high content screening method can be performed in a high-throughput 384-well format using adherent immortalized murine Raw264.7 macrophages and LPS with seven fluorescent probes: nuclei, Golgi, actin, pHH3, tubulin, EdU, and mitochondria. We demonstrate that it is feasible to utilize raw images to train a DNN classifier to identify primary anti-inflammatory hits based on the unstimulated morphology of the cells. For the dose-response follow-up on the primary hits we included the iNOS probe to the HCS assay because it is an effective direct readout for inflammation. This will replace the mitotic marker pHH3 in future HCS inflammation screens. We predict that the inclusion of this probe and screening at more test-compound concentrations will filter out more false positives and improve this

screening assay. Furthermore, cytokine multiplexing is sensitive enough to measure cytokine expression from 50uL of supernatant from ~2,500 cells grown in a microtiter 384-well plate. It is possible to transfer the supernatant from the wells to a new plate or eppendorf tubes before fixing the cells for HCS. Storage of the supernatant is accomplished by freezing. This method increases the already high-dimensional information rich images with the possibility of any future cytokine expression follow-up. Finally, raw images collected from this HCS approach can be directly fed into our DNN architectures for further identification of new bioactives that modulate the cellular phenotypic response to LPS.

For the DNN studies, we test deep learning parameters such as four different image resolutions and three DNN models. We report on the results of the deep learning parameters, confirming that the level of detail necessary to reliably train a DNN model for classification does not have to be high resolution (more pixels) but rather more context (full image less pixels). The reduction of a full image with a resolution of 1080 x 1080px resized to 270 x 270px (r1080) exhibited the best performance to classify the unstimulated and LPS-stimulated controls for all of the deep learning models and stain sets. DNN approaches typically require large image datasets (>1,000) for training, however, our CTM performed best with the lowest image training size of 302 having a high accuracy of 97%-100% depending on the image resolution, closely followed by EM/STM(ss2) and EM/STM(ss1). Stain set #2 (ss2: nuclei, tubulin, EdU, and mitochondria) performs slightly better than stain set #1 (ss1: nuclei, Golgi, actin, and pHH3) amongst all of the input formats and DNN models. We determined that both

image sets are important based on the high accuracy of the CTM, however, the larger the training size (1,000+ images) the better for performance of the DNN model regardless of the input format and individual stain set.

We examine the resulting primary hits from the best performing DNN models CTM, EM(ss1), and EM(ss2) trained with the r1080 input format. The largest target classes revealed are PI3K, MEK, mTOR, natural products, JAK, STAT, Ikk, interleukin related, histamine receptors, and more. The hits selected include, TLR4 antagonist (TAK-242), IRAK-4 (IRAK inhibitor 1), MEK1/2 (MEK162, PD0325901, and U0126), Epigenetic reader domain (I-BET-762) inhibitor, and non-deep learning hit ROCK (Y-27632) inhibitor. Cross-talk and redundancy in the TLR4 signaling pathways upon LPS stimulation leads to variable cytokine expression profiles for all of the test compounds. Taken together, these data demonstrate the complexity of anti-inflammatory drug discovery based on varying mechanistic immunomodulatory effects of drugs from different MOAs and their unique differences in cytokine expression levels. Despite these complexities, we demonstrate that it possible to identify compounds that modulate the LPS response in macrophages based on cell morphology using this HCS deep learning screening approach and is relevant for anti-inflammatory drug discovery.

Materials and Methods

Reagents

The murine monocyte/macrophage Raw264.7 cells were purchased from ATCC (Manassas, VA). LPS-EB Ultrapure (E. coli 0111:B4) (catalog number: t1rl-3pelps, InvivoGen). High glucose DMEM no phenol red (Catalog number 25-501C, Genesee Scientific Corporation), Heat-inactivated FBS (Lot# 1982147, Gibco), penicillin/streptomycin, black clear bottom 384-well plates (#3764, corning). MitoTracker Red CMXRos-#9082 (catalog number: M22426, Invitrogen), rabbit antiphosphohistone H3 (catalog number: 701258, Invitrogen), mouse anti-GM130 (catalog number: 610823, BD Biosciences), EdU, 6.6uM fluorescent-Phalloidin, chicken anti-mouse Alexa-488 secondary antibody (catalog #: A21441, Life Technologies), goat anti-rabbit Alexa-647 secondary antibody (catalog #: A27040), Hoechst stain.

Screening plates and dosing

SelleckChem chemicals at 25uM (7 compound plates), MCE inflammation chemicals at 25uM and 5uM (1 compound plate), and Macmillan at 10ug/mL (1 compound plate), and Linington natural product fractions were screened at 1000 x dilution from stock (1 compound plate), and Lokey macrocyclic synthetic library at 75uM (1 compound plate). 11 compound plates total.

Cell culture conditions

The murine monocyte/macrophage Raw264.7 cells were purchased from ATCC (Manassas, VA) and cultured in high glucose DMEM no phenol red (Catalog number 25-501C, Genesee Scientific Corporation) supplemented with 10% heat-inactivated FBS (Lot# 1982147, Gibco) and 1% penicillin/streptomycin and maintained at 37°C with 5% carbon dioxide.

Immuno-Cytological Profiling

Cell seeding

Cells were seeded at a 2.5×10^3 cells/well density onto black clear bottom 384-well plates (#3764, corning) in 25uL of high glucose DMEM no phenol red supplemented with 10% heat-inactivated FBS and 1% penicillin/streptomycin (media) and incubated for at least 18- 24h at 37°C with 5% carbon dioxide before treatments.

Dosing

Cells were pinned with 100nL of pure compounds and test fractions using a Janus MDT robot (PerkinElmer). All control wells (columns 1-2 and 23-24) in plates were treated with DMSO. Cells were primed with compounds for 4h at 37°C with 5% carbon dioxide.

+/- 50ng/mL LPS stimulation

After 4h of priming with compound, positive control wells (columns 1-2) were treated with 25uL of media and negative control wells (columns 23-24) were treated with 25uL

of 0.1ug/mL LPS-EB Ultrapure (E. coli 0111:B4) in media for a final concentration of 50ng/mL. The plates treated with compound only were supplemented with 25uL of media (columns 1-22) and the plates treated with compound and LPS (columns 3-24) were supplemented with 25uL of 0.1ug/mL LPS in media. The plates were incubated at 37°C with 5% carbon dioxide for 19-20h.

Immunofluorescence

After the incubation each plate is stained with a different stain set #1 (nuclei, GM130, actin, pHH3) and stain set #2 (nuclei, tubulin, EdU, mitochondria). Stain set #2 is given a 20uM pulse of the thymidine analog 5-ethynyl-2'-deoxyuridine (EdU) and 100nM MitoTracker Deep Red FM (catalog number: M22426) for 1 h at 37°C with 5% carbon dioxide. At 25°C (room temperature) cells were fixed with 4% formaldehyde for 20min, washed with PBS, treated with 0.5% Triton X-100 in PBS for 10min, washed with PBS, and blocked with 2% BSA PBS solution for 20 min - 1 h. Stain set #2 plates are washed with PBS and stained with rhodamine-azide using click chemistry by incubation with 4mM CuSO₄, 2mg/mL sodium ascorbate, and 1mg/mL rhodamine azide in 100mM TRIS buffer for 1 h at 25°C in the dark. After washing with PBS stain set #2 plates are incubated with mouse anti-Tubulin FITC (catalog number: F2168-2mL, Sigma) in 2% BSA in PBS overnight at 4°C. Plates were rinsed with PBS and 1:1000 chicken anti-mouse Alexa-488 secondary antibody (catalog number: A21441, Life Technologies) and 1:10,000 Hoechst stain in 2% BSA in PBS were added for 1 h at 25°C. Plates are washed two times with PBS and left in 0.1% azide in PBS. Stain set

#1 plates at 25°C (room temperature) cells were fixed with 4% formaldehyde for 20min, washed with PBS, treated with 0.5% Triton X-100 in PBS for 10min, washed with PBS, and blocked with 2% BSA PBS solution for 20 min-1 h. After washing with PBS plates are incubated with rabbit antiphosphohistone H3 (catalog number: 701258, Invitrogen), mouse anti-GM130 (catalog number: 610823, BD Biosciences), and 6.6uM fluorescent-Phalloidin in 2% BSA overnight at 4°C. Plates were rinsed with PBS and 1:1000 chicken anti-mouse Alexa-488 secondary antibody, 1:1000 goat anti-rabbit Alexa-647 secondary antibody, and 1:10,000 Hoechst stain in 2% BSA in PBS were added for 1 h at 25°C. Plates are washed two times with PBS and left in 0.1% azide in PBS.

Imaging

Plates were imaged using a 20x Nikon objective ImageXpress Micro XLS automated epifluorescence microscope (Molecular Devices, Sunnyvale). Four images per well for each wavelength in a plate resulting in 6144 images per plate (~15Gb of images/plate).

Cytological Profiling fingerprint

Images were analyzed with MetaXpress software (Molecular devices). Measurements were taken using built-in morphometry metrics, the multi-wavelength cell scoring, transfluor, and pits and vesicles modules. Custom written scripts were used to compare treated measurements with the measurements of the unstimulated and LPS-stimulated treated control wells, then convert each feature to a "histogram difference" (HD) score (Woehrmann et al., 2013). This produced a 345 feature vector fingerprint.

Uninformative features with zero standard deviation across all perturbations were removed. In addition, redundancy was further reduced using the `findCorrelation` function in the R-package `caret`. Briefly all feature pairs with Pearson correlation coefficients greater than 0.95 were flagged and the member of each pair with the highest mean correlation to all other features was removed, resulting in the final CP fingerprint for each of the treatment conditions. `Caret` package version 6.0-79; R-version 3.3.3

Architecture/Models

Costume built DNN architecture, called *Tower*, based on the assumption that the features which we will observe are at a constant scale. Hence, we only use three convolutional layers with 16, 32, and 64 channels respectively and 3 x 3 pixel convolutions, followed by a dropout (rate=0.2) and two fully connected layers. As activation function we use the Rectified Linear Unit (ReLU) and a sigmoid function for the final classification. As a baseline deep learning model we used a EfficientNet B3, a backbone feature extraction architecture identified by neural architecture search for image classification and compared it to our own models (Tan & Le, 2020). In our experiments, we compare the performance of naive model ensembling with a machine learning based approach for the tower models. Due to the resource limitations we were not able to train the combined stain sets (ss1+ss2) using the EfficientNet model. Hence, the set of architectures we compare consists of a single Tower, two combined Towers,

and EfficientNet. As loss function we used binary cross entropy and for training we use the Adam optimization algorithm with a learning rate of $1e-5$ ($\beta_1=0.5$ and $\beta_2=0.9$).

Deep learning based classification

Each screening plate has a set of controls which consist of the same number of unstimulated and LPS-stimulated wells. Control images from each plate are used to train a deep neural network (DNN) based classifier. The data set is split into 70:15:15 for training, validation, and testing. Training each model was ~ 1 to 3 hours depending on the architecture and the input format. We used two Nvidia GeForce GTX 1080Ti GPUs with two Intel Xenon E5-2640 (40 cores total).

Assessment of cytokine production

The production of mouse cytokine levels from supernatant were measured by Eve Technologies Corporation (Calgary, Alberta, Canada) using a Milliplex mouse cytokine/chemokine 32-plex kit (Millipore, St. Charles, MO). Raw264.7 cells were plated into 384-well plates (2.5×10^3 cells/well) and grown overnight at 37°C with 5% CO_2 . Cells were pre-treated with a dose-response range of 25 μM - 0.5nM of compound for 4h or vehicle control 0.01% DMSO then stimulated +/- 50ng/mL LPS for a total of 24h. The cell supernatant from the 5 μM concentration was collected, frozen and sent to Eve Technologies for a cytokine/chemokine 32-plex cytokine analysis. The resulting data consists of 32 cytokine/chemokine measurements for 16 treatment samples (7 known bioactive compounds +/- LPS =14 and 2 controls) in triplicate. Cytokines measured are, eotaxin, granulocyte-macrophage colony stimulating factor (GM-CSF),

granulocyte colony stimulating factor (G-CSF), interferon (IFN)- γ , IL-1 α , IL-1 β , IL-2, IL-3, IL-4, IL-5, IL-6, IL-7, IL-9, IL-10, IL-12(P40), IL-12(P70), IL-13, IL-15, IL-17, IFN- γ -induced protein-10 (IP-10), keratinocyte chemoattractant (KC), leukemia inhibitory factor (LIF), LPS-induced CXC chemokine (LIX), monocyte chemoattractant protein-1 (MCP-1), macrophage colony stimulating factor (M-CSF), monokine induced by IFN- γ (MIG), macrophage inflammatory protein (MIP)-1 α , MIP-1 β , MIP-2, chemokine C-C motif ligand 5 (CCL5/RANTES), tumor necrosis factor (TNF)- α , and vascular endothelial growth factor (VEGF). The heat map represents distance score calculations using a z-score range of three standard deviations from the mean for the +/-LPS compound treated samples and of the controls (unstimulated and LPS-stimulated). To calculate the inhibition of compounds on cytokine release the following formula was used: $((\text{LPS response} - \text{LPS response in presence of inhibitors}) / 3(\text{sum of the standard deviations})) / ((\text{LPS response} - \text{unstimulated response}) / 3(\text{sum of the standard deviations}))$.

Acknowledgements

Research reported in this publication was supported by the National Center For Complementary & Integrative Health of the National Institutes of Health under Award Number F31AT010322. The content is solely the responsibility of the authors and does not necessarily represent the official views of the National Institutes of Health.

**2.2 FIGURES FOR:
High-content image-based screening and deep learning for the detection of anti-inflammatory drug leads**

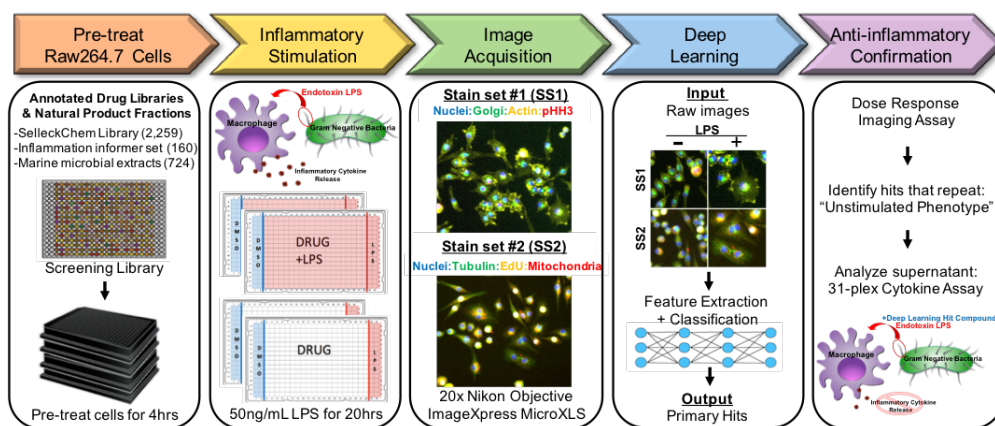
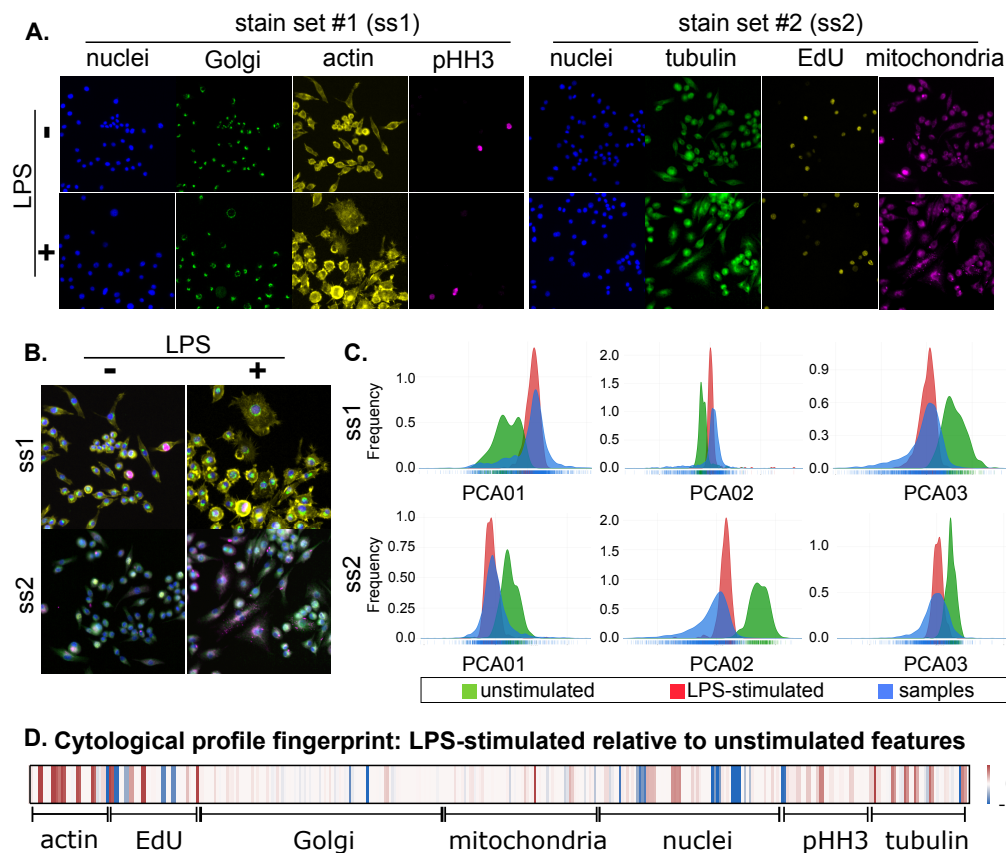


Figure 1. Workflow to identify anti-inflammatory hits using deep learning.

Raw264.7 cells were primed with chemical screening libraries for 4 h, then each plate either received media alone or media with 50ng/mL LPS for 24 h. Each plate contains 64 non-drug treated controls (32 unstimulated controls and 32 LPS stimulated controls). The cells are fixed, processed, and stained with the established probes that target cell cycle, organelles, and cytoskeletal features. The generated images from a ImageXpress MicoXLS at 20x are used to train a deep neural network classifier on unstimulated and LPS-stimulated macrophages. Primary hit compounds that exhibit the unstimulated phenotype are selected for dose-response and cytokine assays based on high potency, selectivity, and desirable pharmacokinetic properties. The image data generated from this screen is nearly 500 gigabytes.



Raw264.7 feature changes with LPS stimulation:

- Enlarged cell and organelles: actin, tubulin, nuclei, mitochondria, golgi
- Exaggerated actin and tubulin filopodia and protrusions
- Increased Golgi dispersal and pixel intensity
- Increased mitochondria fragmentation
- Increased cell division events (EdU and pHH3 counts)

Figure 2. Measured differences in Raw264.7 cellular features with LPS stimulation.

A. Images of unstimulated and LPS-stimulated (non-drug treated) Raw264.7 macrophages. Stain set #1(ss1): **Nuclei** (hoechst, blue), **Golgi** (GM130, green), **Actin** (phalloidin, yellow), **Mitosis** (phospho-Histone H3, Red). Stain set #2 (ss2): **nuclei** (Hoechst, blue), **tubulin** (alpha-tubulin, green), **S-phase** (EdU, yellow), **mitochondria** (MitoTracker, red). **B.** Merged images of unstimulated and LPS-stimulated cells **C.** Principal component analysis (PCA) histograms describing little overlap in features between unstimulated (green) and LPS-stimulated features (red) and the overall spread of the samples (blue) amongst the controls **D.** Cytological profile fingerprint is composed of 375 extracted cellular features of LPS treated relative to the unstimulated controls. Red features indicate positive LPS-stimulated values relative to unstimulated control values, blue features indicate negative LPS-stimulated values relative to

unstimulated control, and white features are identical to those in both of the controls. Description of features changes in the presence of LPS.

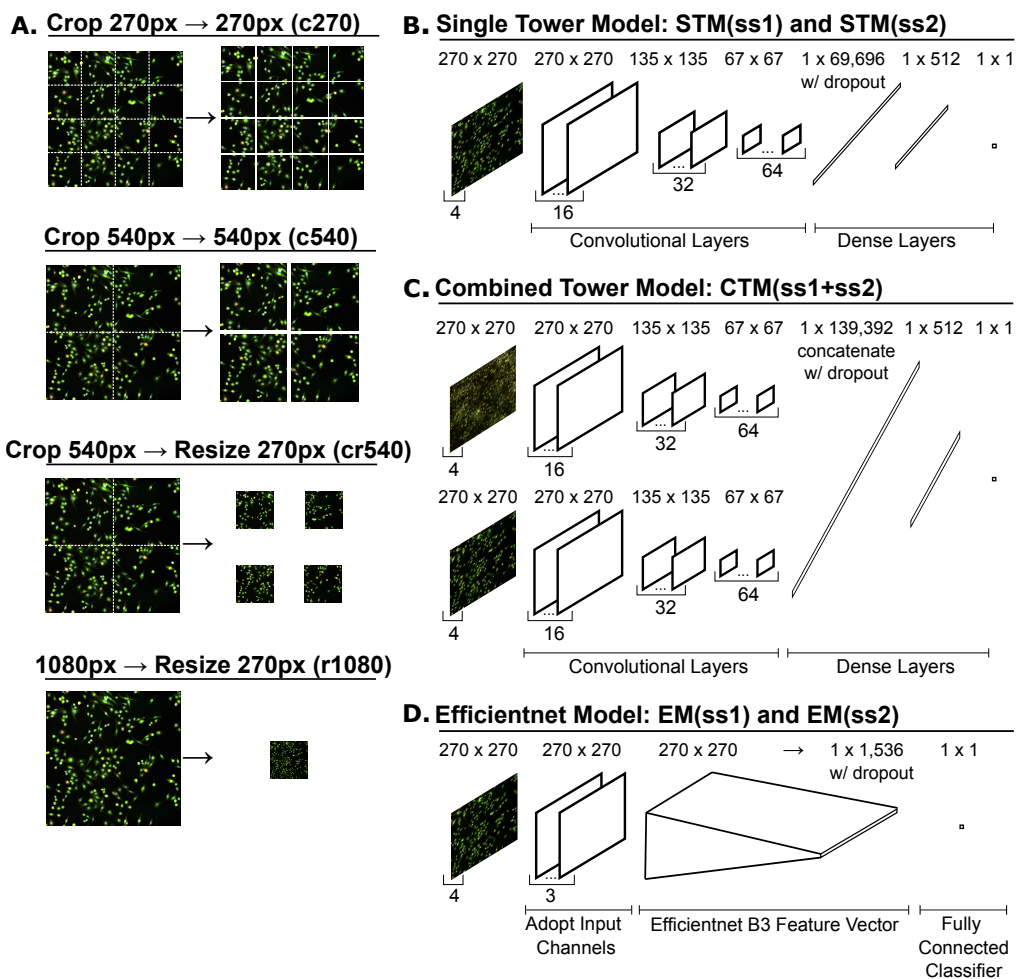


Figure 3. Deep learning parameters: image resolution and DNN models.

A. Image resolution input format: starting with image size 1080 x 1080 pixels (px) that are cropped into sixteen: 270 x 270 px images (c270); cropped into four: 540x540px (c540); cropped into four: 540x540px and resized to 270x270px (cr270); and one: resized to 270x270px (r1080). **B.** Single Tower Model (STM) costume built simple 3-layer deep model that analyzes individual stain sets separately (ss1 and ss2) **C.** Combined Tower Model (CTM) a Siamese network which consists of a simple 3-layer tower and brings together both image stain sets (ss1+ss2) in a single head. **D.** EfficientNet Model (EM) is an image classification baseline model that analyzes individual stain sets separately (ss1 and ss2).

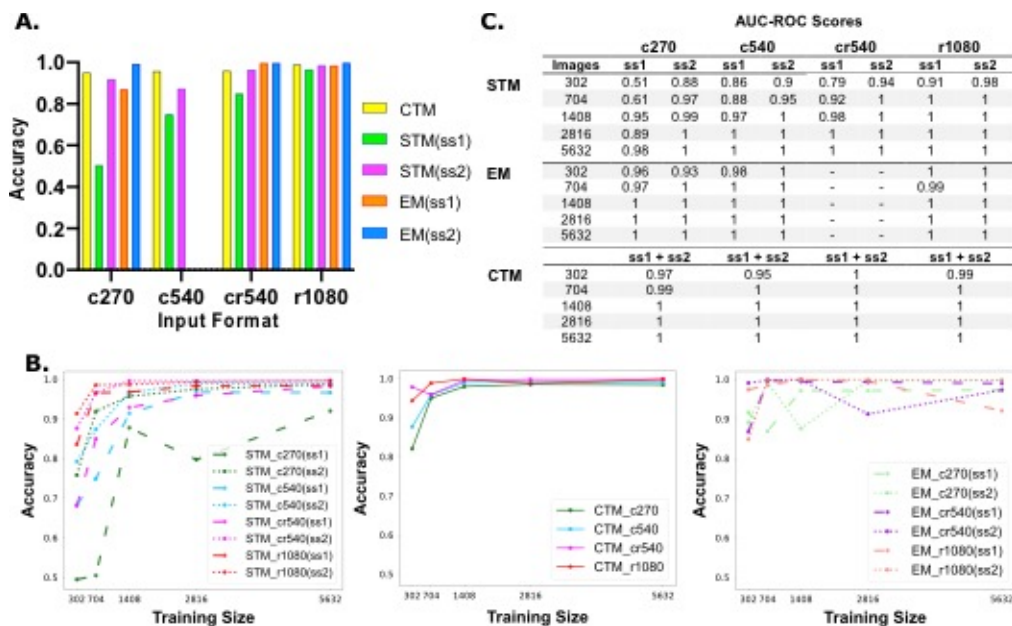


Figure 4. Best classification performance. Image resolution r1080 and cr540 and DNN architecture: CTM, EM(ss1), and EM(ss2)

Image context seems to be more important for classification. Improvements based on training size saturates around 1,000 images. **A.** Comparison of the classifier performance of varying image resolutions (c270, c540, cr540, r1080), models (STM, CTM, EM), and stain sets (ss1 and ss2). **B.** Comparison of the classifier performance on varying training dataset sizes. Training was performed on 302, 704, 2816, and 5632 images. **C.** Table summarizing the model classification confidence, measured by the Receiver Operating Characteristic (ROC curve) and Area Under the Curve (AUC) metric. Data is split into 70:15:15. Each model is trained on 70% of the unstimulated and LPS-stimulated controls images, then 15% is for validation during training, and 15% are used for testing. Information for EfficientNet c540 (cropped 540 x 540px) is missing due to its high complexity and the lack of computational power. Training each model took in between 1 to 3 hours depending on the architecture and the input format. We used two Nvidia GeForce GTX 1080Ti GPUs with two Intel Xenon E5-2640 (40 cores total).

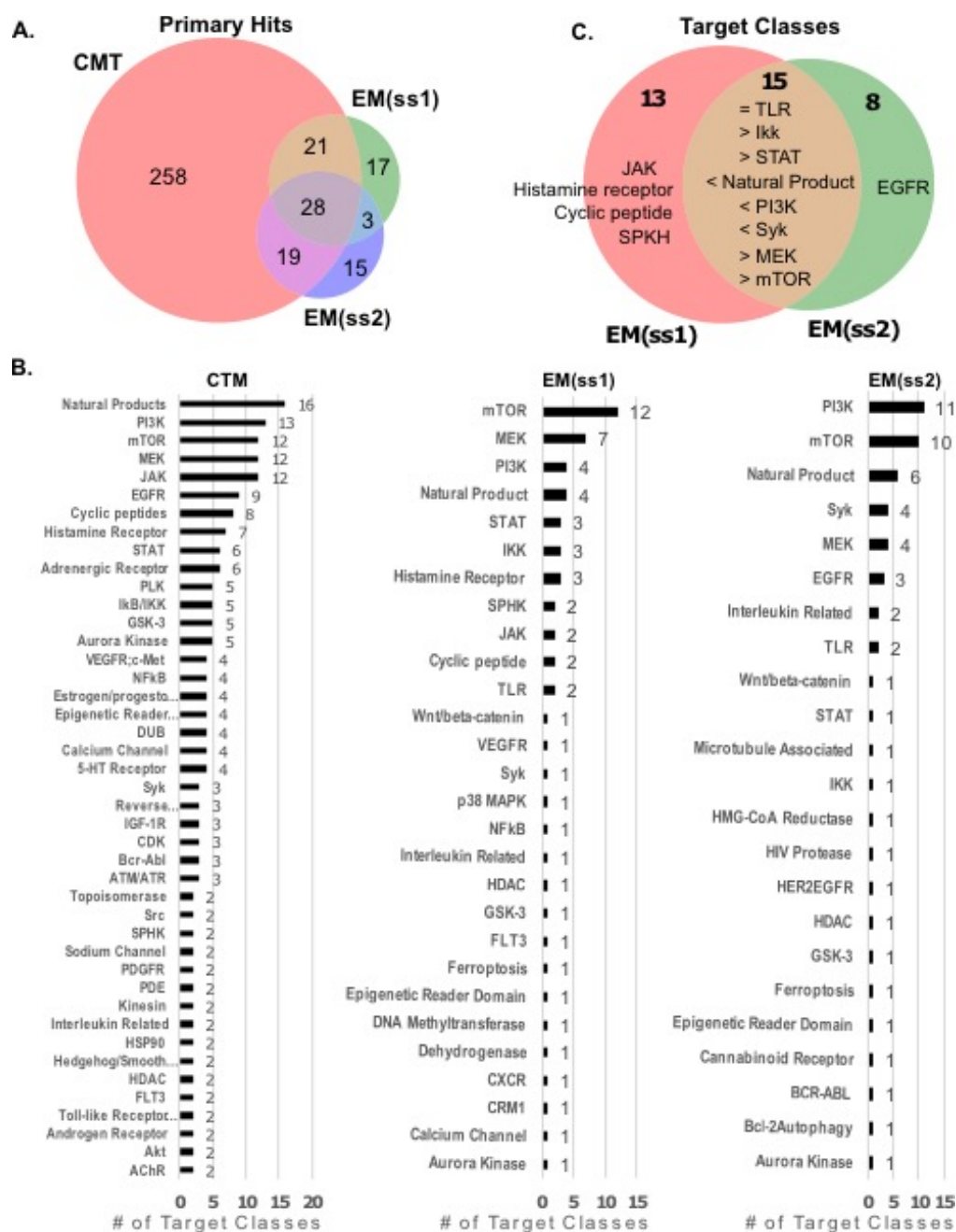


Figure 5. The largest target classes from deep learning hits are PI3K, MEK, mTOR, and natural products.

Comparison of the primary hits from the input format resized 1080 and deep learning models: CTM, EM(ss1), and EM(ss2). **A.** Venn diagram illustrating the number of unique and shared primary hits between the DNN models. CTM resulted in 326 total hits sharing 68 compounds with the EMs. EM(ss1) resulted in 69 total hits and EM(ss2)

resulted in 65 total hits, sharing 31 compounds. **B.** Analysis of primary hit target classes. CTM exhibits a total of 45 target classes with at least two annotated compounds in each respective class. Not graphed are 60 single target classes and 67 annotated as others. EM(ss1) resulted in a total of 29 classes, not graphed are 8 annotated as others. EM(ss2) resulted with a total of 24 classes, not graphed are 8 annotated as others. **C.** Venn diagram comparing the EfficientNet model and stain sets, illustrating the unique and shared target classes for each.

Table 1. List of Selected Deep Learning Hits

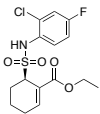
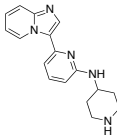
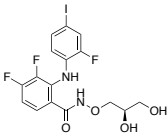
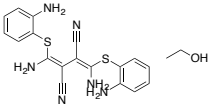
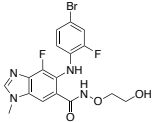
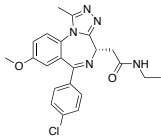
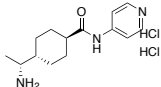
Common Name	Annotation/MOA	Structure	PubChem CID
1 TAK-242/ Resatorvid	TLR4 inhibitor		11703255
2 IRAK inhibitor 1	IRAK-4 inhibitor		44449078
3 PD0325901	MEK inhibitor		9826528
4 U0126-EtOH	MEK 1/2 inhibitor		73014263
5 MEK162/ Binimetinib	MEK 1/2 inhibitor		10288191
6 I-BET-762/ Molibresib	BET inhibitor		46943432
7 Y-27632 2HCl	Rho Kinase inhibitor		9901617

Table 1. Selected deep learning hit list.

Selected subset with different mechanistic classes. Compounds were selected for secondary screening based on availability and biological interests. **Y-27632 (ROCK inhibitor) is not a deep learning hit.

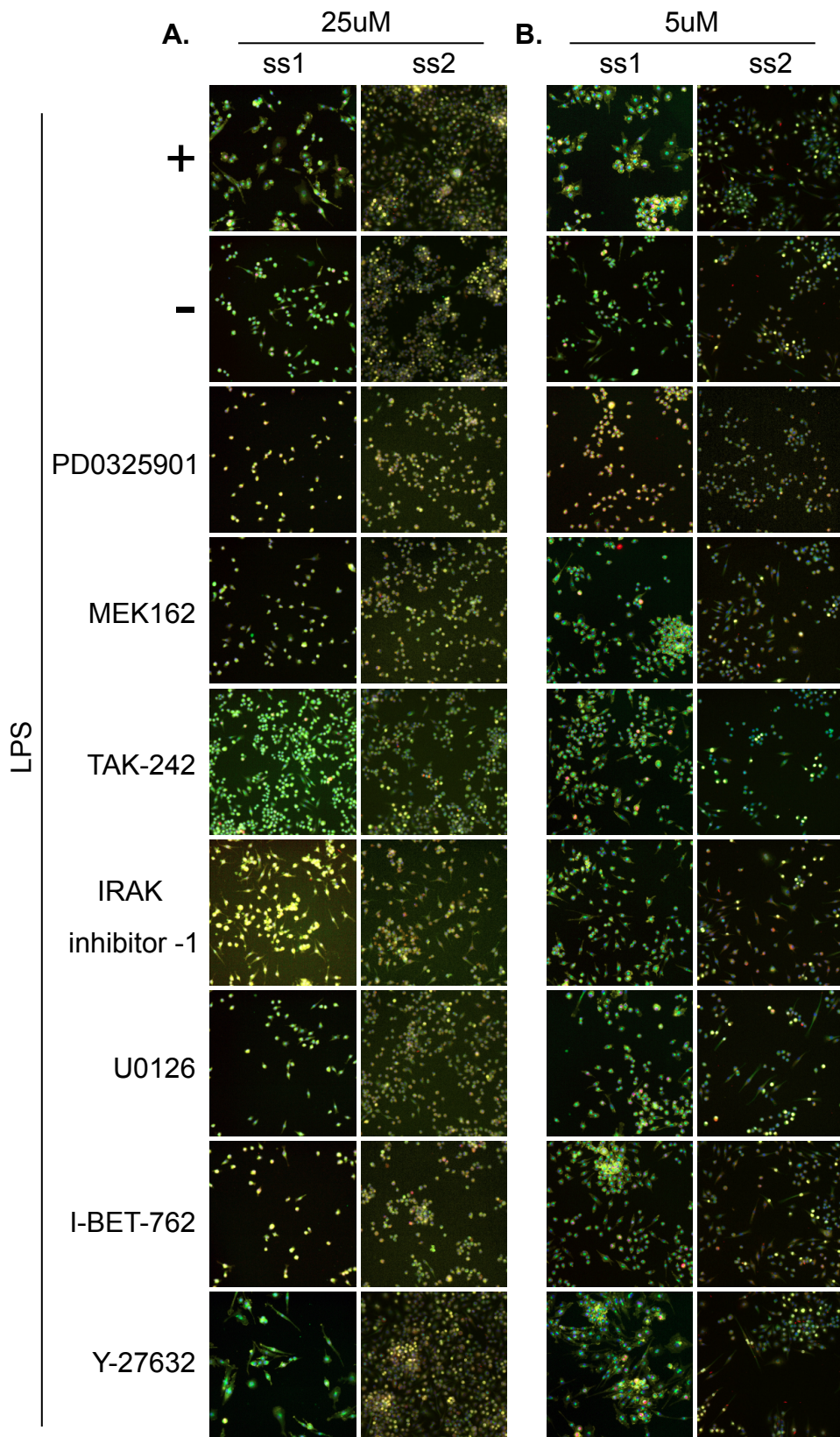


Figure 6. Deep learning selected hits exhibit the reversal of the LPS-phenotype. Stain sets 1 and 2 merged images of cells treated with 25uM and 5uM of test-compound and 50ng/mL LPS. **A.** Primary screen images at 25uM. **B.** Follow up on selected hits at a lower concentration 5uM, to confirm the reversal of LPS-stimulated phenotype.

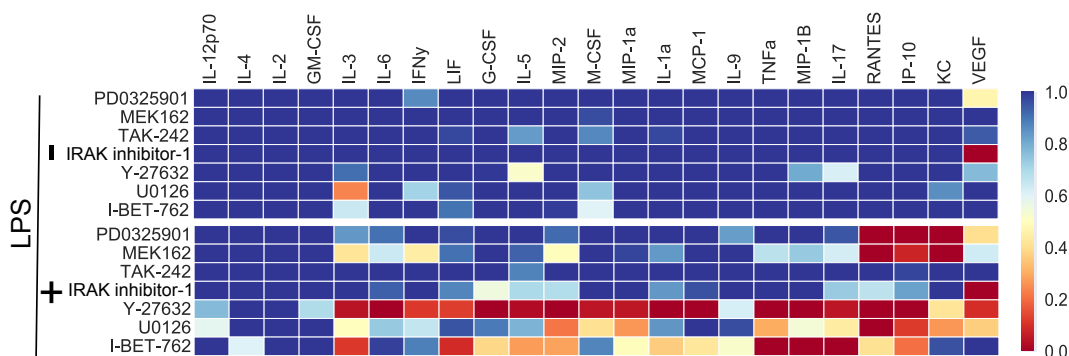


Figure 7. Deep learning selected hits exhibit anti-inflammatory effects based on pro-inflammatory mediators' expression profiles.

Heat map indicating reduction in 50ng/mL LPS stimulated cytokine profiles following 24hrs of 5uM chemical compound exposure (n=3). Blue (1) indicates similar cytokine expression levels to unstimulated control and red (0) indicates similar cytokine expression levels to the LPS-stimulated control. The heat map represents distance score calculations using a z-score range of three standard deviations from the mean for the +/-LPS compound treated samples and the controls (unstimulated and LPS-stimulated). To calculate the inhibition of compounds on cytokine release the following formula was used: $((LPS \text{ response} - LPS \text{ response in presence of inhibitors}) / 3(\text{sum of the standard deviations})) / ((LPS \text{ response} - \text{unstimulated response}) / 3(\text{sum of the standard deviations}))$.

2.2 SUPPORTING INFORMATION FOR:

High content image-based screening and deep learning for the detection of anti-inflammatory drug leads

Tannia A. Lau¹, Elmar Mair², Scott Lokey¹

¹Department of Chemistry and Biochemistry,
University of California Santa Cruz, Santa Cruz, CA 95064.

²No Affiliation, Santa Cruz, CA 95060

Contents of the files supplied:

SI Table 1: Deep learning primary hits

SI Table 2: Target class comparison for EfficientNet models

SI Table 3: Compounds for follow-up

SI Figure 1: iNOS dose-response curves

SI Figure 2: 32-plex cytokine/chemokine

SI Table 1. Deep learning hits for CTM, EM(ss1), and EM(ss2)

SI Table 1. Deep learning hits for CTM, EM(ss1), and EM(ss2)

CTM		
LY2784544_JAK_25uM	Chlorquinaldol_Others_25uM	Simvastatin_Others_25uM
RLUS-2144F	Gynostemma Extract_Others_25uM	Tebipenem Pivoxil_Others_25uM
Afacalcidol_Others_25uM	PhepB-2Me	RLUS-2140E
BGT226 (NVP-BGT226)_PI3KmTOR_25uM	BIX 02188_MEK_25uM	PR-619_DUB_25uM
1NMe3-26F	Bexarotene_Others_25uM	Fenticonazole Nitrate_Others_25uM
TCS 359_FLT3_25uM	Pifithrin-_p53_25uM	Desloratadine_Histamine Receptor_25uM
SW203051	CCT128930_Akt_25uM	VE-821_ATM/ATR_25uM
WZ4002_EGFR_25uM	Valnemulin HCl_Others_25uM	Sertaconazole nitrate_Others_25uM
XMD8-92_ERK_25uM	SH-4-54_STAT_25uM	Quinacrine 2HCl_Others_25uM
NVP-BKM120 (Hydrochloride)_PI3K_25uM	GSK461364_PLK_25uM	FLI-06_Notch_25uM
ZM 306416_VEGFR_25uM	IM-12_GSK-3_25uM	CCCP_IFNAR:STING_25uM
Ruxolitinib (INCB018424)_JAK_25uM	Lopinavir_HIV Protease_25uM	Fenspiride HCl_Others_25uM
Rilpivirine_Reverse Transcriptase_25uM	PJ34_PARP_25uM	Dronedrone HCl_Others_25uM
(S)-crizotinib_MTH_25uM	LY2608204_Others_25uM	HMN-214_PLK_25uM
BMS-536924_IGF-1R_25uM	Sulconazole Nitrate_Others_25uM	Retapamulin_Others_25uM
(-)-MK 801 Maleate_GluR_25uM	RLUS-2143D	TAK-733_MEK_25uM
K145 (hydrochloride)_SPHK_25uM	I-BET-762_Epigenetic Reader Domain_25uM	Rimonabant_Cannabinoid Receptor_25uM
Gimeracil_Dehydrogenase_25uM	BMS-833923_Hedgehog/Smoothened_25uM	Mefloquine HCl_Others_25uM
Oridonin_Others_25uM	1NMe3-2Ala3E6F	Afatinib (BIBW2992)_EGFRHER2_25uM
Triflupromazine HCl_25uM	GF109203X_PKC_25uM	CP-673451_PDGFR_25uM
Felodipine_Calcium Channel_25uM	Loperamide HCl_Opioid Receptor/Autophagy_25uM	NSC697923_E2_25uM
Dasatinib_Bcr-Ablc-KitSrc_25uM	Clomifene citrate_Estrogen/progesterone Receptor_25uM	Ticagrelor_P2 Receptor_25uM
Dydrogesterone_Others_25uM	BIO_GSK-3_25uM	Ibrutinib (PCI-32765)_BTK_25uM
Albendazole_Others_25uM	AZD3514_Androgen Receptor_25uM	NVP-ADW742_IGF-1R_25uM
LDK378_ALK_25uM	Fluvoxamine maleate_5-HT Receptor_25uM	Thonzonium Bromide_25uM
SL-327_MEK_25uM	Etravirine (TMC125)_Reverse Transcriptase_25uM	PP242_mTORAutophagy_25uM
Lomitapide_Others_25uM	TG100713_PI3K_25uM	Phenazopyridine HCl_Others_25uM
Solfifenacin succinate_AChR_25uM	Oxethazaine_25uM	Zinc Pyrithione_Proton Pump_25uM
LDN-57444_DUB_25uM		Volasertib (BI 6727)_PLK_25uM
Golvatinib (E7050)_VEGFRc-Met_25uM		PP2_Src_25uM

H 89 2HCl_PKA_25uM	NMS-P937 (NMS1286937)_PLK_25uM	AZ 3146_Kinesin_25uM
Nifedipine_Others_25uM	RLUS-2092D	K-Ras(G12C) inhibitor 9_Rho_25uM
NVP-AEW541_IGF-1R_25uM	MK591_FLAP_25uM	ABT-263 (Navitoclax)_Bcl-2_25uM
SW202317	Lacidipine_Calcium Channel_25uM	RLUS-2143E
Stattic_STAT_25uM	BAPTA-AM_Others_25uM	Luteolin_PDE_25uM
IKK-16 (IKK Inhibitor VII)_IkB/IKK_25uM	Mometasone furoate_Others_25uM	BAY 11-7082_IkB/IKKE2 conjugating_25uM
GSK2334470_PDK-1_25uM	AS1517499_STAT;STAT_5uM	Cetylpyridinium Chloride_Others_25uM
NVP-BKM120 (Hydrochloride)_PI3K_5uM	A-674563_PKACDKAkt_25uM	VER-49009_HSP90_25uM
AZD1480_JAK_25uM	Roscovitine (Seliciclib/CYC202)_CDK_25uM	BAY 11-7085_NF-kB_25uM
Idebenone_Others_25uM	LY2835219_CDK_25uM	Carvedilol_Adrenergic Receptor_25uM
LY2228820_p38 MAPK_25uM	IRAK inhibitor 1_IRAK;IRAK_25uM	Bay 11-7085_NF-kappa B_25uM
WP1066_JAK_25uM	R406_SykFLT3_25uM	Enoxolone_Others_25uM
Montelukast Sodium_Others_25uM	Penfluridol_Others_25uM	RLUS-2140D
RLUS-2142D	Torin 2_ATM/ATRmTOR_25uM	KPT-185_CRM1_25uM
PP121_DNA-PKPDGFRmTOR_25uM	Ro3280_PLK_25uM	AZD1080_GSK-3_25uM
Caffeic Acid Phenethyl Ester_NFkB_25uM	Alexidine HCl_25uM	Crenolanib (CP-868596)_PDGFR_25uM
Pizotifen Malate_Others_25uM	SW203050	ZM 447439_Aurora Kinase_25uM
HA*-25NMe	SKI II_S1P Receptor_25uM	MK-8776 (SCH 900776)_CDKChk_25uM
RLUS-2146F	TG101209_JAKFLT3c-RET_25uM	XL888_HSP (e.g. HSP90)_25uM
RLUS-2147E	SB743921_Kinesin_25uM	Verapamil HCl_Others_25uM
NU7441 (KU-57788)_DNA-PKPI3K_25uM	Tubacin_HDAC_25uM	Benzethonium Chloride_Others_25uM
AZD1208_Pim_25uM	1NMe3-3EV	Deltarasin_PDE_25uM
Pelitinib (EKB-569)_EGFR_25uM	Ketoprofen_COX_25uM	CPI-203_Epigenetic Reader Do_25uM
Tetracycline HCl_Others_25uM	SNS-314 Mesylate_Aurora Kinase_25uM	JNK-IN-8_JNK_25uM
Schisandrin B (Sch B)_Others_25uM	RLUS-2079D	1NMe3'-L5lpg
PHA-665752_c-Met_25uM	Domiphen Bromide_Others_25uM	2-Methoxyestradiol (2-MeOE2)_HIF_25uM
Azaguanine-8_Others_25uM	TG101348 (SAR302503)_JAK_25uM	Cyclosporin A_Others_25uM
MG-132_Proteasome_25uM	Lomerizine HCl_Others_25uM	PP1_Src_25uM
Degrasyn (WP1130)_DUBBcr-Abl_25uM	RKI-1447_ROCK_25uM	Haloperidol_Others_25uM
Butein_EGFR_25uM	Toltrazuril_Others_25uM	1NMe33-1Me6F
AZD9291_EGFR_25uM	Fluoxetine HCl_5-HT Receptor_25uM	HO-3867_STAT_25uM
Pimecrolimus_25uM	Propafenone HCl_Sodium Channel_25uM	Thiondiazine HCl_25uM
Isoconazole nitrate_Others_25uM	AZ191_Others_25uM	Progesterone_Others_25uM
BMS-345541 (free base)_IKK_5uM	Ranolazine 2HCl_Calcium Channel_25uM	Menadione_Others_25uM
Darifenacin HBr_AChR_25uM	755-8	Canagliflozin_SGLT_25uM

RITA (NSC 652287)_E3 Ligase p53_25uM	BGT226 (NVP-BGT226)_PI3K_mTOR_25uM	GSK461364_PLK_25uM
Tioconazole_Others_25uM	1NMe3-26F	IM-12_GSK-3_25uM
Mitoxantrone_Topoisomerase_25uM	TCS 359_FLT3_25uM	Lopinavir_HIV Protease_25uM
Econazole nitrate_Others_25uM	SW203051	PJ34_PARP_25uM
NPS-2143_CaSR_25uM	WZ4002_EGFR_25uM	LY2608204_Others_25uM
PD318088_MEK_25uM	XMD8-92_ERK_25uM	Sulconazole Nitrate_Others_25uM
MRT67307_ULK;Autophagy;IKK_25uM	NVP-BKM120 (Hydrochloride)_PI3K_25uM	RLUS-2143D
Duloxetine HCl_5-HT Receptor_25uM	ZM 306416_VEGFR_25uM	I-BET-762_Epigenetic Reader Domain_25uM
Amlodipine_Calcium Channel_25uM	Ruxolitinib (INCB018424)_JAK_25uM	BMS-833923_Hedgehog/Smoothened_25uM
ZM 39923 HCl_JAK_25uM	Rilpivirine_Reverse Transcriptase_25uM	1NMe3-2Ala3E6F
Filgotinib (GLPG0634)_JAK_25uM	(S)-crizotinib_MTH_25uM	GF109203X_PKC_25uM
OTX015_BET_25uM	BMS-536924_IGF-1R_25uM	Loperamide HCl_Opioid Receptor/Autophagy_25uM
VS-5584 (SB2343)_PI3K_25uM	(-)-MK 801 Maleate_GluR_25uM	Clomifene citrate_Estrogen/progesterone Receptor_25uM
PTC-209 HBr_Others_25uM	K145 (hydrochloride)_SPHK_25uM	BIO_GSK-3_25uM
RS-127445_5-HT Receptor_25uM	Gimeracil_Dehydrogenase_25uM	AZD3514_Androgen Receptor_25uM
Phenothiazine_Others_25uM	Oridonin_Others_25uM	Fluvoxamine maleate_5-HT Receptor_25uM
BMS-794833_VEGFRc-Met_25uM	Triflupromazine HCl_25uM	Etravirine (TMC125)_Reverse Transcriptase_25uM
PD184352 (CI-1040)_MEK_25uM	Felodipine_Calcium Channel_25uM	TG100713_P13K_25uM
Mianserin HCl_Histamine Receptor_25uM	Dasatinib_Bcr-Ablc-KitSrc_25uM	Oxethazaine_25uM
CEP-33779_JAK_25uM	Dydrogesterone_Others_25uM	Simvastatin_Others_25uM
Palomid 529 (P529)_mTOR_25uM	Albendazole_Others_25uM	Tebipenem Pivoxil_Others_25uM
Bardoxolone Methyl_kB/IKK_25uM	LDK378_ALK_25uM	RLUS-2140E
Golgicide A_ATPase_25uM	SL-327_MEK_25uM	PR-619_DUB_25uM
Bafetinib (INNO-406)_Bcr-Abl_25uM	Lomitapide_Others_25uM	Fenticonazole Nitrate_Others_25uM
Mitoxantrone HCl_Others_25uM	Solifenacin succinate_AChR_25uM	Desloratadine_Histamine Receptor_25uM
Disulfiram_Others_25uM	LDN-57444_DUB_25uM	VE-821_ATM/ATR_25uM
NH125_ELF2_25uM	Golvatinib (E7050)_VEGFRc-Met_25uM	Sertaconazole nitrate_Others_25uM
Dicyclomine HCl_25uM	Chlorquinaldol_Others_25uM	Quinacrine 2HCl_Others_25uM
Beta-Lapachone_Topoisomerase_25uM	Gynostemma Extract_Others_25uM	FLI-06_Notch_25uM
P22077_DUB_25uM	PhepB-2Me	CCCP_IFNAR;STING_25uM
Oxcarbazepine_Sodium Channel_25uM	BIX 02188_MEK_25uM	Fenspiride HCl_Others_25uM
PD168393_EGFR_25uM	Bexarotene_Others_25uM	Dronedarone HCl_Others_25uM
LY2784544_JAK_25uM	Pifithrin-_p53_25uM	HMN-214_PLK_25uM
RLUS-2144F	CCT128930_Akt_25uM	
Alfacalcidol_Others_25uM	Valnemulin HCl_Others_25uM	
	SH-4-54_STAT_25uM	

Retapamulin_Others_25uM	RLUS-2147E	Tubacin_HDAC_25uM
TAK-733_MEK_25uM	NU7441 (KU-57788)_DNA-PKPI3K_25uM	1NMe3-3EV
Rimonabant_Cannabinoid Receptor_25uM	AZD1208_Pim_25uM	Ketoprofen_COX_25uM
Mefloquine HCl_Others_25uM	Pelitinib (EKB-569)_EGFR_25uM	SNS-314 Mesylate_Aurora Kinase_25uM
Afatinib (BIBW2992)_EGFRHER2_25uM	Tetracycline HCl_Others_25uM	RLUS-2079D
CP-673451_PDGFR_25uM	Schisandrin B (Sch B)_Others_25uM	Domiphen Bromide_Others_25uM
NSC697923_E2_25uM	PHA-665752_c-Met_25uM	TG101348 (SAR302503)_JAK_25uM
Ticagrelor_P2 Receptor_25uM	Azaguanine-8_Others_25uM	Lomerizine HCl_Others_25uM
Ibrutinib (PCI-32765)_BTK_25uM	MG-132_Proteasome_25uM	RKI-1447_ROCK_25uM
NVP-ADW742_IGF-1R_25uM	Degrasyn (WP1130)_DUBBcr-Abl_25uM	Toltrazuril_Others_25uM
Thonzonium Bromide_25uM	Butein_EGFR_25uM	Fluoxetine HCl_5-HT Receptor_25uM
PP242_mTORAutophagy_25uM	AZD9291_EGFR_25uM	Propafenone HCl_Sodium Channel_25uM
Phenazopyridine HCl_Others_25uM	Pimecrolimus_25uM	AZ191_Others_25uM
Zinc Pyrithione_Proton Pump_25uM	Isoconazole nitrate_Others_25uM	Ranolazine 2HCl_Calcium Channel_25uM
Volasertib (BI 6727)_PLK_25uM	BMS-345541 (free base)_IKK_5uM	755-8
PP2_Src_25uM	Darifenacin HBr_AChR_25uM	AZ 3146_Kinesin_25uM
H 89 2HCl_PKA_25uM	NMS-P937 (NMS1286937)_PLK_25uM	K-Ras(G12C) inhibitor 9_Rho_25uM
Nifedipine_Others_25uM	RLUS-2092D	ABT-263 (Navitoclax)_Bcl-2_25uM
NVP-AEW541_IGF-1R_25uM	MK591_FLAP_25uM	RLUS-2143E
SW202317	Lacidipine_Calcium Channel_25uM	Luteolin_PDE_25uM
Stattic_STAT_25uM	BAPTA-AM_Others_25uM	BAY 11-7082_IkB/IKKE2 conjugating_25uM
IKK-16 (IKK Inhibitor VII)_IkB/IKK_25uM	Mometasone furoate_Others_25uM	Cetylpyridinium Chloride_Others_25uM
GSK2334470_PDK-1_25uM	AS1517499_STAT;STAT_5uM	VER-49009_HSP90_25uM
NVP-BKM120 (Hydrochloride)_PI3K_5uM	A-674563_PKACDKAkt_25uM	BAY 11-7085_NF-kB_25uM
AZD1480_JAK_25uM	Roscovitine (SeliciclibCYC202)_CDK_25uM	Carvedilol_Adrenergic Receptor_25uM
Idebenone_Others_25uM	LY2835219_CDK_25uM	Bay 11-7085_NF-kappa B_25uM
LY2228820_p38 MAPK_25uM	IRAK inhibitor 1_IRAK;IRAK_25uM	Enoxolone_Others_25uM
WP1066_JAK_25uM	R406_SykFLT3_25uM	RLUS-2140D
Montelukast Sodium_Others_25uM	Penfluridol_Others_25uM	KPT-185_CRM1_25uM
RLUS-2142D	Torin 2_ATM/ATRmTOR_25uM	AZD1080_GSK-3_25uM
PP121_DNA-PKPDGFRmTOR_25uM	Ro3280_PLK_25uM	Crenolanib (CP-868596)_PDGFR_25uM
Caffeic Acid Phenethyl Ester_NFKB_25uM	Alexidine HCl_25uM	ZM 447439_Aurora Kinase_25uM
Pizotifen Malate_Others_25uM	SW203050	MK-8776 (SCH 900776)_CDKChk_25uM
HA*-25NMe	SKI II_S1P Receptor_25uM	XL888_HSP (e.g. HSP90)_25uM
RLUS-2146F	TG101209_JAKFLT3c-RET_25uM	Verapamil HCl_Others_25uM
	SB743921_Kinesin_25uM	

Benzethonium Chloride_Others_25uM	RITA (NSC 652287)_E3 Ligase p53_25uM	BMS-794833_VEGFRc-Met_25uM
Deltarasin_PDE_25uM	Tioconazole_Others_25uM	PD184352 (CI-1040)_MEK_25uM
CPI-203_Epigenetic Reader Do_25uM	Mitoxantrone_Topoisomerase_25uM	Mianserin HCl_Histamine Receptor_25uM
JNK-IN-8_JNK_25uM	Econazole nitrate _Others_25uM	CEP-33779_JAK_25uM
1NMe3'-L5ipg	NPS-2143_CaSR_25uM	Palomid 529 (P529)_mTOR_25uM
2-Methoxyestradiol (2-MeOE2)_HIF_25uM	PD318088_MEK_25uM	Bardoxolone Methyl_kB/IKK_25uM
Cyclosporin A _Others_25uM	MRT67307_ULK;Autophagy;IKK_25uM	Golgicide A_ATPase_25uM
PP1_Src_25uM	Duloxetine HCl_5-HT Receptor_25uM	Bafetinib (INNO-406)_Bcr-Abl_25uM
Haloperidol _Others_25uM	Amlodipine _Calcium Channel_25uM	Mitoxantrone HCl_Others_25uM
1NMe33-1Me6F	ZM 39923 HCl_JAK_25uM	Disulfiram _Others_25uM
HO-3867_STAT_25uM	Filgotinib (GLPG0634)_JAK_25uM	NH125_ELF2_25uM
Thioridazine HCl_25uM	OTX015_BET_25uM	Dicyclomine HCl_25uM
Progesterone_Others_25uM	VS-5584 (SB2343)_PI3K_25uM	Beta-Lapachone_Topoisomerase_25uM
Menadione_Others_25uM	PTC-209 HBr_Others_25uM	P22077_DUB_25uM
Canagliflozin_SGLT_25uM	RS-127445_5-HT Receptor_25uM	Oxcarbazepine_Sodium Channel_25uM
	Phenothiazine_Others_25uM	PD168393_EGFR_25uM

EM(ss1)	EM(ss2)	EM(ss1) & EM(ss2)
BMS-345541 (free base)_IKK_25uM	TAK-659 (hydrochloride)_Syk_5uM	SW203056
Cabozantinib malate (XL184)_VEGFR_25uM	Valganciclovir HCl_Others_25uM	Napabucasin_STAT;STAT_5uM
Bakuchiol_p38 MAPK_25uM	Acalisib_PI3K_25uM	SW203055
IKK 16_LRRK2;IKK_25uM	Acalisib_PI3K_5uM	
Cyclosporine _Others_25uM	AST-1306_EGFR_25uM	
1NMe3perNH-26Ala3Cha	ZSTK474_PI3K;Autophagy_25uM	
SW203054	Obatoclox Mesylate (GX15-070)_Bcl-2Autophagy_25uM	
Everolimus (RAD001)_mTOR_25uM	Pitavastatin Calcium _Others_25uM	
Mianserin (hydrochloride)_Histamine Receptor;Histamine Receptor_25uM	ZSTK474_PI3K_25uM	
KPT-330_CRM1_25uM	AM251_Cannabinoid Receptor_25uM	
Zotarolimus(ABT-578)_mTOR_25uM	Nelfinavir Mesylate_HIV Protease_25uM	
KN-93 Phosphate_Others_25uM	TGX-221_PI3K_25uM	
SGC-CBP30_Epigenetic Reader Domain_25uM	INH6_Microtubule Associat_25uM	
Manipipine 2HCl_Calcium Channel_25uM	GS-9973_Syk_5uM	
755-6	LY2409881_IKK_5uM	
Sodium Nitrite_Others_25uM		
Fingolimod_SPHK_5uM		

CTM & EM(ss2)	CTM & EM(ss1) & EM(ss2)	CTM & EM(ss1)
AZD6482_Pi3K_25uM	PRT-060318_Syk_5uM	PD0325901_MEK_25uM
RVX-208_Epigenetic Reader Domain_25uM	Selumetinib (AZD6244)_MEK_25uM	CHIR-99021 (CT99021) HCl_GSK-3_25uM
SW203049	Pimasertib (AS-703026)_MEK_25uM	Mycophenolic acid_Others_25uM
Y-320_Interleukin Related_5uM	AZD8330_MEK_25uM	SKI II_SPHK_5uM
PD173955_BCR-ABL_25uM	TAK-242_Autophagy;Toll-like Receptor (TLR)_5uM	Quizartinib (AC220)_FLT3_25uM
SAR245409 (XL765)_PI3KmTOR_25uM	Dinitolmide_Others_25uM	Aurora A Inhibitor I_Aurora Kinase_25uM
GSK1059615_Pi3KmTOR_25uM	Y-320_Interleukin Related_25uM	Napabucasin_STAT;STAT_25uM
CCT129202_Aurora Kinase_25uM	OSI-027_mTOR_25uM	LY2409881_IKK_25uM
CH5132799_mTORPI3K_25uM	Trametinib (GSK1120212)_MEK_25uM	Mianserin (hydrochloride)_Histamine Receptor;Histamine Receptor_5uM
Cefditoren Pivoxil_Others_25uM	Colistimethate Sodium__25uM	IT1t (dihydrochloride)_CXCR;CXCR_25uM
Varlitinib_EGFR_25uM	GDC-0349_mTOR_25uM	BEZ235 (Tosylate)_PI3K;mTOR;Autophagy_25uM
TWS119_GSK-3_25uM	WYE-125132_mTOR_5uM	AS1517499_STAT;STAT_25uM
Lapatinib_EGFR_25uM	WYE-125132 (WYE-132)_mTOR_25uM	U0126-EtOH_MEK_25uM
Lapatinib (GW-572016)	AZD8055_mTOR_25uM	MEK162 (ARRY-162 ARRY-438162)_MEK_25uM
Ditosylate_HER2EGFR_25uM	KY02111_Wnt/beta-catenin_25uM	ABT-239_Histamine Receptor;Histamine Receptor;TRP Channel_25uM
MI-2 (MALT1 inhibitor)_Others_25uM	BEZ235 (Tosylate)_PI3K;mTOR;Autophagy_5uM	BAY 11-7085_NF-kB_5uM
Doxycycline Hyclate_Others_25uM	BYL719_Pi3K_25uM	Mycophenolate Mofetil_Dehydrogenase_25uM
SW203057	TAK-242_Autophagy;Toll-like Receptor (TLR)_25uM	PF-04691502_AktmTORPI3K_25uM
Fluvastatin Sodium_HMG-CoA Reductase_25uM	AZD2014_mTOR_25uM	WP1066_JAK;JAK;JAK;STAT;STAT_25uM
GS-9973_Syk_25uM	Y-320_Others_25uM	MLPG0634_JAK;JAK;JAK_25uM
	INK 128 (MLN0128)_mTOR_25uM	Azacitidine_DNA Methyltransferase_25uM
	GDC-0980 (RG7422)_mTORPI3K_25uM	
	Vilazodone HCl_Others_25uM	
	PI-103_Pi3KAutophagyDNA-PKmTOR_25uM	
	Santacruzamate A (CAY10683)_HDAC_25uM	
	WYE-125132_mTOR_25uM	
	SW203052	
	Erastin_Ferroptosis_25uM	

SI Table 1. Deep learning primary hits based on the classification accuracy of models CTM (ss1+ss2), EM(ss1), and EM(ss2) using the input format 'resized 1080' and the largest classification training size of 5,632 images.

The binary classification model assigns the unstimulated class 0 and the LPS-stimulated class 1. The goal is to classify images with similar phenotypical expressions as the unstimulated controls and, we specified all classifications between 0 and 0.1 to be 'hits'. The CTM model resulted in a total of 326 hits, EM(ss1) 69 hits, and EM(ss2) 65 hits. Compounds in bold were selected for follow-up.

SI Table 2. Comparison of target classes for EM(ss1) and EM(ss2)

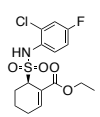
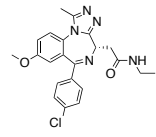
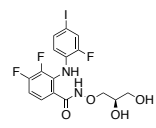
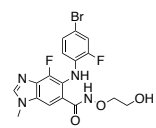
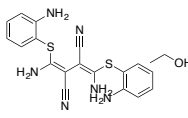
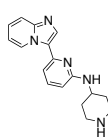
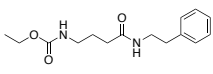
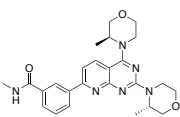
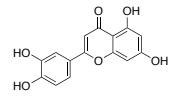
SI Table 2. Comparison of target classes for EM(ss1) and EM(ss2)

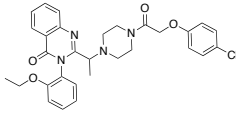
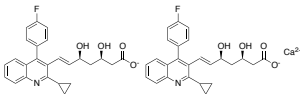
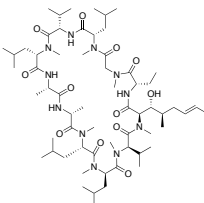
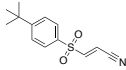
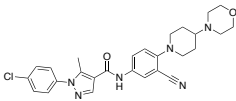
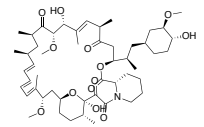
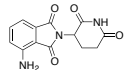
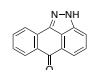
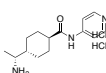
EM(ss1)	EM(ss2)	in common
Calcium Channel	BCR-ABL	Ferroptosis
CXCR	HIV Protease	Autophagy;Toll-like Receptor (TLR)
FLT3	EGFR	IKK
NFkB	Bcl-2Autophagy	Interleukin Related
CRM1	HMG-CoA Reductase	Aurora Kinase
Histamine Receptor	HER2EGFR	Wnt/beta-catenin
Cyclic peptide	Cannabinoid Receptor	STAT
JAK	Microtubule Associated	mTOR
SPHK		PI3K
p38 MAPK		Epigenetic Reader Domain
VEGFR		Syk
Dehydrogenase		HDAC
DNA		GSK-3
Methyltransferase		MEK
		Natural Product

SI Table 2. Comparison of target classes for EM ss1 and ss2. Compound hits with two or more similar annotated target classes reveal unique target classes associated with each stain set. Unique to each stain set are ss1: histamine receptor, JAK, SPHK, and synthetic cyclic peptides, and, for ss2: only EGFR. Those in common between the two stain sets are TLR, Ikk, STAT, mTOR, Syk, MEK, and natural products. However, individual stain sets perform better at detecting certain classes. ss1 detects more target classes such as Ikk, STAT, mTOR, and MEK, whereas, ss2 detects more classes for PI3k, Syk, and natural products.

SI Table 3. Deep learning primary hits for dose response assay

Supplementary Table 2
Deep learning primary hits

	Common Name	Annotation/MOA	Structure	PubChemCID
1	TAK-242/ Resatorvid	TLR4 antagonist		11703255
2	I-BET-762 / Molibresib	Epigenetic Reader Domain inhibitor		46943432
3	PD0325901/ Trametinib	MEK1/2 inhibitor		9826528
4	MEK162/ Binimetinib	MEK1/2 inhibitor		10288191
5	U0126	MEK1/2 inhibitor		73014263
6	IRAK inhibitor-1	IRAK-4 inhibitor		44449078
7	Santacruzmate A	HDAC2 inhibitor		72946782
8	AZD2014	mTORC1 and 2 inhibitor		25262792
9	Luteolin	Phosphodiesterase inhibitor		5280445

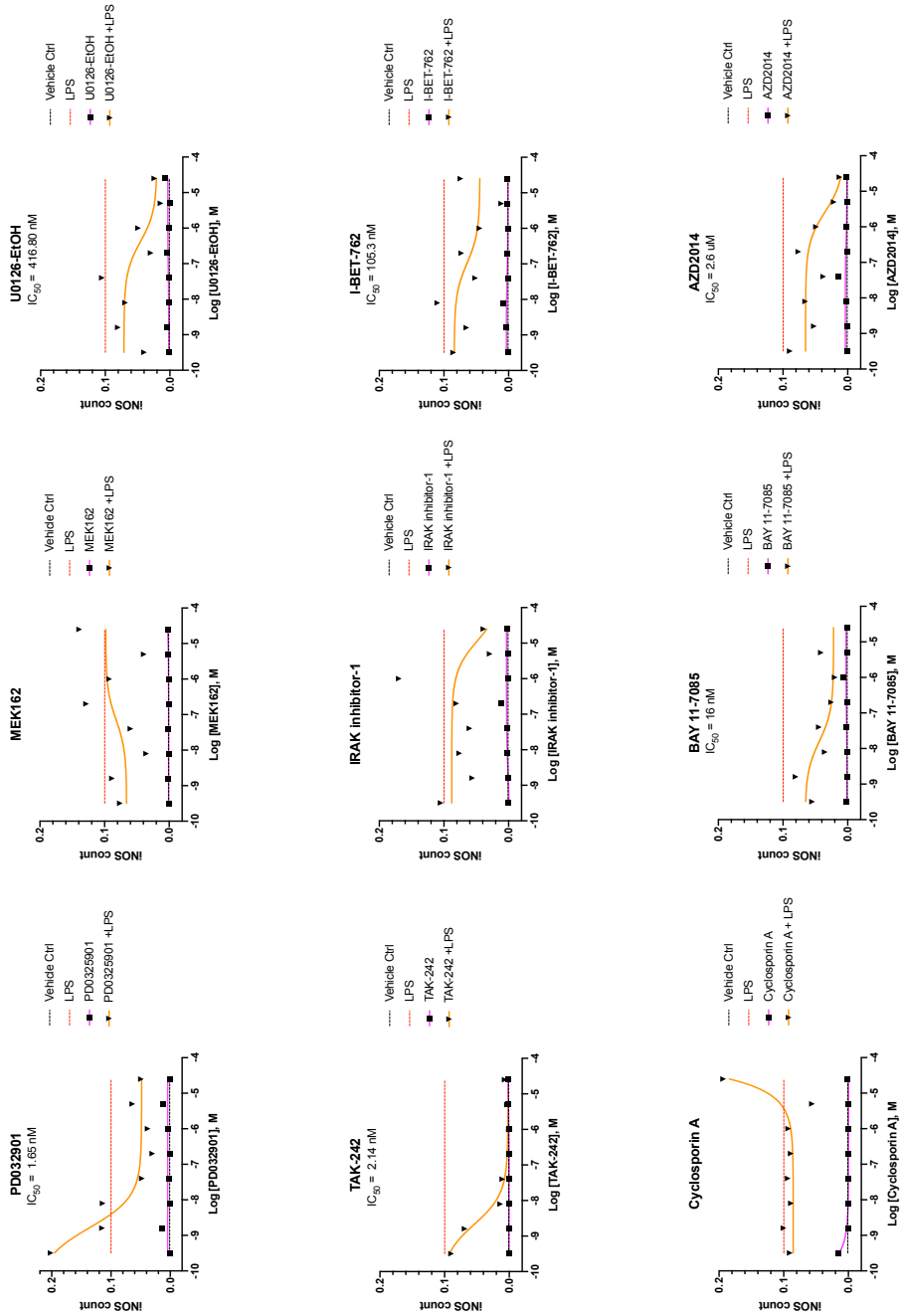
10	Erastin	Ferroptosis inhibitor		11214940
11	Pitavastatin Calcium	HMG-CoA reductase		5282451
12	Cyclosporine A	Calcineurin inhibitor		5284373
13	BAY 11-7085	NFKappa-B inhibitor		5353432
14	Y-320	Interleukin related inhibitor		22227931
15	Rapamycin/Sirolimus*	mTOR inhibitor		5284616
16	Pomalidomide*	TNF-alpha inhibitor		134780
17	SP600125*	JNK inhibitor		8515
18	Y-27632*	ROCK inhibitor		9901617

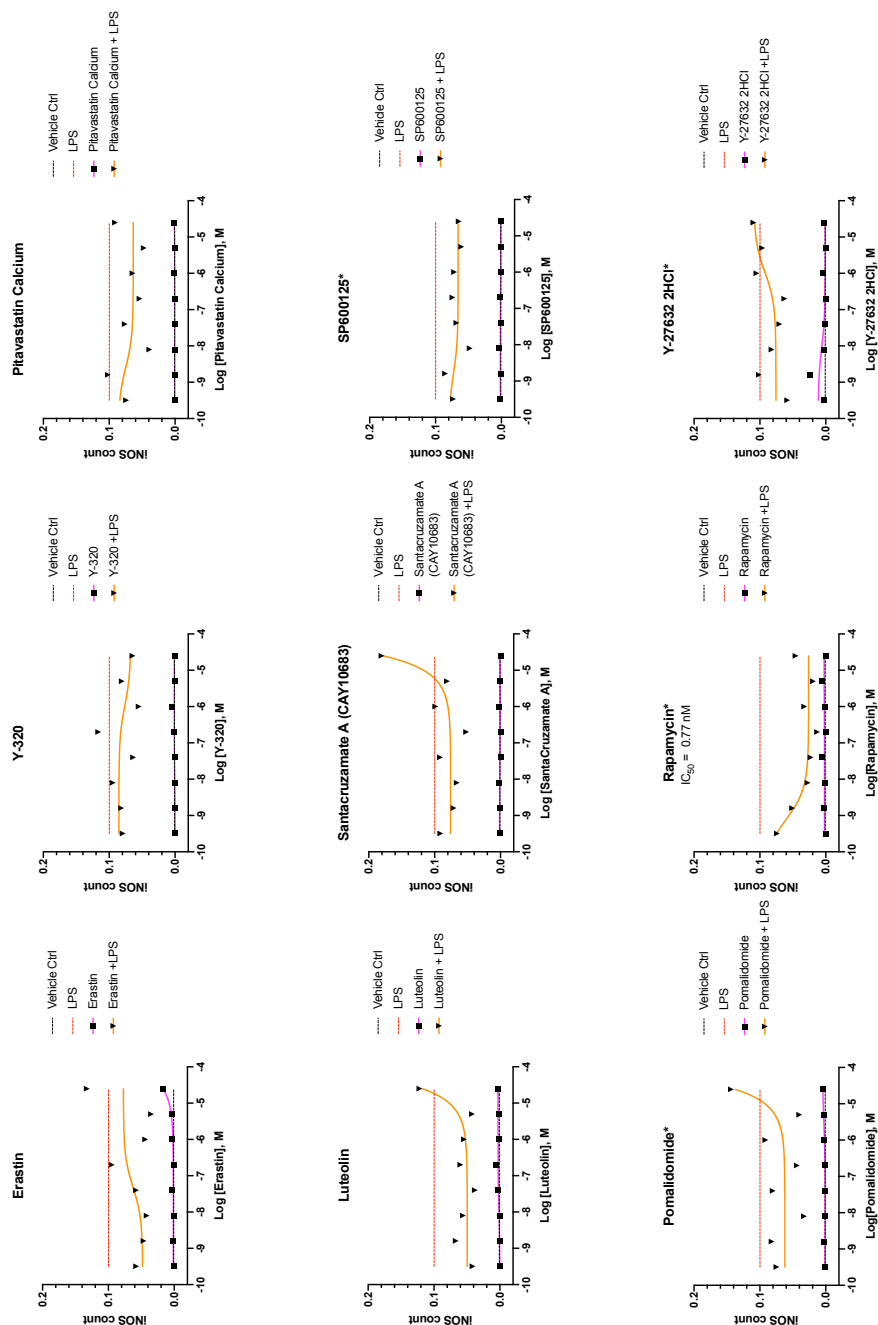
*Not deep learning hits

SI Table 3. Primary hits selected for dose-response follow-up. We selected a subset that represents different mechanistic classes and based on literature precedent could be modulating the innate immune response. We selected thirteen primary deep learning hits and four non-deep learning hits: three annotated as anti-inflammatory and one ROCK inhibitor.

SI Figure 1. iNOS dose-response curves

Deep Learning Hits - iNOS Count Dose-Response

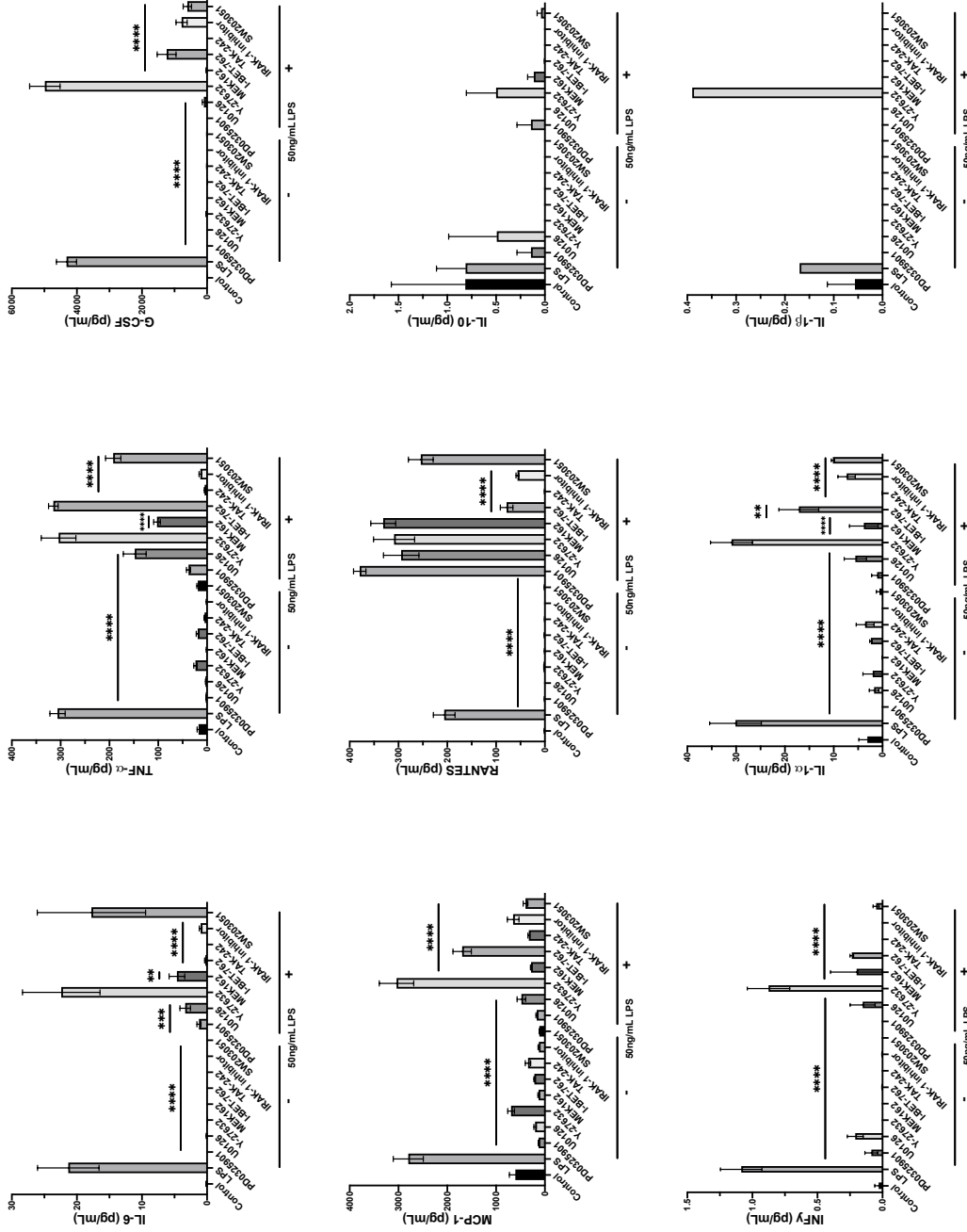


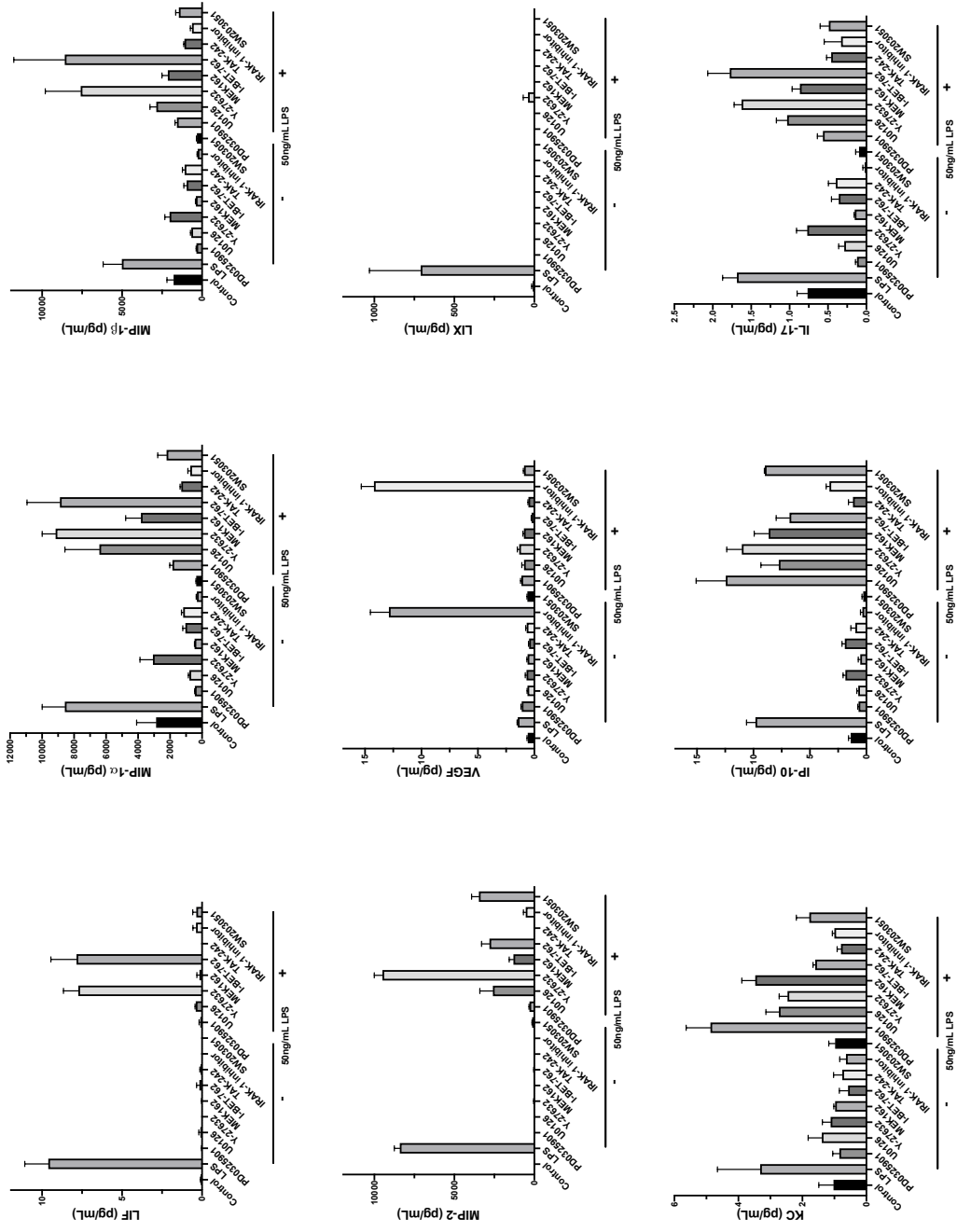


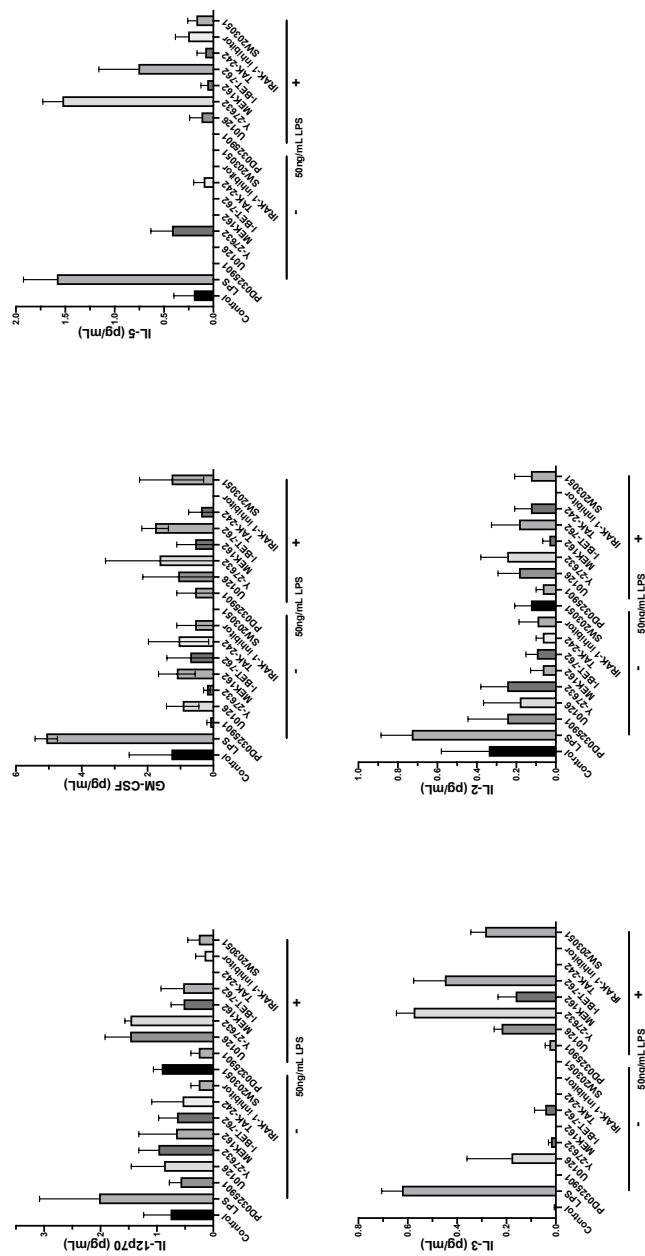
*Not Deep Learning Hits

SI Figure 1. HCS dose-response assay with iNOS. One compound (TAK-242) reduced iNOS counts to baseline levels whereas, six compounds (PD032901, U0126, I-BET-762, Bay 11-7085, AZD2014, and Rapamycin) modestly reduced iNOS counts in a dose-dependent manner. Others have LPS levels of iNOS counts.

SI Figure 2. 32-plex cytokine/chemokine data







SI Figure 2. Raw 32-multiplex cytokine data. Among 32 cytokines examined, 22 cytokines were enhanced, IL-1 α , IL-2, IL-3, IL-4, IL-5, IL-6, IL-9, IL-12(P70), IL-17A, IFN- γ , IP-10, KC, LIF, GM-CSF, G-CSF, MCP-1, MIP-1 α , MIP-1 β , MIP-2, RANTES, TNF- α , and VEGF by LPS-stimulation. Whereas, the other 10 cytokines, IL-1 β , IL-5, IL-7, IL-10, IL-12(P40), IL-13, IL-15, LIX, eotaxin, and MIG were notably low or undetectable in the culture supernatant of the treated samples.

References

- Anwar, M. A., Shah, M., Kim, J., & Choi, S. (2019). Recent clinical trends in Toll-like receptor targeting therapeutics. *Med Res Rev*, *39*(3), 1053-1090. doi:10.1002/med.21553
- Baturcam, E., Vollmer, S., Schluter, H., Maciewicz, R. A., Kurian, N., Vaarala, O., . . . Cunoosamy, D. M. (2019). MEK inhibition drives anti-viral defence in RV but not RSV challenged human airway epithelial cells through AKT/p70S6K/4E-BP1 signalling. *Cell Commun Signal*, *17*(1), 78. doi:10.1186/s12964-019-0378-7
- Belkina, A. C., Nikolajczyk, B. S., & Denis, G. V. (2013). BET protein function is required for inflammation: Brd2 genetic disruption and BET inhibitor JQ1 impair mouse macrophage inflammatory responses. *J Immunol*, *190*(7), 3670-3678. doi:10.4049/jimmunol.1202838
- Bergqvist, F., Sundstrom, Y., Shang, M. M., Gunnarsson, I., Lundberg, I. E., Sundstrom, M., . . . Berg, L. (2020). Anti-Inflammatory Properties of Chemical Probes in Human Whole Blood: Focus on Prostaglandin E2 Production. *Front Pharmacol*, *11*, 613. doi:10.3389/fphar.2020.00613
- Bhattacharya, S., Piya, S., & Borthakur, G. (2018). Bromodomain inhibitors: what does the future hold? *Clin Adv Hematol Oncol*, *16*(7), 504-515. Retrieved from <https://www.ncbi.nlm.nih.gov/pubmed/30067623>
- Bhattacharyya, S., Wang, W., Tamaki, Z., Shi, B., Yeldandi, A., Tsukimi, Y., . . . Varga, J. (2018). Pharmacological Inhibition of Toll-Like Receptor-4 Signaling by TAK242 Prevents and Induces Regression of Experimental Organ Fibrosis. *Front Immunol*, *9*, 2434. doi:10.3389/fimmu.2018.02434
- Bourzac, K. M., Botham, C. M., & Guillemin, K. (2007). Helicobacter pylori CagA induces AGS cell elongation through a cell retraction defect that is independent of Cdc42, Rac1, and Arp2/3. *Infect Immun*, *75*(3), 1203-1213. doi:10.1128/IAI.01702-06
- Cargnello, M., & Roux, P. P. (2011). Activation and function of the MAPKs and their substrates, the MAPK-activated protein kinases. *Microbiol Mol Biol Rev*, *75*(1), 50-83. doi:10.1128/MMBR.00031-10
- Chappell, W. H., Steelman, L. S., Long, J. M., Kempf, R. C., Abrams, S. L., Franklin, R. A., . . . McCubrey, J. A. (2011). Ras/Raf/MEK/ERK and PI3K/PTEN/Akt/mTOR inhibitors: rationale and importance to inhibiting these pathways in human health. *oncotarget*, *2*(3), 135-164. doi:10.18632/oncotarget.240
- Cheng, Y., & Tian, H. (2017). Current Development Status of MEK Inhibitors. *Molecules*, *22*(10). doi:10.3390/molecules22101551

- Christophe, T., Ewann, F., Jeon, H. K., Cechetto, J., & Brodin, P. (2010). High-content imaging of *Mycobacterium tuberculosis*-infected macrophages: an in vitro model for tuberculosis drug discovery. *Future Med Chem*, 2(8), 1283-1293. doi:10.4155/fmc.10.223
- Cochran, A. G., Conery, A. R., & Sims, R. J., 3rd. (2019). Bromodomains: a new target class for drug development. *Nat Rev Drug Discov*, 18(8), 609-628. doi:10.1038/s41573-019-0030-7
- Correa-da-Silva, F., Pereira, J. A. S., de Aguiar, C. F., & de Moraes-Vieira, P. M. M. (2018). Mitoimmunity-when mitochondria dictates macrophage function. *Cell Biol Int*, 42(6), 651-655. doi:10.1002/cbin.10921
- Dinareello, C. A. (2010). Anti-inflammatory Agents: Present and Future. *Cell*, 140(6), 935-950. doi:10.1016/j.cell.2010.02.043
- Ding, J., & Liu, Q. (2019). Toll-like receptor 4: A promising therapeutic target for pneumonia caused by Gram-negative bacteria. *J Cell Mol Med*, 23(9), 5868-5875. doi:10.1111/jcmm.14529
- Eswarappa, S. M., Pareek, V., & Chakravorty, D. (2008). Role of actin cytoskeleton in LPS-induced NF-kappaB activation and nitric oxide production in murine macrophages. *Innate Immun*, 14(5), 309-318. doi:10.1177/1753425908096856
- Faust, J. J., Balabiyev, A., Heddleston, J. M., Podolnikova, N. P., Baluch, D. P., Chew, T.-L., . . . Théry, M. (2019). An actin-based protrusion originating from a podosome-enriched region initiates macrophage fusion. *Molecular Biology of the Cell*, 30(17), 2254-2267. doi:10.1091/mbc.E19-01-0009
- Hanania, R., Sun, H. S., Xu, K., Pustyl'nik, S., Jeganathan, S., & Harrison, R. E. (2012). Classically activated macrophages use stable microtubules for matrix metalloproteinase-9 (MMP-9) secretion. *J Biol Chem*, 287(11), 8468-8483. doi:10.1074/jbc.M111.290676
- Hu, G., Su, Y., Kang, B. H., Fan, Z., Dong, T., Brown, D. R., . . . Chen, J. (2021). High-throughput phenotypic screen and transcriptional analysis identify new compounds and targets for macrophage reprogramming. *Nat Commun*, 12(1), 773. doi:10.1038/s41467-021-21066-x
- Isowa, N., Keshavjee, S. H., & Liu, M. (2000). Role of microtubules in LPS-induced macrophage inflammatory protein-2 production from rat pneumocytes. *Am J Physiol Lung Cell Mol Physiol*, 279(6), L1075-1082. doi:10.1152/ajplung.2000.279.6.L1075
- Jaffee, B. D., Manos, E. J., Collins, R. J., Czerniak, P. M., Favata, M. F., Magolda, R. L., . . . Trzaskos, J. M. (2000). Inhibition of MAP kinase kinase (MEK) results in an anti-inflammatory response in vivo. *Biochem Biophys Res Commun*, 268(2), 647-651. doi:10.1006/bbrc.2000.2184

- Kapetanovic, R., Afroz, S. F., Ramnath, D., Lawrence, G. M., Okada, T., Curson, J. E., . . . Sweet, M. J. (2020). Lipopolysaccharide promotes Drp1-dependent mitochondrial fission and associated inflammatory responses in macrophages. *Immunol Cell Biol*, 98(7), 528-539. doi:10.1111/imcb.12363
- Kasahara, E., Sekiyama, A., Hori, M., Hara, K., Takahashi, N., Konishi, M., . . . Inoue, M. (2011). Mitochondrial density contributes to the immune response of macrophages to lipopolysaccharide via the MAPK pathway. *FEBS Lett*, 585(14), 2263-2268. doi:10.1016/j.febslet.2011.05.049
- Koch, P. D., Miller, H. R., Yu, G., Tallarico, J. A., Sorger, P. K., Wang, Y., . . . Mitchison, T. (2018). A High Content Screen in Macrophages Identifies Small Molecule Modulators of STING-IRF3 and NFkB Signaling. *ACS Chem Biol*, 13(4), 1066-1081. doi:10.1021/acscchembio.7b01060
- Koziczak-Holbro, M., Gluck, A., Tschopp, C., Mathison, J. C., & Gram, H. (2008). IRAK-4 kinase activity-dependent and -independent regulation of lipopolysaccharide-inducible genes. *Eur J Immunol*, 38(3), 788-796. doi:10.1002/eji.200737886
- Kurian, N., Cohen, T. S., Oberg, L., De Zan, E., Skogberg, G., Vollmer, S., . . . Cunoosamy, D. M. (2019). Dual Role For A MEK Inhibitor As A Modulator Of Inflammation And Host Defense Mechanisms With Potential Therapeutic Application In COPD. *Int J Chron Obstruct Pulmon Dis*, 14, 2611-2624. doi:10.2147/COPD.S211619
- Kuzmich, N. N., Sivak, K. V., Chubarev, V. N., Porozov, Y. B., Savateeva-Lyubimova, T. N., & Peri, F. (2017). TLR4 Signaling Pathway Modulators as Potential Therapeutics in Inflammation and Sepsis. *Vaccines (Basel)*, 5(4). doi:10.3390/vaccines5040034
- Li, P., Wu, Y., Li, M., Qiu, X., Bai, X., & Zhao, X. (2015). AS-703026 Inhibits LPS-Induced TNFalpha Production through MEK/ERK Dependent and Independent Mechanisms. *PLoS One*, 10(9), e0137107. doi:10.1371/journal.pone.0137107
- Liu, L., Lu, Y., Martinez, J., Bi, Y., Lian, G., Wang, T., . . . Wang, R. (2016). Proinflammatory signal suppresses proliferation and shifts macrophage metabolism from Myc-dependent to HIF1alpha-dependent. *Proc Natl Acad Sci U S A*, 113(6), 1564-1569. doi:10.1073/pnas.1518000113
- Liu, Y., Tejpal, N., You, J., Li, X. C., Ghobrial, R. M., & Kloc, M. (2016). ROCK inhibition impedes macrophage polarity and functions. *Cell Immunol*, 300, 54-62. doi:10.1016/j.cellimm.2015.12.005
- Long, M. E., Eddy, W. E., Gong, K. Q., Lovelace-Macon, L. L., McMahan, R. S., Charron, J., . . . Manicone, A. M. (2017). MEK1/2 Inhibition Promotes Macrophage Reparative Properties. *J Immunol*, 198(2), 862-872. doi:10.4049/jimmunol.1601059

- Long, M. E., Gong, K. Q., Eddy, W. E., Liles, W. C., & Manicone, A. M. (2017). Pharmacologic inhibition of MEK1/2 reduces lung inflammation without impairing bacterial clearance in experimental *Pseudomonas aeruginosa* pneumonia. *Pneumonia (Nathan)*, *9*, 13. doi:10.1186/s41479-017-0037-y
- Lu, Y. C., Yeh, W. C., & Ohashi, P. S. (2008). LPS/TLR4 signal transduction pathway. *Cytokine*, *42*(2), 145-151. doi:10.1016/j.cyto.2008.01.006
- Mages, J., Dietrich, H., & Lang, R. (2007). A genome-wide analysis of LPS tolerance in macrophages. *Immunobiology*, *212*(9-10), 723-737. doi:10.1016/j.imbio.2007.09.015
- Maksylewicz, A., Bysiek, A., Lagosz, K. B., Macina, J. M., Kantorowicz, M., Bereta, G., . . . Grabcic, A. M. (2019). BET Bromodomain Inhibitors Suppress Inflammatory Activation of Gingival Fibroblasts and Epithelial Cells From Periodontitis Patients. *Front Immunol*, *10*, 933. doi:10.3389/fimmu.2019.00933
- Marshall, J. C. (2014). Why have clinical trials in sepsis failed? *Trends Mol Med*, *20*(4), 195-203. doi:10.1016/j.molmed.2014.01.007
- McWhorter, F. Y., Davis, C. T., & Liu, W. F. (2015). Physical and mechanical regulation of macrophage phenotype and function. *Cell Mol Life Sci*, *72*(7), 1303-1316. doi:10.1007/s00018-014-1796-8
- Meng, S., Zhang, L., Tang, Y., Tu, Q., Zheng, L., Yu, L., . . . Chen, J. (2014). BET Inhibitor JQ1 Blocks Inflammation and Bone Destruction. *J Dent Res*, *93*(7), 657-662. doi:10.1177/0022034514534261
- Mullard, A. (2020). IRAK4 degrader to take on innate immunity. *Nat Biotechnol*, *38*(11), 1221-1223. doi:10.1038/s41587-020-0724-8
- Nagatoya, K., Moriyama, T., Kawada, N., Takeji, M., Oseto, S., Murozono, T., . . . Hori, M. (2002). Y-27632 prevents tubulointerstitial fibrosis in mouse kidneys with unilateral ureteral obstruction. *Kidney Int*, *61*(5), 1684-1695. doi:10.1046/j.1523-1755.2002.00328.x
- Nicodeme, E., Jeffrey, K. L., Schaefer, U., Beinke, S., Dewell, S., Chung, C. W., . . . Tarakhovsky, A. (2010). Suppression of inflammation by a synthetic histone mimic. *Nature*, *468*(7327), 1119-1123. doi:10.1038/nature09589
- Nobutaka Suzuki, S. S. a. W.-C. Y. (2002). IRAK-4 as the central TIR signaling mediator in innate immunity. *TRENDS in Immunology*, *23*, 503-506. doi:doi:10.1016/s1471-4906(02)02298-6
- Omta, W. A., van Heesbeen, R. G., Pagliero, R. J., van der Velden, L. M., Lelieveld, D., Nellen, M., . . . Egan, D. A. (2016). HC StratoMineR: A Web-Based Tool for the Rapid Analysis of High-Content Datasets. *Assay Drug Dev Technol*, *14*(8), 439-452. doi:10.1089/adt.2016.726

- Ono, Y., Maejima, Y., Saito, M., Sakamoto, K., Horita, S., Shimomura, K., . . . Kotani, J. (2020). TAK-242, a specific inhibitor of Toll-like receptor 4 signalling, prevents endotoxemia-induced skeletal muscle wasting in mice. *Sci Rep*, *10*(1), 694. doi:10.1038/s41598-020-57714-3
- Opal, S. M., Laterre, P. F., Francois, B., LaRosa, S. P., Angus, D. C., Mira, J. P., . . . Group, A. S. (2013). Effect of eritoran, an antagonist of MD2-TLR4, on mortality in patients with severe sepsis: the ACCESS randomized trial. *JAMA*, *309*(11), 1154-1162. doi:10.1001/jama.2013.2194
- Park, S. H., Baek, S. I., Yun, J., Lee, S., Yoon, D. Y., Jung, J. K., . . . Kim, Y. (2015). IRAK4 as a molecular target in the amelioration of innate immunity-related endotoxic shock and acute liver injury by chlorogenic acid. *J Immunol*, *194*(3), 1122-1130. doi:10.4049/jimmunol.1402101
- Park, S. H., Roh, E., Kim, H. S., Baek, S. I., Choi, N. S., Kim, N., . . . Kim, Y. (2013). Inhibition of IRAK-4 activity for rescuing endotoxin LPS-induced septic mortality in mice by *Ionicerae flos* extract. *Biochem Biophys Res Commun*, *442*(3-4), 183-188. doi:10.1016/j.bbrc.2013.11.045
- Perry, M. M., Durham, A. L., Austin, P. J., Adcock, I. M., & Chung, K. F. (2015). BET bromodomains regulate transforming growth factor-beta-induced proliferation and cytokine release in asthmatic airway smooth muscle. *J Biol Chem*, *290*(14), 9111-9121. doi:10.1074/jbc.M114.612671
- Picard, C., Puel, A., Bonnet, M., Ku, C. L., Bustamante, J., Yang, K., . . . Casanova, J. L. (2003). Pyogenic bacterial infections in humans with IRAK-4 deficiency. *Science*, *299*(5615), 2076-2079. doi:10.1126/science.1081902
- Ramond, E., Jamet, A., Coureuil, M., & Charbit, A. (2019). Pivotal Role of Mitochondria in Macrophage Response to Bacterial Pathogens. *Front Immunol*, *10*, 2461. doi:10.3389/fimmu.2019.02461
- Rao, J., Ye, Z., Tang, H., Wang, C., Peng, H., Lai, W., . . . Lou, T. (2017). The RhoA/ROCK Pathway Ameliorates Adhesion and Inflammatory Infiltration Induced by AGEs in Glomerular Endothelial Cells. *Sci Rep*, *7*, 39727. doi:10.1038/srep39727
- Rostam, H. M., Reynolds, P. M., Alexander, M. R., Gadegaard, N., & Ghaemmaghami, A. M. (2017). Image based Machine Learning for identification of macrophage subsets. *Sci Rep*, *7*(1), 3521. doi:10.1038/s41598-017-03780-z
- Rudman, M. D., Choi, J. S., Lee, H. E., Tan, S. K., Ayad, N. G., & Lee, J. K. (2018). Bromodomain and extraterminal domain-containing protein inhibition attenuates acute inflammation after spinal cord injury. *Exp Neurol*, *309*, 181-192. doi:10.1016/j.expneurol.2018.08.005

- Samarpita, S., Kim, J. Y., Rasool, M. K., & Kim, K. S. (2020). Investigation of toll-like receptor (TLR) 4 inhibitor TAK-242 as a new potential anti-rheumatoid arthritis drug. *Arthritis Res Ther*, 22(1), 16. doi:10.1186/s13075-020-2097-2
- Sanchez-Ventura, J., Amo-Aparicio, J., Navarro, X., & Penas, C. (2019). BET protein inhibition regulates cytokine production and promotes neuroprotection after spinal cord injury. *J Neuroinflammation*, 16(1), 124. doi:10.1186/s12974-019-1511-7
- Shi-Lin, D., Yuan, X., Zhan, S., Luo-Jia, T., & Chao-Yang, T. (2015). Trametinib, a novel MEK kinase inhibitor, suppresses lipopolysaccharide-induced tumor necrosis factor (TNF)-alpha production and endotoxin shock. *Biochem Biophys Res Commun*, 458(3), 667-673. doi:10.1016/j.bbrc.2015.01.160
- Siqueira-Neto, J. L., Moon, S., Jang, J., Yang, G., Lee, C., Moon, H. K., . . . Freitas-Junior, L. H. (2012). An image-based high-content screening assay for compounds targeting intracellular *Leishmania donovani* amastigotes in human macrophages. *PLoS Negl Trop Dis*, 6(6), e1671. doi:10.1371/journal.pntd.0001671
- Smith, J. A., Mayeux, P. R., & Schnellmann, R. G. (2016). Delayed Mitogen-Activated Protein Kinase/Extracellular Signal-Regulated Kinase Inhibition by Trametinib Attenuates Systemic Inflammatory Responses and Multiple Organ Injury in Murine Sepsis. *Crit Care Med*, 44(8), e711-720. doi:10.1097/CCM.0000000000001672
- Tan, M., & Le, Q. V. (2020). EfficientNet- Rethinking Model Scaling for Convolutional Neural Networks. *International Conference on Machine Learning, 2019*. Retrieved from arXiv:1905.11946v5
- Tao, Y., Yang, Y., Zhou, R., & Gong, T. (2020). Golgi Apparatus: An Emerging Platform for Innate Immunity. *Trends Cell Biol*, 30(6), 467-477. doi:10.1016/j.tcb.2020.02.008
- Tasaka, S., Koh, H., Yamada, W., Shimizu, M., Ogawa, Y., Hasegawa, N., . . . Ishizaka, A. (2005). Attenuation of endotoxin-induced acute lung injury by the Rho-associated kinase inhibitor, Y-27632. *Am J Respir Cell Mol Biol*, 32(6), 504-510. doi:10.1165/rcmb.2004-0009OC
- Tough, D. F., Tak, P. P., Tarakhovsky, A., & Prinjha, R. K. (2016). Epigenetic drug discovery: breaking through the immune barrier. *Nat Rev Drug Discov*, 15(12), 835-853. doi:10.1038/nrd.2016.185
- Vadiveloo, P. K., Keramidaris, E., Morrison, W. A., & Stewart, A. G. (2001). Lipopolysaccharide-induced cell cycle arrest in macrophages occurs independently of nitric oxide synthase II induction. *Biochim Biophys Acta*, 1539(1-2), 140-146. doi:10.1016/s0167-4889(01)00102-1
- Wang, H., Fu, H., Zhu, R., Wu, X., Ji, X., Li, X., . . . Chen, H. (2020). BRD4 contributes to LPS-induced macrophage senescence and promotes progression of atherosclerosis-associated lipid uptake. *Aging (Albany NY)*, 12(10), 9240-9259. doi:10.18632/aging.103200

- Wiese, M. D., Manning-Bennett, A. T., & Abuhelwa, A. Y. (2020). Investigational IRAK-4 inhibitors for the treatment of rheumatoid arthritis. *Expert Opin Investig Drugs*, 29(5), 475-482. doi:10.1080/13543784.2020.1752660
- Woehrmann, M. H., Bray, W. M., Durbin, J. K., Nisam, S. C., Michael, A. K., Glassey, E., . . . Lokey, R. S. (2013). Large-scale cytological profiling for functional analysis of bioactive compounds. *Mol Biosyst*, 9(11), 2604-2617. doi:10.1039/c3mb70245f
- Wu, J., Li, M., Liu, L., An, Q., Zhang, J., Zhang, J., . . . Luo, C. (2013). Nitric oxide and interleukins are involved in cell proliferation of RAW264.7 macrophages activated by viili exopolysaccharides. *Inflammation*, 36(4), 954-961. doi:10.1007/s10753-013-9626-y
- Yang, L., & Ding, J. L. (2019). MEK1/2 Inhibitors Unlock the Constrained Interferon Response in Macrophages Through IRF1 Signaling. *Front Immunol*, 10, 2020. doi:10.3389/fimmu.2019.02020
- Zi Zhao Lieu, J. G. L., Luke A. Hammond, Nicole L. La Gruta, Jennifer L. Stow, and Paul A. Gleeson. (2008). A trans-Golgi network golgin is required for the regulated secretion of TNF in activated macrophages in vivo. *Proceedings of the National Academy of Sciences*, 105, 3351-3356. doi:doi:10.1073/pnas.0800137105

2.3 Online image viewer database: <https://immunocp.pbsci.ucsc.edu/>

The following work was a collaboration between:

Tannia A. Lau¹, Joe Lau³, Alison Lindberg², Rion Parsons²

¹Department of Chemistry and Biochemistry, University of California Santa Cruz,
Santa Cruz, California

²ADC/PBSci IT Services, University of California Santa Cruz, Santa Cruz, California

³No Affiliation, San Francisco, CA

HCS image accessibility challenges

High throughput image-based screen image accessibility is challenging due to restrictive commercial software accessibility and overwhelming data sizes that require meticulous management and organization. Also, online image repositories entail complicated user interface formats or fees depending on data size. For reference a single screen of ~3,000 test compounds will generate >500 gigabytes (GB) of imaging data. Therefore, we developed an online custom-built image viewing database that allows for quick and easy inspection of images from our HCS screens. Direct image inspection of your compounds of interest is complicated with current commercial software which limits the user to open these images one at a time from each screening plate without associated compound information. This database brings side-by-side comparisons of macrophages treated with compounds \pm LPS stimuli and both stain sets. Also, it includes a search function and access to metadata about the compound's structure, molecular targets, solubility, and concentration. These images are accessible to the public via website <https://immunocp.pbsci.ucsc.edu/experiment>.

The HCS project and data generated

Raw264.7 cells were seeded at a density of 2,500 cells/well and incubated at 37 degrees Celsius and 5 % carbon dioxide 24 hours before pinning with test compounds. 11 drug plates: SP0135-SP0141 [25uM], SP20264 [50ug/mL], SP20265 [50ug/mL], SP40188 [37.5uM], and SP20299 [25uM and 5uM] x 2 conditions +/- 50ng/mL LPS x 2 stain sets (ss1: nuclei, Golgi, actin, pHH3 and ss2: nuclei, tubulin, EdU, mitochondria) = 44

total 384 well plates. The screen was split in half to manage all of the plates. The first stain set (ss1) was screened in a set of 20 plates (10 drug plates listed above, not including SP20299). Soon after another set of 24 plates were screened for the second stain set (ss2), this time including SP20299 (probing both ss1 and ss2). Each plate has control wells DMSO (column 1-2) and LPS (column 23-24). All 44 plates are pre-treated with the compound for 4 hours then half the plates (22) are treated with media alone and the other half (22) are treated with 50ng/mL LPS and media. Following 24 hours later, 40uL of supernatant is collected into a new 384 well plate and frozen for potential secondary assays (ex. cytokine) follow-up. Then cells are fixed and stained and imaged on a MicroXLS Molecular Devices automated microscope at 20x. Imaging 4 channels (DAPI, FITC, TRITC, and Cy5) and 4 sites/well = 16 images/well. Each image is 2.3 megabytes (MB) and 1080 x 1080 pixels. Each 384 well plate generates ~15 gigabytes (GB) of image data (.tiff format). 15GB x 44 experiments (384 well plates) = 660 GB total. In order to make this into a website friendly format, we converted the .tiff images to .jpg and pseudo-colored each channel: nuclei (blue), Golgi/Tubulin (green), Actin/EdU (yellow), and pHH3/mitochondria (red). In addition to the pseudo-colored single channel .jpg images we merged the composites of the respective channels creating an overlay image. This .tiff to .jpg conversion reduced the image data size of 15GB to 2GB/384 well plate and 88GB total. We project to generate a minimum of 10 terabytes (TB) of images in the next 5 years.

Overcoming image accessibility barriers with costume-built online image database

The website was developed with a combination of technologies for powering the web application. Frontend and business logic are powered by Javascript via the NodeJS framework and backend models are handled by Postgresql. The website layout allows for the researcher to view the whole drug plate layout under "Experiment" (**Fig.1**) or based on various search criteria under "Molecule" (**Fig.2**). The ability to search based on the compound name or other characteristics (ex. target, pathway, plate map, etc...) allows for quick and easy interrogation of your compound of interest. Furthermore, metadata from the chemical library supplier accompanies the compound, including the SMILE strings which are converted to the structure on the website.

Taken together, the image accessibility of Raw264.7 cells +/- LPS treated with annotated and unknown chemical libraries in this format is the first of it's kind and is geared toward easy inspection of images for collaborators.

2.3 FIGURES FOR Online Image Viewer Database

The screenshot displays the 'Experiments' tab of the Online Image Viewer Database. At the top, there is a search bar and a 'Column visibility' dropdown. Below this is a table listing experiments with the following columns: Experiment, platemap name, image name, measurement name, cell lines, magnification, experiment date, ixmw1, ixmw2, ixmw3, and ixmw4. The table contains 14 rows of data, each representing a different experiment with unique identifiers and parameters.

Experiment	platemap name	image name	measurement name	cell lines	magnification	experiment date	ixmw1	ixmw2	ixmw3	ixmw4
190905-RAW-SP0135-CYTO-20x	SP0135_web.csv	IXM5845	MX4865	RAW	20x	20190905	Nuclei	Golgi	Actin	pHH3
190905-RAW-SP0136-CYTO-20x	SP0136_web.csv	IXM5846	MX4864	RAW	20x	20190905	Nuclei	Golgi	Actin	pHH3
190905-RAW-SP0138-CYTO-20x	SP0138_web.csv	IXM5848	MX4862	RAW	20x	20190905	Nuclei	Golgi	Actin	pHH3
190905-RAW-SP0137-CYTO-20x	SP0137_web.csv	IXM5847	MX4863	RAW	20x	20190905	Nuclei	Golgi	Actin	pHH3
190905-RAW-SP0139-CYTO-20x	SP0139_web.csv	IXM5849	MX4861	RAW	20x	20190905	Nuclei	Golgi	Actin	pHH3
190905-RAW-SP0140-CYTO-20x	SP0140_web.csv	IXM5850	MX4860	RAW	20x	20190905	Nuclei	Golgi	Actin	pHH3
190905-RAW-SP0141-CYTO-20x	SP0141_web.csv	IXM5851	MX4928	RAW	20x	20190905	Nuclei	Golgi	Actin	pHH3
190905-RAW-SP20264-CYTO-20x	SP20264_web.csv	IXM5854	MX4857	RAW	20x	20190905	Nuclei	Golgi	Actin	pHH3
190905-RAW-SP40188-CYTO-20x	SP40188_web.csv	IXM5852	MX4858	RAW	20x	20190905	Nuclei	Golgi	Actin	pHH3
190905-RAW-SP20265-CYTO-20x	SP20265_web.csv	IXM5856	MX4855	RAW	20x	20190905	Nuclei	Golgi	Actin	pHH3
190905-RAW-SP40188-CYTO-20x	SP40188_web.csv	IXM5857	MX4859	RAW	20x	20190905	Nuclei	Golgi	Actin	pHH3

Below the table, the interface shows a grid of 12 panels. Each panel contains a 2x2 grid of fluorescence microscopy images (top) and a chemical structure diagram (bottom). The images show cells stained for various markers, and the chemical structures represent the compounds used in the experiments. The bottom part of the interface displays a detailed metadata table for each experiment, including columns for Experiment, Compound, Cell Line, Magnification, Experiment Date, and Image Wells (ixmw1-4).

Figure 1. Experiment tab: displays a list of experiments and shows the entire drug plate layout.

Clicking one or more compound(s) will display images from experiments +/- LPS and both stain sets. This enables you to visualize these images side-by-side. They are all accompanied with metadata as well as chemical structures.

Chrome File Edit View History Bookmarks People Tab Window Help

https://immunocp.pbsci.ucsc.edu/molecule

Let Experiment & Molecule Upload

Molecules

Show 50 entries

Select all Deselect all Column visibility

Search:

name	info	molarity_nm	pathway	targets	cell	platemap
Nepafenac	Nepafenac is a non-steroidal anti-inflammatory agent.	10	Others	Others	B07	SP0130_web.csv
Rolipram	Rolipram is a PDE4-inhibitor and an anti-inflammatory agent.Phase 1.	10	Metabolism	PDE	J10	SP0135_web.csv
Cloimilast	Cloimilast is a potent PDE4 inhibitor with IC50 of about 110 nM, has anti-inflammatory activity and low central nervous system activity.	10	Metabolism	PDE	L14	SP0135_web.csv
Betamethasone	Betamethasone is a glucocorticoid steroid with anti-inflammatory and immunosuppressive properties.	10	Others	Others	L22	SP0135_web.csv
Resveratrol	Resveratrol is a phytoalexin produced naturally by several plants with anti-cancer, anti-inflammatory, blood-sugar-lowering and other beneficial cardiovascular effects.	10	Epigenetics	Sirtuin, Autophagy	N06	SP0135_web.csv
Dexamethasone (DHAP)	Dexamethasone is an anti-inflammatory and immunosuppressant.	10	Others	Autophagy, IL Receptor	N15	SP0135_web.csv
Betamethasone Dipropionate (Dipropione)	Betamethasone Dipropionate is a glucocorticoid steroid with anti-inflammatory and immunosuppressive abilities.	10			A08	SP0130_web.csv
Sulindac	Sulindac (Clinoril) is a non-steroidal anti-inflammatory agent of the arylalkanoic acid class.	10	Others	Others	B06	SP0130_web.csv

Search name: anti-inflammatory Search molarity_nm: Search pathway: Search targets: Search cell: Search platemap:

Showing 1 to 50 of 97 entries 0 rows selected

Previous Next

Selected molecules

Nepafenac Rolipram Cloimilast Betamethasone Resveratrol Dexamethasone (DHAP) Betamethasone Dipropionate (Dipropione) Sulindac

View molecules +

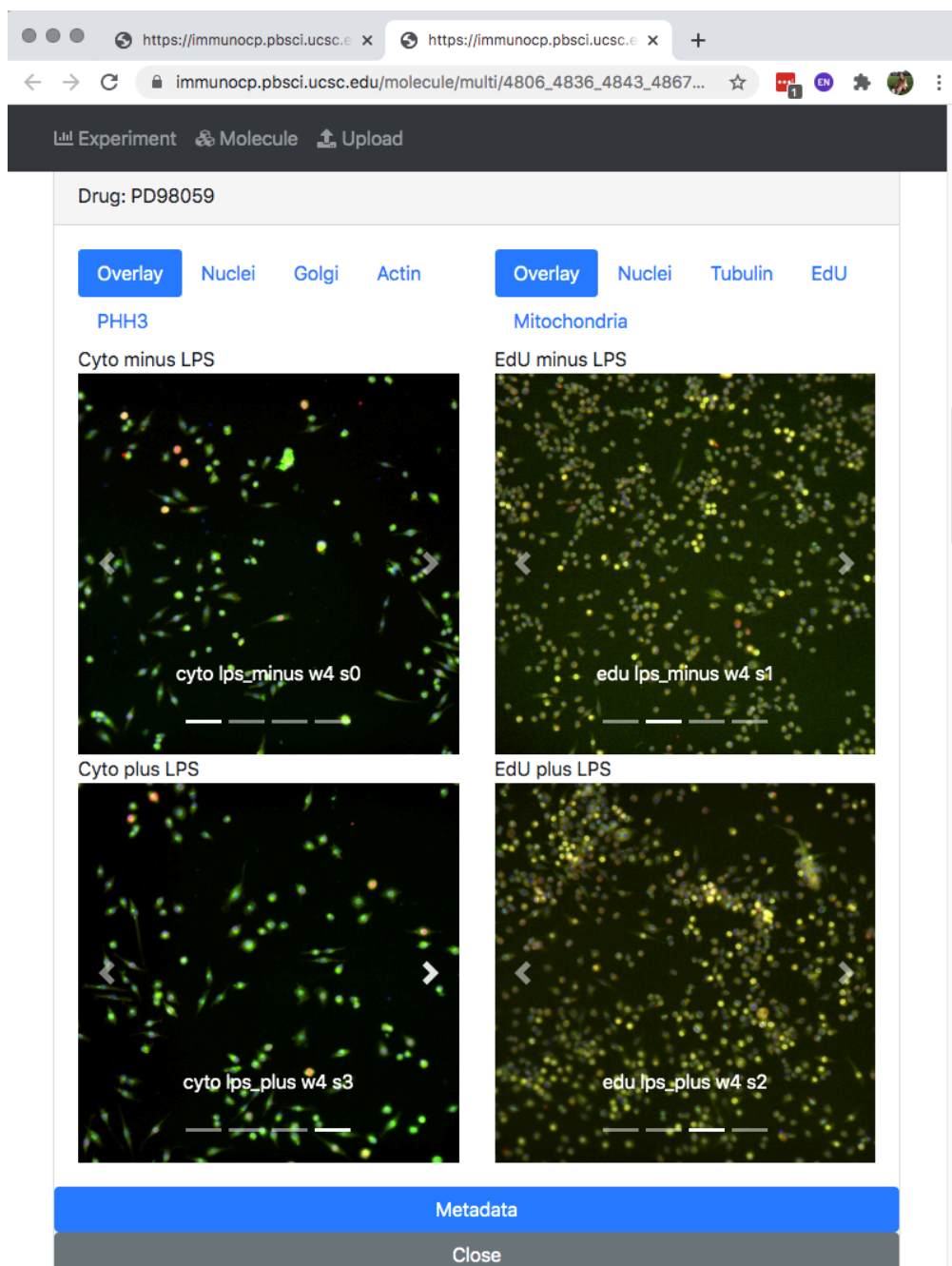


Figure 2. Molecule tab: displays a list of molecules and provides search options to narrow your search.

Selecting the molecules of choice from the list and the "plus (+) sign" button will add your compounds to the "Selected Molecule" list. Once you are finished compiling your list you click "View Molecules". A new page will appear and images of your selected molecules will appear.

Thank you!